University of Liège
School of Engineering
Department of Electrical Engineering & Computer Science

MODELLING AND CONTROL OF ACTIVE DISTRIBUTION NETWORKS

a PhD dissertation

by Antonin Colot

Thesis submitted in partial fullfilment of the requirements for the Degree of Doctor of Philosophy (PhD) in Engineering Science.

Advisor:
Professor Bertrand Cornélusse
May 2025

JURY MEMBERS

Louveaux Quentin, Université de Liège, President;

Cornélusse Bertrand, Université de Liège, Advisor;

Paoletti Simone, University of Siena;

Giannitrapani Antonio, University of Siena;

Dall'Anese Emiliano, Boston University;

Frebel Fabrice, Université de Liège;

Chaspierre Gilles, Elia Grid International;

ABSTRACT

Modern power systems face massive integration of distributed energy resources (small and modular energy generation or storage) interfaced with electrical distribution networks through power electronic converters. Active distribution networks are the result of this integration, where the distribution network is no longer a passive load sink, but actively participates in the power system operation. Power converters are electronic devices that enable the integration of renewable energy resources in power systems by converting electrical energy from one form to another. The increased integration of these devices alters the power system dynamics; the fairly slow electromechanical phenomena driven by synchronous machines are now dominated by the complex fast-response of power converters. Traditional control strategies are not able to cope with the new dynamics, and may fail at guaranteeing the safe operation of the electrical network. Furthermore, power converters usually interface renewable energy production, or flexible loads with the grid, and their intermittent nature requires new fast control strategies to continuously track the time-varying grid conditions.

In the first part of this thesis, we derive new modelling tools to represent the dynamic behavior of power converters. In particular, we focus on models that are particularly well-adapted to system-level studies. They are designed to analyze the system's dynamics in different operating conditions. Also, they are computationally lightweight compared to detailed models, which allows for simulations of large systems with many different assets.

In the second part, we consider the problem of controlling inverter-interfaced distributed energy resources to ensure voltage regulation in a distribution network while minimizing resource usage. Voltage issues can occur due to the massive integration of renewable energy resources. In particular, excessive production of solar energy in residential low voltage networks can lead to overvoltages. We first propose a centralized online feedback optimization method that drives controllable power setpoints to a solution of an optimization problem, while ensuring anytime satisfaction of voltage constraints. We then propose a decentralized incremental Volt/Var control strategy, where the gains are derived in order to minimize resource usage and satisfy voltage constraints with a prescribed probability. The optimization problem is solved centrally, but the method requires only occasional communication. Finally, we propose a distributed controller where an optimization problem is decomposed and solved node by node, with only local communication between neighboring nodes.

Finally, we conclude this manuscript with a discussion on why modelling tools are required to validate new control strategies for active distribution networks. New advanced control strategies run at a faster timescale, so that there is no longer a timescale separation between the plant dynamics and the controller dynamics. This can lead to unstable

closed-loop systems that should be investigated with care. Theoretical guarantees can not always be provided, and one has to rely on simulation results. The first part of this manuscript focuses on modelling tools that are computationally lightweight, and well suited for large-scale systems simulations. These modelling tools help to validate new control strategies that are considered in the second part of this thesis. These are crucial aspects for the integration of new control strategies in the operation of active distribution networks, that would allow for a greater integration of renewable energy resources in distribution networks.

CONTENTS

1 INTRODUCTION 1
1.1 Motivation . . . 1
1.2 Contributions . . . 2
1.2.1 Modelling power electronic converters . . . 3
1.2.2 Voltage regulation in distribution networks . . . 6
1.2.3 Other works . . . 9
1.3 References and Authorship . . . 9

I MODELLING POWER ELECTRONIC CONVERTERS 11

2 BACKGROUND AND PRELIMINARIES 15
2.1 Switched models . . . 15
2.2 Averaged models . . . 18
2.3 Small-signal models . . . 19
2.4 Closed-loop system modelling . . . 20

3 LARGE-SIGNAL BLACK-BOX MODELS 23
3.1 Literature review . . . 23
3.1.1 Motivations . . . 24
3.1.2 Multimodel approach . . . 24
3.1.3 Contributions . . . 25
3.2 Overview of our multimodel approach . . . 26
3.2.1 Model structure . . . 26
3.2.2 Illustration on the Single-Machine Infinite Bus system . . . 27
3.2.2.1 Weighting functions . . . 28
3.2.2.2 Numerical experiments . . . 29
3.3 *PM-net*: Enhanced Neural Network-based Polytopic Model . . . 32
3.3.1 Neural network-based weighting functions . . . 32
3.3.2 Partitioning procedure . . . 34
3.3.3 Illustration on a toy example . . . 36
3.4 Numerical Experiments . . . 39
3.4.1 PID-voltage-regulated DC-DC boost converter . . . 39
3.4.1.1 Experiments design and model structure . . . 40
3.4.1.2 Results . . . 43
3.4.2 PI-Voltage-regulated DC-DC boost converter . . . 47
3.4.2.1 Experiments design and model structure . . . 47
3.4.2.2 Results . . . 48
3.4.3 Industrial DC-DC power converter . . . 50
3.4.3.1 Experiments design and model structure . . . 50

3.4.3.2 Results . . . 51
3.4.4 System-level studies . . . 53
3.4.4.1 Battery-DC-DC converter-DC motor system . . . 53
3.4.4.2 Battery-DC-DC converter-RL load system . . . 56
3.4.4.3 HyPoSol system . . . 58
3.5 Modified state update technique . . . 62
3.5.1 Limitations of input-dependent weighting functions . . . 62
3.5.2 Proposed approach . . . 63
4 CONCLUSION AND PERSPECTIVES 67
4.1 Conclusion . . . 67
4.2 Perspectives . . . 67

II VOLTAGE REGULATION IN DISTRIBUTION NETWORKS 69
5 BACKGROUND AND PROBLEM STATEMENT 73
5.1 Power flow analysis . . . 74
5.2 Impact of distributed energy resources on network voltages . . . 75
5.3 Problem statement . . . 78
6 CENTRALIZED CONTROLLER 81
6.1 Literature review . . . 81
6.1.1 Feedback-based optimization algorithms . . . 83
6.1.2 Contributions . . . 84
6.2 Feedback-based safe gradient flow . . . 84
6.2.1 Design principles . . . 85
6.2.2 Linear approximation . . . 87
6.2.3 Proposed approach . . . 88
6.2.4 Illustration on a single-phase distribution network . . . 91
6.2.4.1 Simulation setup . . . 91
6.2.4.2 Results . . . 95
6.3 An application to regulation of virtual power plants . . . 100
6.3.1 Proposed approach . . . 103
6.3.2 Experimental results . . . 104
6.3.2.1 Simulation setup . . . 104
6.3.2.2 Results . . . 106
6.4 Summary . . . 109
7 DECENTRALIZED CONTROLLER 111
7.1 Literature review . . . 111
7.1.1 Incremental Volt/Var control . . . 113
7.1.2 Contributions . . . 115
7.2 Proposed Incremental Volt/Var Controller . . . 115
7.2.1 Controller design . . . 116
7.2.2 Controller gains design . . . 117

7.2.3 Multi-period chance-constrained formulation . . . 119
7.2.4 Controller implementation . . . 123
7.2.5 Experimental results . . . 126
7.2.5.1 Simulation setup . . . 126
7.2.5.2 Results . . . 127
7.3 A robust formulation . . . 131
7.4 Extension to a three-phase unbalanced distribution system . . . 134
7.5 Summary . . . 139
8 DISTRIBUTED CONTROLLER 141
8.1 Literature review . . . 141
8.1.1 Solving an AC-OPF using consensus-based ADMM . . . 142
8.1.2 Contributions . . . 142
8.2 Proposed consensus-based ADMM approach . . . 142
8.2.1 Iterative procedure . . . 144
8.2.2 Experimental results . . . 147
8.2.2.1 Simulation setup . . . 147
8.2.2.2 Results . . . 148
8.3 Summary . . . 151
9 CONCLUSION AND PERSPECTIVES 153
9.1 Conclusion . . . 153
9.2 Perspectives . . . 154

III GENERAL CONCLUSION 157
10 GENERAL CONCLUSION 159

IV APPENDIX 163
A APPENDIX 165
A.1 Feedback-based safe gradient flow . . . 165
A.1.1 Stability analysis and constraint satisfaction guarantees . . . 165
A.2 Incremental Volt/Var control . . . 170
A.2.1 Derivations of M . . . 170
A.2.2 Convergence guarantees for Algorithm 7.1 . . . 171
B REFERENCES 173

1 INTRODUCTION

1.1 MOTIVATION

Modern power systems face massive integration of distributed energy resources (DERs) because of rising energy costs or for locally enhancing electric power reliability. The term DERs refers to small and modular energy generation or storage, that can be connected to a local electric power grid through power electronic converters. Their increasing penetration drives a paradigm shift in distribution networks, moving away from a centralized power generation scheme and embracing decentralized production systems. Historically, the power flowed from the high-voltage transmission system, down to the end customers connected to the distribution networks. Nowadays, the flexibility of DERs and the variability of renewable energy resources create reversed power flows, challenging the stability and reliability of distribution networks. Traditional regulation techniques may become insufficient to guarantee an acceptable power quality. For instance, for the voltage regulation in distribution networks, load tap changers or capacitor banks are no longer adapted as the increasing variability of renewable-based DER production can shorten their lifespan and render them ineffective. On the other hand, the versatility of DERs paves the way for new regulation techniques to ensure the reliable and secure operation of distribution networks and provide ancillary services to the high-voltage transmission system. Active distribution networks are the result of the integration of DERs into traditional distribution networks, and illustrate the shift from passive distribution networks acting as load sinks toward distribution networks with operation and control capabilities.

In recent years, extensive research has been conducted on optimal control of DERs to achieve operational and performance goals within distribution networks. Operational goals are related, e. g., to power quality or hardware limits of the grid infrastructure and the devices connected to it, while the performance goals usually consider resource usage minimization, e. g., minimizing active power curtailment, or reactive power compensation. Designing a system-level controller that would steer and coordinate DERs power setpoints to achieve these goals is challenging. The controller must be able to cope with the fast changing grid conditions that come from the variability of renewable-based DER production. Furthermore, the increased electrification of our energy needs that is foreseen in the coming years will cause additional variability and greater uncertainty in the load consumption. Finally, the penetration of power converters and their complex fast-response can soon completely dominate the slow electromechanical phenomena driven by synchronous machines, altering the power system dynamics. Traditional control techniques that rely on solving complex optimization problems offline can fail at tracking the

fast time-varying conditions of distribution networks, and dispatch outdated and suboptimal power setpoints to DERs. For instance, solving an AC optimal power flow (AC-OPF) problem in an open-loop fashion and dispatching new power setpoints to DERs is not suitable for real-time control of distribution networks for three reasons. First, it requires measuring the net power injections at every node, which might be hard to achieve in distribution networks. Second, the distribution network dynamics can be faster than the time required to solve the AC-OPF because of the computational complexity, thus leading to outdated setpoints. Finally, the AC-OPF is solved in an open-loop fashion and is therefore prone to modelling errors. There is a need to develop new control algorithms that can operate in real-time, leveraging the flexibility of DERs to ensure operational constraint satisfaction in distribution networks while minimizing the usage of resources.

Active distribution networks integrate many different assets and form complex systems with new dynamics. The complexity stems from the variety in power electronic converter topology since every manufacturer can develop its converter which, to some extent, interacts differently with the underlying distribution systems. Modelling and simulation tools are crucial to validate new control strategies, and guarantee the safe operation of the system in every possible scenario. Generic models of power electronic converters exist, but they miss some important dynamics of some particular topologies, which leads to significant simulation errors. On the other hand, detailed models are too computationally expensive to perform system-level simulations. Also, they may not be readily available because of data privacy. Indeed, manufacturers do not want to disclose some information required to derive a model of the power electronic converter. There is a need for simple models of power electronic converters, with limited computational burden, describing accurately some dynamics based on the type of simulation needed. These models should not rely on detailed information about the topology of the power electronic converter, since these may not be available.

In this thesis, the first contribution is (*c1*) a new system identification technique for power electronic converters, to derive models compatible with system-level simulations, i. e., sufficiently computationally light and targeting specific dynamics. In particular, these models are derived based on measurements collected on the power electronic converter, and do not require a-priori knowledge about the internal structure of the power electronic converter. The second contribution is (*c2*) to develop new control algorithms to perform voltage regulation in distribution networks that are suitable for real-time applications, and that leverage DERs capabilities.

1.2 CONTRIBUTIONS

In the following, we summarize the two main contributions of this thesis, and present the corresponding works.

1.2.1 *Modelling power electronic converters*

Power electronic converters play a major role in the energy transition. Various manufacturers develop versatile devices to integrate renewable energy resources more efficiently. Power electronic converters are complex time-varying and most often non-linear systems, and in modern power systems, these devices bring new types of dynamic interactions. There is a need for modelling and simulation tools to guarantee the system's integrity in the presence of power converters. Based on the following observations:

- Detailed models of power electronic converters are not available due to data privacy,
- Even if detailed models were available, they are not appropriate to run system-level studies as they are computationally expensive,
- Generic models are not able to represent specific dynamics when we consider large-signal perturbations,

we seek to solve the following problem:

Problem 1.1. *Developing power electronic converters' models that (i) do not require a-priori knowledge about their internal structure, (ii) are computationally lightweight, and (iii) are valid for system-level studies.* □

To tackle this problem, we focus on data-driven models of power converters. The goal is to develop measurement-based models capable of representing the non-linear dynamics of the converters. Figure 1.1 illustrates the type of model we aim to develop; models of power converters that are appropriate to perform system-level studies. In the following, we summarize the associated works.

In Colot et al. [2023c], we proposed *PM-net*, a multimodel approach combining linear models' responses using a neural network-based function, and that can capture the non-linear system behavior over a large operating range.

In a multimodel approach, the idea is to decompose the non-linear system operating space into operating regions. We consider that the operating space of the non-linear system corresponds to the closed set of values the inputs, outputs and states of the system can take and that the operating regions correspond to subsets of the operating space. For each operating region, we identify a linear model that estimates the system's behavior within this region. A weighting function is used to determine which linear model to use depending on the state of the system, i. e., the weighting function determines the validity of the linear model at a given point in the operating space. Essentially, this weighting function can take a maximum value of one, when the system's behavior is perfectly represented by one linear model, and a value between zero and one otherwise. This approach permits to combine multiple linear models responses when one linear model is not capable of accurately describing the system's behavior.

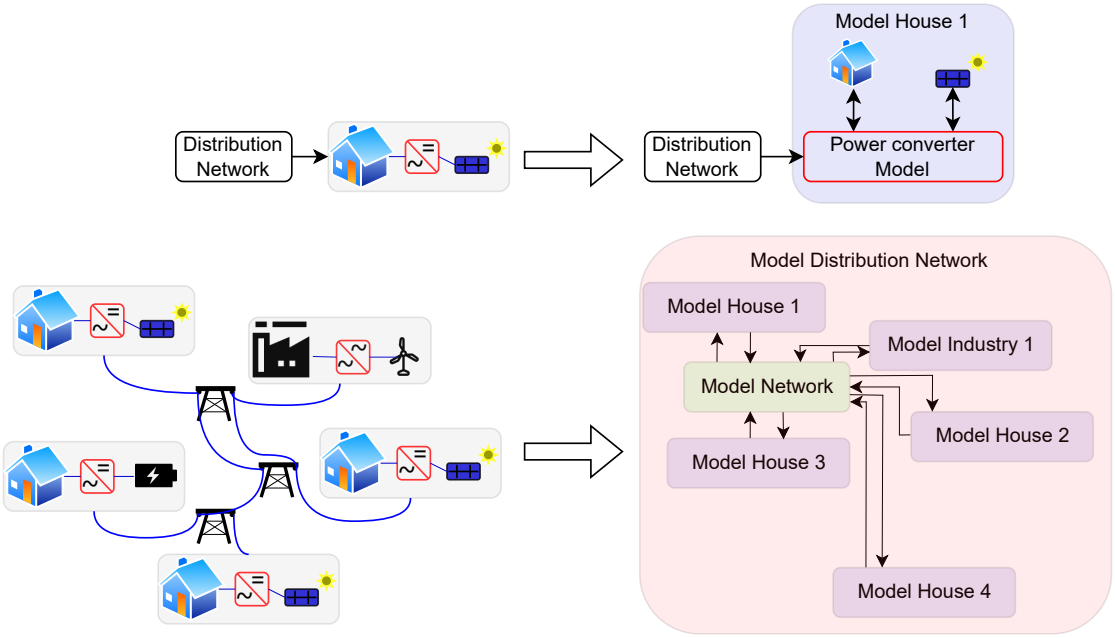

Figure 1.1: Illustration of Problem 1.1; component and system modelling.

Two problems arise when applying this to power converter modelling. First, the mathematical description of complex power converters involves multiple states, thus a broad operating space. It increases exponentially the number of required operating regions to cover the operating space. Second, gathering the measurements to identify the linear models can be challenging. For instance, consider a non-linear system in which one state corresponds to the derivative of an inductor current. An operating region is defined as a given range of values for this derivative, let us say between 1A/s and 2A/s. It is difficult to set up an experiment in which the derivative of the inductor current is kept between 1A/s and 2A/s.

In *PM-net*, the operating space consists only of the closed set of values the system inputs can take. It makes the experiments simpler than if we were considering the non-linear system states, e. g., the derivative of the inductor current. It also limits the size of the operating space, thus the number of operating regions needed. However, one challenge remains on how to construct the model, i. e., what are the inputs and outputs. This is a modelling choice that has to be carefully thought, in particular when the model has to be embedded in a larger system. For instance, one cannot combine two models that would impose a voltage magnitude at the same point.

In *PM-net*, we start with an orthotope-based partition of the operating space. We perform experiments on the converter to gather appropriate measurements for each operating region. Those experiments' design allow us to get rich measurements and identify linear models mimicking the converter's behavior over a wide frequency spectrum. Since

our interest is to develop models for system-level studies; we focus on the low-frequency dynamics of the converters. Actually, we aim to derive averaged models, we do not consider the switching nature of power converters. Notice that it is a common assumption, in particular when one wants to design the control algorithm of a power converter. In general, one considers an averaged and linearized model of the power converter, derived based on its topological equations.

The *PM-net* structure embeds the linear models associated with the operating regions and a neural network-based weighting function. In a traditional polytopic model framework, the user must choose the weighting function and the operating space partitioning. In *PM-net*, we train an artificial neural network to minimize the discrepancies between the converter's dynamics and the model response by appropriately tuning the weighting function, we aim to find the optimal combination of the linear models responses to fit the converter's response. The weighting function depends only on the inputs to improve the model's interpretability.

Since no prior information is given to the neural network regarding the partitioning of the operating space, the weighting function may have unexpected outputs. For instance, some linear models can have constant small weights over the entire operating space, while others may see sharp changes when slightly changing the inputs.

Based on the analysis of those weighting functions, we can delete linear models with small weights (small impact on the overall model response) and create new partitions of the operating space where we have sharp changes in the weighting function. It allows *PM-net* to be computationally lightweight while capturing the behavior of the non-linear system over a large operating range, thus making it suitable for system-level studies.

In Colot et al. [2023b], we proposed a C-HIL application to obtain synthetic measurements of a power converter, and then derive a black-box model. One application of *PM-net* models is to create a shareable black-box model of a product. It is useful when sharing models with third parties without disclosing trade secrets. We thus have access to the topology of the converter, but we want to derive a black-box model for data privacy issues. On the other hand, we might not have access to measurement devices that would allow us to develop a data-driven model. In Colot et al. [2023b] we built a digital twin of the converter and use it to generate synthetic measurements. We can then derive a *PM-net* model based on those measurements. The digital twin used is a C-HIL model interfacing the actual controller of the converter with a real-time simulator of the converter's electrical circuit. We showed that the *PM-net* model successfully represented the converter's behavior when connected to different electrical devices, and forming a small system.

In Colot et al. [2023a], we worked on an industrial system consisting of a battery, PV inverters, and a three-port converter. Our task was to develop a model of the system to perform system-level studies. The topologies of the PV inverters were unknown. Thus, we developed a *PM-net* model for the PV inverters. We aggregated the *PM-net* model

with other models for the battery and the three-port converter. The overall system model successfully represented the behavior of the industrial system.

In Colot et al. [2025b], we summarized the *PM-net* methodology and extended the framework to a state-space model formulation. We also introduced a state update technique to enhance the performance when the input signals change abruptly, and illustrated the technique on a Single-Machine Infinite Bus system.

1.2.2 *Voltage regulation in distribution networks*

The second part of this thesis focuses on the design of control algorithms for voltage regulation in distribution networks with massive integration of distributed energy resources. It is motivated by the following observations:

- Increased integration of renewable energy resources and load management strategies lead to operational and reliability challenges,
- The underlying dynamics of distribution networks are too fast to regulate power setpoints based on traditional AC optimal power flow techniques,
- Limited information is available at the distribution side, and there is a lack of communication infrastructure,

that we seek to solve the following problem:

Problem 1.2. *Develop control algorithms that (i) leverage DERs' flexibility to ensure operational constraint satisfaction in distribution networks while minimizing the usage of resources, (ii) operate in real-time to ensure proper operation of the network, (iii) do not require extensive monitoring of the distribution network.* □

Distribution networks typically have a meshed topology but are operated radially. Substations connect high-voltage networks to low-voltage networks through transformers. Multiple feeders connect the substation with the distribution nodes. Depending on the network voltage level the distribution nodes can be medium to large industries or households. Previously, active power flowed unidirectionally from the substation to the distribution nodes, which led to a progressive decrease in the voltage magnitudes along the feeder. The tap changers were used to maintain consistent voltage levels along the feeders by appropriately regulating the voltage at the substation. The rise of prosumers, electrical consumers who can inject or draw power at their connection point, creates bidirectional power flows, challenging voltage regulation. The voltage level at the substation is no longer always greater than the voltage level along the feeders, and it changes multiple times during the day as a function of unpredictable renewable energy production. Regulating the voltage at the substation with tap changers is no longer a viable solution to maintain consistent voltages along the feeders. On the other hand, DER integration,

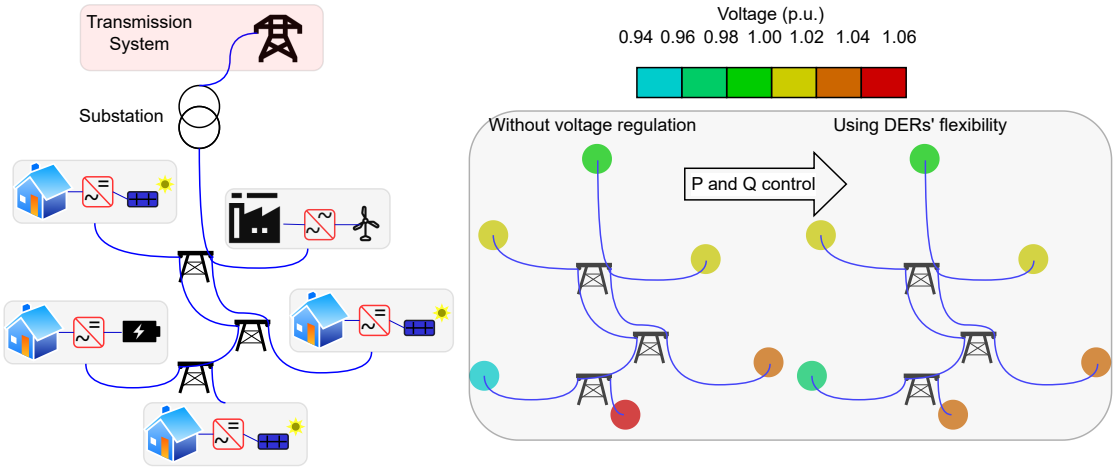

Figure 1.2: Illustration of voltage issues in distribution networks with high penetration of DERs, and how DERs' flexibility can mitigate them.

although being the root cause of voltage issues in distribution networks, offers some opportunities for regulation. In Figure 1.2, we illustrate the voltage regulation problem in distribution networks with increased penetration of DERs, and how DERs' flexibility can mitigate these issues. For this part of the thesis, we have investigated three different control structures; centralized, decentralized and distributed. These methods have different requirements in terms of communication infrastructure, and computational power.

Centralized. In Colot et al. [2025a], we proposed a feedback-based safe gradient flow algorithm to solve OPF problems. The safe gradient flow leverages the theory of control barrier functions to ensure constraints are satisfied at any time. In Colot et al. [2025a], we incorporated feedback into the initial formulation of the safe gradient flow, so that the algorithm continuously pursues the optimal solution as the network conditions change. It is a centralized method; an aggregator collects measurements over the network, then solves the optimization problem and dispatches the new decision variables. Notice that compared to traditional techniques based on solving the AC-OPF problem offline, in our method the number of constraints depends on the number of nodes where we perform voltage regulation, which significantly reduces the complexity of the algorithm. Furthermore, traditional AC-OPF techniques require load power measurements and a system model to compute the voltages. In our method, the feedback comes from the voltage measurements, which means there is no need to measure load power consumption and a system model to compute the voltages. This is the main idea behind feedback-based optimization; the system model and measurements of disturbances are replaced by directly measuring system states. The optimization problem to be solved is a quadratic programming problem for which efficient solving techniques exist. Although the method applies to general AC-OPF problems, we showed numerical results for the voltage regulation

problem in a single-phase equivalent 93-node medium voltage network. In Colot et al. [2024a], we extended the methodology proposed in Colot et al. [2025a] to the three-phase unbalanced IEEE 37-node test system. Distribution networks are most often unbalanced due to the different types of connections; wye or delta-connected and to which phase the device is connected; single-phase or three-phase connection. We also introduced the concept of *Virtual Power Plant* (VPP) which we defined as an aggregation of DERs in a distribution network, capable of providing ancillary services to the bulk power system while satisfying operational constraints within the distribution network such as voltage constraints.

Decentralized. In Colot et al. [2024b], we proposed a decentralized control algorithm for voltage regulation within distribution network. In particular, we aim to use reactive power compensation, provided by DERs, to mitigate voltage issues. The control is fully local, there is no need for communications in real-time. We require minimal communication days/hours ahead to dispatch gains for an incremental Volt/Var controller. The gains are obtained by solving a multi-period chance-constrained optimization problem. We seek to optimize the gains of the Volt/Var control in order to satisfy, with a prescribed probability, the voltage constraints while minimizing the reactive power usage. The methodology has been tested on a single-phase equivalent 42-node distribution network, and on the three-phase unbalanced IEEE 123-node test system. In Colot et al. [2024c], we extended the approach proposed in Colot et al. [2024b] by formulating a robust controller. The controller considers worst-case scenarios to always ensure voltage limits satisfaction. This is based on a heuristic to determine the worst-case scenario.

Distributed. In Colot et al. [2023d], we investigated how to distribute the optimal power flow (OPF) problem using the alternating direction method of multipliers (ADMM). Distributing OPF problems brings several advantages, such as minimizing computational burden, less requirements in terms of communication infrastructure compared to a centralized controller and ensuring data privacy by sharing information with neighbours only. One cannot distribute the OPF problem by construction because of the power flow equation constraints. The voltage at one node depends on the net power injections at every node, creating a dependency among all the nodes. ADMM breaks down large optimization problems into smaller ones and the procedure coordinates the small problem solutions to find the global problem solution. Furthermore, ADMM benefits from the advantages of dual decomposition techniques and the convergence rate of augmented Lagrangian techniques. We used the consensus version of the ADMM to distribute our OPF problem and the branch flow model for modelling the power flow equations. ADMM is an iterative procedure, and at every iteration, each electrical node solves its optimization problem with local variables, but in order to satisfy power flow equations, one needs to ensure that local variables of different subproblems representing the same quantities (such as branch currents) converge toward a global value. A consensus variable is built

by averaging local variables at every iteration, and the deviation from this consensus is penalized in each subproblem. In our formulation, we leveraged the iterative procedure of ADMM to derive a convex surrogate of our initial global optimization problem. We proposed to use the iterative procedure of ADMM to estimate branch currents and remove the non-linear equality constraints, considering the branch currents as parameters of the optimization problem. We used ADMM in an online setting since electrical network conditions always change, thus, we apply the decision variables found after each intermediate iterate. However, the intermediate iterates of ADMM do not satisfy power flow equations. Therefore, we penalized the discrepancy between the local voltage measurements and the local voltage variables to enhance the convergence of our algorithm toward solutions satisfying power flow equations. We illustrated our method on a single-phase equivalent 122-node system.

1.2.3 *Other works*

In addition to the two main contributions, in Colot et al. [2024d] we analyzed the stability of a transmission system subject to cyber-attacks. In particular, we considered transmission systems composed of frequency-responsive DERs, and we investigated non-periodic cyber-attacks targeting the damping coefficient of the DERs. We proposed sufficient conditions on the average activation time of the attacks to ensure the stability of the system. The theoretical bound on the average activation time is obtained by solving a class of bilinear matrix inequalities. We illustrated our results on the IEEE39-bus test system. This work is not presented in this manuscript, as it focuses on transmission systems, and analyzes the impact of cyber-attacks on the system's stability.

1.3 REFERENCES AND AUTHORSHIP

The works presented in this thesis are the result of collaborations with other researchers. In this section, we detail the authorship of those works.

Modelling Power Electronic Converters

• Colot, A., Giannitrapani, A., Paoletti, S., and Cornélusse, B. (2023c). Enhanced neural network-based polytopic model for large-signal black-box modeling of power electronic converters. In *2023 IEEE Belgrade PowerTech*, pages 01–06

Contribution: lead author.

• Colot, A., Ewbank, B., Glavic, M., and Cornélusse, B. (2023b). A C-HIL based data-driven DC-DC power electronics converter model for system-level studies. In *2023 IEEE PES Innovative Smart Grid Technologies Europe (ISGT EUROPE)*, pages 1–5

Contribution: co-author. My co-author developed the digital twin and the setup to perform experiments. I developed the *PM-net* model and performed the experiments.

• Colot, A., Bastin, B., Ewbank, B., Frebel, F., Bidaine, B., and Cornélusse, B. (2023a). Hybrid power solution modelling based on artificial intelligence. *IET Conference Proceedings*, 2023:3114–3119

Contribution: lead author.

• Colot, A., Paoletti, S., Giannitrapani, A., Glavic, M., and Cornélusse, B. (2025b). Interpretable large-signal black-box models of power electronic converters: a multimodel approach. *Submitted to IEEE Transactions on Power Delivery*

Contribution: lead author.

Voltage Regulation in Distribution Networks

• Colot, A., Chen, Y., Cornélusse, B., Cortés, J., and Dall'Anese, E. (2025a). Optimal power flow pursuit via feedback-based safe gradient flow. *IEEE Transactions on Control Systems Technology*, 33(2):658–670

Contribution: co-author. My co-author developed the theoretical framework. I formulated the safe gradient flow algorithm for the AC-OPF problem and performed the experiments.

• Colot, A., Cornélusse, B., Cortés, J., and Dall'Anese, E. (2024a). Feedback-based safe gradient flow for optimal regulation of virtual power plants. In *IET Conference Proceedings CP904*, volume 2024, pages 1–6. IET

Contribution: lead author.

• Colot, A., Perotti, E., Glavic, M., and Dall'Anese, E. (2024b). Incremental Volt/-Var control for distribution networks via chance-constrained optimization. *Accepted for publication in IEEE Transactions on Power Systems*

Contribution: co-author. My co-author and I developed the theoretical framework and formulated the optimization problem. I performed the experiments.

• Colot, A., Perotti, E., Glavic, M., and Dall'Anese, E. (2024c). A robust incremental Volt/VAR control for distribution networks. In *2024 IEEE PES Innovative Smart Grid Technologies Europe (ISGT EUROPE)*, pages 1–5. IEEE *This paper is the recipient of the IEEE PES ISGT EUROPE 2025 Best Paper Award.*

Contribution: co-author. My co-author and I developed the theoretical framework and formulated the optimization problem. I performed the experiments.

• Colot, A., Stegen, T., and Cornélusse, B. (2023d). Fully distributed real-time voltage control in active distribution networks with large penetration of solar inverters. In *2023 IEEE Belgrade PowerTech*, pages 01–06

Contribution: co-author. My co-author and I formulated the optimization problem and performed the experiments.

Other Works

• Colot, A., Shenoy, V., Cavraro, G., Dall'Anese, E., and Poveda, J. I. (2024d). On the stability of power transmission systems under persistent inverter attacks: A bi-linear matrix approach. *IEEE Control Systems Letters*, 8:1853–1858

Contribution: co-author. My co-author developed the theoretical framework. I developed the power system model and performed the experiments.

Part I

MODELLING POWER ELECTRONIC CONVERTERS

NOTATIONS

$\mathbf{x}$	Column vector
X	Matrix
$\mathcal{X}$	Set
$(.)^\top$	Transpose of a vector or a matrix
$\dot{(.)}$, $\frac{d}{dt}$	Time derivative
$\tilde{(.)}$	Small-signal variable
$\|(.)\|$	Euclidean norm
$\mathbb{R}$	Real numbers
$\mathcal{N}$	Set of indices for linear submodels
N	Number of linear submodels
$\mathbf{u}$	vector of inputs
$\mathbf{y}$	vector of outputs
d	Duty cycle
$s(t)$	Switching signal

2

BACKGROUND AND PRELIMINARIES

Power electronic converters convert electrical power using controllable electronic devices [Bacha et al., 2014]. Essentially, they are composed of passive components; inductors, resistors, capacitors, and controllable active components acting as switches. In particular, power-switching converters alternate between different electrical configurations based on the state of the switches. A local control algorithm drives the switches to process the raw input power effectively. Notice that in this part of the manuscript, when we mention local control algorithms, we do not consider algorithms that steer power setpoints to achieve system-level operational performance. We consider local controllers, such as proportional-integral controllers, that are responsible for driving the switches of power converters. Also, in the following, when mentioning power converters, we consider the combination of the electrical configuration and the local controller responsible for driving the active components.

There are different types of converters: DC-DC, DC-AC, AC-DC, or AC-AC converters, which are used depending on the input voltage and the desired output voltage. Among those different types, thousands of configurations exist based on the number of switches or the configuration of the passive components.

In the following, we introduce three modelling techniques for power converters. The *switched model*, which focuses on the switching nature of the converter, is capable of describing the high and low-frequency dynamics, but, it is computationally expensive. On the other hand, the *averaged model* reduces the computational burden, but can only describe the low-frequency dynamics since it considers averaged signals. We also introduce the *small-signal model*, which is a linear model often used to design controllers for power converters. We emphasize the poor performance of linear models of power converters for system-level studies.

2.1 SWITCHED MODELS

A power converter naturally switches among different configurations to achieve target performance (inverting, redressing, amplifying output voltages, etc.). If one denotes $\mathbf{x} \in \mathbb{R}^N$ the state vector and $\mathbf{u} \in \mathbb{R}^N$ the input of a state-space model, a power converter with N configurations of switches can be mathematically described as:

$$\dot{\mathbf{x}}(t) = \sum_{i=1}^{N} s_i(t)(A_i(t)\mathbf{x}(t) + B_i(t)\mathbf{u}(t)), \tag{2.1}$$

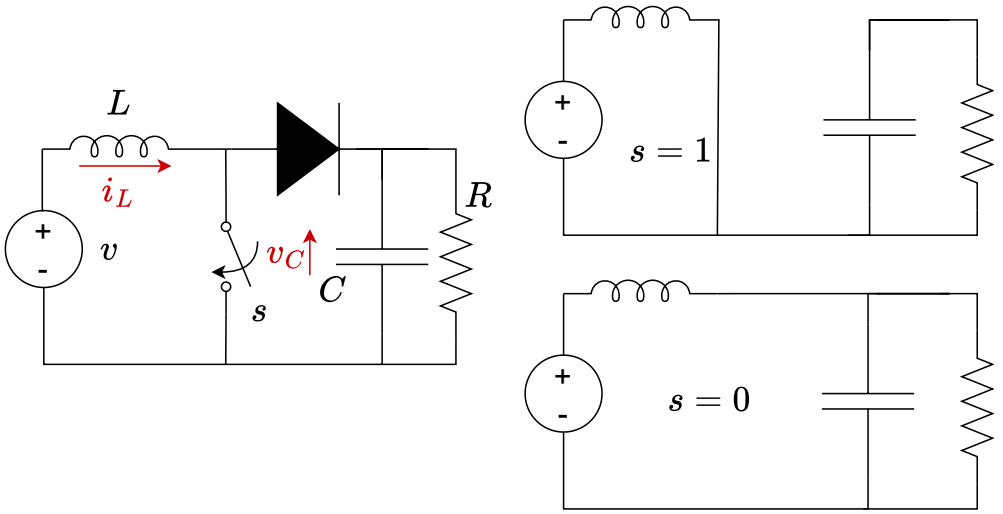

Figure 2.1: Illustration of a DC-DC boost converter, and the different conduction configurations.

where each configuration $i \in \{1, ..., N\}$ is described by the state model with matrix pairs (A_i, B_i), and s_i is a time-varying signal that takes a value of 1 or 0, such that at every time t, $\sum_{i=1}^{N} s_i(t) = 1$. The signal s_i is called the *switching signal*. The switching signal is generated by a control algorithm that drives the switches.

The system (2.1) is linear, but *time-varying* as the signal s_i changes the dynamics of the system. Furthermore, the matrix pairs are also *time-varying* since some passive components can exhibit a *time-varying* behavior. For instance, the heat generated by Joules losses can impact the resistive properties of some passive components. Also, in the most general case, passive components behave non-linearly because of saturation effects, and the switches or generators are not ideal, which renders the switching model of power converters *non-linear* and *time-varying*.

For the sake of simplicity, in the following we consider ideal switches, linear and invariant passive elements, and perfect generators (voltage and current sources). That is a common assumption in the literature, and it allows us to focus on the switching nature of the converter.

Consider the DC-DC boost converter represented in Figure 2.1 as an example. The state vector $\mathbf{x} = [i_L, v_C]^\top$ represents the inductor current and the capacitor voltage, and the input $\mathbf{u} = v$ the input DC voltage. If the switch is closed, then $s = 1$, and the matrix pair (A_1, B_1) is:

$$A_1 = \begin{pmatrix} 0 & 0 \\ 0 & -\frac{1}{RC} \end{pmatrix}, B_1 = \begin{pmatrix} \frac{1}{L} \\ 0 \end{pmatrix}. \tag{2.2}$$

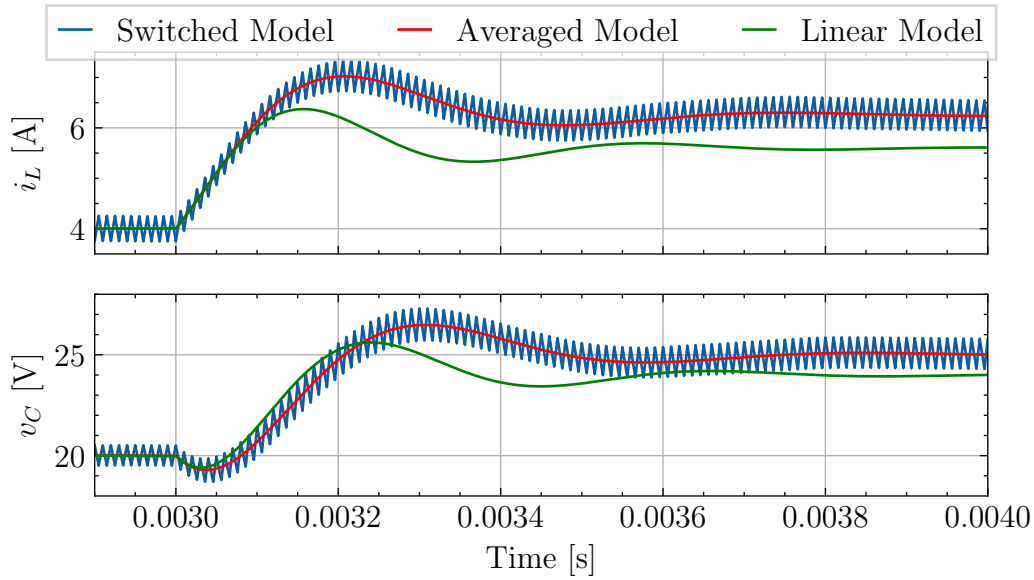

Figure 2.2: Comparison between a switched model, an averaged model, and the linearized averaged model for a DC-DC boost converter.

If the switch is open, then $s = 0$, and the matrix pair (A_2, B_2) is:

$$A_2 = \begin{pmatrix} 0 & -\frac{1}{L} \\ \frac{1}{C} & -\frac{1}{RC} \end{pmatrix}, B_2 = \begin{pmatrix} \frac{1}{L} \\ 0 \end{pmatrix}. \tag{2.3}$$

We consider the converter to be operated in *continuous conduction mode*, i. e., the inductor current never reaches 0. Therefore, there exist only two conduction configurations (switch closed or open). In *discontinuous conduction mode*, the inductor current reaches 0 at some point, and the converter operates in three conduction configurations.

Notice that one can write the state-space model of our DC-DC boost converter as:

$$\dot{\mathbf{x}}(t) = A(t)\mathbf{x}(t) + B(t)\mathbf{u}(t), \tag{2.4}$$

with $A(t) := s(t)A_1 + (1 - s(t))A_2$, and $B(t) := s(t)B_1 + (1 - s(t))B_2$. Figure 2.2 shows the evolution of the state variables of the boost converter when the input voltage is set to 10V and the switch is operated to increase the capacitor voltage from 20V to 25V. One can notice the ripples in the inductor current and the capacitor voltage. The ripples are due to the switching nature of the converter, and are high-frequency signals that are not captured by an averaged model.

2.2 AVERAGED MODELS

We define the average of a signal $\mathbf{x}(t)$ over a period T as:

$$\bar{\mathbf{x}}(t) = \frac{1}{T}\int_{t-T/2}^{t+T/2} \mathbf{x}(\tau)d\tau. \tag{2.5}$$

We also define the periodic switching signal $s(t)$ with T the switching period and d the duty cycle $\in [0, 1]$ the ratio of time the switch is closed over T as:

$$s(t) = \begin{cases} 1 & \text{if } 0 \leq t < dT \\ 0 & \text{if } dT \leq t < T \end{cases}, \qquad s(t-T) = s(t) \qquad \forall t. \tag{2.6}$$

Notice that $d = \bar{s}(t)$ corresponds to the average of the switching signal over a period T. The averaged model is obtained by averaging the state model over the switching period T of the power converter:

$$\dot{\bar{\mathbf{x}}}(t) = \bar{A}\bar{\mathbf{x}}(t) + \bar{B}\bar{\mathbf{u}}(t), \tag{2.7}$$

with:

$$\bar{A} = \frac{1}{T}\int_{t-T/2}^{t+T/2} A(\tau)d\tau, \tag{2.8}$$

$$\bar{B} = \frac{1}{T}\int_{t-T/2}^{t+T/2} B(\tau)d\tau, \tag{2.9}$$

where the time-varying matrices $A(t)$ and $B(t)$ become *time-invariant*. For our DC-DC boost converter, the averaged model is:

$$\bar{A} = \frac{1}{T}\int_{t-T/2}^{t+T/2} s(\tau)A_1 + (1 - s(\tau))A_2 d\tau, \tag{2.10a}$$

$$= A_2 + (A_1 - A_2)\frac{1}{T}\int_{t-T/2}^{t+T/2} s(\tau)d\tau, \tag{2.10b}$$

$$= A_2 + (A_1 - A_2)d. \tag{2.10c}$$

Following the same reasoning, one obtains $\bar{B} = B_2 + (B_1 - B_2)d$. As shown in Figure 2.2, the averaged model captures the low-frequency dynamics of the converter, but not the high-frequency ripples. The system (2.7) becomes *time-invariant*. However, notice that the duty cycle is most often a function of the state variables and the input, as one wants to drive the switches to steer the converter outputs. Therefore, d varies with time. The system (2.7) then becomes *non-linear* due to the product of the matrices $\bar{A}$ and $\bar{B}$ with the duty cycle d. If the duty cycle is constant, the system is linear. Averaged models are most often *non-linear* and *time-invariant* systems.

2.3 SMALL-SIGNAL MODELS

In practice, if one wants to design a controller for a converter, it is often preferred to consider a linear model since one can then rely on control theory for linear systems. A linear small-signal model is obtained by linearizing the averaged model around an operating point $(\mathbf{x}_e, \mathbf{u}_e, d_e)$, where d_e is the duty cycle at the operating point. For instance, in the case of a DC-DC boost converter, one may want to control the voltage across the resistor R. Let us consider we want it equal to $x_{e,2} = 20V$ where $x_{e,2}$ is the capacitor voltage at equilibrium, $\mathbf{x} = [x_{e,1}, x_{e,2}]^\top = [i_{L,e}, v_{C,e}]^\top$. Given $u_e = 10V$, and using the state-space models defined in equations (2.2), (2.3), we have:

$$\left(\frac{-1}{L} + d_e\frac{1}{L}\right) x_{e,2} + \frac{1}{L}u_e = 0 \tag{2.11a}$$

$$\left(\frac{1}{C} - d_e\frac{1}{C}\right) x_{e,1} - \frac{1}{RC}x_{e,2} = 0 \tag{2.11b}$$

Using $x_{e,2} = 20V$ and $u_e = 10V$, we obtain:

$$d_e = \frac{-u_e}{x_{e,2}} + 1 = 1 - \frac{10}{20} = 0.5 \tag{2.12}$$

Notice that the relationship between output voltage and input voltage is $d_e = 1 - \frac{\text{input voltage}}{\text{output voltage}}$, such that, to increase the output voltage, one needs to increase the duty cycle.

Let us now derive a small-signal model, starting from the averaged model defined in (2.7). For that purpose, we define the following small-signal variables: $\tilde{\mathbf{x}}(t) = \bar{\mathbf{x}}(t) - \mathbf{x}_e$, $\tilde{\mathbf{u}}(t) = \bar{\mathbf{u}}(t) - \mathbf{u}_e$, and $\tilde{d}(t) = d(t) - d_e$. The averaged model (2.7) can be written as:

$$\dot{\bar{\mathbf{x}}} = (A_2 + (A_1 - A_2)d)\,\bar{\mathbf{x}} + (B_2 + (B_1 - B_2)d)\,\bar{\mathbf{u}} \tag{2.13a}$$

$$\dot{\tilde{\mathbf{x}}} + \dot{\mathbf{x}}_e = \Big(A_2 + (A_1 - A_2)(\tilde{d} + d_e)\Big)\,(\tilde{\mathbf{x}} + \mathbf{x}_e) + \tag{2.13b}$$

$$\Big(B_2 + (B_1 - B_2)(\tilde{d} + d_e)\Big)\,(\tilde{\mathbf{u}} + \mathbf{u}_e) \tag{2.13c}$$

$$\dot{\tilde{\mathbf{x}}} = (A_2 + (A_1 - A_2)d_e)\,\tilde{\mathbf{x}} + \Big(A_2 + (A_1 - A_2)(\tilde{d} + d_e)\Big)\,\mathbf{x}_e + (B_2 + (B_1 - B_2)d_e)\,\tilde{\mathbf{u}} + \Big(B_2 + (B_1 - B_2)(\tilde{d} + d_e)\Big)\,\mathbf{u}_e, \tag{2.13d}$$

where we omit to write the time dependency t of some variables for clarity. If we discard the second-order term $\tilde{d}\tilde{\mathbf{x}}$ and $\tilde{d}\tilde{\mathbf{u}}$, we obtain the following linear model:

$$\dot{\tilde{\mathbf{x}}}(t) = A_{ss}\tilde{\mathbf{x}}(t) + B_{ss}\tilde{\mathbf{u}}(t) + E_{ss}\tilde{d}(t) + H \tag{2.14}$$

where $A_{ss} = A_2 + (A_1 - A_2)d_e, B_{ss} = B_2 + (B_1 - B_2)d_e, E_{ss} = (A_1 - A_2)\mathbf{x}_e + (B_1 - B_2)\mathbf{u}_e, H = (A_2 + (A_1 - A_2)d_e)\,\mathbf{x}_e + (B_2 + (B_1 - B_2)d_e)\,\mathbf{u}_e$. Figure 2.2 shows the performance of the linearized averaged model with respect to the averaged and the switched

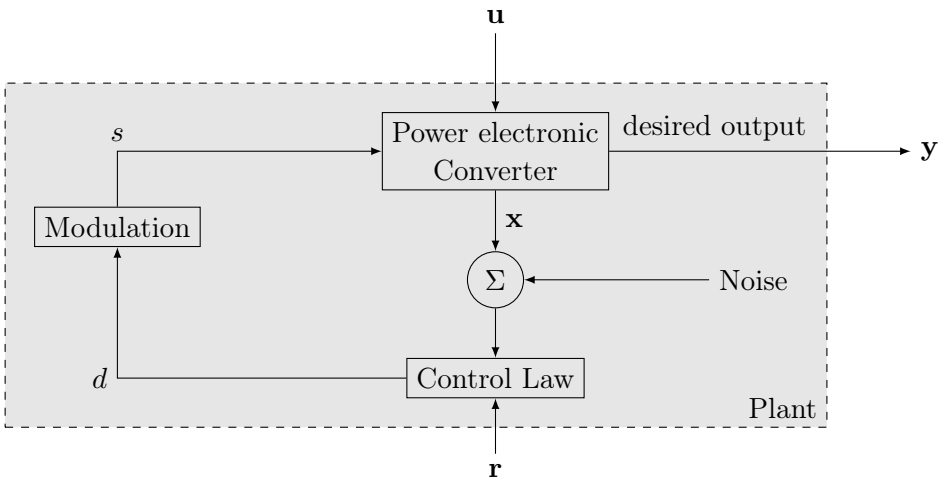

Figure 2.3: Illustration of a closed-loop system.

models. As the averaged model, the linearized averaged model is not capable of representing the high frequency dynamics. One can also observe that the linearized averaged model is not accurate when simulating the behavior of the converter on a different operating point than the one used to linearize the averaged model.

Despite this drawback, those small-signal models are very useful to design the controller to operate the switches, as one can rely on control theory for linear systems. For instance, one can consider a feedback controller of the form:

$$\dot{\tilde{d}}(t) = -\mathbf{k}_p^\top(\dot{\tilde{\mathbf{x}}}(t) - \dot{\mathbf{r}}(t)) - \mathbf{k}_i^\top(\tilde{\mathbf{x}}(t) - \mathbf{r}(t)) \tag{2.15}$$

where $\mathbf{k}_p = [k_{p,1}, k_{p,2}]^\top, \mathbf{k}_i = [k_{i,1}, k_{i,2}]^\top$. In practice, using the small-signal model (2.14), on can derive values for $\mathbf{k}_p, \mathbf{k}_i$ such that the closed-loop system is stable, and the controller achieves the desired goal. The task of developing a controller based on the non-linear averaged model (2.7) is much more complex, and requires advanced control techniques. Since the topic of designing controller for operating switches in power converters is outside the scope of this thesis, we refer the reader to [Bacha et al., 2014] for detailed explanation. In the following, we consider the closed-loop system that is composed of the power converter and its controller, and introduce the challenges of modelling the closed-loop system for system-level studies.

2.4 CLOSED-LOOP SYSTEM MODELLING

In practice, for system-level studies, one wants to model the closed-loop system. The power converter closed-loop system is illustrated in Figure 2.3 and is composed of the converter, the modulation, and the control law. The control law drives the active components of the converter to achieve a desired output, and produce a signal d that is sent

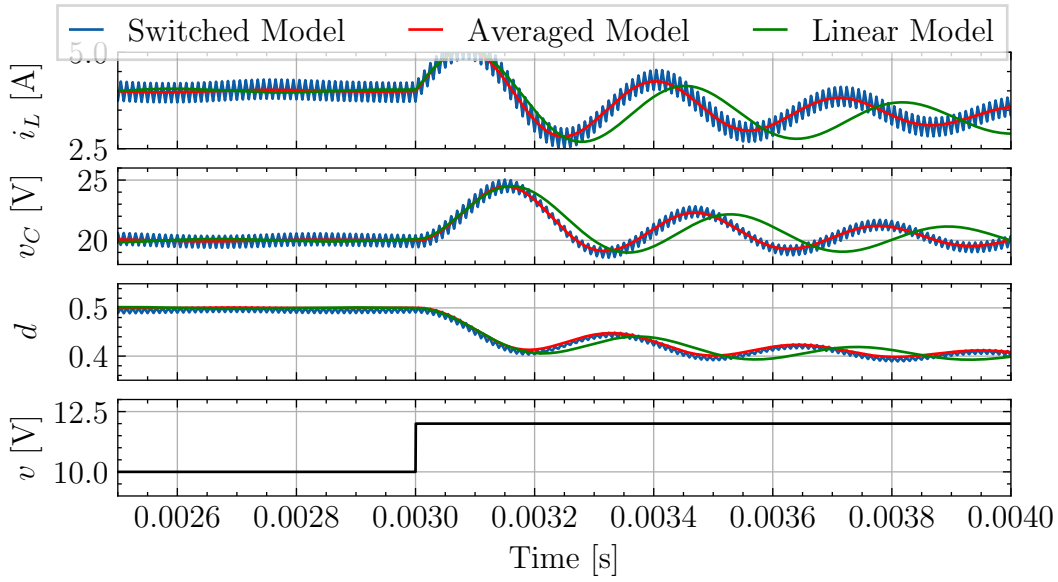

Figure 2.4: Comparison between a switched model, an averaged model and the linearized averaged model for a voltage-regulated DC-DC boost converter.

to the modulation. The modulation is responsible for generating the switching signals $s(t)$. The output of the plant is then fed back to the control law. As explained above, the control law can be designed using the small-signal model of the converter, and classical theory for linear control systems. In this manuscript, we are interested in deriving a model of the closed-loop system that is simple enough to be used for large scale system-level studies, but accurate enough to capture the desired dynamics of the system.

Let us consider our boost converter, the goal of the controller defined by equation (2.15) is to regulate the voltage across the capacitor. To achieve this objective, we set $\mathbf{k}_p = [0, 0.01]^\top, \mathbf{k}_i = [0, 100]^\top$ in (2.15). The reference is $\mathbf{r} = [0, 20]^\top$, where the first element of $\mathbf{r}$ does not play any role since the associated controller gains correspond to 0.

In Figure 2.4, we compare the response of the closed-loop system modelled using the switched model, the averaged model, and the linearized averaged model. One can observe that the closed-loop system is not accurately represented by the linearized averaged model. That is because the closed-loop system is non-linear.

When it comes to system-level studies, and in particular, modelling systems with different components, as illustrated in Figure 1.1, linear models are not suitable. First, because the closed-loop system that is the power converter can be highly non-linear, and because the power converter can be operated around various operating points. In the following, we introduce a multimodel approach to model the closed-loop system of power converters.

3

LARGE-SIGNAL BLACK-BOX MODELS

Outline

This chapter introduces a multimodel approach to develop system-level models of power converters to tackle Problem 1.1 introduced in Section 1.2.1. Our approach combines a set of linear models' responses using a neural-network based weighting function to simulate the input-output behavior of a power converter. The chapter is organized as follows: Section 3.1 presents different large-signal models of power converters, and the contributions of this thesis with respect to the existing literature, Section 3.2 introduces the multimodel approach, and in particular, some inherent drawbacks of this approach, Section 3.3 introduces our methodology that aims at mitigating the major drawbacks of the multimodel approach, Section 3.4 provides practical examples of our approach on real test cases, both for modelling power converters and to perform system-level studies, and Section 3.5 proposes a modified state update technique to enhance performance of multimodel approach with input-dependent weighting functions.

3.1 LITERATURE REVIEW

Power electronic converters are often non-linear, time-varying systems [Bacha et al., 2014]. We showed in Chapter 2, that one can remove the time-variance by applying some averaging techniques. However, averaged models remain non-linear if the initial time-varying system is non-linear, and can actually become non-linear because of the averaging technique. Therefore, to identify averaged models of power converters, one has to rely on *non-linear system identification* techniques.

Non-linear system identification is much more challenging than linear system identification as far as the number of possible model structures, and experiment design, as well as the difficulty of parameter estimation are concerned [Schoukens and Ljung, 2019]. Before diving into the tedious task of identifying non-linear systems, one has to wonder if the performance of a linear model is sufficient for the target application. As shown in Chapter 2, and in particular in Figure 2.4, linear models have some limitations when considering power converters, as they cannot adequately capture their large-signal behaviors. Linear models are not appropriate for system-level studies since converters' dynamics may depend heavily on the operating point. Referring to Problem 1.1 introduced in Section 1.2.1,

we want to derive a model that is simple enough to be used for system-level studies, but accurate enough to capture the dynamics of the system to be modelled.

3.1.1 *Motivations*

There exist many different model structures for non-linear system identification, therefore, it is important to define what we expect from the model. We want *simulation* models, since the goal is to ensure the good behavior of the system under different operating conditions. Furthermore, modern power systems often incorporate *Off-The-Shelf* converters from different manufacturers [Valdivia et al., 2013, Francés et al., 2016a] with limited available data provided to the user that calls for the development of *black-box* models [Arnedo et al., 2008]. Finally, we do not want to represent fast dynamics, as the goal is to model the power converters for system-level studies, and not at a component-level; our focus is on *averaged* models of power converters capable of representing dynamics up to several hundred Hz.

3.1.2 *Multimodel approach*

In this thesis, we introduce a multimodel approach to derive *large-signal black-box* models for power converters. Our modelling technique is suitable for system-level design and analysis because of its low computational burden and inherent interpretability. The multimodel approach computes the global model output as a weighted combination of some linear submodel responses. The weighting function represents the linear submodel's validity within a specific operating range [Adeniran and El Ferik, 2016]. This approach is simple, mathematically tractable, and built upon the well-known theory of linear system identification. The multimodel framework accommodates different type of models, i. e., input-output or state-space models, therefore, several paradigms can be found in the literature. For instance, in *Takagi-Sugeno* fuzzy models [Takagi and Sugeno, 1985], a linear membership function and a model are associated with each fuzzy set, and the final model output is inferred from the weighted sum of the model outputs of the different fuzzy sets. On the other hand, *linear parameter-varying* models can also be cast as a multimodel approach as the model parameters are function of a scheduling variable [Zhu and Xu, 2008],[Sadeghzadeh and Garoche, 2023].

Multimodel approaches have already been investigated for modelling large-signal black-box models of power converters. In Francés et al. [2016a], authors propose a black-box polytopic modelling approach for system-level design of DC-based nanogrids. The DC-based nanogrid is composed of *Off-The-Shelf* converters, for which one does not have access to topological information. Different modelling methodology are compared; *block-oriented* structure such as *Wiener-Hammerstein* models, small-signal *G-parameters* models and a polytopic model. It is shown that polytopic models exhibit the best perfomance for system-level studies. In Frances et al. [2017], a review of different modelling techniques

is proposed for system-level studies of DC microgrids. In Arnedo et al. [2008], and Francés et al. [2016b], authors propose a polytopic model with a double sigmoid weighting function for power converters, and with pre-defined partitioning of the operating space.

Notice that full neural-network based models have been proposed for power converters modelling. In Rojas-Dueñas et al. [2021], authors compare polytopic models with a wavelet convolutional neural network trained to represent the power converter behavioral response. In Rojas-Dueñas et al. [2020], authors use a recurrent neural network to approximate the power converter's dynamics. Although full neural network-based models lead to a better representation of the behavioral response of the converter, they may lack interpretability and rely heavily on data quality [Sahoo et al., 2021]. Ensuring sufficient data quality and availability may be challenging for power converter applications, and the lack of physical insights behind those full neural network-based models may challenge the analysis of systems composed of different converters. We note that model interpretability might be crucial for some applications. Indeed, interpretability makes the model transparent, and allows the user to trust the model outputs. Also, it allows the user to understand the model's behavior, and to make decisions based on the simulation results.

Other modelling techniques exist [Al-Greer et al., 2018], such as *Hammerstein* models [Alonge et al., 2007]. Those methods are *block-oriented* structures and combine static non-linear blocks with dynamical linear systems. They are very convenient when the non-linearity stems from saturation, sensors and actuators, etc. [Francés et al., 2016a]. However, when the non-linearity comes from the switching nature of the converter, the range of applicability of these methods is limited since the dynamics of the system becomes dependent on the operating point.

3.1.3 *Contributions*

For a given multimodel structure, one can identify four challenges: *(i)* how to identify the linear submodels, *(ii)* how to design the weighting function that is used for obtaining the global model output, *(iii)* how to partition the operating space into different operating regions, and *(iv)* how to combine the different linear submodels.

In our approach, we propose:
(c1) to derive linear submodels using input-output data collected by measuring converter's response around a given operating point and using linear system identification techniques,
(c2) to design the weighting function using a neural network that is trained based on measurements collected on the converter,
(c3) to partition the operating space by applying post-analysis of the trained neural network,
(c4) and to derive the global model output using a weighted sum of the linear submodels' responses.

3.2 OVERVIEW OF OUR MULTIMODEL APPROACH

In the following, we present the multimodel structure considered in this manuscript, and we illustrate the rationale behind our choice of input-dependent weighting function.

3.2.1 *Model structure*

We consider a discrete-time non-linear dynamical system of the form:

$$\mathbf{x}(k+1) = f(\mathbf{x}(k), \mathbf{u}(k)), \tag{3.1a}$$
$$\mathbf{y}(k) = h(\mathbf{x}(k), \mathbf{u}(k)), \tag{3.1b}$$

where $\mathbf{x} \in \mathbb{R}^{n_x}$,$\mathbf{u} \in \mathbb{R}^{n_u}$, $\mathbf{y} \in \mathbb{R}^{n_y}$ are the system state, input and output, respectively, $f : \mathbb{R}^{n_x \times n_u} \mapsto \mathbb{R}^{n_x}$ is the state update function, $h : \mathbb{R}^{n_x \times n_u} \mapsto \mathbb{R}^{n_y}$ is the output function and $\mathbf{x}(k), \mathbf{u}(k)$ and $\mathbf{y}(k)$ are the state, input and output values at continuous time $k\tau$ with $\tau \in \mathbb{R}$ the time step considered. We want to approximate the dynamics of the non-linear system (3.1) using a multimodel approach. To this purpose, we combine the outputs of the linear submodels through a weighting function [Adeniran and El Ferik, 2016]. This allows us to have heterogeneous submodels compared to other multimodel approaches where, for instance, the state of the global system is a weighted sum of the states of each submodel. In the latter case, the different linear submodels have to share the same state space dimensionality as in some LPV systems [Sadeghzadeh and Garoche, 2023].

Let us consider the set $\mathcal{N} := \{1, ..., N\}$ of indices of the different linear submodels. The linear submodel $i \in \mathcal{N}$, obtained around the operating point $(\mathbf{u}_i^e, \mathbf{y}_i^e)$, for instance, via linearization techniques, is described by the following state-space equation:

$$\tilde{\mathbf{x}}_i(k+1) = A_i\tilde{\mathbf{x}}_i(k) + B_i\tilde{\mathbf{u}}_i(k), \tag{3.2a}$$
$$\mathbf{y}_i(k) = C_i\tilde{\mathbf{x}}_i(k) + D_i\tilde{\mathbf{u}}_i(k) + H_i, \tag{3.2b}$$

with $\tilde{\mathbf{u}}_i := \mathbf{u} - \mathbf{u}_i^e \in \mathbb{R}^{n_u}$, $\tilde{\mathbf{x}}_i \in \mathbb{R}^{n_{x,i}}$,$\mathbf{y}_i \in \mathbb{R}^{n_y}$, and $A_i \in \mathbb{R}^{n_{x,i} \times n_{x,i}}$, $B_i \in \mathbb{R}^{n_{x,i} \times n_u}$, $C_i \in \mathbb{R}^{n_y \times n_{x,i}}$, $D_i \in \mathbb{R}^{n_y \times n_u}$, $H_i \in \mathbb{R}^{n_y}$

The polytopic model considered in this thesis combines different linear submodels' outputs as follows:

$$\mathbf{y}_{\mathrm{PM}}(k) = \sum_{i \in \mathcal{N}} \omega_i(\mathbf{u}(k))\mathbf{y}_i(k), \tag{3.3}$$

with $\omega_i : \mathbb{R}^{n_u} \mapsto \mathbb{R}$ a weighting function for the linear submodel i, such that $\omega_i(\mathbf{u}(k)) \in [0, 1]$ and $\sum_{i \in \mathcal{N}} \omega_i(\mathbf{u}(k)) = 1$ at every step k.

We claim that our approach is *interpretable* because our multimodel structure combines linear models, and those are inherently interpretable (intuitive meaning of its parameters, they are additive, etc.) [Raz, 2024].

Furthermore, the weighting functions $\omega_i(\cdot)$ depend on $\mathbf{u}(k)$ only. For one constant input $\mathbf{u}^*$, the linear submodel i^* mostly responsible for the global model behavior has the largest associated weight $\omega_{i^*}(\mathbf{u}^*)$. On the other hand, it leads to a suboptimal combination of submodel responses during "jumps" in the inputs. In Frances et al. [2019], authors propose dynamic weighting functions to mitigate this drawback. Another approach is discussed later in Section 3.5. In the following, we introduce a common non-linear system that appears in power systems, and for which we want to derive a large-signal model.

3.2.2 *Illustration on the Single-Machine Infinite Bus system*

Some challenges related to the modelling of non-linear dynamical systems with our multimodel approach and the rationale behind the input-dependent weighting function used in (3.3) are illustrated with the Single-Machine Infinite Bus (SMIB) system.

The SMIB system consists of one equivalent synchronous machine connected to an infinite bus through a line of reactance X. The dynamics of the equivalent synchronous machine are described with the swing equations. Although simple, this system is often used in power system practices through one-machine infinite bus transformation of the equivalent system for both large-signal [Pavella et al., 2000] and small-signal stability problems [Rezaee et al., 2020].

Consider the SMIB system:

$$\delta(k+1) = \delta(k) + \tau\omega_{\mathrm{s}}\Delta\omega(k), \tag{3.4a}$$

$$\Delta\omega(k+1) = \Delta\omega(k) + \frac{\tau}{M}\left(P_{\mathrm{m}} - D\Delta\omega(k) - \frac{VV_\infty \sin\left(\delta(k)\right)}{X}\right), \tag{3.4b}$$

where δ is the rotor angle of the single machine, $\Delta\omega$ the deviation of the angular speed from the nominal angular speed of the machine in per unit, P_{m} is the mechanical power in per unit, D the damping parameter, X the reactance of the line connecting the single machine to the infinite bus system, M the moment of inertia of the machine, V the voltage magnitude of the single machine, and V_∞ the voltage magnitude of the infinite bus system (phase to ground). For this system, let us consider the input $u = V_\infty$, the output $\mathbf{y}(k) = [\delta(k), \Delta\omega(k)]^\top$, the state vector $\mathbf{x}(k) = [\delta(k), \Delta\omega(k)]^\top$, and the parameters $\omega_{\mathrm{s}} = 2\pi 60$ [rads^{-1}], $P_{\mathrm{m}} = 0.5$ [pu], $D = 5$ [pu], $V = 1$ [pu], $X = 1.5$ [pu], $M = 8$ [s]. Finally, let us consider $\tau = 1e-2$ [s].

One equilibrium point $\mathbf{x}^e = [\delta^e, \Delta\omega^e]^\top$ of the system (3.4) is:

$$\delta^e = \arcsin\left(\frac{P_{\mathrm{m}}X}{VV_\infty}\right) \in [0, \pi/2] \tag{3.5a}$$

$$\Delta\omega^e = 0 \tag{3.5b}$$

Now, let us consider that $V_\infty \in [0.85, 1.15]$ pu, and we define $N = 3$ linear systems around the equilibrium points $x_i^e = [\delta_i^e, 0]^\top$ as follows:

$$A_i = \begin{bmatrix} 1 & \tau\omega_\mathrm{s} \\ -\tau\frac{VV_{\infty,i}\cos(\delta_i^e)}{MX} & -\tau\frac{D}{M}+1 \end{bmatrix}, B_i = \begin{bmatrix} 0 \\ -\tau\frac{V\sin(\delta_i^e)}{XM} \end{bmatrix}, \tag{3.6a}$$

$$C_i = \begin{bmatrix} 1 & 0 \\ 0 & 1 \end{bmatrix}, D_i = \begin{bmatrix} 0 \\ 0 \end{bmatrix}, H_i = \begin{bmatrix} \delta_i^e \\ 0 \end{bmatrix}, \tag{3.6b}$$

where $V_{\infty,1} = 0.9\text{pu}, V_{\infty,2} = 1.0\text{pu}, V_{\infty,3} = 1.1\text{pu}$ and $\delta_i^e \ \forall i \in \mathcal{N}$ are obtained from equation (3.5a).

3.2.2.1 *Weighting functions*

We consider two types of weighting functions ($\omega_i : \mathbb{R}^{n_u} \mapsto \mathbb{R}$ defined in equation (3.3)) that are shown in Figure 3.1. The first type is a piecewise-affine function, and the second type is a double sigmoid function.

Piecewise-Affine (PWA): We consider the case where only one linear submodel is active for a given input u. We define $d = 0.1$, that is the difference between two input linearization points, i. e., $V_{\infty,i} - V_{\infty,i-1} \ \forall i \in \{2, 3\}$. In this simple example, notice that the input operating space $u \in [0.85, 1.15]$ is divided into three similar operating regions, i. e., linear submodel LM0 should be valid for $u \in [0.85, 0.95]$, linear submodel LM1 for $u \in [0.95, 1.05]$ and linear submodel LM2 for $u \in [1.05, 1.15]$. Now, we write:

$$\omega_i(u) = \omega_i(V_\infty) = \begin{cases} 1 \text{ if } |V_\infty - V_{\infty,i}| \leq \frac{d}{2}, \\ 0 \text{ else.} \end{cases} \tag{3.7}$$

Notice that for $V_\infty = 0.95$ and $V_\infty = 1.05$, there are two weights equal to 1. In practice, we activate only one linear submodel to ensure that $\sum_{i\in\mathcal{N}} \omega_i(\mathbf{u}(k)) = 1$.

Double Sigmoid (DS): The second type of weighting function proposes a smooth transition from one linear submodel to another when the input is slowly changing. We write:

$$\omega_i(V_\infty) = \frac{1}{1+\exp\left(-s_i^+(V_\infty - (V_{\infty,i} - d))\right)} - \frac{1}{1+\exp\left(-s_i^-(V_\infty - (V_{\infty,i} + d))\right)}, \tag{3.8}$$

where $s_i^+ \in \mathbb{R}$ and $s_i^- \in \mathbb{R}$ are the slopes of the double sigmoid, and should be sufficiently large such that $\omega_i(V_{\infty,i}) = \frac{1}{1+\exp\left(-s_i^+ d\right)} - \frac{1}{1+\exp\left(s_i^- d\right)} \approx 1$.

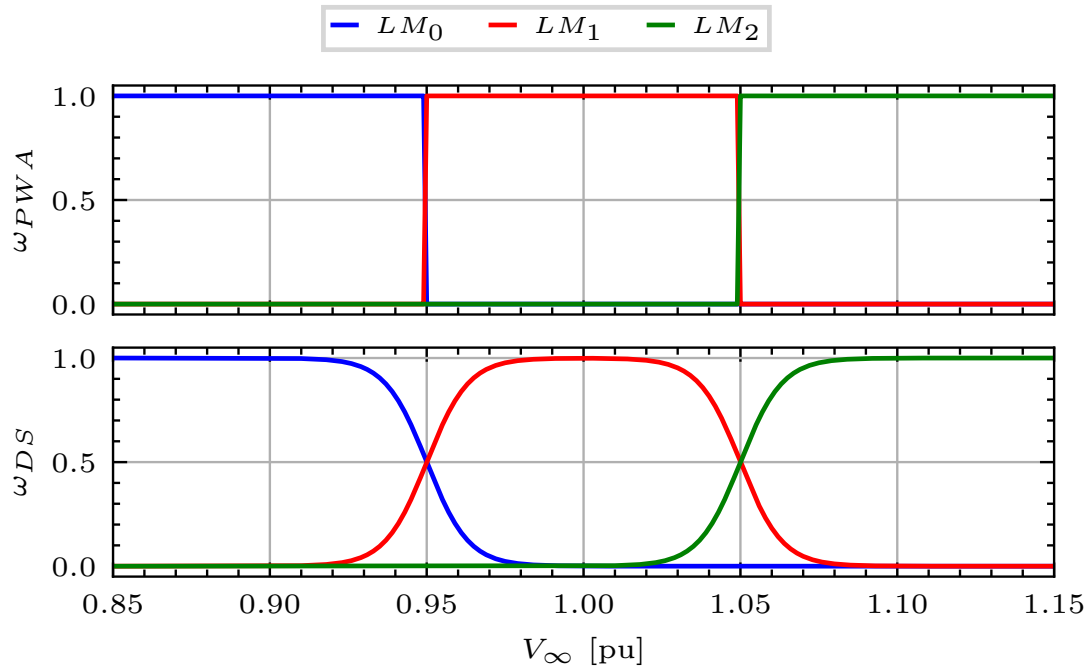

Figure 3.1: PWA and double sigmoid weighting functions.

3.2.2.2 *Numerical experiments*

We consider a slowly time-varying input $u(k) = 1 + 0.15\sin(0.3\pi k\tau)$, and compare the performance of a linear model identified for $V_\infty = 1$ pu, denoted $L(V_\infty = 1.0)$, and that of two polytopic models with PWA and DS weighting functions. To evaluate the estimation accuracy, we use the coefficient of determination defined as:

$$R_j^2 = 1 - \frac{\|\mathbf{y}_j - \hat{\mathbf{y}}_j\|^2}{\|\mathbf{y}_j - \bar{y}_j\mathbf{1}\|^2}, \tag{3.9}$$

where $\hat{\mathbf{y}}_j$ is the vector including the samples $y_j(k)$ of the j^{th} output of the approximate model, while $\mathbf{y}_j$ corresponds to the j^{th} output of the true non-linear system and $\bar{y}_j$ the mean value of $\mathbf{y}_j$. For the SMIB system, recall that $\mathbf{y}(k) = [\mathbf{y}_1(k), \mathbf{y}_2(k)]^\top = [\delta(k), \Delta\omega(k)]^\top$. The $R^2 = [R_\delta^2, R_{\Delta\omega}^2]$ scores for the linear model, the PWA polytopic model and the DS polytopic model are [0.928,821], [0.993, 0.901], [0.993, 0.908], respectively. The simulation results are shown in Figure 3.2 where NL is the output of the true nonlinear system.

We then consider a piecewise constant input signal. The R^2 scores for the linear model, the PWA polytopic model and the DS polytopic model are [0.673,0.047], [0.924,0.768], [0.924,0.768], respectively. Notice that PWA and DS polytopic models have the same R^2 scores. In this simulation we want to emphasize the behavior of the multimodel approach

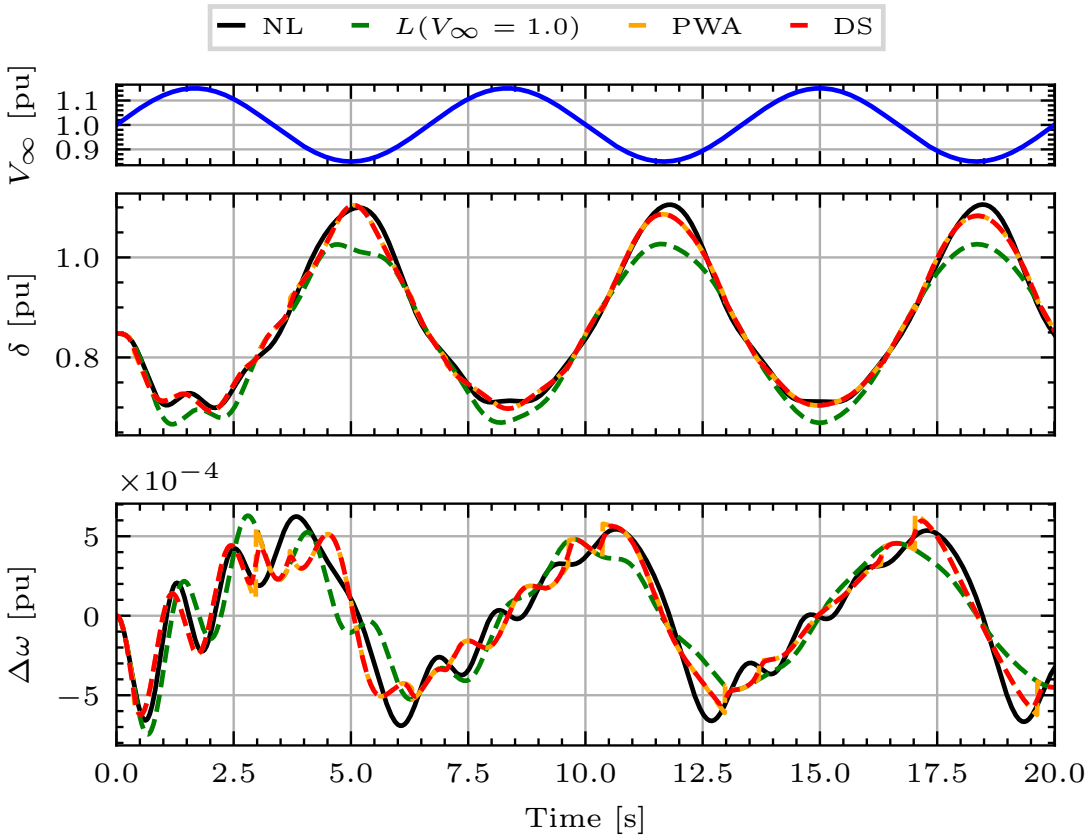

Figure 3.2: Comparison between a linear model and polytopic models with two different weighting functions.

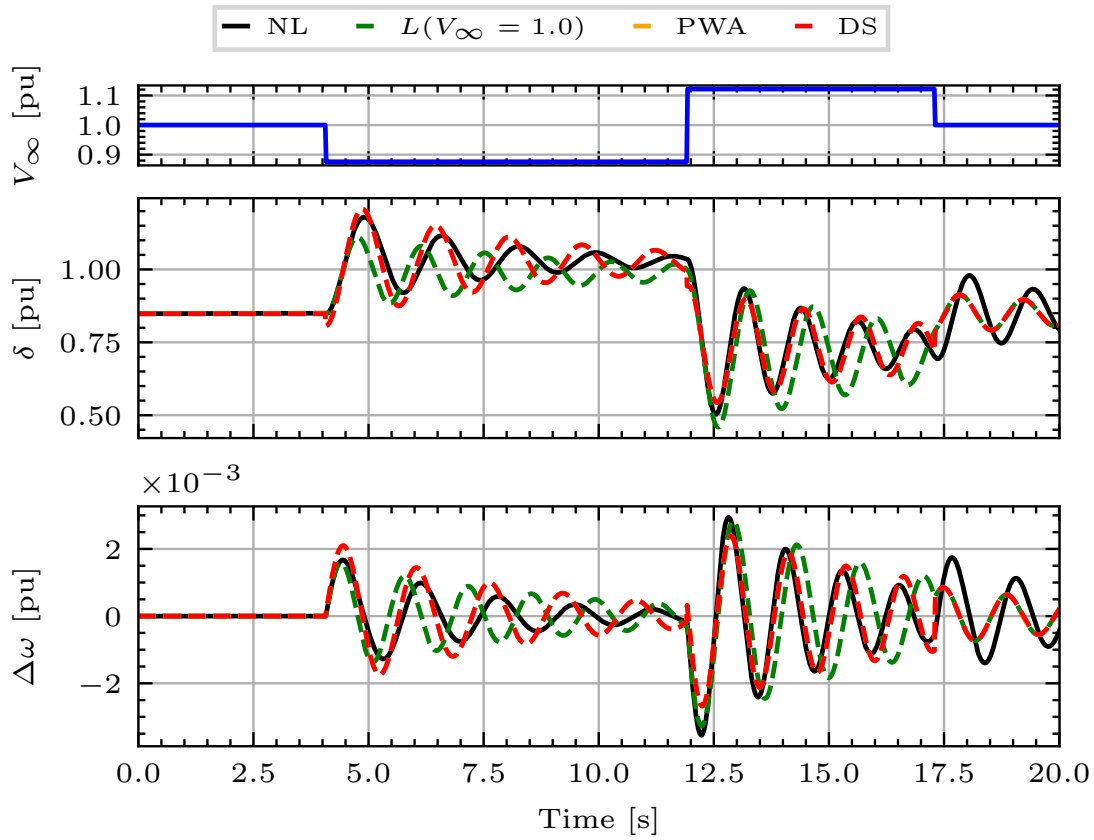

Figure 3.3: Comparison between a linear model and polytopic models with two different weighting functions

during "jumps" in the inputs. Therefore, the simulation results have been zoomed in over a small acquisition window, which can introduce some bias in the performance indicators. For a full analysis of this study case, one should consider a larger acquisition window. The simulation results are shown in Figure 3.3.

Overall, one can observe better performance of the polytopic models compared to the linear model. One can improve performance of polytopic models by adding more linear models in order to better cover the operating space. Also, although in the case of the SMIB system the weighting function does not play a significant role, for more complex systems with multiple inputs, the choice of the weighting function is crucial. In the following, we introduce our neural network-based weighting functions and a partitioning procedure to improve the performance of our polytopic models.

3.3 *PM-NET*: ENHANCED NEURAL NETWORK-BASED POLYTOPIC MODEL

Our *PM-net* model is a multimodel structure that combines linear submodels' responses using a neural network-based weighting function. The neural network is trained using measurements of the non-linear system response to time-varying inputs to address the challenge of how to design weighting functions. We propose a partitioning procedure to improve the performance of the polytopic model that is based on the post-analysis of the trained neural network, which addresses the partitioning problem of the multimodel approach.

3.3.1 *Neural network-based weighting functions*

Figure 3.4 shows the overall architecture of the proposed polytopic model (*PM-net*) including the neural-network based weighting functions (*NN-WF*). It is composed of one dense neural network for each input v_j that is called a premise variable. For every discrete time k, *NN WF* takes as input the value of $\mathbf{v}(k) = [v_1(k), ..., v_{n_u}(k)]^\top$ and returns a weight value $\omega_i(k)$ comprised in $[0, 1]$ for each linear submodel $i \in \mathcal{N}$. The premise variables $\mathbf{v}$ may differ from the actual system inputs $\mathbf{u}$ if one wants to normalize the inputs fed to the neural network through a function $f(\cdot) : \mathbb{R}^{n_u} \mapsto \mathbb{R}^{n_u}$. The output of *NN WF* corresponding to each input $v_j(k)$ is $\boldsymbol{\beta}_j(k) = [\beta_j^1(k), ..., \beta_j^N(k)]^\top \in \mathbb{R}^N$, each element corresponding to one linear submodel. The end layer of each neural network is a *Softmax* function such that the weights for each submodel $i \in \mathcal{N}$ for one specific input $v_j(k)$ sum to one:

$$\sum_{i \in \mathcal{N}} \beta_j^i(k) = 1. \tag{3.10}$$

The non-normalized weight corresponding to linear submodel i is computed as follows:

$$\gamma_i(k) = \prod_{j=1}^{n_u} \beta_j^i(k). \tag{3.11}$$

Then the weight associated with each linear submodel i is computed as:

$$\omega_i(k) = \frac{\gamma_i(k)}{\sum_{i \in \mathcal{N}} \gamma_i(k)}. \tag{3.12}$$

To train the neural network, we used measurements of the non-linear system response to time-varying inputs taking values in the pre-defined operating space. The non-linear system is perturbed with time-varying inputs that would correspond to a normal operation of the system. For instance, for the SMIB system, typical values of the input V_∞ can be between 0.8 and 1.2 pu, but it would not make sense to have a value of $V_\infty = 10$ pu, i. e., that cannot happen in a normal operation of the system. The time-varying input signal also has to be rich enough in order to extract meaningful information, i. e.,

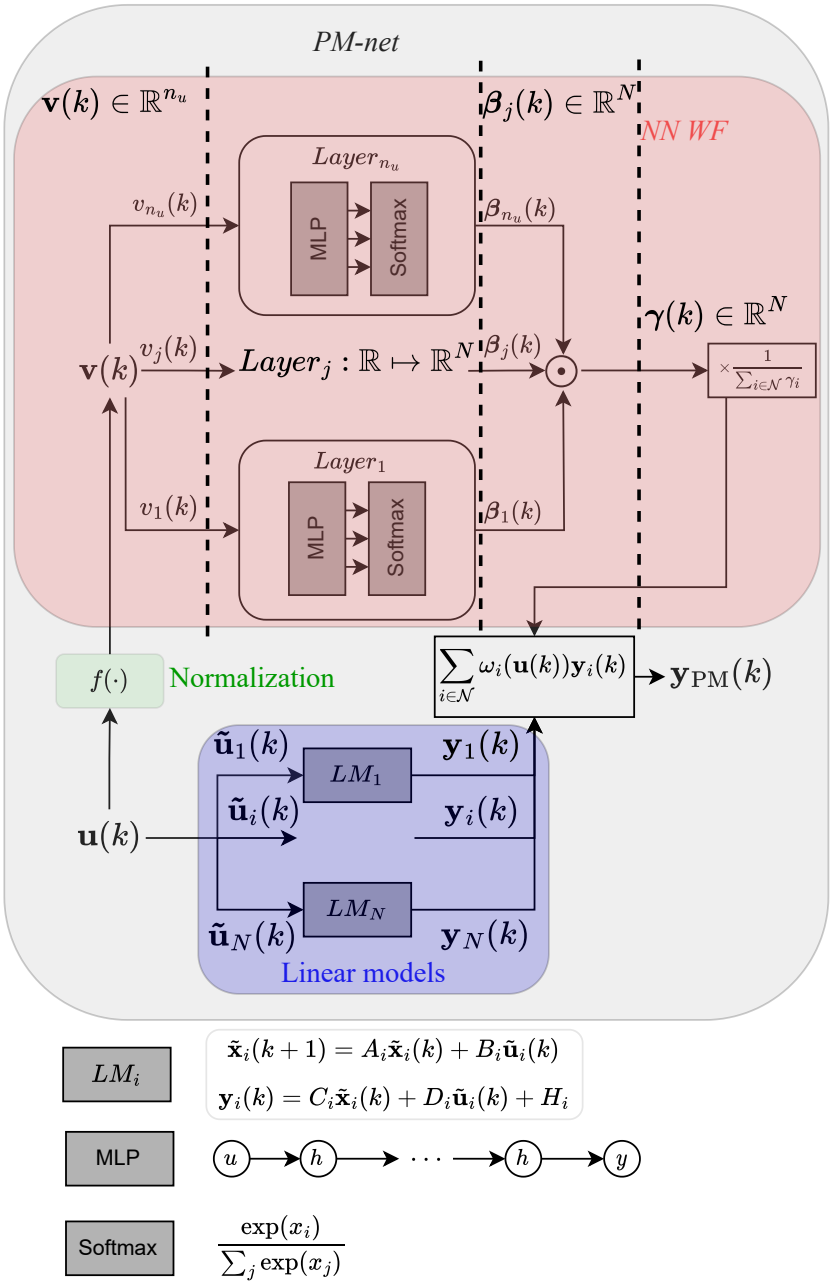

Figure 3.4: Structure of *PM-net*: *NN WF* topology and its interconnection with the linear sub-models.

Pseudo-Random Binary Sequence (PRBS) signal is a great choice since it can span a wide frequency spectrum. Finally, we use an RMSE as a loss function to train the neural network. In the following, we propose a partitioning procedure to improve the performance of the polytopic model that is based on the post-analysis of the trained *NN WF*.

3.3.2 *Partitioning procedure*

We propose the methodology shown in Algorithm 3.1 for deriving a model *PM-net* for any kind of non-linear system, although this model structure is particularly adapted to power converters. It takes as input the desired operating space $\mathcal{S}$ on which the resulting black-box model should be valid. We start with an orthotope-based partition and identify the linear submodels on the resulting operating points (the centers of the orthotopes) using specifically designed experiments. Then, we train the neural network over a large dataset that excites the system dynamics over its entire operating space. Finally, we analyze the weighting functions associated with each submodel. The latter is divided into two steps: a pruning and a segregation procedure.

The pruning procedure removes submodels to reduce the overall model complexity. If the weight associated with a submodel is always below a specified threshold α, it can be removed since it does not significantly impact the overall model response. This may happen if two submodels have similar parameters as the system behaves linearly along one input, or if one submodel was badly identified. The threshold value is a tuning parameter to achieve the desired overall model complexity.

If no model can be removed, we enter into the segregation procedure. First, one needs to identify the submodel which performs the worst, so that we can identify an operating region where the overall model response can be improved. For each submodel $i \in \mathcal{N}$, we compute the value of a weighted loss function. Let us consider a mean squared error loss function. The weighted loss L_i associated with submodel i can be written as:

$$L_i = \frac{1}{l} \sum_{k=1}^{l} \left[\omega_i(\mathbf{u}(k))(\mathbf{y}(k) - \mathbf{y}_i(k)) \right]^2, \tag{3.13}$$

with l being the number of measurements and $\mathbf{y}(k)$ the output of the non-linear system. The worst submodel i has the largest weighted loss value, that is

$$i^* = \arg\max_{i \in \mathcal{N}} L_i, \tag{3.14}$$

where i^* is the index of the worst submodel. In operating regions where the submodel i is not expected to perform well, the weight ω_i is close to 0, and the loss associated does not significantly increase. The weighted loss function is also used in Nelles [1997], where authors described the Local Linear Model Trees methodology (LOLIMOT). The working principle of LOLIMOT is to analyze every feasible re-partitioning in the operating region associated with the worst model. Then, after identifying the new submodels, they select

the best partitioning and continue the procedure. In an n-dimensional operating space, this would imply n re-partitionings and $2 \times n$ submodels to be identified. For complex systems with multiple inputs and outputs, the process of identifying new submodels is time-consuming. Achieving a successful identification of a submodel implies the design of new experiments and the measurements of the system response, which requires human-in-the-loop. This part should be minimized to speed up the modeling. Thus, in this work, we analyze the *NN WF* to find one cutting direction that can lead to good partitioning. At every step of the procedure, one must identify only two submodels based on new measurements, which significantly reduces the number of new experiments that have to be carried out on the system.

The cutting direction index j^* is found by looking at the evolution of $\beta_j^{i^*}$ for every $j = 1, ..., n_u$. Through the normalization function $f(\cdot)$, the values of the premise variables v_j are bounded within [-1,1]. Thus, we compute the values of $\beta_j^{i^*}$ for every $j = 1, ..., n_u$ and for values of v_j between -1 and 1, and then numerically compute the gradients using finite differences. The index of the cutting direction is computed as:

$$j^* = \arg\max_{j=1,...,n_u} \left\{ \max_{v_j \in [-1,1]} \left| \frac{\partial \beta_j^{i^*}}{\partial v_j} \right| \right\}. \tag{3.15}$$

Let us consider a multi-input system with a linear behavior with respect to one input u. Two submodels $\mathrm{LM}_1, \mathrm{LM}_2$ identified around two different values of input u have the same parameters. Therefore, the weight associated with LM_1 (β_u^1) or with LM_2 (β_u^2) along various values of u does not vary, as no improvement can be gained by promoting one submodel over the other when u changes. One of the two submodels may be dropped during the pruning procedure. If a system strongly behaves non-linearly along one input, one submodel quickly performs better than the others and the weight associated with that model varies steeply. We thus decide that the best cutting direction corresponds to the input along which the weight varies the steepest.

Let us consider the submodel LM_λ identified around the operating point corresponding to the input $\mathbf{c}^\lambda = [c_1^\lambda, \cdots, c_{n_u}^\lambda]^\top$. We can define an operating region $\mathcal{S}_\lambda \subset \mathcal{S}$ in which the submodel LM_λ is supposed to perform better than the other submodels. Once we found the cutting direction index j^*, we define three new orthotopic regions, $\mathcal{S}_{\lambda-1}$,$\mathcal{S}_\lambda$ and $\mathcal{S}_{\lambda+1}$. We can compute two new operating points, $\mathbf{c}^{\lambda-1}, \mathbf{c}^{\lambda+1}$ from which we can build two perturbation signals to be applied on the system to extract its response. Based on those measurements, we can identify two linear models, $\mathrm{LM}_{\lambda-1}$ and $\mathrm{LM}_{\lambda+1}$, that will be associated with operating regions $\mathcal{S}_{\lambda-1}$ and $\mathcal{S}_{\lambda+1}$. The operating regions for one model i can change from one step to another, as it depends on the number of linear models identified on operating points close to the operating points used to identify model i.

The algorithm terminates when a desired accuracy ϵ is reached.

Algorithm 3.1: Operating space partitioning for a non-linear system with n_u inputs. In red, steps that require human-in-the-loop.

input : $\mathcal{S}$
Initialization : $N = 2^{n_u}$, Orthotope partition: $\mathcal{S}_i \ \forall i \in \mathcal{N}$, Identify LM_i valid in $\mathcal{S}_i \ \forall i \in \mathcal{N}$.
while `Loss` *(PM-net)*$> \epsilon$ **do**
  `Train` (*NN WF*);
  `// Pruning procedure`
  for $i \leftarrow 1$ **to** N **do**
    if `max`$(\omega_i) < \alpha$ **then**
      Remove model LM_i;
  if *no model removed* **then**
    `// Segregation procedure`
    $i^* \leftarrow$ from (3.13),(3.14);
    $j^* \leftarrow$ from (3.15);
    Define $\mathcal{S}_{i^*-1}, \mathcal{S}_{i^*+1} \rightarrow$ along direction j^*;
    Identify $\text{LM}_{i^*-1}, \text{LM}_{i^*+1}$;

3.3.3 *Illustration on a toy example*

We compare the performance of classic polytopic models (with traditional weighting functions and no partitioning procedure) and *PM-net* at estimating the behavior of the following non-linear system:

$$y(k) = 0.95y(k-1) - 0.5p(k-1) + 0.1u(k) + 0.5\arctan(u(k-2)^2), \tag{3.16}$$

where y is the output, and p, u are inputs of the system. Assuming we want our model to be valid on $p \in [-2, 2], u \in [-5, 5]$, we identified 4 linear models at points $[p_i, u_i]^\top \in \{[-1, -2.5]^\top, [1, -2.5]^\top, [-1, 2.5]^\top, [1, 2.5]^\top\}$. A linear model valid around operating point $[p_i, u_i]^\top$ is defined in the *z-domain* as:

$$Y(z) = \frac{1}{1 - 0.95z^{-1}} \begin{pmatrix} -0.5z^{-1} \\ 0.1 + 0.5f(u_i)z^{-2} \end{pmatrix}^\top \begin{pmatrix} P(z) \\ U(z) \end{pmatrix}, \tag{3.17}$$

where $Y(z), P(z), U(z)$ are the *z-domain* representation of the output and input signals, respectively and with

$$f(u_i) = \frac{2u_i}{1 + (u_i)^4}. \tag{3.18}$$

We consider two weighting functions, the *Piecewise-Affine* (PWA) function, and the *Double Sigmoid* (DS), and we train the neural network-based weighting function *NN WF* to combine the linear models.

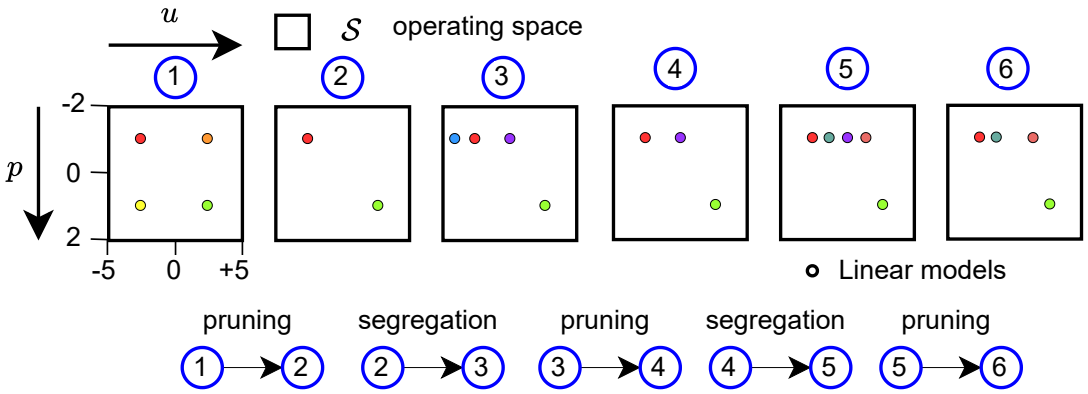

Figure 3.5: Results after 6 iterations of Algorithm 3.1.

Figures 3.5 illustrates the different steps of Algorithm 3.1 for our non-linear system. In the first iteration, the operating space $\mathcal{S}$ is split into four operating regions. Two of the four models can be dropped as the system behaves linearly along p. In the third iteration, we train the *NN WF* and compute the weighted loss L_i for the two remaining linear models. The operating region associated with the worst performing model measured based on (3.14) is re-partitioned. We analyze the gradient of the weighting function to identify the cutting direction following (3.15), and observe that the gradient along u is the largest. Two new linear models are added to enhance the model's performance, and new operating regions are defined. The algorithm stops after six iterations after reaching the prescribed accuracy.

Figure 3.6 compares the performance of the polytopic models with different weighting functions (*Piecewise-Affine*: PWA, *Double Sigmoid*: DS and *PM-net*). The mean squared error (MSE) is used to compare their performance at estimating the non-linear system defined in (3.16). The system is simulated for 500 seconds, with a sampling frequency of 20Hz, and the MSE is computed based on the error between the actual output of the system and the estimate at the sampling points. The *PM-net* model has improved performance compared to the other techniques for the same number of linear models, even though no information about the identification process of the linear models or the structure of the non-linear system has been given to *NN WF*.

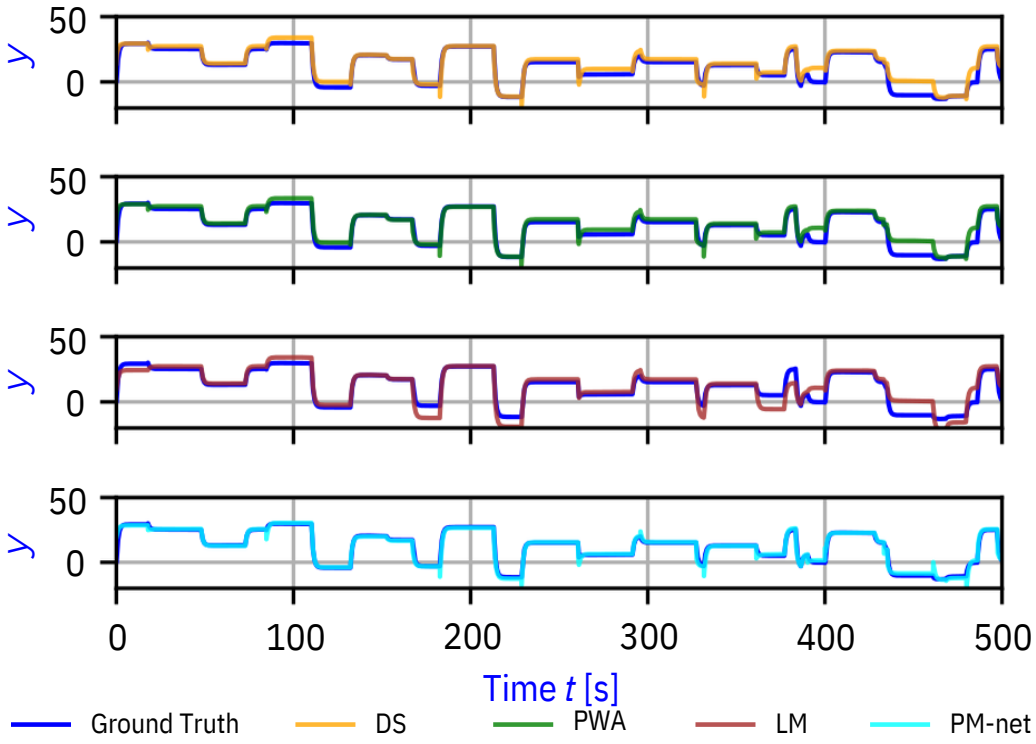

Figure 3.6: Performance of the polytopic models and a linear model (LM) on estimating the response of the non-linear system (3.16). MSE for LM: 1.5264, PWA: 0.9426, DS: 0.9210, *PM-net*: 0.1060

3.4 NUMERICAL EXPERIMENTS

In the following, we present three DC-DC converters, with different local controllers and different topologies, modelled with *PM-net*, and compare their performance with other modelling techniques.

3.4.1 *PID-voltage-regulated DC-DC boost converter*

Figure 3.7a illustrates a PID-voltage-regulated DC-DC boost converter with a simple topology, but non-linear dynamics that strongly depend on the operating point [Frances et al., 2019].

The Pulse-Width Modulation (PWM) produces a binary signal s that triggers the switch. We consider an ideal switch and an ideal diode, i. e., there are no losses or forward voltage drop. We also do not consider saturation of the magnetic cores. When the switch is open, the diode is conducting and the governing dynamical equations for the converter are equations (3.19). On the other hand, when the switch is closed, the dynamical equations are equations (3.20).

$$\frac{di}{dt} = \frac{v - v_o - R_L i}{L} \tag{3.19a}$$

$$\frac{dv_o}{dt} = \frac{1}{C(1 + R_c/R_{Load})} \left(\left(\frac{-1}{R_{Load}} - R_c \frac{C}{L} \right) v_o + \left(1 - R_c R_L \frac{C}{L} \right) i + R_c \frac{C}{L} v \right) \tag{3.19b}$$

$$\frac{di}{dt} = \frac{v - R_L i}{L} \tag{3.20a}$$

$$\frac{dv_o}{dt} = \frac{-v_o}{C\,(R_{Load} + R_c)} \tag{3.20b}$$

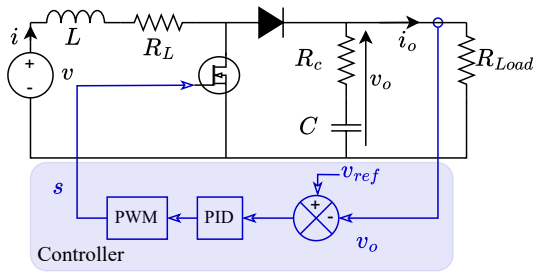

(a) Power converter topology.

Inductor L	0.5 mH
Inductor losses R_L	0.1 Ω
Capacitor C	470 μF
Equivalent series resistor R_C	0.01 Ω
Switching frequency f_s	100 kHz
Proportional term P	0.005 V^{-1}
Integral term I	120 $V^{-1}s^{-1}$
Derivator term D	10^{-5} $V^{-1}s$

(b) PID-voltage-regulated DC-DC boost converter parameters.

Figure 3.7: PID-voltage-regulated DC-DC boost converter feeding a resistive load, and with a reference voltage v_{ref} set to 48V.

Figure 3.8 shows a typical operation of the boost converter, and Table 3.7b the converter's parameters.

We will derive a *PM-net* model of the converter and compare its performance with the switching model, and other polytopic models. Notice that the switching model of the power converter is capable of representing ripples. One major advantage is that our black-box model can be run with a larger time step, leading to less computational burden. One drawback however, is that averaged models cannot represent high frequency dynamics of the converter, i. e., it cannot represent voltage and current ripples for instance.

3.4.1.1 *Experiments design and model structure*

Model structure

We consider the inputs $\mathbf{u} = [v, R_{Load}]^\top$ and outputs $\mathbf{y} = [i, v_o]^\top$. In the following, we assume that $v \in [20, 30]$ V and $R_{Load} \in [20, 50]$ Ω, that is the operating space of the power converter.

Simulation setup

We simulate in PYTHON the power converter using the switching equations (3.19)–(3.20). A digital implementation of the PID controller as well as the PWM are responsible for producing the signal s, which selects whether equation (3.19) or equation (3.20) simulates the dynamical system.

Linear model identification

We simulate the switching equations of a power converter, and use the simulation results as synthetic measurements. However, the methodology proposed to identify the linear submodels can easily be reproduced on a real power converter. The steps in the input voltage can be performed with a controllable DC voltage source, while the steps in the load resistance can be performed by connecting and disconnecting a parallel resistor to the converter. In practice, the dynamics of external devices such as voltage sources or sensors may interfere when taking measurements to identify the system. However, there exist techniques to remove undesired dynamics by post-processing measurements [Cvetkovic et al., 2011].

We identify four state-space linear models based on an orthotope partitioning of the operating space, i. e., $u_1 = [22.5, 27.5], u_2 = [22.5, 42.5], u_3 = [27.5, 27.5], u_4 = [27.5, 42.5]$. For each setpoint u_i $\forall i \in \{1, \cdots, 4\}$, we design an experiment to gather some measurements on the converter. The experiments are realized with PRBS signals as shown in Figure 3.9. The linear models are *state-space* models estimated using subspace method with time-domain data (*N4SID* [Van Overschee and De Moor, 2012]).

Neural network-based weighting functions

The neural network is trained using measurements gathered on the converter for inputs ranging the operating space by connecting/disconnecting parallel resistors and varying the input voltage source. The normalization function used in *NN WF* is

$$f(u_i(k)) = v_i(k) = 2\left(\frac{u_i(k) - \min_k u_i(k)}{\max_k u_i(k) - \min_k u_i(k)} - 0.5\right), \tag{3.21}$$

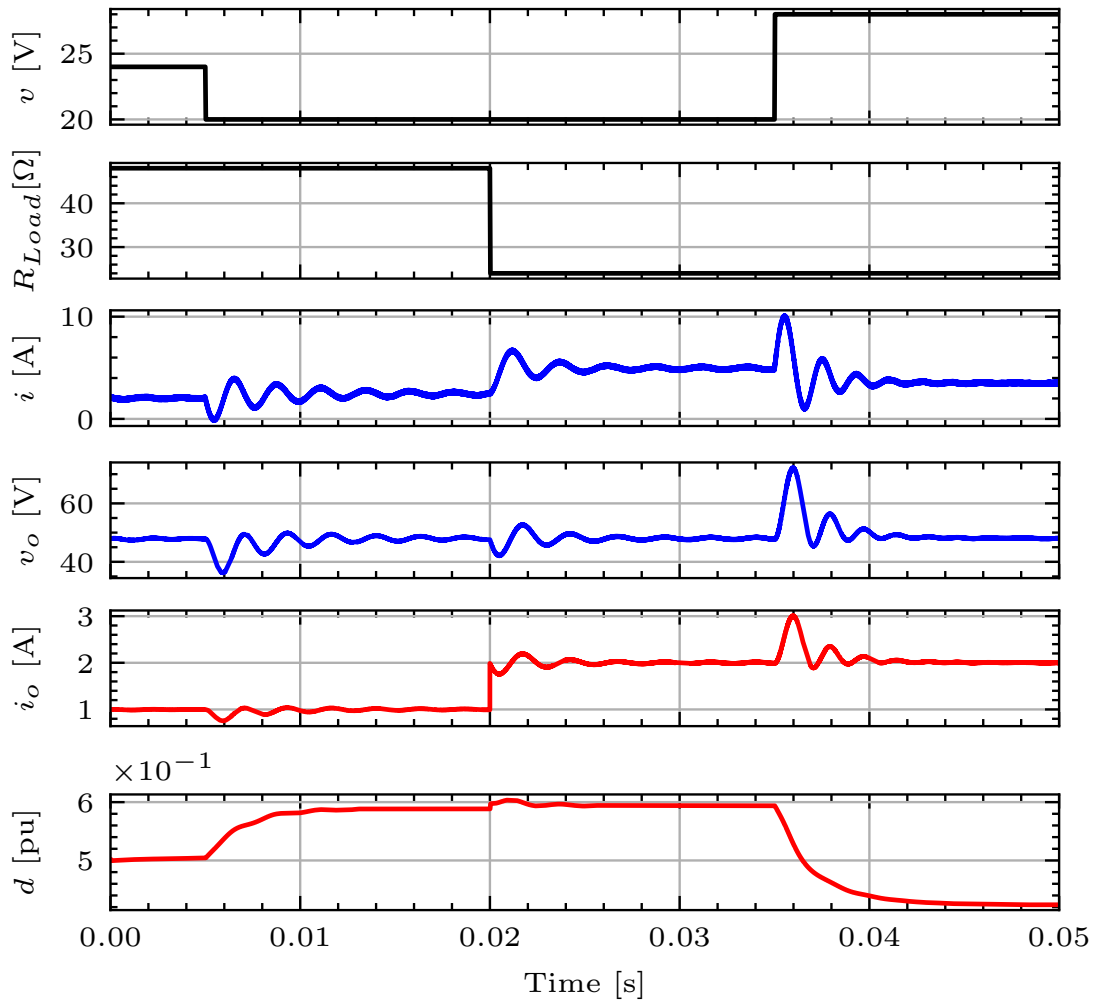

Figure 3.8: Typical operation of the PID-voltage-regulated DC-DC boost converter simulated using the switch equations, where we recall that d is the duty cycle.

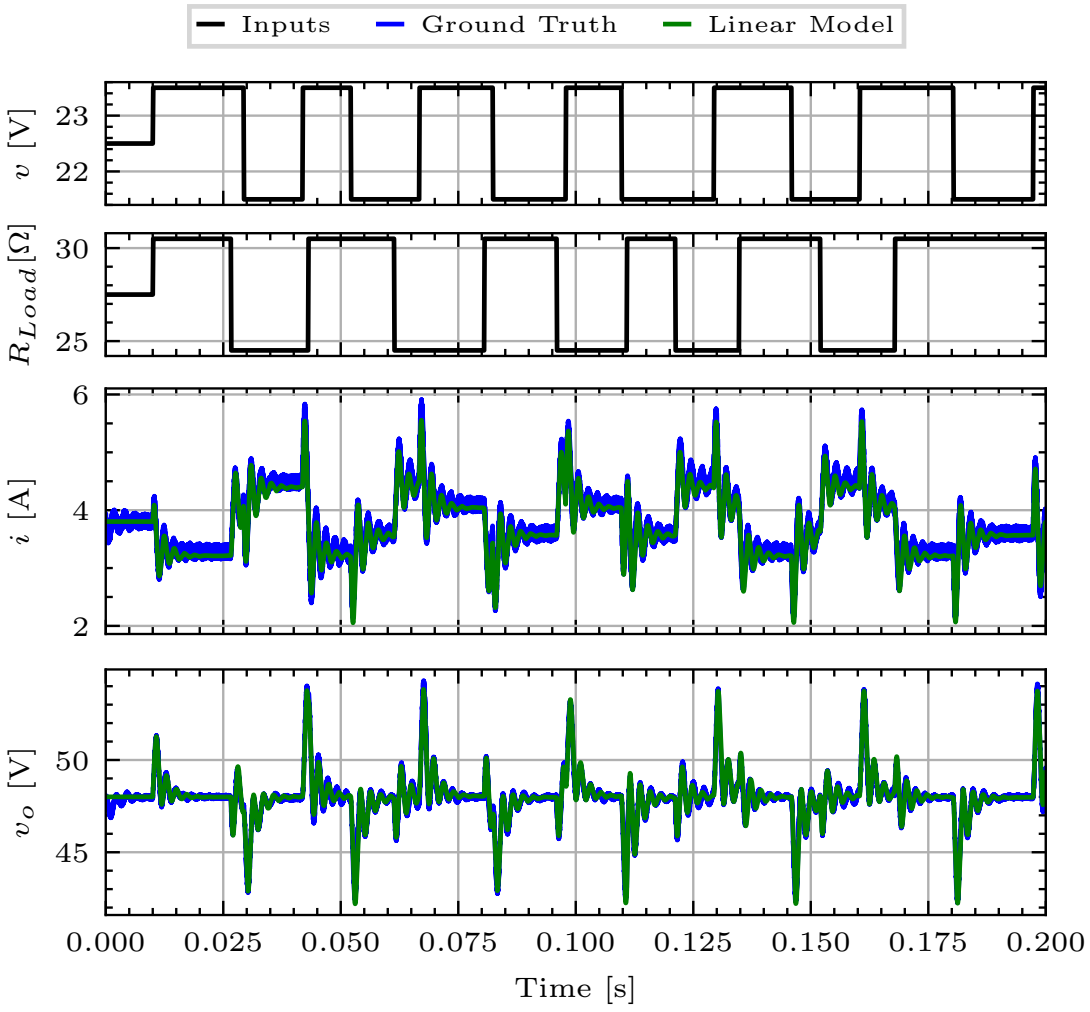

Figure 3.9: Identification of linear models for the PID-voltage-regulated DC-DC boost converter.

where the operators $\min_k$ and $\max_k$ correspond to minimum and maximum values over all the samples k, ensures that every input $v_i(k) \in [-1, 1]\ \forall i \in \{1, \cdots, n_u\}$. Also, the MLP layers for each input $v_i(k)$ correspond to a linear layer $\mathbb{R} \mapsto \mathbb{R}^{10}$, an hyperbolic tangent activation function, and another linear layer $\mathbb{R}^{10} \mapsto \mathbb{R}^N$ where N denotes the number of linear submodels. The weights obtained are shown in Figure 3.10 and compared with weights produced by the *Piecewise-Affine* function.

3.4.1.2 *Results*

We use the coefficient of determination (3.9) to compare the different modelling techniques. We compare in Figure 3.11 the performance of the polytopic model with the neural network-based weighting functions and the PWA weighting functions illustrated in Figure 3.10 and a linear model. The $R^2 = [R^2_{v_0}, R^2_i]$ scores are $[0.887, 0.906]$,$[0.794, 0.848]$ and $[0.727, 0.652]$ for the polytopic model with the neural network-based, PWA weighting function and the linear model, respectively. It shows that the polytopic model with the neural network-based weighting function outperforms the other models, even after the first stage of the Algorithm 3.1.

We then follow the Algorithm 3.1, and set the target accuracy ϵ as an R^2 score greater than 0.9 for both output variables. After 6 iterations, we reached an $R^2 = [0.907, 0.925]$ with 7 linear submodels. The results are shown in Figure 3.12.

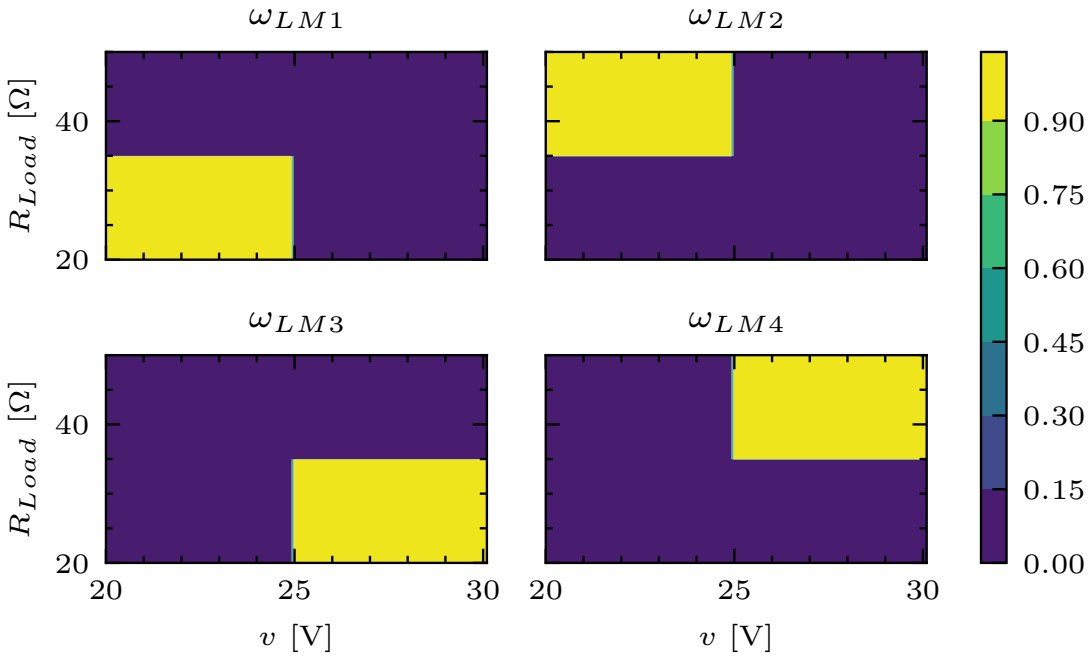

(a)

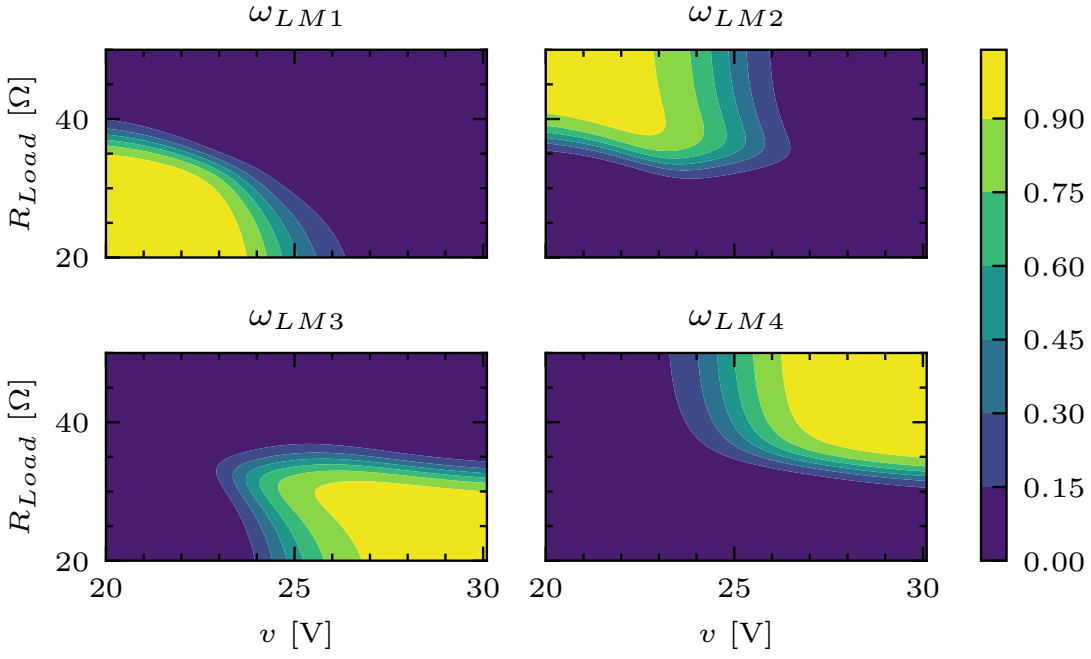

(b)

Figure 3.10: (a) PWA and (b) neural network-based weighting functions.

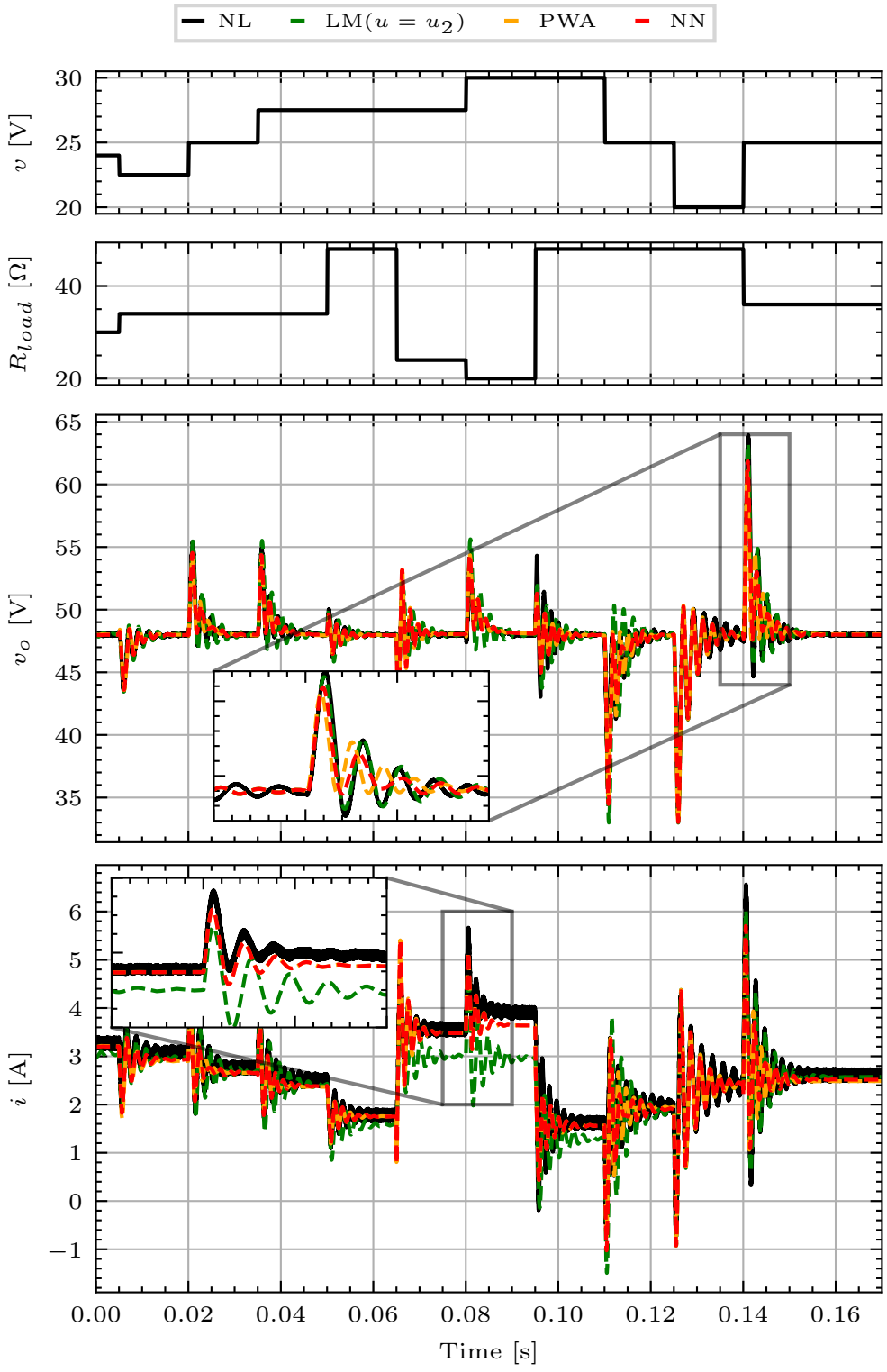

Figure 3.11: Performance comparison between a polytopic model with PWA weighting function, neural-network based weighting function **before** the *Partitioning Procedure* and a linear model.

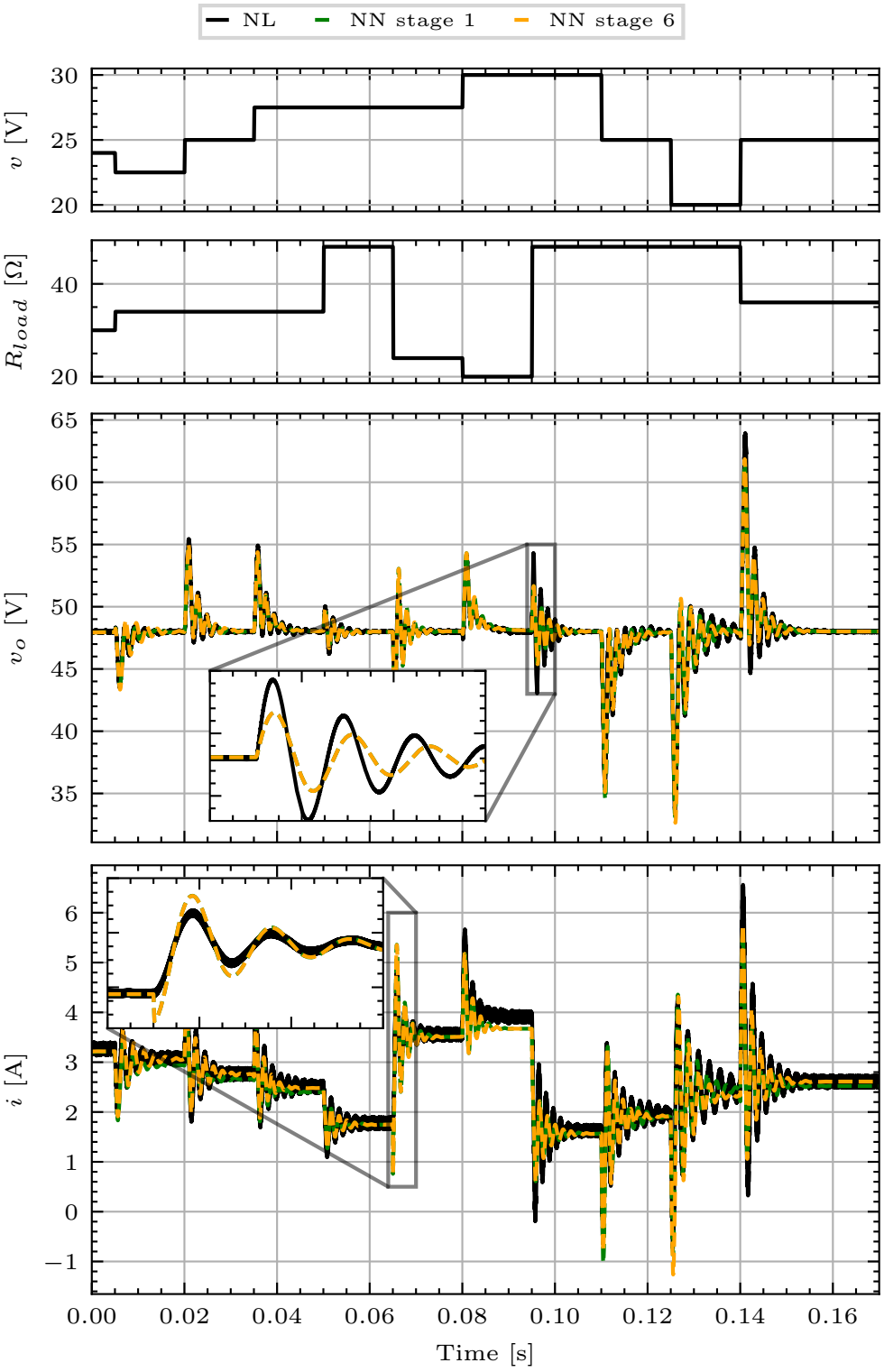

Figure 3.12: Performance comparison between a polytopic model with neural-network based weighting function at two different stages (1 and 6) of Algorithm 3.1.

3.4.2 *PI-Voltage-regulated DC-DC boost converter*

We analyze another voltage-regulated DC-DC boost converter regulated with a PI controller and feeding a current sink that is represented in Figure 3.13a. One can find the converter's parameters in Table 3.13b.

3.4.2.1 *Experiments design and model structure*

Model structure

The converter has three inputs and two outputs. We consider *G-parameters* models for the linear submodels. The *G-parameters* model is a two-port representation of a converter. Each block in the two-port representation corresponds to a transfer function, mapping one input to an output. The inputs and outputs of the *G-parameters* models are $\mathbf{u} = [v_{in}, p_{out}, k]^\top$ and $\mathbf{y} = [v_{out}, i_{in}]^\top$, respectively, with $k = \frac{v_{out}^{ref}}{v_{in}}$ the reference output to input voltage ratio and $p_{out} = v_{out}^{ref}\ i_{out}$ the reference load power. The operating space considered is $v_{in} \in [30, 40]V, p_{out} \in [10, 210]W, k \in [1, 2]$. The *G-parameters* model of the converter defined in the *z-domain* represented in Figure 3.13a is given by:

$$\begin{pmatrix} \tilde{v}_{out} \\ \tilde{i}_{in} \end{pmatrix} = \begin{pmatrix} G(z) & Z(z) & G_{v-vref}(z) \\ Y(z) & H(z) & G_{i-vref}(z) \end{pmatrix} \begin{pmatrix} \tilde{v}_{in} \\ \tilde{p}_{out} \\ \tilde{k} \end{pmatrix} \tag{3.22}$$

The control loop that sets the duty cycle, as well as the PWM modulator providing the switching signal, are included in the two-port model $(G_{v-vref}(z), G_{i-vref}(z))$. The inputs of the *G-parameters* model are small deviations from a specified operating point, i. e., $\tilde{v}_{in} = v_{in} - V_{in}$ where V_{in} is the value of the input voltage for the specified operating point. v_{in} corresponds to the input DC voltage, v_{out} is the output DC voltage and v_{out}^{ref} the reference setpoint for the output DC voltage. i_{in} is the inductor current, and i_{out}

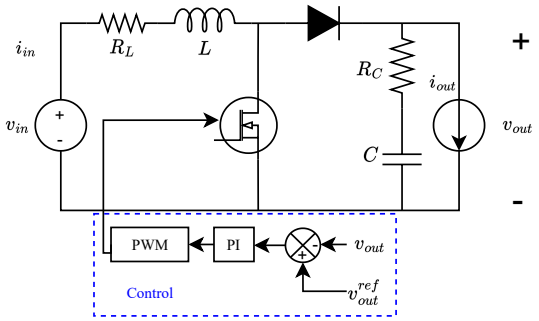

(a) Power converter topology.

Inductor L	1 mH
Inductor losses R_L	0.1 Ω
Capacitor C	810 μF
Equivalent series resistor R_C	0.01 Ω
Switching frequency f_s	50 kHz
Proportional term P	0.006 V^{-1}
Integral term I	0.436 $V^{-1}s^{-1}$

(b) PI-voltage-regulated DC-DC boost converter parameters.

Figure 3.13: PI-voltage-regulated DC-DC boost converter feeding a current sink.

corresponds to the load current. In steady-state, $v_{out} = v_{out}^{ref}$ if there is no saturation and $i_{in} = \frac{v_{out}\ i_{out}}{\eta\ v_{in}}$, where η is the converter efficiency, which depends on the operating point.

Simulation setup

A detailed model of the converter is built in TYPHOON HIL, a real-time digital simulator of power converters. We use the simulation results as synthetic measurements.

Linear model identification

Each transfer function composing the *G-parameters* model (3.22) is identified by setting all the values of $\mathbf{u}$ to zero except one where we apply a small-disturbance. The small disturbance corresponds to a PRBS signal. Each transfer function corresponds to Output-Error (OE) models. The parameters' identification of the OE models depends on the user choice. In this work, we use the function OE in MATLAB. The order of each transfer function is then reduced using the function BALRED based on the Hankel singular values, i. e., states with low energy are dropped.

Neural network-based weighting functions

The normalization function used in *NN WF* is the same as in (3.21). The MLP layers for each input $v_i(k)$ correspond to a linear layer $\mathbb{R} \mapsto \mathbb{R}^{64}$, an hyperbolic tangent activation function, and another linear layer $\mathbb{R}^{64} \mapsto \mathbb{R}^N$ where N denotes the number of linear submodels.

3.4.2.2 *Results*

Figure 3.14 compares performance of a single linear model, a polytopic model with a double sigmoid weighting function and *PM-net*. The loss function:

$$Loss = \frac{1}{l}\sum_{i=0}^{l}\left(\left(\frac{v_{out,i} - \hat{v}_{out,i}}{V_{base}}\right)^2 + \left(\frac{i_{in,i} - \hat{i}_{in,i}}{I_{base}}\right)^2\right), \tag{3.23}$$

where V_{base} and I_{base} correspond to base values defined as the maximum value of $v_{out,i}$ and $i_{in,i}$ calculated over the number of measurements l of the dataset, respectively, where $i = 0, .., l$ is the index of the measurement, is computed for the different modelling techniques with the true response of the system. The linear model scores 2.071, the polytopic model with double sigmoid weighting function (DS) scores 0.666 while the *PM-net* outperforms the two other modelling techniques and get a loss value of 0.155. Furthermore, *PM-net* only needs five linear models while the double sigmoid (DS) uses eight. It can be observed that, while the input current response (I_{in}) matches well the ground truth, the output voltage response (V_{out}) is less accurate. This probably stems from the design of the loss function that promotes the current response over the voltage response. The loss function can be modified to give more weight to the output voltage response.

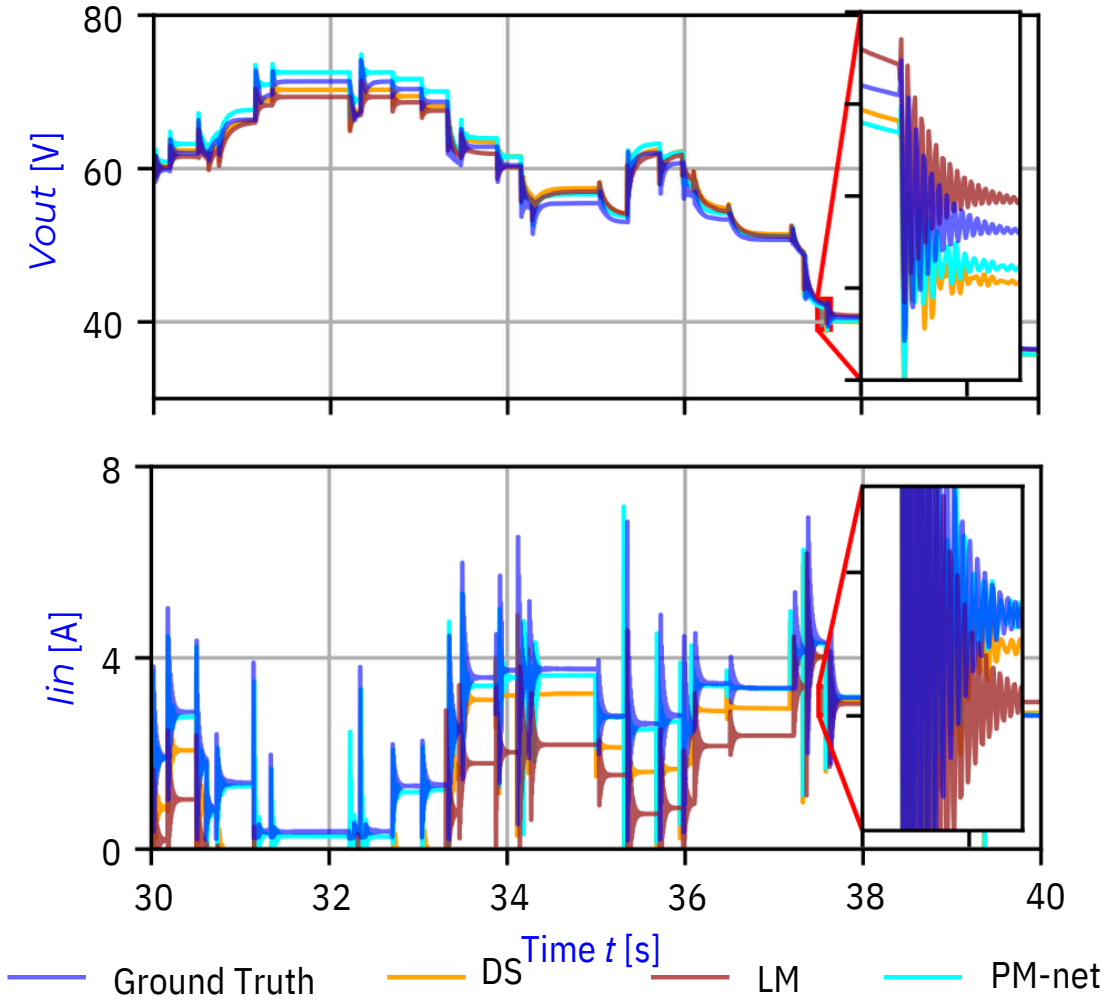

Figure 3.14: Comparison between the different modelling techniques over 10 seconds out of 60 seconds of simulation results.

3.4.3 *Industrial DC-DC power converter*

The power converter illustrated in Figure 3.15 is a DC-DC two-port bidirectional power converter, i. e., the power can flow in both directions. The DC-DC converter has been designed to regulate a power transfer in order to balance each port voltage around 380 V. If the voltage is greater on the input port than on the output one, the power should flow from the input toward the output and conversely. This behavior is designed for DC microgrid applications where some bus voltages have to be regulated to stay close to a specified nominal voltage. The user can provide some threshold voltages to the control algorithm that define the direction of the power flow, and a deadband where there is no power flowing.

3.4.3.1 *Experiments design and model structure*

Model structure

The DC-DC converter has two inputs and two outputs. We consider *G-parameters* models for the linear submodels. The *G-parameters* model in the *z-domain* for the DC-DC converter represented in Figure 3.15 is given by:

$$\begin{pmatrix} \tilde{v}_{out} \\ \tilde{i}_{in} \end{pmatrix} = \begin{pmatrix} G(z) & Z(z) \\ Y(z) & H(z) \end{pmatrix} \begin{pmatrix} \tilde{v}_{in} \\ \tilde{i}_{out} \end{pmatrix} \tag{3.24}$$

The inputs of the *G-parameters* model are small deviations from a specified operating point. The operating space is $v_{in} \in [360, 390]V, i_{out} \in [-6, 6]A$.

Simulation setup

We do not have access to the control algorithm directly, but we have access to the actual controller board with the associate firmware already loaded on the chip. Furthermore, we know the topology of the power converter. In order to collect measurements for the identification of the linear models, we use C-HIL simulation techniques, which interface

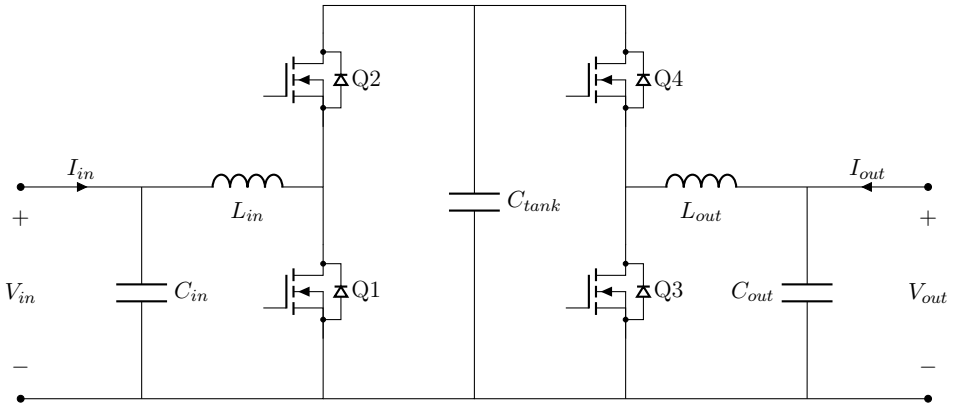

Figure 3.15: Industrial DC-DC power converter.

the local controller with a real-time digital simulator. Compared to what we presented in Section 3.4.2 where the controller and the electrical circuit were modelled in TYPHOON HIL, in this case, only the electrical circuit is implemented in TYPHOON HIL, while the controller is the actual one. C-HIL simulations have been used in Liu et al. [2009] to help to tune the parameters of a new controller or in Tarrasó et al. [2021] to validate the architecture of a grid resynchronization algorithm for grid forming inverters. The fidelity of the C-HIL simulation compared to a complete hardware system has been studied and confirmed in Chai et al. [2013]. C-HIL simulations are therefore accurate, and ease the process of collecting measurements for the identification of the linear models.

Linear model identification

To collect measurements, controlled current and voltage sources are added in the C-HIL emulator to excite the inputs with external PRBS signals. Each transfer function corresponds to Output-Error (OE) models identified using the function OE in MATLAB. The order of each transfer function is then reduced using the function BALRED based on the Hankel singular values.

Neural network-based weighting functions

The normalization function used in *NN WF* is the same as in (3.21). The MLP layers for each input $v_i(k)$ correspond to a linear layer $\mathbb{R} \mapsto \mathbb{R}^{20}$, an hyperbolic tangent activation function, and another linear layer $\mathbb{R}^{20} \mapsto \mathbb{R}^N$ where N denotes the number of linear submodels. Notice that the architecture of the neural network differs from one application to another. A common practice is to start with a small number of neurons and layers and increase the complexity of the neural network if the performance is not satisfactory during the first step of the procedure. Then, once the structure is fixed, it is kept the same for the rest of the procedure.

3.4.3.2 *Results*

We compare the performance of our *PM-net* with that of C-HIL modelling (controller interfaced with a digital simulation of the electrical circuit) and true measurements collected during a specific experiment. The converter is supplied with a constant input voltage, and its output port is connected to an *R-L* series circuit at time 0s. The output current I_{out} is the response of the *R-L* series circuit to a voltage V_{out}.

In Figure 3.16, we observe that *PM-net* exhibits a greater voltage *nadir* than in measurements and C-HIL modelling. However, the overall behavior is similar, and the steady-state values are less than one volt apart for output voltage V_{out} and superpose for the input current I_{in}. We also see that *PM-net* is not capable of representing fast transients caused by quick changes in the duty cycle as it is an averaged model. Nevertheless, the primary objective of *PM-net* is rather to describe the general behavior of converters when connected to various system configurations, and not predicting fast transients that are irrelevant for system-level studies.

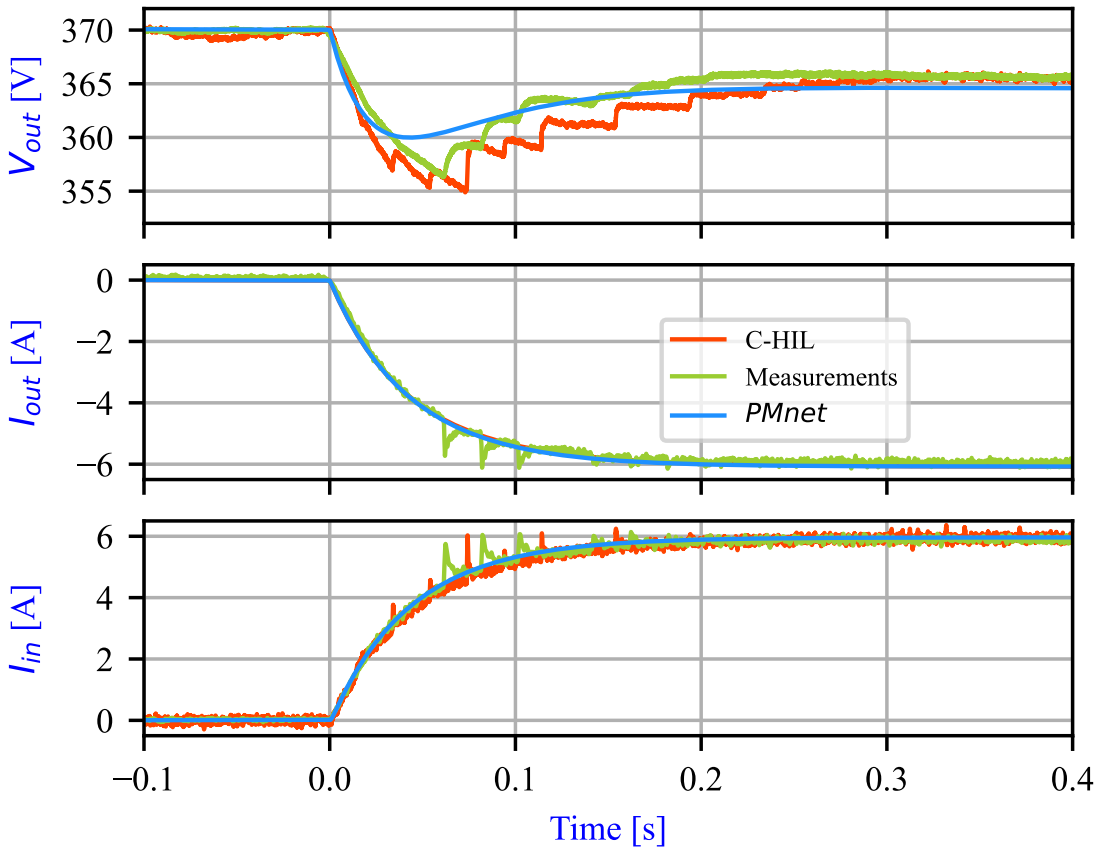

Figure 3.16: Comparison between the measurements and two different modelling techniques when the industrial DC-DC converter is connected to R-L series circuit.

3.4.4 *System-level studies*

In the following, we present three different models of small systems composed of different components where a *PM-net* model has been integrated.

3.4.4.1 *Battery-DC-DC converter-DC motor system*

The first system is composed of a battery, the *PM-net* model developed in Section 3.4.1, and a DC motor that is illustrated in Figure 3.17. The battery is modelled using *Tremblay*'s model Tremblay and Dessaint [2009]:

$$v = \begin{cases} E_0 - Ri - K\frac{Q}{Q-\int idt}(\int idt + i_{\text{filtered}}) + A\exp(-B\int idt) & \text{if discharging,} \\ E_0 - Ri - K\frac{Q}{Q-\int idt}(\int idt) - K\frac{Q}{\int idt - 0.1Q}(i_{\text{filtered}}) + A\exp(-B\int idt) & \text{if charging,} \end{cases} \tag{3.25}$$

where R is the internal resistance, Q the battery capacity, i_{filtered} the filtered current, $\int idt$ the discharge capacity and E_0, K, A, B parameters that are identified to match a nominal voltage of 48V and a given discharge curve [Colot et al., 2023a]. The DC motor is modelled as in Konstantopoulos and Alexandridis [2015]:

$$L_a\frac{di_o}{dt} = v_o - R_a i_o - K_e\omega, \tag{3.26a}$$

$$J\dot{\omega} = K_e i_o - b\omega - T_L, \tag{3.26b}$$

where L_a, R_a are the armature inductance and resistance, respectively, K_e is the motor constant, J the motor inertia, b the friction coefficient and T_L the load torque. This system is solved sequentially. The system is initialized with a value for v and R_{Load}. The converter outputs the input current i and the output voltage v_o. The input current i is used in the battery model (3.25) to obtain the input voltage v, while the output voltage is used in the DC motor model (3.26) to obtain the output current i_o. One can then build an equivalent resistance $R_{Load} = \frac{v_o}{i_o}$ that is fed into the DC-DC boost converter model. Assuming proper initialization of the state variables, the sequence is described in the following:

$$v_o(k), i(k) = \text{Converter}(v(k), R_{Load}(k)) \tag{3.27a}$$

$$v(k+1) = \text{Battery}(i(k)) \tag{3.27b}$$

$$i_o(k+1) = \text{Motor}(v_o(k)) \tag{3.27c}$$

$$R_{Load}(k+1) = \frac{v_o(k)}{i_o(k+1)} \tag{3.27d}$$

In Figure 3.18, we show the simulation results of the small system, when the PID-voltage-regulated DC-DC boost converter is modelled using the switching model, and

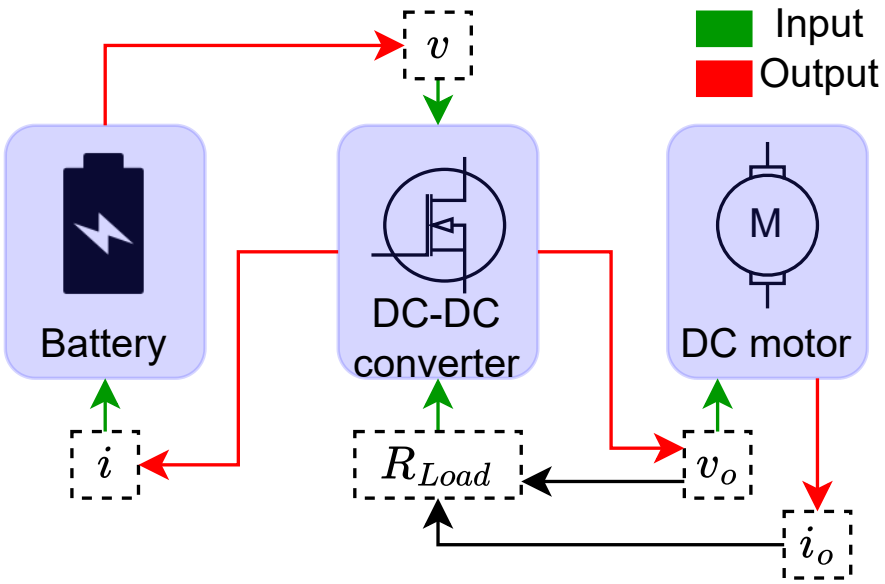

Figure 3.17: Illustration of the small system.

when it is modelled using our multimodel approach. One can see that our multimodel approach describes accurately the dynamics of the small system. Notice that, compared to the switching model, the multimodel approach is less computationally expensive. The switching model requires a time step of 1μs (the switching frequency of the converter is 100kHz) to accurately represent the dynamics of the system, while the multimodel approach can be run with a time step of 20μs. This is a significant improvement in terms of computational burden. However, our multimodel approach cannot represent the ripples since this is an averaged model.

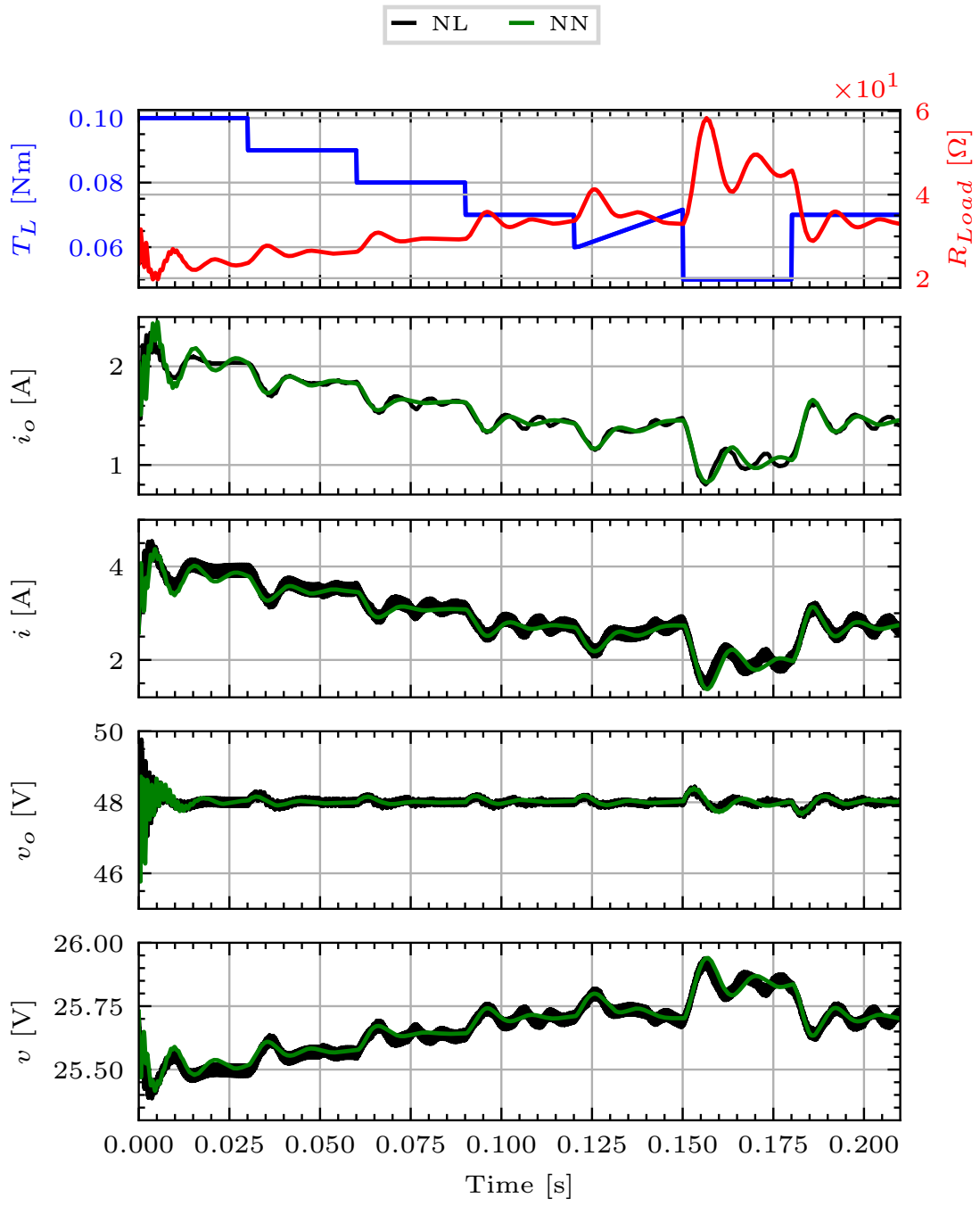

Figure 3.18: Performance of the *PM-net* model developed in Section 3.4.1 for system-level analysis: small DC system with a battery, a converter and a DC motor.

3.4.4.2 *Battery-DC-DC converter-RL load system*

We compare the *PM-net* model developed in Section 3.4.2 with the C-HIL model on a system comprising the converter illustrated in Figure 3.15, a lithium-ion battery, a variable current source and a variable *R-L* series load. The battery is modelled using *Tremblay*'s model (3.25). The system is represented in Figure 3.19.

We conduct a test where we vary the values of three components over time and observe the voltage and current responses. Initially, we consider a simple *R-L* series circuit with varying values, followed by setting the inductance to zero to obtain a pure resistance load. Then, we add a current source to reverse the power flow to simulate battery charging. Finally, we reconnect a *R-L* series. Results are shown in Figure 3.20. The only slight discrepancy is observed in the time interval between 4 and 5 seconds, where *PM-net* slightly underestimates the transient rise of the output voltage but eventually reaches the same steady-state value. As for the input current I_{in}, *PM-net* follows the general trend perfectly. Despite not being trained with data from the converter response when connected to a *R-L* series circuit and a battery, *PM-net* accurately describes the general behavior. This indicates that the model performs reliably under different conditions, confirming it as a viable option for system-level studies.

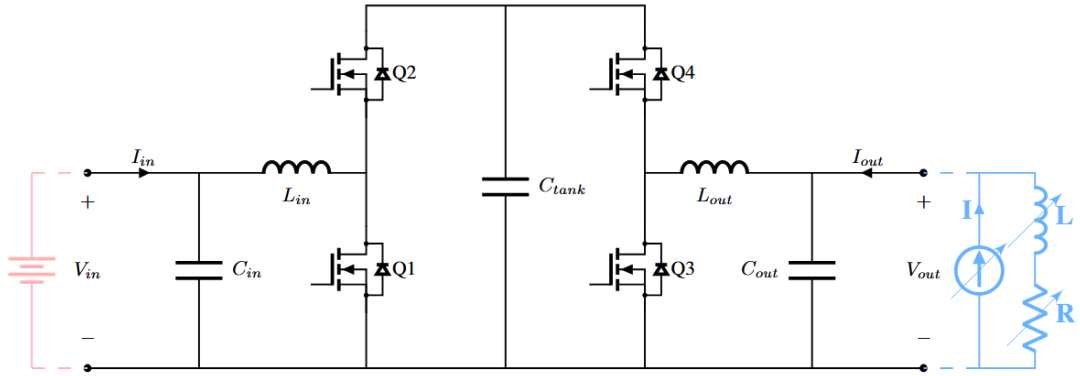

Figure 3.19: Small test system comprising the converter illustrated in Figure 3.15, a lithium-ion battery, a variable current source and a variable R-L series load.

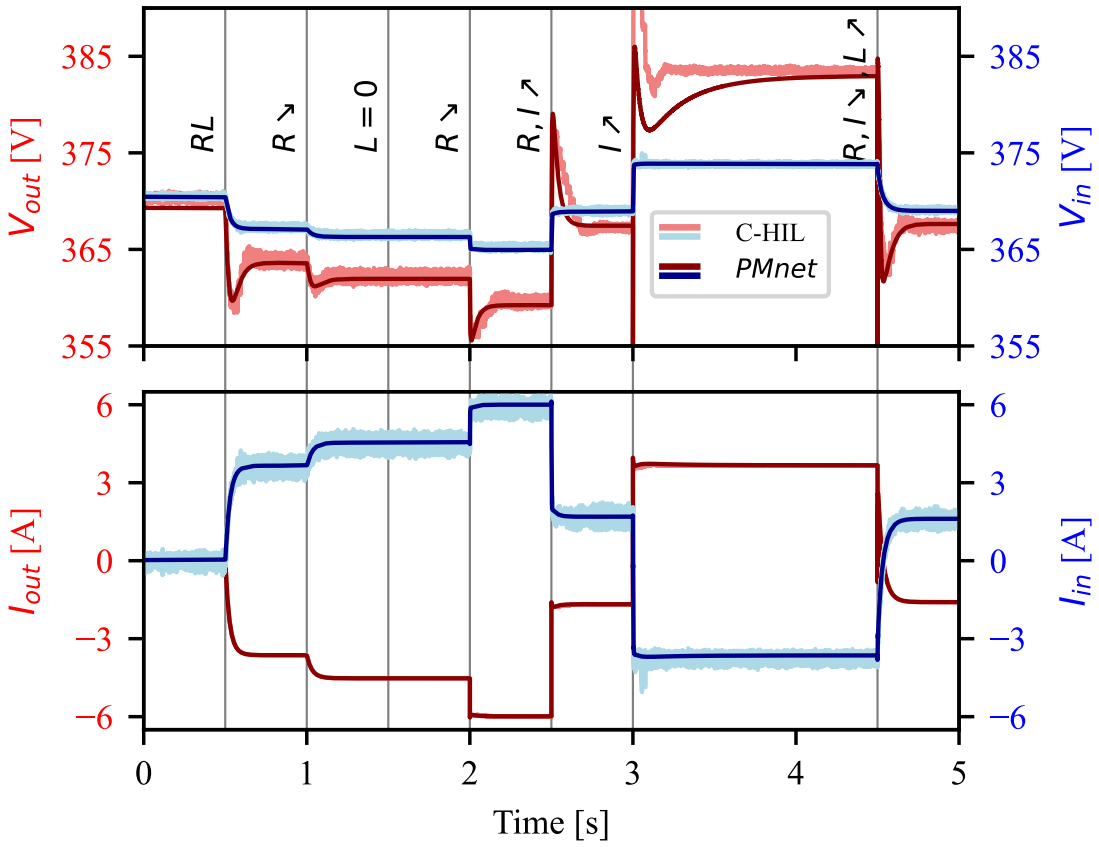

Figure 3.20: Comparison between *PM-net* and the C-HIL modelling technique when the DC-DC converter of Section 3.4.2 is integrated into a small DC system.

3.4.4.3 *HyPoSol system*

The HyPoSol (for Hybrid Power Solution) system illustrated in Figure 3.21 is a multi-component system designed to maximize the use of renewable energy. It uses the battery's flexibility and solar production to feed electrical loads. When both sources are insufficient, the system can connect to the electrical grid with the AC-IN port of the three-port converter (Sierra).

The challenge here is to ensure the stable operation of the complete system while each component has its own constraints for continuous operation or stabilizing after a contingency event. The HyPoSol system may be set in many different configurations that can be met at customer sites. The modelling tool helps to investigate the stability of the different possible configurations without relying on time-consuming and expensive real-world tests.

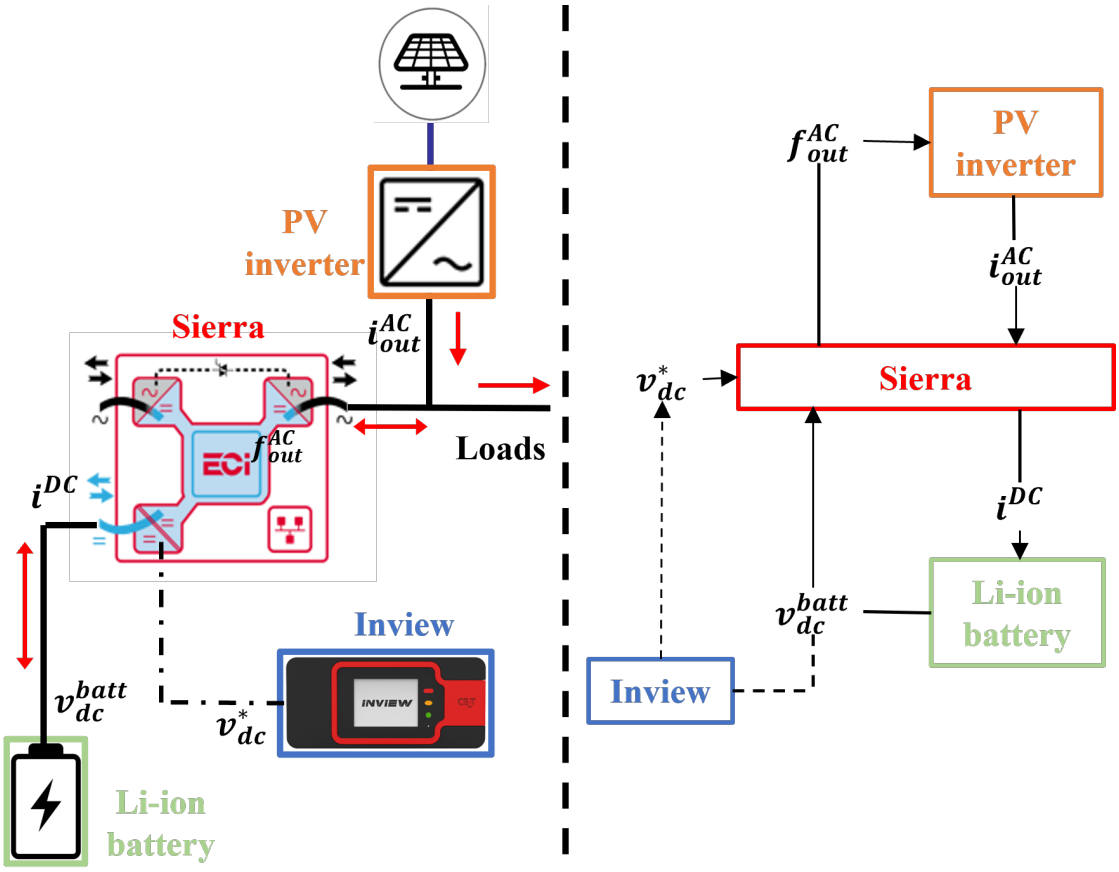

Figure 3.21: HyPoSol system representation with the physical system on the left and the schematic of the overall model on the right.

The HyPoSol system is composed of three different components: a photovoltaic (PV) inverter, a Lithium-Ion battery, and a three-port converter (Sierra). The Inview controller is in charge of sending setpoints to the three-port converter and acts as a supervisory controller.

PV inverter

For the PV inverter, we do not have inside details of the inverter's structure or the control algorithm. Therefore, we will derive a *PM-net* model. We are interested in how the inverter's current (i_{out}^{AC}) changes when the AC out frequency (f_{out}^{AC}) changes. The following equation, defined in the *z-domain*, expresses the transfer function relating i_{out}^{AC} with f_{out}^{AC}:

$$i_{out}^{AC} = F(z) f_{out}^{AC}, \tag{3.28}$$

where $F(z)$ is a single input, single output (SISO) system. There is a non-linear dependency between i_{out}^{AC} and f_{out}^{AC}. Indeed, if f_{out}^{AC} increases and goes above 50Hz, i_{out}^{AC} decreases, until it eventually reaches zero. A further increment in f_{out}^{AC} has no impact on i_{out}^{AC} as the current cannot be negative. If f_{out}^{AC} goes below 50Hz, i_{out}^{AC} does not change. We collect measurements on the PV inverter to identify a linear system $G(z)$ as an estimate of $F(z)$ around a given operating. However, $G(z)$ can only be valid in the neighborhood of the operating point at which the measurements were collected. The aim of the HyPoSol system is to control the battery current by modulating the AC-OUT frequency. A local estimation of $F(z)$ is therefore not accurate enough, and one needs to rely on a large-signal model such as our multimodel approach.

The linear models $G_i(z)\ \forall i \in \mathcal{N}$ are identified using the OE function in MATLAB. To create the perturbation signals, we use a grid simulator connected to the output port of the PV inverter to modulate the frequency while we measure the inverter's current. We identified five linear models around five different operating points $f_{out}^{AC} \in \{47.5, 50, 51.5, 52.5, 53\}$. The results comparing the measurements with our *PM-net* model are shown in Figure 3.22.

Battery

The battery is modelled according to the equations (3.25) and the parameters are tuned to match the discharge curve of the actual battery.

Three-port converter (Sierra)

The Sierra converters impose an AC-OUT frequency f_{out}^{AC} for reducing the inverter's output current i_{out}^{AC}. We assume that f_{out}^{AC} settles much faster than i_{out}^{AC}, as the Sierra quickly modulates the frequency. Therefore, we can neglect the Sierra dynamics. However, we implement the control algorithm embedded in the Sierra and postulate that once the new frequency setpoint is computed, it is directly applied to the AC-OUT port. The control algorithm has the following form:

$$f_{out}^{AC} = h(v_{dc}^{batt}, v_{dc}^{*}), \tag{3.29}$$

where v_{dc}^{*} is the voltage setpoint provided by the supervisory controller (Inview).

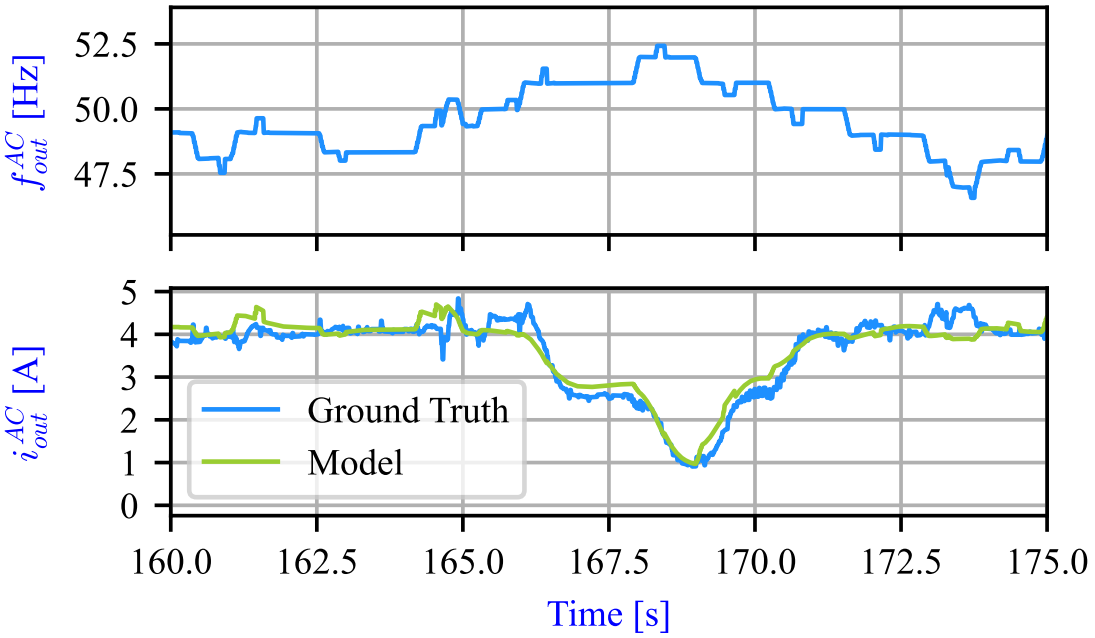

Figure 3.22: Comparison between the *PM-net* PV inverter model and measurements for different values of f_{out}^{AC}.

The DC current i^{DC} is computed based on the assumption of energy conservation from AC-OUT port to DC port:

$$v_{dc}^{batt} i^{DC} = 3 v_{out}^{AC} i_{out}^{AC}, \tag{3.30}$$

where v_{out}^{AC} is assumed to be constant and equal to 230V.

Supervisory controller (Inview)

The Inview algorithm is emulated and sends a command signal (v_{dc}^{*}) to the Sierra converter. The AC-OUT frequency setpoints are sent every second after receiving the measured battery's terminal voltage. The battery's terminal voltage is updated every millisecond after the system state is computed.

Control logics and results

PV inverters and AC loads are connected to the AC-OUT port in the HyPoSol system. The battery, connected to the DC port, charges if the solar production exceeds the load consumption. The battery can also be discharged to feed the AC loads if the solar output is insufficient. The Sierra modulates the AC-OUT frequency to control the battery charges and discharges. Two control logics exist to control the power going into the battery: one can set a constant current (CC) or a constant voltage (CV). The following results introduce these two controls (CC and CV) and how Sierra modulates the frequency f_{out}^{AC}.

Constant voltage mode (CV): It is possible to set a constant voltage to control the power entering the battery. The DC voltage at the battery's terminal rises during charging

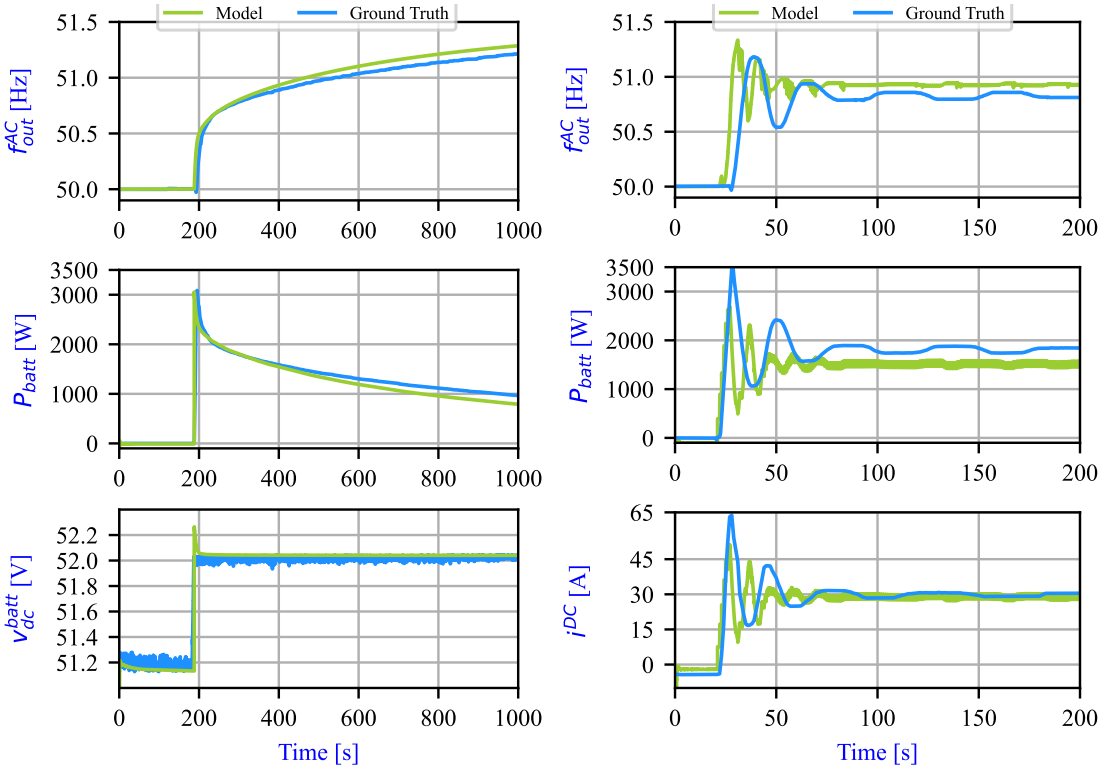

Figure 3.23: Comparison between HyPoSol model and measurements. (a) Constant voltage setpoint of 52V and maximum active power from PV inverter of 3kW. (b) Constant current setpoint of 30A and maximum active power from PV inverter of 3kW.

until it reaches the constant voltage setpoint. Then, the Sierra converter modifies the frequency f_{out}^{AC} to curtail solar production. Since the PV inverters have a certification for grid interaction, their power output are reduced if the frequency is higher than 50Hz. To compare the model outcomes with the measurements, Figure 3.23a displays the frequency and active power entering the battery (P_{batt}) in that particular scenario. It also shows the DC voltage at the battery's terminal.

The DC voltage at the battery terminal equals 51.2V when there is no solar production. The DC voltage setpoint for the constant voltage mode is set to 52V. After 200 seconds, the PV panels start injecting power into the battery (P_{batt} on Figure 3.23a). The battery's terminal voltage rises due to the inrush current and exceeds the DC voltage setpoint. The Sierra converter modifies the frequency to reduce the power injection. The initial portion of the frequency curve has a strong slope because the solar output is promptly reduced to lower the DC terminal voltage. After that, the frequency slowly rises to reduce the solar power gradually and to maintain the battery voltage at 52 V.

In Figure 3.23a, one can see the quick DC voltage rise once active power enters the battery. This is due to the battery's internal resistance, which causes a voltage rise due to the inrush current. Because of that, the DC voltage passes above the voltage setpoint imposed by the Inview control algorithm, which forces the Sierra to increase the AC-OUT frequency. In this case, the Inview controller did not play a significant role since the DC voltage setpoint is constant throughout the simulation. In the second case in which we consider a constant current, the Inview controls the system by dynamically adjusting the DC voltage setpoint.

Constant current mode (CC): In the second test, we set the maximum current to 30A on the DC side (around 1500W); the other parameters remain the same. The Inview controller computes v_{dc}^* which is applied by the Sierra converters. To take into account the current limit, Inview estimates the battery impedance and compute v_{dc}^* based on this impedance and the maximum current.

Since the current in the battery is controlled by a dynamic DC setpoint computed by the Inview controller, the frequency increases to limit the current flowing into the battery. Due to dynamic changes in the DC voltage setpoint, the f_{out}^{AC} oscillates before reaching an equilibrium. While the frequency oscillates, it induces oscillations in the active power and DC current.

The results of the simulations and measurements on the real system are presented in Figure 3.23b. The model outcome predicts the system response, but some inaccuracies can be observed during transient. However, the final steady-state value is the same. It is explained by some missing dynamics in the Sierra converters model which should be refined.

3.5 MODIFIED STATE UPDATE TECHNIQUE

In this section, we propose a modified state update technique to improve the performance of the polytopic model when abrupt changes in the input occur.

3.5.1 *Limitations of input-dependent weighting functions*

One inherent drawback with our approach, and more specifically, our input-dependent weighting function is that it leads to a suboptimal combination of submodel responses during jumps in the inputs. This can be illustrated with the SMIB system introduced earlier. When the input signal switches rapidly, the weights associated with each linear submodel also changes quickly since the weighting function only depends on the input. Hence, the state of the non-active linear model, when it becomes active, might be far away from the operating region where the linear submodel was identified. This creates jumps in the states and the outputs of the global model, as shown in Figure 3.24.

This drawback is well-known, and techniques such as dynamic weighting function [Frances et al., 2019], in which the input is filtered, has been proposed to mitigate this issue. How-

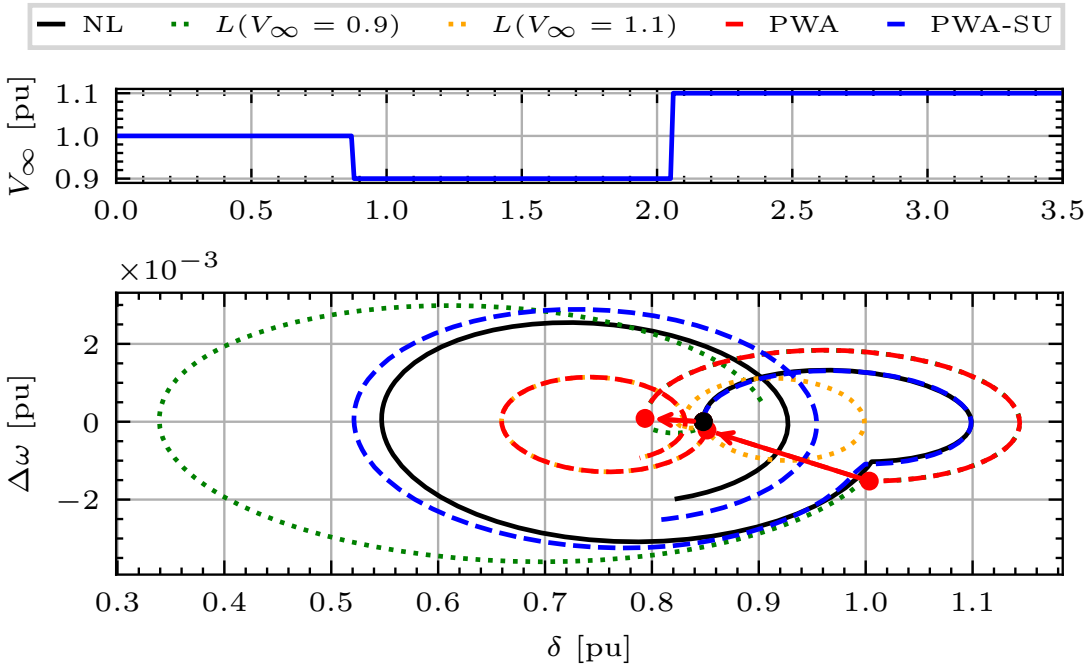

Figure 3.24: Phase portrait comparison between different modelling techniques.

ever, it can come at the cost of losing interpretability, as the weighting function is no longer a static function of the input, but also incorporates the dynamics of the input. Therefore, for a given operating point, it might be challenging to clearly identify which linear submodel is mostly responsible for the global model response. In the following, we proposed a different approach to mitigate this issue by introducing a modified state update technique.

3.5.2 *Proposed approach*

In our framework, the weighting function only depends on the inputs $\mathbf{u}$. This makes the partitioning in different operating regions, and the realization of experiments on the system, much easier. However, the polytopic model may perform poorly when the input changes quickly, as shown in Figure 3.24. In the following, we investigate a state update technique to smooth out the response of the polytopic model for abrupt changes in the input.

The idea is to find the state $\tilde{\mathbf{x}}_i^{\text{es}}(k)$ at every step k such that the distance between the output trajectory of the linear submodel and the one of the polytopic model is minimized.

First, define $\mathbf{z}_{PM}(k-1) \in \mathbb{R}^{T \cdot n_y}, \mathbf{z}_i(k-1) \in \mathbb{R}^{T \cdot n_y}$ as the vectors that contain the T previous outputs of the polytopic model and of the linear submodel i, respectively:

$$\mathbf{z}_{PM}(k-1) = \begin{pmatrix} \mathbf{y}_{PM}(k-T) \\ \mathbf{y}_{PM}(k-T+1) \\ \vdots \\ \mathbf{y}_{PM}(k-1) \end{pmatrix}, \mathbf{z}_i(k-1) = \begin{pmatrix} \mathbf{y}_i(k-T) \\ \mathbf{y}_i(k-T+1) \\ \vdots \\ \mathbf{y}_i(k-1) \end{pmatrix}. \tag{3.31}$$

We consider the sequence $\{\tilde{\mathbf{x}}_i(k-T), \tilde{\mathbf{x}}_i(k-T+1), ..., \tilde{\mathbf{x}}_i(k-1)\}$ obtained via (3.2) that yields the output sequence $\mathbf{z}_i(k-1)$. We obtain the initial state $\tilde{\mathbf{x}}_i^{\text{es}}(k-T)$ by minimizing the difference between the output vector of the linear submodel i and the output vector of the polytopic model:

$$\tilde{\mathbf{x}}_i^{\text{es}}(k-T) = \arg \min_{\tilde{\mathbf{x}}_i(k-T)} \|\mathbf{z}_{PM}(k-1) - \mathbf{z}_i(k-1)\|^2, \tag{3.32}$$

where $\mathbf{z}_i(k-1)$ is a function of $\tilde{\mathbf{x}}_i(k-T)$. Using (3.2), we have

$$\mathbf{z}_i(k-1) = \begin{pmatrix} C_i \\ C_iA_i \\ \vdots \\ C_i(A_i)^{T-1} \end{pmatrix} \tilde{\mathbf{x}}_i(k-T) + \begin{pmatrix} D_i & & \\ C_iB_i & D_i & \\ \vdots & & \\ C_iA_i^{T-2}B_i & \dots & D_i \end{pmatrix} \begin{pmatrix} \tilde{\mathbf{u}}_i(k-T) \\ \tilde{\mathbf{u}}_i(k-T+1) \\ \vdots \\ \tilde{\mathbf{u}}_i(k-1) \end{pmatrix} + \begin{pmatrix} H_i \\ H_i \\ \vdots \\ H_i \end{pmatrix} \tag{3.33}$$

that can be written as

$$\mathbf{z}_i(k-1) - R_i = \mathcal{O}_i \tilde{\mathbf{x}}_i(k-T), \tag{3.34}$$

with $\mathcal{O}_i \in \mathbb{R}^{T \cdot n_y \times n_{x,i}}$ the observability matrix and $R_i \in \mathbb{R}^{T \cdot n_y}$ is easily obtained from (3.33). Therefore, we estimate $\tilde{\mathbf{x}}_i$ by replacing $\mathbf{z}_i$ with $\mathbf{z}_{PM}$ in (3.34) and then solving for $\tilde{\mathbf{x}}_i$. This gives:

$$\tilde{\mathbf{x}}_i^{\text{es}}(k-T) = \left(\mathcal{O}_i^\top \mathcal{O}_i\right)^{-1} \mathcal{O}_i^\top \left(\mathbf{z}_{PM}(k-1) - R_i\right), \tag{3.35}$$

provided that $\mathcal{O}_i^\top \mathcal{O}_i$ is invertible, which allows one to obtain $\tilde{\mathbf{x}}_i^{\text{es}}(k)$ as:

$$\tilde{\mathbf{x}}_i^{\text{es}}(k) = A_i^T \tilde{\mathbf{x}}_i^{\text{es}}(k-T) + \sum_{j=1}^{T} A_i^{j-1} B_i \tilde{\mathbf{u}}_i(k-j). \tag{3.36}$$

The estimated state $\tilde{\mathbf{x}}_i^{\text{es}}(k)$ is then used to obtain the next state $\tilde{\mathbf{x}}_i(k+1)$ following the update equation:

$$\tilde{\mathbf{x}}_i(k+1) = A_i \left((1 - \omega_i(\mathbf{u}(k)))\tilde{\mathbf{x}}_i^{\text{es}}(k) + \omega_i(\mathbf{u}(k))\tilde{\mathbf{x}}_i(k)\right) + B_i \tilde{\mathbf{u}}_i(k). \tag{3.37}$$

Notice that, for weighting functions that can take any values between 0 and 1, two linear submodels may have weights equal to 0.5. In that case, there is no clear *active* linear submodel, rather two *partially active* linear models. Hence, equation (3.37) might badly impact the overall dynamics of the polytopic model. For that reason, we perform the state update (3.37) if the weight associated to one specific linear submodel is below a threshold value. The threshold value is set to 0.1, *i.e.*, if the linear model participates to only 10% of the global model output, its state is updated using equation (3.37). Notice that the value of T should be large enough such that the observability matrix $\mathcal{O}_i$ is full rank. Increasing the value of T will increase the computational burden, and tends to smooth the response of the polytopic model. However, if T is too large, the state update technique will not be able to follow the dynamics of the system.

In Figure 3.24, we show the state trajectories in a phase portrait of the polytopic model with the PWA weighting function with and without the proposed state update technique. One can observe that the state update technique prevent jumps from happening.

The R^2 scores for the linear model, the DS polytopic model and the DS polytopic model with state update are [0.673,0.047], [0.924,0.768], [0.963,0.891], respectively. The simulation results are shown in Figure 3.25, when the simulation time step is set to 0.01s. The modified state update technique helped improve the performance of the polytopic model.

Notice that, by applying the state update technique, we also lose interpretability as equation (3.37) becomes difficult to interpret. However, compared to the technique proposed in [Frances et al., 2019], the input-dependent weighting function remains unchanged, and one can easily apply our *partitioning procedure*.

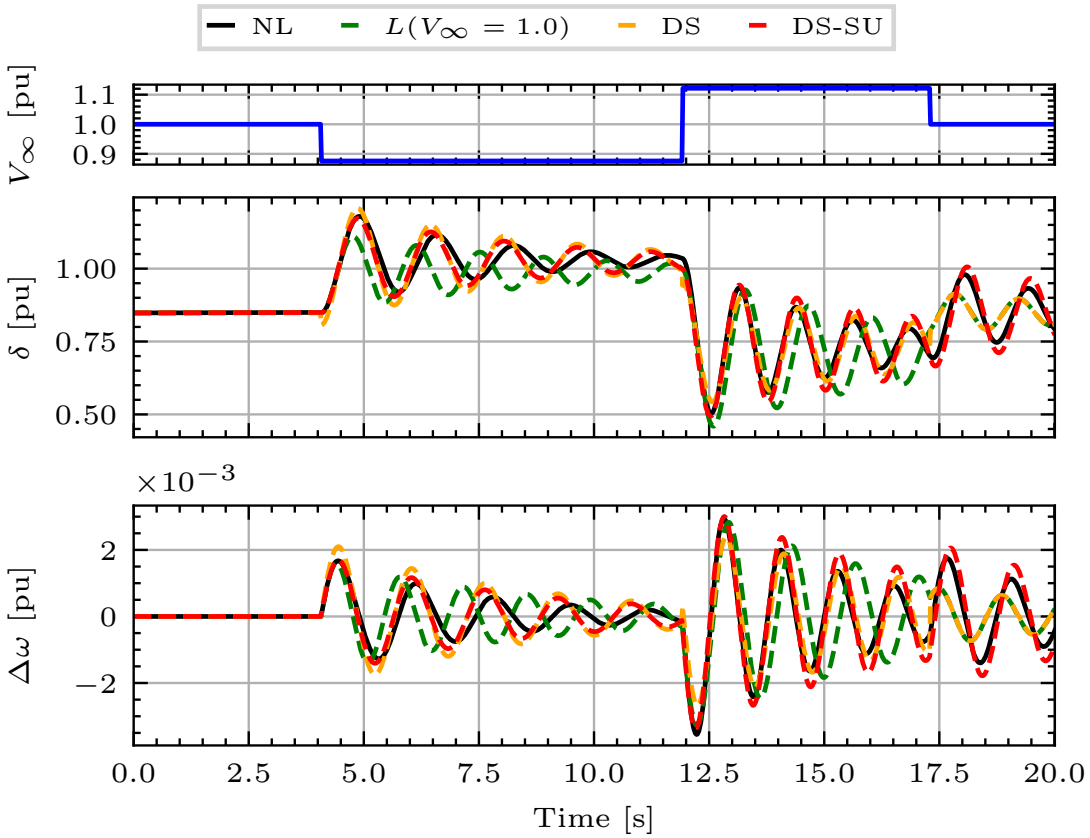

Figure 3.25: Comparison between a linear model and polytopic models with and without the modified state update technique.

4

CONCLUSION AND PERSPECTIVES

4.1 CONCLUSION

In this part, we have presented a novel approach to derive models of power converters that are valid for system-level studies. The proposed multimodel approach (*PM-net*) combines linear models responses with neural network-based weighting functions. It tackles two major challenges of the multimodel approach; how to design the weighting functions, and how to partition the operating space. The weighting functions are feedforward neural networks that are trained based on measurements collected during the operation of the converter, and they depend only on the inputs. They are designed without any prior knowledge of the power converter topology. The multimodel can be further improved by applying a *partitioning procedure* based on the post-analysis of the trained neural network. Linear submodels can be removed if the associated weights never reach a specified threshold values when screening over inputs belonging to the operating space. On the other hand, the analysis of the weighting functions can suggest in which operating regions of the operating space one can add new linear submodels to increase the performance of the multimodel. Compared to other partitioning procedure such as LOLIMOT, our procedure is less computationally expensive as it requires identifying maximum only two new linear models at each iteration. We first tested and validated our approach at modelling three different power converters. Then, we validated our approach for simulating small systems, as the goal is to derive large signal models valid for system-level studies. The proposed approach has been validated on three different power converters, and the results show that the proposed approach outperforms other modelling techniques. We also emphasized that our multimodel approach is interpretable, since it is based on linear models and the weighting function depends only on the inputs. Interpretability is an important aspect when analyzing and simulating small systems, as it gives intuition on how the system behaves around different operating points, and can help to identify causes of instability.

4.2 PERSPECTIVES

The scope of this part was to solve Problem 1.1. Power converters are most often *non-linear* and *time-varying* systems. We take care of the *time-varying* characteristic by considering averaged models of power converters, i. e., models that are not capable of representing ripples. The proposed model can capture the non-linear response of the system, and we illustrate better performance compared to linear models at simulating the

power converter response. However, power converters are complex electronic devices, and their controllers can contain advanced logics in order to properly drive the switches to reach target performance. Those controllers often contain *if-else* rules to properly drive the converter in some specific situations (during start-up, if the converter overheats, if something is happening in the network, etc.). Since we aim at modelling the closed-loop system (the electrical circuit and the associated controller), the overall system can exhibit very different dynamics caused by some specific control logics, or saturation of electrical components, and may even change depending on the network conditions. It is very challenging to derive a model that is capable of representing all those dynamics, and one needs to carefully think about the structure of the overall model, the inputs and outputs, the order of the system, etc., to properly represent the behavior of the power converter. Our multimodel approach can fail at properly representing the behavior when facing some of these particular converter's dynamics, in particular some static non-linearities. It is something we have observed in Figure 3.20, where the industrial DC-DC power converter was integrated into a small system. The controller of the converter has a deadband that is not properly represented by the multimodel. On the bright side, our approach can be combined with other modelling approaches. For instance, considering *block-oriented* structure such as *Wiener-Hammerstein* model, one can imagine combining our *PM-net* structure with saturation blocks to represent static non-linearities. Our multimodel approach is also versatile. We emphasized the importance of having an input-dependent weighting function for obtaining an interpretable model. However, the framework can also accommodate a weighting function that depends on the state of the system. But, this comes at a cost, as it increases the model complexity, and the interpretability is lost. Furthermore, the *partitioning procedure* becomes difficult to implement in practice as the operating space will consist in, not only the inputs, but the states of the system as well. Although we have shown that our approach is capable of modelling the dynamics of power converters, it is important to note that the proposed approach is not limited to power converters, and can be applied to any non-linear system. The choice of an input-dependent weighting function particularly suits power converters as these systems have fast dynamics and quickly converge to a steady-state. However, other systems share similar characteristics, and the proposed approach can be applied to them as well. For instance, this approach could be applied to model the dynamics of an entire distribution network at the point of connection with the transmission network. It can also be applied to represent the behavior of an aggregation of wind turbines at the point of connection with the electrical network. It is also important to keep in mind that the design choices for our multimodel approach have been driven by the application. We wanted an interpretable, computationally lightweight and measurement-based model because the power converters' models are intended to be used in system-level studies, and it is challenging to gather detailed information about the converter's structure. For a different application, the same multimodel approach can be used, but some of these constraints can be relaxed which could enhance the performance of the model.

Part II

VOLTAGE REGULATION IN DISTRIBUTION NETWORKS

NOTATIONS

$\mathbf{x}$	Column vector
X	Matrix
$\mathcal{X}$	Set
$(.)^\top$	Transpose of a vector or a matrix
$\dot{(.)}$, $\frac{d}{dt}$	Time derivative
$\|(.)\|$	Euclidean norm
$\mathbb{0}$	zero vector of appropriate dimension
$\mathbf{1}$	all-ones vector of appropriate dimension
$\mathbb{I}$	Identity matrix
$\mathbb{R}$	Real numbers
$\mathcal{N}$	Set of indices for nodes
$\mathcal{M}$	Set of indices for voltage-regulated nodes
$\mathcal{G}$	Set of indices for DERs
$\mathbf{s}$	vector of complex powers
$\mathbf{p}_l, \mathbf{q}_l$	vectors of active and reactive powers consumed by non-controllable devices
$\mathbf{p}, \mathbf{q}$	vector of active and reactive powers injected by controllable DERs
v,ν	voltage phasor (magnitude and angle), voltage magnitude
$\hat{\nu}$, $\tilde{\nu}$	approximate voltage magnitude, voltage magnitude measurement
$\mathbf{u}$	vector of decision variables
$\underline{V}$,$\bar{V}$	lower and upper voltage bounds

5

BACKGROUND AND PROBLEM STATEMENT

The power system is commonly classified into three different subsystems; the transmission system, the subtransmission system and the distribution system [Kundur, 1994]. The transmission system forms the backbone of the power system; it operates at the highest voltage level, and is responsible for transmitting bulk power from the power plants to the subtransmission level. The subtransmission system is operated at lower voltage levels and supply large industrial consumers and distribution substations. Notice that, in some systems, there is no clear differentiation between the subtransmission and the transmission system. Finally, distribution systems are the medium-low voltage networks supplying small industries to residential and commercial customers.

The development and improvement of power converters, coupled with environmental policies and carbon emission reduction targets, have led to the integration of distributed generation into the distribution systems. Distributed energy resources are small-scale power generation technologies that are located close to the load they serve. Distributed energy resources can span from renewable energy sources such as solar photovoltaic (PV) systems, wind turbines, or fossil fueled engines [Hidalgo et al., 2010]. This integration brings some challenges for the operation and the planning of distribution networks [Walling et al., 2008],[Alam et al., 2020]. In particular, the penetration of renewable energy resources creates bidirectional power flows raising voltage and current issues that traditional control techniques can no longer solve. These challenges have led to the development of active distribution networks; distribution networks embedding systems to control a combination of distributed energy resources (DERs) in order to guarantee the safe operation of the network [D'Adamo et al., 2009].

In this thesis, we focus on voltage regulation in distribution networks, and propose different control architectures to steer DERs power setpoints in order to maintain voltages within admissible limits across the network. In the following, we provide some illustrations of the voltage issues that one can encounter in distribution networks with high penetration of DERs, and why the traditional control techniques may fail at resolving those issues.

We aim at studying the voltage magnitudes throughout a distribution network and analyse the impact of DERs and how the traditional voltage regulation methods work. We are interested in power flow analysis that involves the calculations of the power flows and voltages for specific node configurations. This is a steady-state analysis, and it does not take into account the dynamics of the different system's components. In this part, we assume that dynamics of system's components are much faster than the dynamics

responsible for voltage issues, typically, load patterns and renewable energy productions. This assumption will be discussed in the final conclusion.

5.1 POWER FLOW ANALYSIS

Let us consider an electrical distribution system with $N+1$ nodes and hosting G DERs; these may include inverter-interfaced photovoltaic systems, energy storage systems, variable-speed drives, and electric vehicles, or small-scale generators if any. We consider a balanced three-phase system, this allows us to use a single-phase equivalent. The node 0 is taken to be the substation or the point of common coupling, while $\mathcal{N} := \{1, ..., N\}$ is the set of remaining nodes. We consider a steady-state model where voltages and currents are represented in the phasor domain. Accordingly, let $v_k = \nu_k e^{\mathrm{j}\delta_k} \in \mathbb{C}$, $\nu_k := |v_k|$, and $i_k = |i_k| e^{\mathrm{j}\psi_k} \in \mathbb{C}$ the line-to-ground voltage and current injected at node i, respectively. Moreover, the voltage at node 0 is set to $v_0 = V_0 e^{\mathrm{j}\delta_0}$. Using Ohm's Law and Kirchhoff's Laws, one has the usual phasor relationship that can be written in terms of the nodal admittance matrix:

$$\begin{pmatrix} i_0 \\ \mathbf{i} \end{pmatrix} = \begin{pmatrix} y_0 & \bar{\mathbf{y}}^\top \\ \bar{\mathbf{y}} & \mathbf{Y} \end{pmatrix} \begin{pmatrix} v_0 \\ \mathbf{v} \end{pmatrix} \tag{5.1}$$

where $\mathbf{v} \in \mathbb{C}^N$ collects the nodal voltages $\{v_k\}_{k\in\mathcal{N}}$, $\mathbf{i} \in \mathbb{C}^N$ collects the nodal injection currents $\{i_k\}_{k\in\mathcal{N}}$, and $\mathbf{Y} \in \mathbb{C}^{N\times N}$, $\bar{\mathbf{y}} \in \mathbb{C}^N$, and $y_0 \in \mathbb{C}$ are based on the series and shunt admittances of the distribution lines represented by a standard Π-model [Kersting, 2007]. Using (5.1), it is possible to relate complex powers at the nodes $\mathcal{N}$ with voltages as

$$\mathbf{s}_{\text{net}} = \operatorname{diag}(\mathbf{v}) \left(\bar{\mathbf{y}}^* v_0^* + \mathbf{Y}^* \mathbf{v}^*\right) \tag{5.2}$$

where $\mathbf{s}_{\text{net}} = \mathbf{p}_{\text{net}} + \mathrm{j}\mathbf{q}_{\text{net}} \in \mathbb{C}^N$, with $\mathbf{p}_{\text{net}}$ and $\mathbf{q}_{\text{net}}$ vectors collecting the net active and reactive power injections at nodes $\mathcal{N}$. Note that $\mathbf{p}_{\text{net}}$ and $\mathbf{q}_{\text{net}}$ account for both the powers (injected or consumed) of the DERs and the aggregate powers of the non-controllable loads that are connected to each of the nodes $\mathcal{N}$. In particular, let $\mathbf{p}_l := [p_{l,1}, \ldots, p_{l,N}]^\top \in \mathcal{W}_p, \mathbf{q}_l := [q_{l,1}, \ldots, q_{l,N}]^\top \in \mathcal{W}_q$ with compact sets $\mathcal{W}_p \subset \mathbb{R}^N$ and $\mathcal{W}_q \subset \mathbb{R}^N$, be vectors collecting the net active and reactive power consumed at the nodes by non-controllable devices (positive when the power is consumed). For the G DERs, consider the vector $\mathbf{u} = [p_1, p_2, ..., p_G, q_1, q_2, ..., q_G]^\top$ collecting their active and reactive powers (with a positive sign denoting generation). Moreover, let $\mathcal{G} := \{1, ..., G\}$ be the index for the DERs, and define a function $w : \mathcal{G} \to \mathcal{N}$ which maps a DER index to the node where the DER is connected to. With this notation, note that $\mathcal{G}_n := \{i \in \mathcal{G} : n = w(i)\}$ is the set of DERs connected at node $n \in \mathcal{N}$. Then, the net active and reactive powers are given by $p_{\text{net},n} = \sum_{j\in\mathcal{G}_n} p_j - p_{l,n}$ and $q_{\text{net},n} = \sum_{j\in\mathcal{G}_n} q_j - q_{l,n}$ at each n and $\mathbf{p}_{\text{net}} := \{p_{\text{net},n}\}_{n\in\mathcal{N}}$, $\mathbf{q}_{\text{net}} := \{q_{\text{net},n}\}_{n\in\mathcal{N}}$.

The goal of the power flow analysis is to determine, from equation (5.2), a relationship of the form $\mathbf{v} = f(\mathbf{p}_{\text{net}}, \mathbf{q}_{\text{net}})$, where $f : \mathbb{R}^{2N} \mapsto \mathbb{C}^N$. Such explicit formulation of

the voltages does not always exist as the system of equations (5.2) may have no, one, or many solutions. Therefore, we make the following assumption when restricting to a neighborhood of the nominal voltage profile.

Assumption 5.1 (*Mapping in a neighborhood of the nominal voltage profile*)**.** *There exists a unique continuously differentiable function* $H : \mathcal{U} \times \mathcal{W}_p \times \mathcal{W}_q \to \mathbb{R}^N$ *such that,* $H_i(\mathbf{u}; \mathbf{p}_l, \mathbf{q}_l) = \nu_i = |v_i|$*, for* $i \in \mathcal{N}$*. The Jacobian* $J_H(\mathbf{u}; \mathbf{p}_l, \mathbf{q}_l) := \frac{\partial H(\mathbf{u}; \mathbf{p}_l, \mathbf{q}_l)}{\partial \mathbf{u}}$ *is locally Lipschitz continuous.* □

If multiple solutions exist, we only consider the *practical* solution, i. e., in the neighborhood of the nominal voltage profile, we restrict the attention to the solution that leads to high voltages and small line currents. The existence of the map H is based on the *Implicit Function Theorem* and the results of, e. g., [Bolognani and Zampieri, 2015, Bernstein et al., 2018, Wang et al., 2017] for single-phase and multi-phase distribution networks. Notice that one cannot find an explicit formulation of the map $H(\mathbf{u}; \mathbf{p}_l, \mathbf{q}_l)$, therefore, one has to rely on iterative numerical methods such as *Gauss-Seidel* or *Newton-Raphson* [Kundur, 1994] to solve the power flow equations and obtain the voltages and currents, or use a linear approximation. In this chapter, we will mainly discuss linear approximations to obtain a *voltage model*, and will not rely on iterative numerical methods to resolve power flow equations.

5.2 IMPACT OF DISTRIBUTED ENERGY RESOURCES ON NETWORK VOLTAGES

To illustrate the voltage issues in distribution networks, we consider a simple example shown in Figure 5.1. The network is composed of 4 different nodes, the substation node 0 which imposes a voltage reference, one industrial node, and two residential nodes where DERs are connected.

We consider two scenarios that correspond to two different time of the day; in the morning (P_i^1) when the solar irradiance is low and households consume energy, and around midday (P_i^2), when solar irradiance is high and the residential nodes act as energy producers. We consider that the behavior of the industrial node is constant throughout the day, i. e., always consumes the same amount of power, and that there is no reactive power consumption or injection.

Traditionally, voltage regulation in distribution networks was achieved using load tap changers or switchgears. By altering the number of turns of the substation transformer, the load tap changer can increase or decrease the reference voltage v_0. However, the increasing variability introduced by DERs can shorten their lifespan, and they may become insufficient to resolve voltage issues [McDonald, 2013].

In Figure 5.2, we show the results of a power flow analysis for the two scenarios considered, and when a load tap changer (LTC) is used to regulate the voltages throughout the feeder. When there is no solar production (No PVs), the power flows unidirectionnally from the substation toward the end of the feeder. Distribution network lines

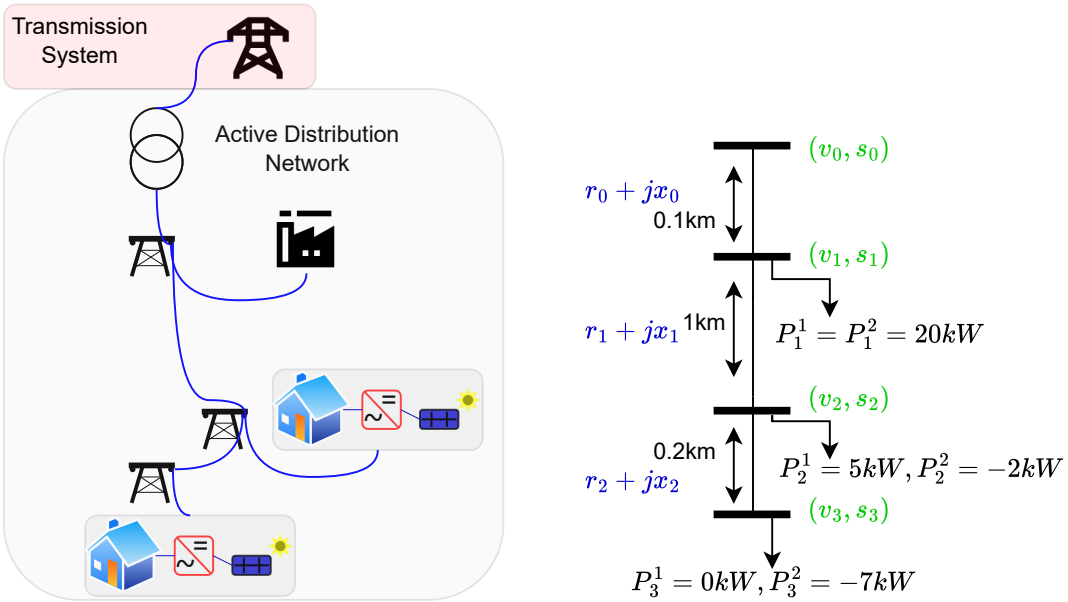

Figure 5.1: Illustrative example for voltage problems in distribution networks.

are mainly resistive (R/X ratio $= 6$ in our case study), and active power flows impact voltage magnitudes. The voltage magnitudes progressively decrease along the feeder, to reach its lowest point at node 3. If one considers the admissible voltage limits being $[\underline{V}, \bar{V}]^\top = [0.95, 1.05]^\top$, then nodes 1, 2 and 3 present undervoltages. The LTC can increase the voltage at the substation v_0 to 1.05 by appropriately selecting the turn ratio of the substation transformer, and increase the voltage level throughout the feeder to ensure admissible voltage levels everywhere. This type of control works effectively without the massive integration of renewable-based DERs, since the load pattern is predictible, and the power is flowing unidirectionnally. On the other hand, when we have solar production (PVs), the voltage drops at the first node but increases toward the end of the feeder, since node 2 and 3 are injecting active power into the network. The power flows in two directions; from the substation to node 1 and from node 2 and 3 to node 1. The voltage profile is no longer monotonic along the feeder, and the LTC can no longer resolve the voltage issues, since we have both undervoltage at node 1 and overvoltage at node 3. Additionally, even if the LTC can effectively resolve the voltage issue, the increasing variability of renewable-based DERs impacts the directions of the power flow and requires many tap changes along the day. This intense usage of LTC can shorten their lifespan and increase the cost of operating the distribution network.

On the other hand, continuous improvements in power electronics converters create new possibilities for the control of DERs, enabling new tools for voltage regulation [Antoniadou-Plytaria et al., 2017]. For instance, reactive power support can be provided by PV inverters to regulate voltages [Alam et al., 2014]. Reactive power support

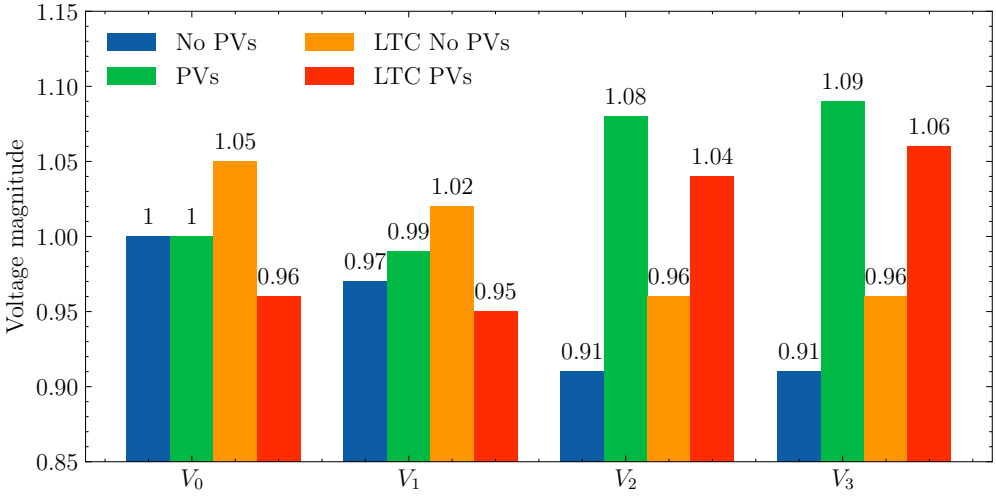

Figure 5.2: Power flow analysis: impact of DERs on voltage magnitudes in a small distribution network.

does not work well in distribution networks because of the high R/X ratio. However, it can improve voltage profile at a very low cost. If reactive power support is not sufficient, one can control active power that consists in curtailing active power production to mitigate overvoltages [Howlader et al., 2020]. This solution comes at higher costs than reactive power control, but it is also more efficient as we will show in the following.

In Figure 5.3, we compare the voltage profiles without any type of control, with Volt/-VAR control (reactive power control) and with Volt/Watt control (active power curtailment). In this case, we control only the PV inverter located at node 3. To ensure voltage profiles are within the admissible values, 12kvAr of reactive power had to be produced by the PV inverter located at node 3 for the Volt/VAR control, and 3.5kW of active power had to be curtailed for the Volt/Watt control. Although Volt/Watt control is more expensive, as it requires limiting the active power production and induces profit losses, this is more efficient and has a bigger impact on voltage profiles compared to Volt/VAR control.

Remark 5.1 (*Fairness in optimization schemes of active power curtailment for voltage regulation*)**.** *Notice that, if we control the PV inverter at node 2, we need 4kW of active power curtailment or 15kvAr of reactive power compensation. This is because the power injections have a stronger impact on voltage magnitudes for nodes electrically distant from the substation compared to nodes electrically close to the substation. When it comes to solving optimization problems to minimize the total usage of resources (active power curtailment, or reactive power support), this raises fairness concerns as some PV plants may experience more significant curtailment depending on their locations in the network [Gupta and Molzahn, 2024]. This fairness can be taken into account by adding a fairness objective along the main objective function of the optimization problem. This*

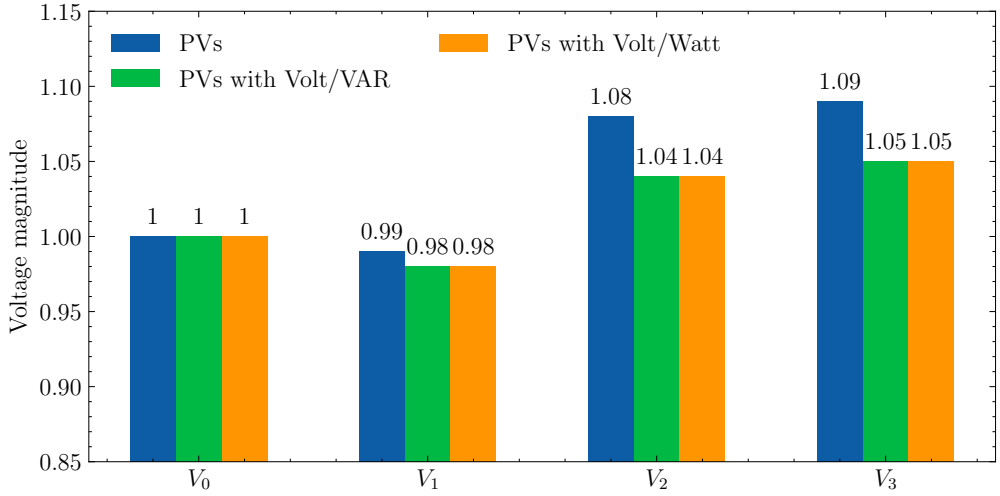

Figure 5.3: Power flow analysis: impact of DERs on voltage magnitudes in a small distribution network.

topic is not covered in this thesis, however, some of the methods proposed naturally embed fairness in their objective functions.

5.3 PROBLEM STATEMENT

In this thesis, we propose different algorithms to solve the voltage regulation problem in distribution networks using DERs' flexibility, i. e., by either providing reactive power support, curtailing active power or both of them.

We seek to solve an OPF problem for distribution systems to obtain power setpoints for the DERs that minimize the operational cost (or maximize performance objectives) for the utilities and the customers, subject to operational constraints that include voltage limits, and hardware limits [Capitanescu, 2016]. The cost associated with the utility companies may favor the minimization of system losses or the usage of controllable resources (e. g., including cost of active power curtailment or reactive power compensation [Dall'Anese and Simonetto, 2016]); on the other hand, customers may want to minimize the power curtailed by renewables or maximize their revenue by providing ancillary services. In what follows, we consider a set of nodes $\mathcal{M} \subseteq \mathcal{N}$ with cardinality $M = |\mathcal{M}|$ where voltages are to be regulated (if the operator would like to monitor and regulate all the voltages, then $\mathcal{M} = \mathcal{N}$). Finally, let $\mathcal{U}_i \subset \mathbb{R}^2$ be a compact set of admissible power setpoints, such that $(p_i, q_i) \in \mathcal{U}_i$ for $i \in \mathcal{G}$. We define $\mathcal{U} := \mathcal{U}_1 \times \mathcal{U}_2 \times \ldots \times \mathcal{U}_G$ so that $\mathbf{u} \in \mathcal{U}$, where $\mathbf{u}$ collects the controllable active and reactive power injections of

DERs. We propose the following formulation of the OPF problem, which focuses on the voltage regulation problem:

$$\begin{aligned} \min_{\boldsymbol{\nu}\in\mathbb{R}^M, \mathbf{u}\in\mathbb{R}^{2G}} \quad & C_v(\boldsymbol{\nu}) + C_p(\mathbf{u}) \\ \text{s.t.} \quad & \underline{V} \leq \nu_i \leq \bar{V} && \forall i \in \mathcal{M} \\ & \nu_i = H_i(\mathbf{u}; \mathbf{p}_l, \mathbf{q}_l) && \forall i \in \mathcal{M} \\ & (p_i, q_i) \in \mathcal{U}_i && \forall i \in \mathcal{G} \end{aligned} \tag{5.3}$$

where the functions $C_v : \mathbb{R}^M \to \mathbb{R}$ and $C_p : \mathbb{R}^{2G} \to \mathbb{R}$ have locally Lipschitz continuous gradients, $\underline{V}$ and $\bar{V}$ are predefined voltage bounds that the operator wants to enforce at nodes $i \in \mathcal{M}$, $H_i(\mathbf{u}; \mathbf{p}_l, \mathbf{q}_l)$ is the ith component of the function $H(\mathbf{u}; \mathbf{p}_l, \mathbf{q}_l)$ (specifying the voltage magnitude ν_i).

In practice, solving problem (5.3) is challenging since the map H does not have an analytical formulation, and the power flow equations are non-linear, which makes the problem non-convex. Furthermore, solving problem (5.3) requires collecting non-controllable power injections at every nodes, which might not be feasible with current distribution network technology. Hence, in this thesis, we aim at finding algorithmic solutions of problem (5.3), such that one can obtain DERs setpoints in a time that is consistent with the distribution network dynamics. We distinguish three different architectures to find algorithmic solutions for problem (5.3): centralized, decentralized, and distributed controllers [Morstyn et al., 2018], that are illustrated in Figure 5.4. Decentralized control strategies only require local information, and therefore, do not rely on a communication infrastructure. However, due to the limited information each asset has access to, these control strategies cannot fully utilise the flexibility of DERs. Centralized control strategies require a complex communication infrastructure, such that each asset communicates with an aggregator. The aggregator usually requires full knowledge about the system, and solves complex optimization problems to optimally coordinate DERs power outputs. Finally, distributed strategies rely on peer-to-peer communication, and leverage problem decomposition in order for each controller to solve a small optimization problem instead of a complex optimization problem. Each of these strategies has advantages and drawbacks; one can obtain better performances if one increase the complexity of the communication infrastructure and the problem to be solved. In distribution networks, communication infrastructures may be non-existent, or data privacy concerns could prevent using control strategies that require communicating information with neighbors or an aggregator. On the other hand, in some applications, one may want to prioritize performance over cost of implementation. In other applications, the size of the system may prevent implementing a centralized architecture, and distributed strategies may be preferred.

In the following, we propose a centralized, a decentralized and a distributed control strategy to solve the voltage regulation problem in distribution networks.

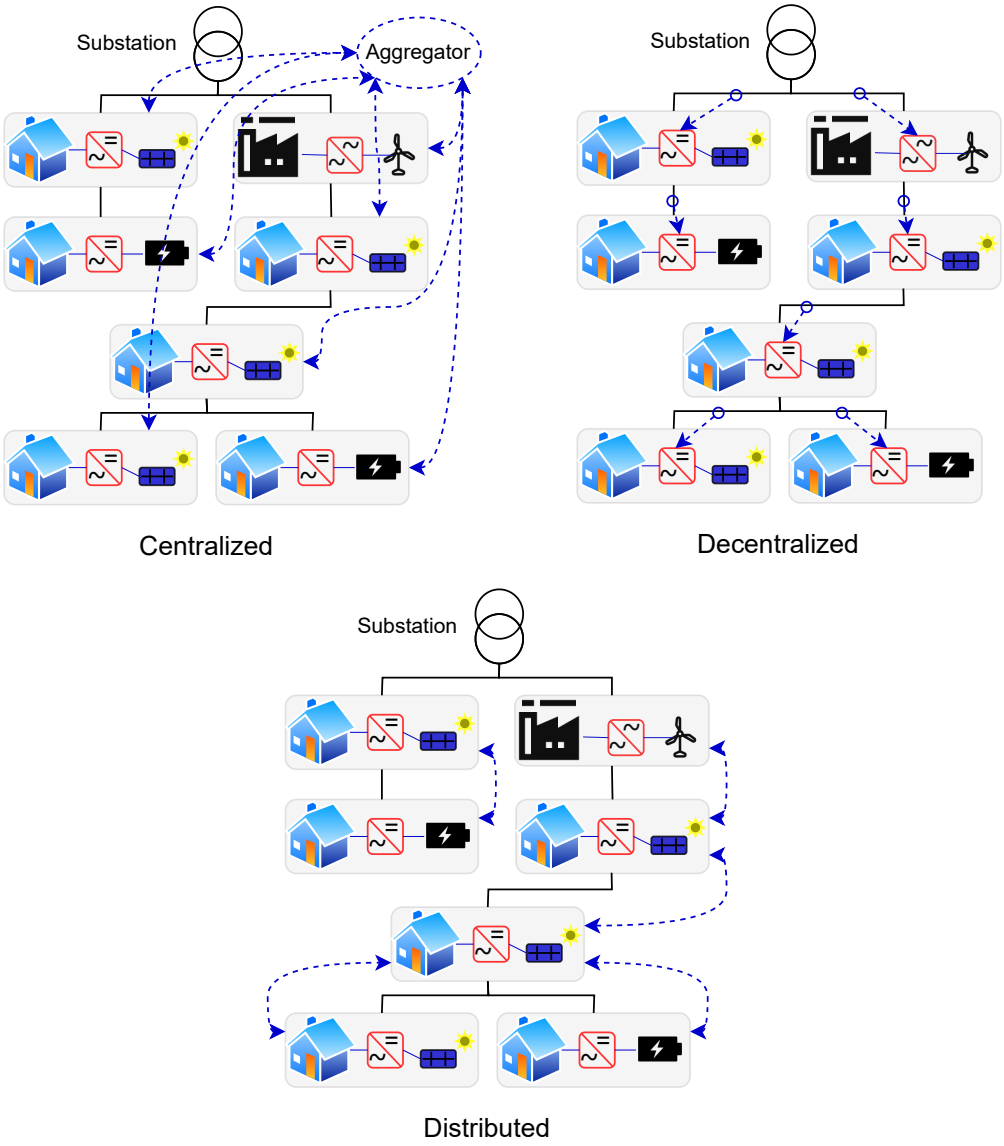

Figure 5.4: Control strategy architectures

6 CENTRALIZED CONTROLLER

Outline

In this chapter, we present a centralized controller that solves the AC-OPF problem in real-time to tackle Problem 1.2 introduced in Section 1.2.2. We leverage the theory of control barrier functions to design a feedback-based optimization algorithm that ensures anytime satisfaction of operational constraints. We illustrate the performance of our algorithm through numerical experiments on a single-phase distribution network and for the optimal regulation of a virtual power plant on a three-phase unbalanced distribution network. The chapter is organized as follows: in Section 6.1, we review the literature on centralized control strategies for voltage regulation in distribution networks and introduce feedback-based optimization algorithms. In Section 6.2, we introduce the feedback-based safe gradient flow algorithm and illustrate its performance on a single-phase distribution network. In Section 6.3, we extend our feedback-based safe gradient flow to solve the problem of optimal regulation of a virtual power plant. Finally, in Section 6.4, we provide a short summary.

6.1 LITERATURE REVIEW

Traditionally, offline algorithms have been widely used in power system applications [Molzahn et al., 2017]. In offline algorithms, given some cost function, and model of the system and some estimates, one can compute the decision variables that are then applied to the system. In particular, in problem (5.3), one would require a *voltage model* $H(\mathbf{u}; \mathbf{p}_l, \mathbf{q}_l)$, and estimates of the power consumptions $\mathbf{p}_l, \mathbf{q}_l$. Solving an AC-OPF problem to ensure that the system operation satisfies the operational constraints (branch currents and node voltages) [Capitanescu, 2016] is not adequate for real-time operation; it is usually used for day-ahead operational planning, since it requires running an iterative method and rely on problem decomposition which comes along with long computation times. Traditional techniques solving an AC-OPF problem for voltage regulation are not adequate for real-time operation of modern distribution networks for the following reasons:

- Conventional generators are replaced by intermittent and distributed generation located in modern distribution systems, which shrinks all timescales [Taylor et al.,

2016]. Control algorithms must operate fast enough to guarantee a secure operation of the network in real-time [Kroposki et al., 2020].

- Traditional techniques solving an AC-OPF problem require collecting information of all non-controllable powers. Collecting measurements of non-controllable powers in distribution networks in real-time (e. g., at the second level) is challenging as distribution systems are historically measurement-scarce, as discussed in Cheng et al. [2023].

- Moreover, collecting load measurements in real-time from *each* meter and distribution transformer is impractical and economically unfeasible [Muscas et al., 2014], and the time required to collect the measurements of the non-controllable powers (if available in real time) and run an iterative method to convergence may be long compared to the fast changing conditions of a modern distribution system [Taylor et al., 2016, Kroposki et al., 2020].

Although recent work on neural networks for AC-OPF can alleviate the computational burden (see, e. g., the representative works [Baker, 2020, Nellikkath and Chatzivasileiadis, 2022]), they still require measurements of all the non-controllable powers $\mathbf{p}_l, \mathbf{q}_l$, and they often rely on heuristics to return a feasible solution.

On the other hand, online algorithms work in closed-loop with the system. They usually need a model of the grid (some online applications are actually model-free), and are based on optimization algorithms that continuously update the control actions based on real-time measurements of the system states. This allows the controller to adapt to changes in the system and maintain optimal performance despite uncertainties and variations in the grid conditions. Practically, the model of the system is replaced with system's measurements, and the optimization algorithm effectively acts as a feedback controller, steering the system towards solutions of an optimization problem. Figure 6.1 compares offline and online methods.

In this chapter, we focus on centralized online or real-time AC-OPF methods, and seek new strategies that exhibit strong performance in terms of achieved operational cost and voltage limit satisfaction (both from analytical and numerical standpoints), while using limited measurements.

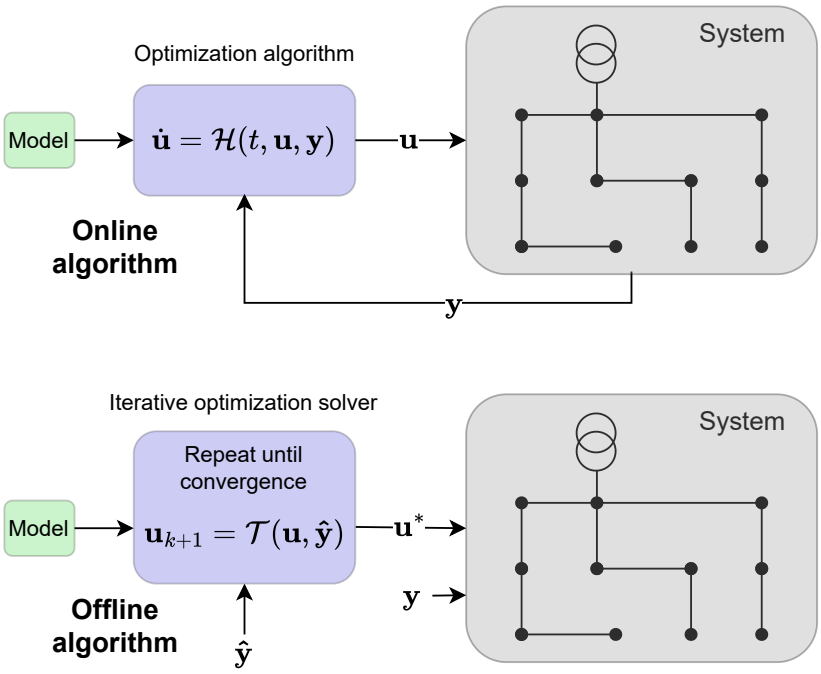

Figure 6.1: Offline and online algorithms

6.1.1 *Feedback-based optimization algorithms*

Several approaches have been explored to develop real-time OPF algorithms. In general, existing solutions leverage online optimization techniques, and incorporate measurements of some network quantities to bypass the need of a system-level model. In Bolognani et al. [2014], authors solve an optimal reactive power flow problem, where they compute reactive power setpoints of microgenerators to minimize system losses and to guarantee voltage constraints satisfaction. Authors consider a linear approximation of the map $H(\mathbf{u}; \mathbf{p}_l, \mathbf{q}_l)$, and use a dual-ascent algorithm that can be implemented in a distributive manner and which uses voltage and reactive power measurements as feedback. In Dall'Anese and Simonetto [2016], authors consider an AC-OPF problem where they minimize active power curtailment and reactive power usage, and the voltage model is approximated using a linearized version of the bus injection model. They use a primal-dual gradient method to solve a time-varying regularized saddle-point problem, and use voltage and power measurements as feedback. Model-free counterparts were proposed in Chen et al. [2020], where the primal step in the primal-dual gradient method is replaced by a zero-order approximation with two function evaluations using a deterministic perturbation signal, and in Olives-Camps et al. [2022] where authors use a perturb-and-observe method to approximate a sensitivity matrix. Continuous-time projected gradient flows were used in Hauswirth et al. [2016] while discrete-time projected gradient algo-

rithms for the OPF problem are employed in Gan and Low [2016] where authors use the *simplified DistFlow* model to derive approximate gradients and reduce the computation time. Online quasi-Newton methods were used in Tang et al. [2017], that are based on an approximation of the Hessian of the cost function.

6.1.2 *Contributions*

Compared to the works in the context of real-time OPF methods mentioned above, the contributions of our centralized algorithm can be described as follows:
(c1) We propose a new approach for the design of real-time OPF algorithms that is grounded on the theory of control barrier functions (CBFs) [Ames et al., 2019]. We leverage a continuous approximation of projected gradient flows [Allibhoy and Cortés, 2024], appropriately modified to accommodate voltage measurements from the power network. Inheriting the properties of CBF methods, the proposed algorithm – here termed feedback-based safe gradient flow (SGF) – ensures anytime satisfaction of the voltage constraints, while reaching solutions of the OPF.
(c2) From a theoretical standpoint, we show that the proposed feedback-based SGF renders isolated optimal solutions of the AC-OPF problem locally exponentially stable and ensures the anytime satisfaction of the voltage constraints. On the other hand, existing feedback-based optimization methods for distribution systems [Dall'Anese and Simonetto, 2016, Hauswirth et al., 2016] do not guarantee anytime satisfaction of the voltage constraints.
(c3) We provide results in terms of practical exponential stability and practical forward invariance when voltage measurements are affected by errors and when the Jacobian matrix of the AC power flow equations is computed only approximately (for example, when a linear approximation of the power flow equations is used).

6.2 FEEDBACK-BASED SAFE GRADIENT FLOW

We note that (5.3) can be equivalently re-written as:

$$\begin{aligned} \min_{\mathbf{u}\in\mathbb{R}^{2G}} \quad & C_v(H(\mathbf{u};\mathbf{p}_l,\mathbf{q}_l)) + C_p(\mathbf{u}) \\ \text{s.t.} \quad & \underline{V} \le H_i(\mathbf{u};\mathbf{p}_l,\mathbf{q}_l) \le \bar{V} \quad \forall i \in \mathcal{M} \\ & (p_i, q_i) \in \mathcal{U}_i \qquad\qquad\quad \forall i \in \mathcal{G} \end{aligned} \tag{6.1}$$

where $\mathbf{u}$ is the only optimization variable. Hereafter, we assume the set $\mathcal{U}_i$ can be expressed as

$$\mathcal{U}_i = \{(p_i, q_i) \in \mathbb{R}^2 : \ell_i(p_i, q_i) \le \mathbb{0}\} \tag{6.2}$$

where $\ell_i : \mathbb{R}^2 \to \mathbb{R}^{n_{c_i}}$ is a vector-valued function modeling power limits, and the inequality is taken entry-wise. For example, if the ith DER is an inverter-interfaced controllable

renewable source, then $\ell_i(p_i, q_i) = [p_i^2 + q_i^2 - s_{n,i}^2, p_i - p_{\max,i}, -p_i]^\top$, where $s_{n,i}$ and $p_{\max,i}$ denote the inverter rated size and the maximum available active power, respectively; that is, $\mathcal{U}_i = \{(p_i, q_i) \in \mathbb{R}^2 : p_i^2 + q_i^2 \leq s_{n,i}^2, p_i \leq p_{\max,i}, p_i \geq 0\}$.

We want to design a feedback-optimization algorithm to solve problem (6.1). In particular, we seek to solve the following problem:

Problem 6.1. *Designing an online feedback-optimization algorithm that drives the DERs' power setpoints to solutions of an AC-OPF problem, such as the one presented in (5.3), without requiring a complete non-linear AC model and knowledge of all the non-controllable powers throughout the nodes of the system.*

From a practical standpoint, we focus on algorithms that are implemented in a centralized unit; for instance, these algorithms can be integrated into a Distributed Energy Resource Management System (DERMS) for distribution operators. We also assume that the unit implementing our feedback-based online algorithm has access to synchronized voltage measurements at nodes where voltage constraints are enforced, and can transmit new power setpoints to the DERs. This can be done by leveraging existing communication and metering infrastructure or through a SCADA system.

6.2.1 *Design principles*

Let us define the function g:

$$g(\mathbf{u}) = [\{\underline{V} - H_i(\mathbf{u}; \mathbf{p}_l, \mathbf{q}_l)\}_{i\in\mathcal{M}}, \{H_i(\mathbf{u}; \mathbf{p}_l, \mathbf{q}_l) - \bar{V}\}_{i\in\mathcal{M}}, \{\ell_i(p_i, q_i)\}_{i\in\mathcal{G}}]^\top \tag{6.3}$$

such that the admissible set of problem (6.1) is $\mathcal{F} := \{\mathbf{u} : g(\mathbf{u}) \leq \mathbb{0}\}$ and problem (6.1) can be written:

$$\min_{\mathbf{u}\in\mathcal{F}} \quad f(\mathbf{u}), \tag{6.4}$$

with $f(\mathbf{u}) = C_v(H(\mathbf{u}; \mathbf{p}_l, \mathbf{q}_l)) + C_p(\mathbf{u})$.

We impose the following assumption on (6.4), which is typical in the AC-OPF context.

Assumption 6.1 (Regularity of isolated solutions)**.** *Assume that (6.4) is feasible and let $\mathbf{u}^*$ be a local minimizer and an isolated Karush-Kuhn-Tucker (KKT) point for (6.4), for given $\mathbf{p}_l, \mathbf{q}_l$. Assume that the following hold:*
i) Strict complementarity slackness [Fiacco, 1976] and the linear independence constraint qualification (LICQ) [Hauswirth et al., 2018] hold at $\mathbf{u}^*$.
ii) The maps $\mathbf{u} \mapsto C_p(\mathbf{u})$, $\mathbf{u} \mapsto C_v(H(\mathbf{u}; \mathbf{p}_l, \mathbf{q}_l))$ and $\mathbf{u} \mapsto H(\mathbf{u}; \mathbf{p}_l, \mathbf{q}_l)$ are twice continuously differentiable over some open neighborhood $\mathcal{B}(\mathbf{u}^*, r_1) := \{\mathbf{u} : \|\mathbf{u} - \mathbf{u}^*\| < r_1\}$ of $\mathbf{u}^*$, and their Hessian matrices are positive semi-definite at $\mathbf{u}^*$.
iii) The Hessian $\nabla^2 C_p(\mathbf{u}^*)$ is positive definite. □

Assumption 6.1 imposes some mild regularity assumptions on a neighborhood of a strict locally optimal solution. If (6.4) is formulated based on the linearized AC power flow equations [Bolognani et al., 2014, Dall'Anese and Simonetto, 2016] and the cost is strongly convex, then Assumption 6.1 is satisfied. For the most general nonlinear AC OPF problem, Assumption 6.1 is supported by the results of Hauswirth et al. [2018], where LICQ is investigated.

If $\bar{\mathbf{u}} \in \mathcal{F}$ is a local optimizer of problem (6.4) and assuming regularity assumptions (6.1) hold at $\bar{\mathbf{u}}$, then it exists $\bar{\mathbf{y}}$ such that the *Karush-Kuhn-Tucker* (KKT) conditions hold:

$$\nabla f(\bar{\mathbf{u}}) + \frac{\partial g(\bar{\mathbf{u}})}{\partial \mathbf{u}}^{\top} \bar{\mathbf{y}} = \mathbb{0}, \tag{6.5a}$$

$$g(\bar{\mathbf{u}}) \leq \mathbb{0}, \bar{\mathbf{y}} \geq \mathbb{0}, (\bar{\mathbf{y}})^{\top} g(\bar{\mathbf{u}}) = \mathbb{0}. \tag{6.5b}$$

As proposed in Allibhoy and Cortés [2024], for solving problem (6.4), one can consider the following control-affine system:

$$\dot{\mathbf{u}} = -\nabla f(\mathbf{u}) - \frac{\partial g(\mathbf{u})}{\partial \mathbf{u}}^{\top} \mathbf{y}, \tag{6.6}$$

that can be interpreted as the standard gradient flow, with a *drift term* depending on the control actions $\mathbf{y}$. The general idea is to find the control actions $\mathbf{y}$ such that the admissible set $\mathcal{F}$ is *forward-invariant*; if the system states $\mathbf{u}$ start inside the set $\mathcal{F}$, the state trajectories are confined in that set at all times. Furthermore, if the system states start outside the admissible set $\mathcal{F}$, the system trajectories should converge to the admissible set $\mathcal{F}$. One can obtain the control actions $\mathbf{y}^{\sharp}$ by solving:

$$\mathbf{y}^{\sharp} = \arg \min_{\mathbf{y} \in K_{\beta}(\mathbf{u})} \left\| \frac{\partial g(\mathbf{u})}{\partial \mathbf{u}}^{\top} \mathbf{y} \right\|^2 \tag{6.7}$$

where the *drift term* is minimized, and the admissible set for $\mathbf{y}$:

$$K_{\beta}(\mathbf{u}) := \left\{ \mathbf{y} : -\frac{\partial g}{\partial \mathbf{u}} \frac{\partial g}{\partial \mathbf{u}}^{\top} \mathbf{y} \leq \frac{\partial g}{\partial \mathbf{u}} \nabla f(\mathbf{u}) - \beta g(\mathbf{u}) \right\} \tag{6.8}$$

is defined such that the set $\mathcal{F}$ is *forward-invariant*, with $\beta > 0$ a design parameter. The set $K_{\beta}(\mathbf{u})$ is inspired by Control Barrier Functions arguments [Ames et al., 2019], and obtained considering $\mathcal{F}$ as the safe set, and g as a vector-control barrier function (see Allibhoy and Cortés [2024] for further details). In Allibhoy and Cortés [2024], it is shown that (6.6) with the control actions obtained solving (6.7) is equivalent to dynamics of the form $\dot{\mathbf{u}} = F_{\beta}(\mathbf{u})$ with

$$\begin{aligned} F_{\beta}(\mathbf{u}) := \arg\min_{\boldsymbol{\theta}} \quad & \frac{1}{2} \|\boldsymbol{\theta} + \nabla f(\mathbf{u})\|^2 \\ \text{s.t.} \quad & \frac{\partial g(\mathbf{u})}{\partial \mathbf{u}}^{\top} \boldsymbol{\theta} \leq -\beta g(\mathbf{u}). \end{aligned} \tag{6.9}$$

Recall that the vector function $g(\mathbf{u})$ contains the map $H(\mathbf{u}; \mathbf{p}_l, \mathbf{q}_l)$ (see (6.3)), therefore, equations (6.9) requires (i) the Jacobian of the map H : $J_H(\mathbf{u}; \mathbf{p}_l, \mathbf{q}_l)$, (ii) and the knowledge of power consumptions since the function evaluation $g(\mathbf{u})$, appears explicitly on the right-hand side of the inequality term. Following Assumption (5.1), the map H exists, but we do not have an explicit formulation. Hence, for (i), we rely on a linear approximation of the power flow equations. For (ii), the *voltage model* $H(\mathbf{u}; \mathbf{p}_l, \mathbf{q}_l)$, is appropriately replaced by voltage measurements, which allows us to avoid collecting power consumptions. In the following, we introduce the linear approximation of the power flow equations that we use for our approach, and then show how feedback from the system can be appropriately integrated in the formulation of the feedback-based safe gradient flow.

6.2.2 *Linear approximation*

We start with the power flow equations (5.2) that we linearize around a given voltage profile $\bar{\mathbf{v}} = [\bar{v}_1, ..., \bar{v}_N]^\top$. Let us consider $\mathbf{d} \in \mathbb{R}^N$ capturing the deviations around the linearization point. We have:

$$\mathbf{s} = \operatorname{diag}(\bar{\mathbf{v}} + \mathbf{d}) \left(\bar{\mathbf{y}}^* v_0^* + \mathbf{Y}^* \bar{\mathbf{v}}^*\right) + \operatorname{diag}(\bar{\mathbf{v}}) \left(\mathbf{Y}^* \mathbf{d}^*\right) + \operatorname{diag}(\mathbf{d}) \left(\mathbf{Y}^* \mathbf{d}^*\right). \tag{6.10}$$

If we discard the second-order terms $\operatorname{diag}(\mathbf{d}) \left(\mathbf{Y}^* \mathbf{d}^*\right)$, and considering the following choice for the nominal voltage profile:

$$\bar{\mathbf{v}} = -\mathbf{Y}^{-1} \bar{\mathbf{y}} v_0, \tag{6.11}$$

equation (6.10) becomes:

$$\operatorname{diag}(\bar{\mathbf{v}}^*) \mathbf{Y} \mathbf{d} = \mathbf{s}^*. \tag{6.12}$$

Let $\bar{\boldsymbol{\rho}} \in \mathbb{R}^N$ be the vector collecting the magnitudes of voltages $\bar{\mathbf{v}}$, and define $\bar{\mathbf{a}} := \{\cos(\bar{\theta}_n)\}_{n \in \mathcal{N}}$, $\bar{\mathbf{b}} := \{\sin(\bar{\theta}_n)\}_{n \in \mathcal{N}}$ with $\bar{\theta}_i$ the angle of the nominal voltage $\bar{v}_i$. A solution of (6.12) can be expressed as $\mathbf{d} = \mathbf{Y}^{-1} \operatorname{diag}^{-1}(\bar{\mathbf{v}}^*) \mathbf{s}^*$. Expanding this expression, and defining matrices:

$$\begin{aligned} \bar{\mathbf{R}} &= \mathbf{Z}_R \operatorname{diag}(\bar{\mathbf{a}}) (\operatorname{diag}(\bar{\boldsymbol{\rho}}))^{-1} - \mathbf{Z}_I \operatorname{diag}(\bar{\mathbf{b}}) (\operatorname{diag}(\bar{\boldsymbol{\rho}}))^{-1} \\ \bar{\mathbf{B}} &= \mathbf{Z}_I \operatorname{diag}(\bar{\mathbf{a}}) (\operatorname{diag}(\bar{\boldsymbol{\rho}}))^{-1} + \mathbf{Z}_R \operatorname{diag}(\bar{\mathbf{b}}) (\operatorname{diag}(\bar{\boldsymbol{\rho}}))^{-1}, \end{aligned} \tag{6.13}$$

where $\mathbf{Z}_R := \Re\{\mathbf{Y}^{-1}\}$ and $\mathbf{Z}_I := \Im\{\mathbf{Y}^{-1}\}$, one can write:

$$\mathbf{v} \approx \left(\bar{\mathbf{R}} + \mathrm{j}\bar{\mathbf{B}}\right) \mathbf{p}_{\text{net}} + \left(\bar{\mathbf{B}} - \mathrm{j}\bar{\mathbf{R}}\right) \mathbf{q}_{\text{net}} + \bar{\mathbf{v}}. \tag{6.14}$$

If the entries of $\bar{\mathbf{v}}$ dominate those in $\mathbf{d}$, then $\boldsymbol{\rho} + \Re\{\mathbf{d}\}$ serves as a first order approximation for the voltage magnitudes. Thus, one can write:

$$\hat{H}(\mathbf{u}; \mathbf{p}_l, \mathbf{q}_l) := \bar{\mathbf{R}}(\boldsymbol{\Gamma}_R \mathbf{u} + \mathbf{p}_l) + \bar{\mathbf{B}}(\boldsymbol{\Gamma}_B \mathbf{u} + \mathbf{q}_l) + \bar{\boldsymbol{\rho}}, \tag{6.15}$$

with $\mathbf{\Gamma}_R \in \mathbb{R}^{N\times 2G}$ and $\mathbf{\Gamma}_B \in \mathbb{R}^{N\times 2G}$ matrices filled with 0 and 1 such that $\mathbf{\Gamma}_R\mathbf{u}+\mathbf{p}_l = \mathbf{p}_{\text{net}}$ and $\mathbf{\Gamma}_B\mathbf{u} + \mathbf{q}_l = \mathbf{q}_{\text{net}}$. Effectively, the approximate Jacobian $J_{\hat{H}} = \bar{\mathbf{R}}\mathbf{\Gamma}_R + \bar{\mathbf{B}}\mathbf{\Gamma}_B$ no longer depends on $\mathbf{u}$ and the non-controllable powers $\mathbf{p}_l, \mathbf{q}_l$; accordingly, it needs to be re-computed only if there are some topological changes in the network.

The linear model is based on the bus admittance matrix $\mathbf{Y}$ and has constant matrices. This approximation is accurate for lightly loaded systems [Bolognani and Dörfler, 2015]. For heavily loaded system, [Ortmann et al., 2020, Dall'Anese and Simonetto, 2016] showed that feedback-based methods are robust against model mismatch because of the closed-loop implementation; this feature is also pointed out in Molzahn et al. [2017], and will be shown later on.

The bus admittance matrix may be hard to obtain because it requires knowledge of the feeder characteristics, i. e., the line impedances, and the network configuration. However, one can assume that the system operator can obtain some estimates. Furthermore, in the case of network reconfiguration, the bus admittance matrix changes, leading to an incorrect linear model. However, this is not a frequent event and the system operator can update its linear model approximation when such reconfiguration occurs.

6.2.3 *Proposed approach*

To solve our regulation problem, we propose the following feedback-based algorithm:

$$\dot{\mathbf{u}} = \eta \hat{F}_\beta(\mathbf{u}, \tilde{\boldsymbol{\nu}}) \tag{6.16a}$$

$$\begin{aligned} \hat{F}_\beta(\mathbf{u}, \tilde{\boldsymbol{\nu}}) := \arg\min_{\boldsymbol{\theta}\in\mathbb{R}^{2G}} \; & \|\boldsymbol{\theta} + \nabla C_p(\mathbf{u}) + J_{\hat{H}}^\top \nabla C_v(\tilde{\boldsymbol{\nu}})\|^2 \\ \text{s.t.} \quad & -\nabla \hat{H}_i^\top \boldsymbol{\theta} \le -\beta\,(\underline{V} - \tilde{\nu}_i) \quad \forall i \in \mathcal{M} \\ & \nabla \hat{H}_i^\top \boldsymbol{\theta} \le -\beta\,(\tilde{\nu}_i - \bar{V}) \quad \forall i \in \mathcal{M} \\ & J_{\ell_i}(\mathbf{u})^\top \theta \le -\beta \ell_i(p_i, q_i) \quad \forall i \in \mathcal{G} \end{aligned} \tag{6.16b}$$

where $\tilde{\nu}_i$ is a measurement of $|v_i|$ (the voltage magnitude) at node i, $\tilde{\boldsymbol{\nu}} = [\tilde{\nu}_1, ..., \tilde{\nu}_N]^\top$, $J_{\hat{H}}$ and $\{\hat{H}_i\}_{i\in\mathcal{M}}$ are estimates or approximations of J_H and $\{H_i\}_{i\in\mathcal{M}}$, respectively, $\nabla\hat{H}_i(\mathbf{u}; \mathbf{p}_l, \mathbf{q}_l) = [\{(J_{\hat{H}}(\mathbf{u}; \mathbf{p}_l, \mathbf{q}_l))_{i,j}\}_{j\in\mathcal{G}}]^\top$ is a $2G \times 1$ vector collecting the entries of $J_{\hat{H}}(\mathbf{u}; \mathbf{p}_l, \mathbf{q}_l)$ in the ith row and columns corresponding to nodes in $\mathcal{G}$, $J_{\ell_i}(p_i, q_i)$ is the Jacobian of $(p_i, q_i) \mapsto \ell_i(p_i, q_i)$, $\beta > 0$ is a design parameter, and $\eta > 0$ is the controller gain and is a design parameter. For given $\mathbf{u}$ and $\tilde{\boldsymbol{\nu}}$, problem (6.16) is a convex quadratic program (QP) with a strongly convex cost; it can be efficiently solved using standard or high-performance embedded solvers for QPs. We make the distinction between the map $\hat{F}_\beta(\mathbf{u}, \tilde{\boldsymbol{\nu}})$ and $F_\beta(\mathbf{u}, H(\mathbf{u}; \mathbf{p}_l, \mathbf{q}_l))$ illustrated in equation (6.9), because (i) we consider an approximate *voltage model* $\hat{H}(\mathbf{u}; \mathbf{p}_l, \mathbf{q}_l)$ and in particular, its associated Jacobian $J_{\hat{H}}$, and because (ii) we replace the *voltage model* by voltage measurements $\tilde{\boldsymbol{\nu}}$. We discuss the stability analysis and the constraint satisfaction guarantees of our approach in Appendix A.1.1, and prove practical local exponential stability and practical forward invariance.

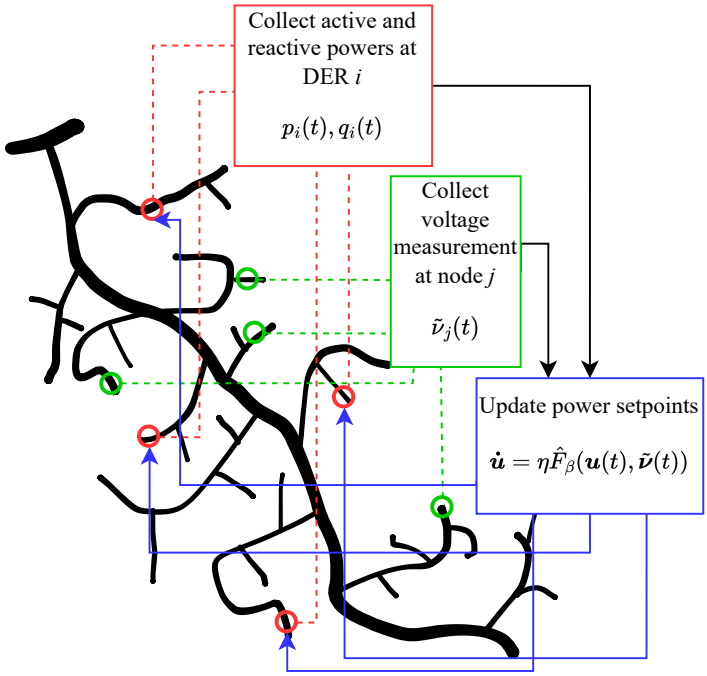

Figure 6.2: Closed-loop implementation of the proposed online feedback optimization algorithm. A central unit (blue box) receives measurements of voltages (from measurement units, green box) and of the DERs' output powers from inverters (red box); based on these measurements, it updates the DERs' setpoints based on the proposed controller $\dot{\mathbf{u}}(t) = \eta \hat{F}_\beta(\mathbf{u}(t), \tilde{\boldsymbol{\nu}}(t))$. Once the setpoints $\mathbf{u}(t)$ are computed, the central unit transmits $\mathbf{u}(t)$ to the DERs' inverters. Through this closed-loop scheme, the proposed controllers drive the distribution system to solutions of the AC OPF problem (6.1).

The algorithm (6.16) is designed to steer the power setpoints of the DERs $\mathbf{u}$ to optimal solutions of the AC OPF, while continuously guaranteeing feasibility (i. e., satisfaction of voltage limits). As shown in Figure 6.2, (6.16) effectively acts as a feedback controller by replacing the *voltage model* $H(\mathbf{u}; \mathbf{p}_l, \mathbf{q}_l)$ with *measurements* $\tilde{\boldsymbol{\nu}}$ of the voltage magnitudes that automatically satisfy the power flow equations [Tang et al., 2017, Molzahn et al., 2017]. This is a key modification that allows one to avoid collecting measurements of $\mathbf{p}_l, \mathbf{q}_l$ [Bolognani et al., 2014, Dall'Anese and Simonetto, 2016, Bernstein and Dall'Anese, 2019].

The proposed feedback-based SGF is summarized in Algorithm 6.1 and illustrated in Figure 6.2.

In terms of implementation of the Algorithm 6.1, we highlight the following practical aspects:

- The main step [S2a] is performed at a central unit (i. e., the blue box in Figure 6.2). This central unit can be integrated, for example, into an advanced distribution

Algorithm 6.1: *Feedback-based safe gradient flow*

Initialization: Compute $J_{\hat{H}}$ and $\{\hat{H}_i, i \in \mathcal{M}\}$. Set $\beta > 0$, $\eta > 0$.
Real-time operation: for $t \geq 0$, repeat:
[S1a] Measure output powers $\{p_i(t), q_i(t), i \in \mathcal{G}\}$
[S1b] Measure voltage magnitudes $\{\tilde{\nu}_i(t), i \in \mathcal{M}\}$
[S2a] Update power setpoints via $\dot{\mathbf{u}}(t) = \eta \hat{F}_\beta(\mathbf{u}(t), \tilde{\boldsymbol{\nu}}(t))$
[S2b] Implement setpoints $\mathbf{u}(t)$
Go to [S1a] and [S1b]

management system for distribution operators. After performing step [S2a], the central unit sends the updated setpoints to the DERs' inverters.

- Step [S1a] is performed at the DERs (a DER is represented by a red box in Figure 6.2); the inverters measure the output powers $\{p_i(t), q_i(t), i \in \mathcal{G}\}$ and send the measurements to the central unit. The inverters also implement step [S2b] after they receive the setpoints from the central unit.

- The safe gradient flow (6.16) relies on measurements of the voltages at the network locations $\mathcal{M}$, as required in the step [S1b]. It is assumed that those measurements are obtained in real-time using sensing devices communicating with the centralized controller, e. g., μPMUs [Sun et al., 2017] or through the advanced metering infrastructure (a meter is represented by a green box in Figure 6.2).

In practice, the proposed measurement-based SGF (6.16) can be implemented with discretization (similar to well-established CBF-based methods [Ames et al., 2019]). The discretization interval depends on the time required to collect voltage measurements and to solve the QP. Linearly-constrained convex QP programs are known to be solved efficiently (e. g., in milliseconds) by both existing open-source solvers (such as IPOPT) and commercial solvers. Synchronized voltage measurements can be obtained via SCADA at fast scale (i. e., second or sub-second level) [Cheng et al., 2023, Sun et al., 2017]. We implement the following controller:

$$\mathbf{u}(t+1) = \mathbf{u}(t) + \Delta t \eta \hat{F}_\beta(\mathbf{u}(t), \tilde{\boldsymbol{\nu}}(t)), \tag{6.17}$$

where the gain η is adapted based on the sampling time Δt. Notice that the proof for practical local exponential stability of our approach discussed in Appendix A.1.1 does not necessarily hold for the discretized version of the controller. However, one can derive a local asymptotic stability result for the discretized controller.

Our framework is applicable to the case where the system operator may utilise a mix of actual voltage measurements and pseudo-measurements [Angioni et al., 2015].

For example, suppose that the system operator can measure voltages at some nodes $\mathcal{M}_{\text{meter}} \subset \mathcal{M}$ and relies on pseudo-measurements at the other nodes. Then,

$$\tilde{\nu}_i = \begin{cases} H_i(\mathbf{u}; \mathbf{p}_l, \mathbf{q}_l) + n_i, & i \in \mathcal{M}_{\text{meter}} \\ H_{i,\text{pseudo}}(\mathbf{u}; \mathbf{p}_l, \mathbf{q}_l), & i \in \mathcal{M} \setminus \mathcal{M}_{\text{meter}} \end{cases} \tag{6.18}$$

where n is a bounded measurement noise, and $H_{i,\text{pseudo}}(\mathbf{u}; \mathbf{p}_l, \mathbf{q}_l)$ represents a model used to generate the pseudo-measurements (i. e., using a state-estimator).

Finally, notice that if the embedded controllers of inverters are guaranteed to implement the power setpoints, in principle, the step [S1a] in Algorithm 6.1 is not needed. However, the operator may want to measure current setpoints $\{p_i(t), q_i(t)\}_{i \in \mathcal{G}}$ for verification purposes and to monitor the state of the DERs' inverters.

6.2.4 *Illustration on a single-phase distribution network*

We consider the medium voltage network (20 kV) shown in Figure 6.3a. We used a modified network from Sarajlic and Rehtanz [2019], in which photovoltaic power (PV) plants have been randomly placed, with inverter-rated size picked randomly among $\{490, 620, 740\}$ kVA. The dynamics of the output power for the inverters are not implemented, as they are much faster than the controller dynamics; see, e. g., [Eggli et al., 2020]. Accordingly, when the controller updates the power setpoints, the inverter implements them instantaneously. In the numerical experiments, we consider a system with PV plants; however, we note that any type of inverter-interfaced DERs can be considered. Figure 6.3b shows the aggregated loads and maximum available active power for PV plants throughout the day. The data is from the Open Power System Data[1], and have been modified to match the initial loads and PV plants nominal values present in the network. The reactive power demand is set such that the power factor is 0.9 (leading). This would represent a typical summer day, with high PV production. We will show that, under these conditions, the electrical distribution network would undergo overvoltages.

6.2.4.1 *Simulation setup*

We compare the proposed measurement-based SGF with: (i) no control (NC); (ii) the online primal-dual method (PDM) proposed in Dall'Anese and Simonetto [2016]; and, (iii) a Volt/Var control (VVC). We also compute the solution of a batch optimization (BO) method, where the AC-OPF problem, with the power flow equations modelled using the nonlinear branch flow model [Baran and Wu, 1989], is solved. The AC-OPF problem with the branch flow model can be written as:

$$\min_{\mathbf{u} \in \mathbb{R}^{2G}} \quad C_v(H(\mathbf{u}; \mathbf{p}_l, \mathbf{q}_l)) + C_p(\mathbf{u}) \tag{6.19a}$$

1 Data available at https://data.open-power-system-data.org/household_data/2020-04-15

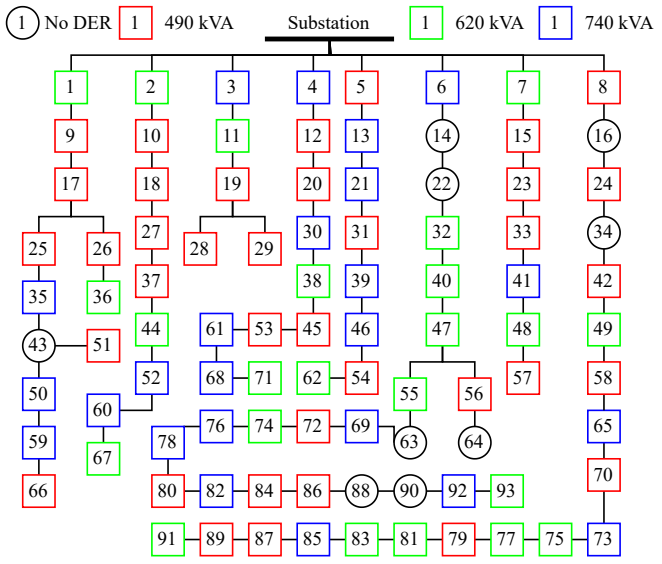

(a)

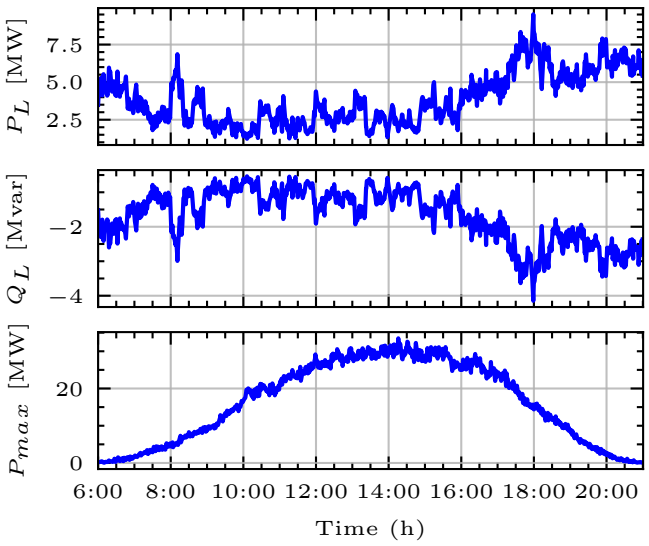

(b)

Figure 6.3: (a) Distribution network used in the simulations. (b) Aggregated load consumption (P_L, Q_L) and PV production profiles (P_{max}) used in the simulations.

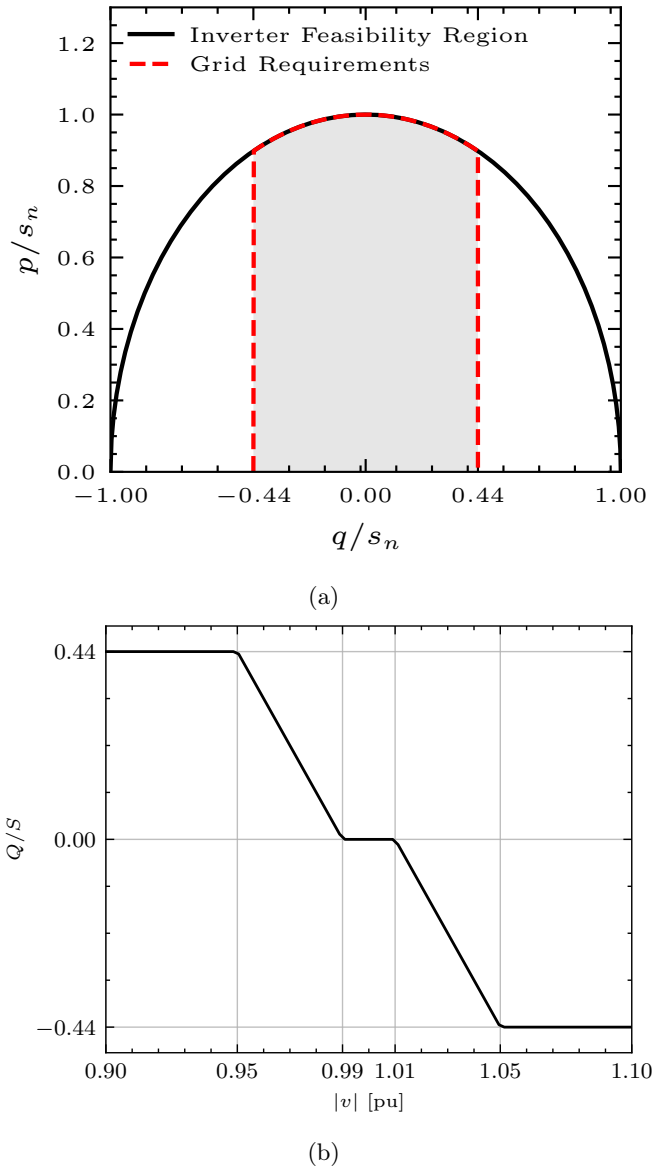

Figure 6.4: (a) Operational set compared to grid code requirements inspired from the *IEEE Std 1547-2018*, where s_n is the inverter rated power. (b) Implementation of IEEE standard *IEEE Std 1547-2018* with Q the reactive power injection, S the nominal apparent power of the DER, Q/S represents the ratio between Q and S, and $|v|$ is the voltage magnitude at the node.

$$\text{s.t.} \quad p_j - p_{l,j} = \sum_{n \in \mathcal{C}_j} P_{jn} - (P_{aj} - r_{aj} I_{aj}^2) \qquad \forall j \in \mathcal{N} \tag{6.19b}$$

$$q_j - q_{l,j} = \sum_{n \in \mathcal{C}_j} Q_{jn} - (Q_{aj} - x_{aj} I_{aj}^2) \qquad \forall j \in \mathcal{N} \tag{6.19c}$$

$$\nu_j^2 = \nu_a^2 - 2(r_{aj} P_{aj} + x_{aj} Q_{aj}) + (r_{aj}^2 + x_{aj}^2) I_{aj}^2 \qquad \forall j \in \mathcal{N} \tag{6.19d}$$

$$I_{aj}^2 = \frac{P_{aj}^2 + Q_{aj}^2}{\nu_a^2} \qquad \forall j \in \mathcal{N} \tag{6.19e}$$

$$(p_i, q_i) \in \mathcal{U}_i \qquad \forall i \in \mathcal{G} \tag{6.19f}$$

$$\underline{V}^2 \leq \nu_i^2 \leq \bar{V}^2 \qquad \forall i \in \mathcal{M} \tag{6.19g}$$

where we consider a single-phase and radial feeder represented by a tree graph, such that node j has only one ancestor a, and children $n \in \mathcal{C}_j$. Furthermore, we denote P_{ij}, Q_{ij}, I_{ij} the active and reactive power, and the current flowing through the branch (ij), and r_{ij}, x_{ij} its associated resistance and reactance, respectively.

Remark 6.2 (*Comments on the non-linear AC-OPF based on the branch flow model*)**.** *In practice, one usually considers a change of variables, such that* $\alpha_i = \nu_i^2 \ \forall i \in \mathcal{N}$ *and* $\beta_{ij} = I_{ij}^2 \ \forall (i,j) \in \mathcal{E}$ *where* $\mathcal{E}$ *is the set of edges of the graph, which renders all the constraints except equation* (6.19e) *linear for problem* (6.19)*. A second-order conic programming approximation of problem* (6.19) *can be derived by replacing equation* (6.19e) *by the following inequality:* $\beta_{aj} \geq \frac{P_{aj}^2 + Q_{aj}^2}{\alpha_a} \qquad \forall j \in \mathcal{N}$*. However, in order to have a tight inequality, one would need to minimize the branch currents in the objective function, which might conflict with other terms in the objective function. In this section, we consider the non-linear, non-convex AC-OPF formulation, and solve it with an interior point method. Recall that this is not adequate for real-time operation, and it is used in this manuscript only for comparison purposes.*

The voltage service limits $\bar{V}$ and $\underline{V}$ are set to 1.05 and 0.95 p.u., respectively. The load and PV production profiles have a granularity of 10 seconds, i. e., active/reactive power consumption and maximum available active power for PV plants change every 10 seconds. For the SGF, it means that every 10 seconds, we pursue a new optimal solution. The SGF (using a forward Euler discretization), PDM and VVC algorithms are run every second.

Based on the IEEE standard *IEEE Std 1547-2018*, we consider the feasible set for the PV plants shown in Figure 6.4a. Although the inverter feasible set consists of a semicircle, there is no interest for PV owners to operate the PV plant at low power factors, i. e., large reactive power absorption/consumption and low active power production. Usually, PV plants are operated at unity power factor, i. e., on the vertical line passing through 0. The distribution system operator (DSO) often imposes grid requirements when a PV plant is connected to its network in order to provide support if needed. The grid requirements vary from one DSO to another. In this thesis, we consider that the maximum reactive

power the inverter can produce/consume is set to 44% of its nominal apparent power. The vector-valued function modelling power limits is therefore

$$\ell_i(p_i, q_i) = [p_i^2 + q_i^2 - s_{n,i}^2, p_i - p_{\max,i}, -p_i, -0.44 s_{n,i} - q_i, q_i - 0.44 s_{n,i}]^\top. \tag{6.20}$$

It is assumed that $p_{\max,i}$ is known at the DERs. For example, one can use the method proposed in Hussain et al. [2018] to estimate the maximum power point of PV arrays, and therefore, the maximum available power $p_{\max,i}$. Finally, we consider the following cost function for the SGF, PDM, and BO:

$$C_p(\mathbf{u}) = \sum_{i \in \mathcal{G}} c_p \left(\frac{s_{n,i} - p_i}{s_{n,i}} \right)^2 + c_q \left(\frac{q_i}{s_{n,i}} \right)^2 \tag{6.21}$$

with $c_p = 3$ and $c_q = 1$, and $C_v(H(\mathbf{u}; \mathbf{p}_l, \mathbf{q}_l)) = 0$. This cost function seeks to minimize active power curtailment and inverter power losses. The first part minimizes the active power curtailment, the second part the reactive power usage, which is also related to the inverter losses as less reactive power usage means less currents and thus, fewer Joules losses.

Volt/Var control: The Volt/Var control is inspired by the IEEE standard *IEEE Std 1547-2018*. The parameters of the Volt/Var control have been adapted to match the voltage service limits considered in this thesis. The maximum reactive power consumed/absorbed is set to 44% of the nominal apparent power of the PV plant. The maximum power absorbed/produced is reached for voltages 1.05/0.95 pu, respectively. Finally, we implemented a dead-band for voltages between 0.99 and 1.01 pu. Our implementation of the IEEE standard *IEEE Std 1547-2018* is shown in Figure 6.4b.

No control: For the no-control test case, we consider an overvoltage protection of PV plants, i. e., the plant is disconnected if the voltage level is too high. We consider three different status for the PV plant: *running*, *idling*, and *disconnected*. When the PV plant is in status *idling* or *disconnected*, it does not inject active power or provide reactive power compensation. The disconnection scheme is inspired from the CENELEC EN50549-2 standard [EN50549-2, 2019], and has been adapted considering the voltage service limits used in this thesis. The PV plant changes status from *running* to *disconnected* if: *(i)* the voltage at the point of connection goes above 1.06 pu, *(ii)* the root-mean square value of the voltages measured at the point of connection for the past 10 minutes goes above 1.05 pu (the voltages are measured every ten seconds).

The PV plant switches to status *idling* if the voltage at the point of connection stays below 1.05 pu for 1 minute. To switch back to *running* status, the PV plant has to be in *idling* status. The switching to *running* status occurs randomly in the interval [1min, 10min] (random, uniformly distributed).

6.2.4.2 *Results*

In the following, we compare the different methods in terms of their cost function values, the system losses, and the voltage levels. Notice that system losses are not integrated in

the cost function (6.21), since they conflict with the term that considers active power curtailment. In this thesis, we design the cost function to promote renewable energy resources, hence maximizing the solar production while keeping voltage levels within predefined bounds. However, the DSO is also concerned by the system losses. Thus, one needs to look how the different methods perform with respect to them.

In Figure 6.5, one can see the maximum voltage (phase-to-ground) observed at every time step, as well as the number of impacted nodes where we observed a voltage greater than $\bar{V}$. It can be seen that only the SGF method does not lead to voltage violations. This is precisely because our approach is based on the theory of control barrier function. PDM leads to voltage violations not only because of the transient of the dual variables, but also because it is designed based on a regularization of the Lagrangian function as explained in Dall'Anese and Simonetto [2016]. VVC performs well, although as shown hereafter, it leads to larger system losses and a greater cumulative cost than SGF or PDM. The overall voltage profile is also shifted downward due to its proportional feedback control. One can observe the spikes in the NC method due to multiple disconnections of DERs because of a prolonged overvoltage duration. Finally, one can see that with PDM, the voltages oscillate around the threshold voltage of 1.05 pu.

In Figure 6.5e, we show the duration of overvoltages. We define $T_{\geq\alpha;i}$ as a vector containing the number of consequent time steps during which node i sees his voltage above the value α. The value $\max T_{\geq\alpha}$ corresponds to the maximum value among all $T_{\geq\alpha;i}$ for $i \in \mathcal{N}$ and corresponds to the maximum consequent time duration during which one nodal voltage was above α. The value mean $T_{\geq\alpha}$ is the maximum of the mean absolute values of every vector $T_{\geq\alpha;i}$ for $i \in \mathcal{N}$, representing the average time duration of overvoltage. Since SGF algorithm does not yield overvoltages, it does not appear on this graph. One can see that the NC method does not perform well, as the active power curtailment is activated only for large overvoltage (above 1.06pu) or for prolonged overvoltage (above 1.05pu).

We show the cumulative cost function in Figure 6.6a, i. e., the cumulative sum of the cost function at every time step. It is clear that the NC method leads to the largest cumulative costs, as its implementation leads to full curtailment of solar production and no usage of reactive power. The VVC shows the second-highest cost because of its inefficient usage of reactive power reserves. We have to bear in mind that these two solutions cannot practically achieve the optimal solutions of the BO method since they can only play with either the active or reactive power output of solar inverters. Furthermore, they are, by design, decentralized control algorithms, and do not have full information of the system state. We observe that PDM has the lowest cumulative cost, which comes at the detriment of voltage violations, as observed in Figure 6.5c. The SGF cumulative cost superposes the BO cost.

The cumulative system losses for the different methods are shown in Figure 6.6b. The NC method leads to the lowest system losses as it drastically reduces the amount of active power flows in the network by fully curtailing solar production. The VVC leads to

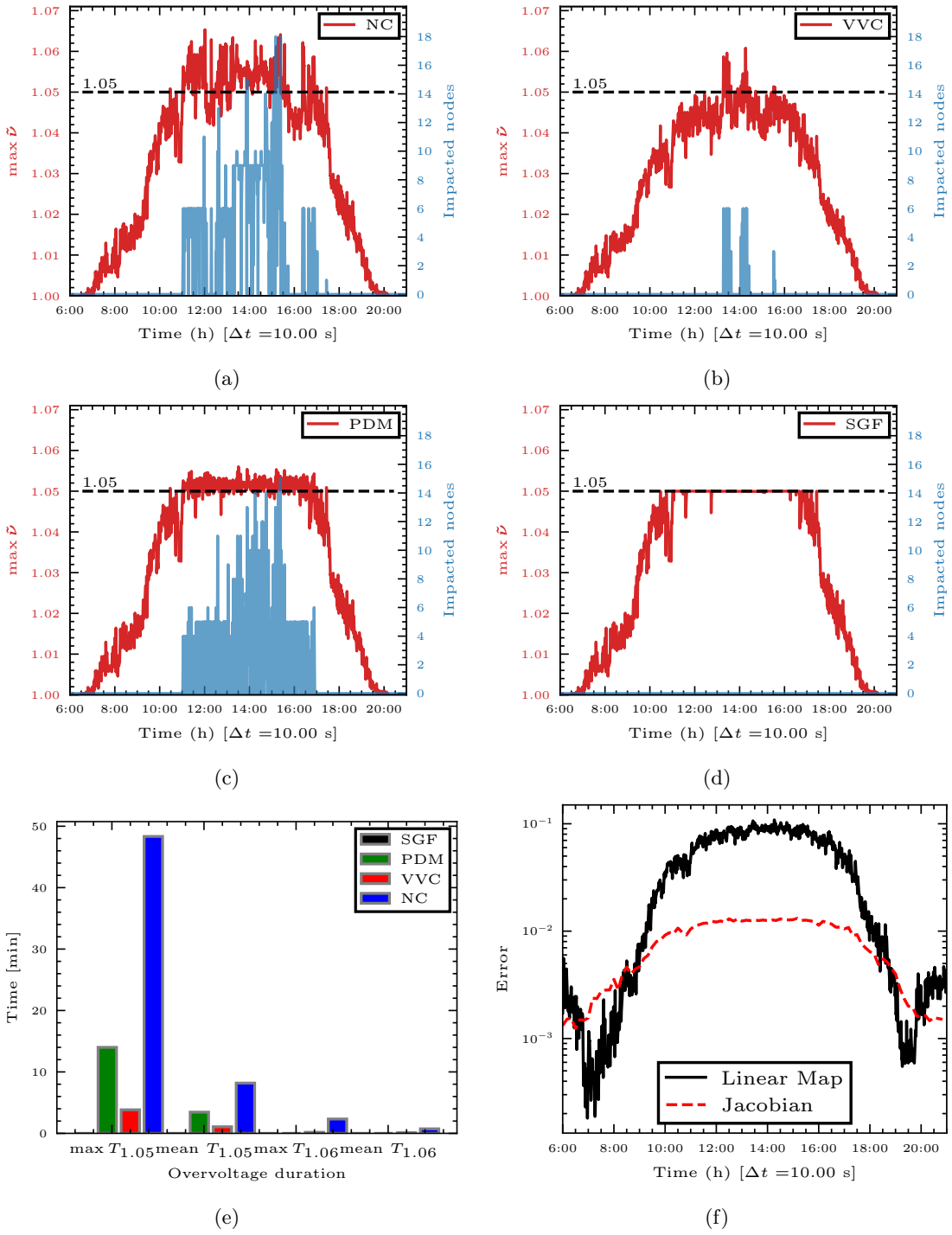

Figure 6.5: (a) Overvoltages for NC. (b) Overvoltage for VVC. (c) Overvoltages for PDM. (d) Overvoltage for SGF. (e) Overvoltage duration time. (f) Linear map error: $||\hat{H}(\mathbf{u};\mathbf{p}_l,\mathbf{q}_l) - H(\mathbf{u};\mathbf{p}_l,\mathbf{q}_l)||$ and Jacobian error: $||J_{\hat{H}} - J_H(\mathbf{u};\mathbf{p}_l,\mathbf{q}_l)||$, where $\mathbf{u}$ is picked from the SGF algorithm.

the highest system losses as it over-uses reactive power compensation to mitigate voltage issues. This results in larger power flows throughout the network, hence larger power system losses. We can observe that PDM, SGF, and BO have similar system losses.

Finally, Figure 6.5f shows the error between the linear approximation of the power flow equations and the non-linear power flow equations, validating our choice for the linear map. It also shows the error between the approximate Jacobian (which is constant), and the true Jacobian computed numerically.

Our method was experimentally tested on a 93-node distribution system with realistic load and production profiles and it exhibited a performance significantly superior in terms of voltage regulation to existing online primal-dual methods and Volt/Var strategies. Notice that our feedback-based safe gradient flow can be extended to solve other optimization problems, and deal with more complex power system models. Actually, distribution networks are most often highly unbalanced, and considering a single-phase equivalent is a strong assumption. In the following, we aim at solving the problem of regulating a virtual power plants consisting in a three-phase unbalanced distribution network with DERs integration.

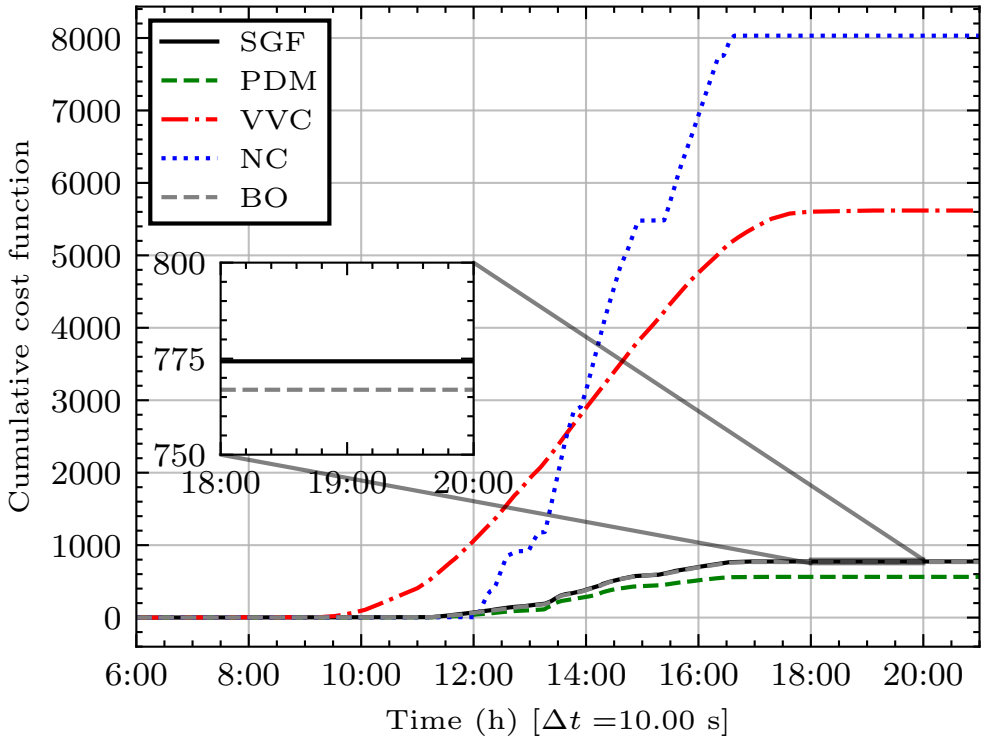

(a)

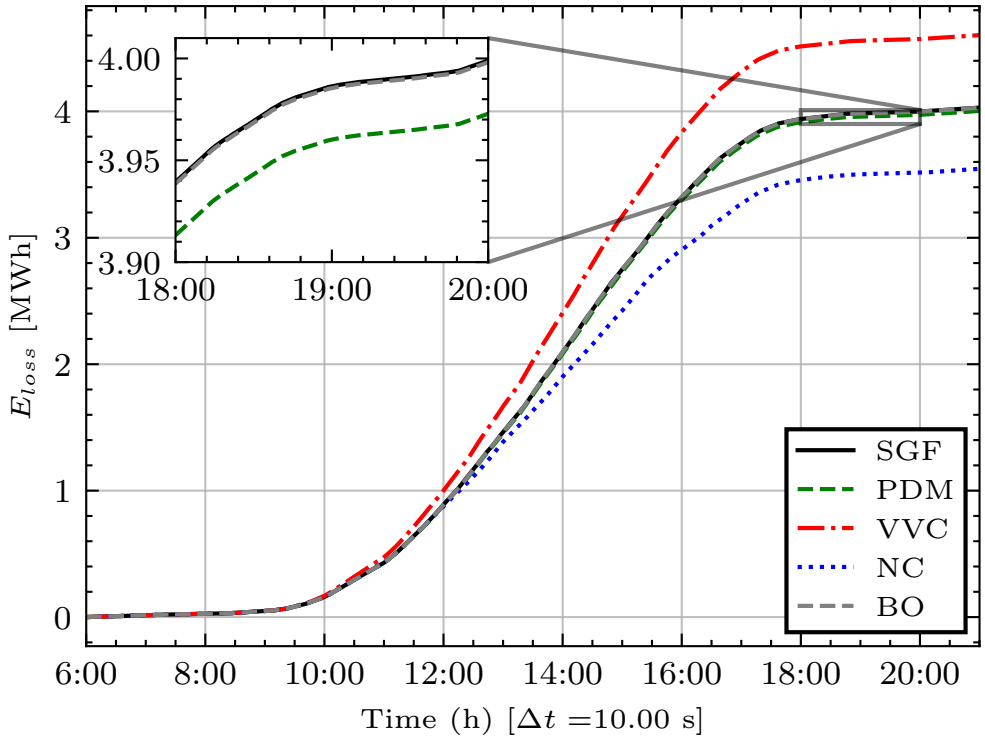

(b)

Figure 6.6: (a) Achieved values of cumulative cost (6.21). (b) Sum of energy losses throughout the day.

6.3 AN APPLICATION TO REGULATION OF VIRTUAL POWER PLANTS

At the transmission level, large-scale synchronous generators provide voltage and frequency support. However, the replacement of conventional power plants by inertia-less power converters alters power system dynamics and weakens the system by removing resources that support voltage and frequency. On the other hand, the continuous improvements in power electronic converters pave the way for new regulation techniques. Distributed energy resources (DERs) can now provide ancillary services to the bulk power system while mitigating voltage issues within distribution networks [Stanojev et al., 2022]. A *virtual power plant* (VPP) [Dall'Anese et al., 2017] is an aggregation of DERs in a distribution network that provides ancillary services to the bulk power system while satisfying operational constraints within the distribution network. A traditional VPP regulation approach involves solving an AC optimal power flow (AC-OPF) problem in an open-loop fashion to dispatch DER power setpoints. Such an approach is inadequate for real-time optimization as mentioned in Bernstein and Dall'Anese [2019], and in Chapter 5. In the following, we leverage our feedback-based algorithm and extend it to a 3-phase unbalanced distribution network, with wye and delta-connected sources. We consider the problem of regulating a VPP such that it can track power references at the substation while meeting voltage constraints within the distribution network. Figure 6.7 illustrates the working principle of the algorithm.

We consider a generic three-phase distribution network with $N+1$ nodes and a combination of wye-connected and delta-connected sources. The node 0 is taken to be the substation node, while $\mathcal{N} := \{1, ..., N\}$ is the set of remaining nodes. Let $\mathbf{s}_j^Y := \{s_j^a, s_j^b, s_j^c\}^\top$ denote the vector of net complex phase-to-ground power injections on each phase $\{a, b, c\}$ at node j. Similarly, let $\mathbf{s}_j^\Delta := \{s_j^{ab}, s_j^{bc}, s_j^{ca}\}^\top$ denote the vector of net complex phase-to-phase power injections at node j on each phase connections $\{ab, bc, ca\}$. Let us denote $\mathbf{v}_j := (v_j^a, v_j^b, v_j^c)^\top, \mathbf{i}_j := (i_j^a, i_j^b, i_j^c)^\top, \mathbf{i}_j^\Delta := (i_j^{ab}, i_j^{bc}, i_j^{ca})^\top$ the vectors collecting the phase-to-ground voltages, the phase current injections, and the phase-to-phase currents for node j, respectively. We define the following quantities $\mathbf{v} := \{(\mathbf{v}_j)^\top\}_{j\in\mathcal{N}}^\top, \mathbf{i} := \{(\mathbf{i}_j)^\top\}_{j\in\mathcal{N}}^\top, \mathbf{i}^\Delta := \{(\mathbf{i}_j^\Delta)^\top\}_{j\in\mathcal{N}}^\top, \mathbf{s}^Y := \{(\mathbf{s}_j^Y)^\top\}_{j\in\mathcal{N}}^\top, \mathbf{s}^\Delta := \{(\mathbf{s}_j^\Delta)^\top\}_{j\in\mathcal{N}}^\top$ to express the power flow equations in matrix form [Bernstein et al., 2018]:

$$\begin{aligned} \operatorname{diag}\left(B^\top(\mathbf{i}^\Delta)^*\right)\mathbf{v} + \mathbf{s}^Y &= \operatorname{diag}(\mathbf{v})\mathbf{i}^*, \\ \mathbf{s}^\Delta &= \operatorname{diag}(B\mathbf{v})(\mathbf{i}^\Delta)^*, \\ \mathbf{i} &= Y_{L0}\mathbf{v}_0 + Y_{LL}\mathbf{v}, \\ \mathbf{s}_0^Y &= \operatorname{diag}(\mathbf{v}_0)(Y_{00}^*\mathbf{v}_0^* + Y_{0L}^*\mathbf{v}^*), \end{aligned} \tag{6.22}$$

where $Y_{00}, Y_{L0}, Y_{0L}, Y_{LL}$ denote the submatrices of the three-phase bus admittance matrix

$$Y := \begin{bmatrix} Y_{00} & Y_{0L} \\ Y_{L0} & Y_{LL} \end{bmatrix} \in \mathbb{C}^{3(N+1)\times 3(N+1)}, \tag{6.23}$$

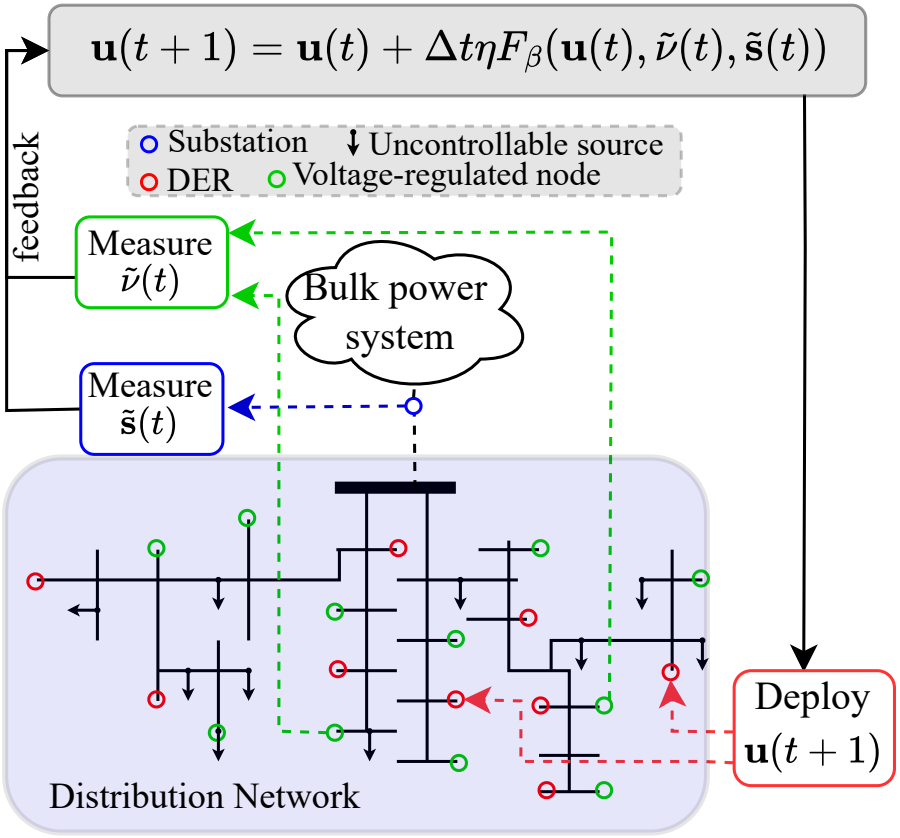

Figure 6.7: Feedback-based safe gradient flow controller for VPP regulation.

that can be derived from the network topology and the π-model of the distribution lines, and B is a block-diagonal matrix defined by

$$B := \text{diag}(\Gamma),\ \Gamma := \begin{bmatrix} 1 & -1 & 0 \\ 0 & 1 & -1 \\ -1 & 0 & 1 \end{bmatrix}. \tag{6.24}$$

One can find the solution $\mathbf{v}$ of the set of equations (6.22), with known $\mathbf{s}^Y, \mathbf{s}^\Delta$ and $\mathbf{v}_0$, using the following fixed-point equation [Bernstein et al., 2018]:

$$\mathbf{v} = \mathbf{w} + Y_{LL}^{-1}\left(\text{diag}(\mathbf{v}^*)^{-1}(\mathbf{s}^Y)^* + B^\top \text{diag}(B\mathbf{v}^*)^{-1}(\mathbf{s}^\Delta)^*\right), \tag{6.25}$$

where $\mathbf{w} := -Y_{LL}^{-1}Y_{L0}\mathbf{v}_0$ is the zero-load voltage.

For convenience, we define the algebraic maps $V := \mathbb{C}^{3N+3N+3} \mapsto \mathbb{C}^{3N}$ and $S := \mathbb{C}^{3N+3N+3} \mapsto \mathbb{C}^3$ such that $\mathbf{v} = V(\mathbf{s}^Y, \mathbf{s}^\Delta, \mathbf{v}_0)$ and $\mathbf{s}_0 = \mathbf{s}_0^Y = S(\mathbf{s}^Y, \mathbf{s}^\Delta, \mathbf{v}_0)$. These maps correspond to the *practical* solution –high voltage, low line currents solution– of the power flow equations described in (6.22).

The goal is to coordinate DERs injections to regulate voltage magnitudes within the distribution network while tracking power reference setpoints at the substation $S_{\text{set}} := \{P_{\phi,\text{set}}, Q_{\phi,\text{set}}\}_{\phi\in\{a,b,c\}}^\top$, where $P_{\phi,\text{set}}, Q_{\phi,\text{set}}$ represent the active and reactive power setpoint at the substation for each phase ϕ, respectively. We formulate the following optimization problem:

$$\begin{aligned} \min_{\mathbf{s}^Y,\mathbf{s}^\Delta,\mathbf{v}_0} \quad & f(\mathbf{s}^Y, \mathbf{s}^\Delta, \mathbf{v}_0) \\ \text{s.t.} \quad & \underline{V} \le |V(\mathbf{s}^Y, \mathbf{s}^\Delta, \mathbf{v}_0)| \le \bar{V}, \\ & -E \le S(\mathbf{s}^Y, \mathbf{s}^\Delta, \mathbf{v}_0) - S_{\text{set}} \le E, \\ & \mathbf{s}^Y, \mathbf{s}^\Delta \in \mathcal{S}, \end{aligned} \tag{6.26}$$

where $\bar{V}, \underline{V}$ denote the vectors of maximum and minimum voltage magnitudes, E is a scalar that can be arbitrary small to track power reference setpoints and $\mathcal{S}$ represents the hardware limits of DERs, i. e., maximum and minimum power injections. One can design the objective function $f(.)$ to minimize the usage of reactive power compensation or active power curtailment or may favor the minimization of system losses or voltage deviations from a nominal voltage profile. Also, one can consider other constraints, such as maximum line ampacity. Solving problem (6.26) is challenging because it contains non-linear constraints and is known to be non-convex. Furthermore, the solution to problem (6.26) heavily depends on the model parameters (e.g., the elements of Y), and there is no guarantee one can satisfy operational constraints under model uncertainties. In the following section, we use our feedback-based safe gradient flow algorithm to provide an algorithmic solution of problem (6.26).

6.3.1 *Proposed approach*

Our feedback-based safe gradient flow requires the jacobian of the maps $|V(\mathbf{s}^Y, \mathbf{s}^\Delta, \mathbf{v}_0)|$ and $S(\mathbf{s}^Y, \mathbf{s}^\Delta, \mathbf{v}_0)$. Unfortunately, explicit formulation of maps $V(.)$ and $S(.)$ do not exist. Therefore, we leverage the linear approximations proposed in Bernstein et al. [2018]:

$$\begin{aligned} |V(\mathbf{s}^Y, \mathbf{s}^\Delta, \mathbf{v}_0)| &\approx K^Y \mathbf{x}^Y + K^\Delta \mathbf{x}^\Delta + \mathbf{b}, \\ S(\mathbf{s}^Y, \mathbf{s}^\Delta, \mathbf{v}_0) &\approx G^Y \mathbf{x}^Y + G^\Delta \mathbf{x}^\Delta + \mathbf{c}, \end{aligned} \tag{6.27}$$

where $\mathbf{x}^Y := ((\mathbf{p}^Y)^\top, (\mathbf{q}^Y)^\top)^\top$ and $\mathbf{x}^\Delta := ((\mathbf{p}^\Delta)^\top, (\mathbf{q}^\Delta)^\top)^\top$ with $\mathbf{p}^Y := \mathcal{R}\{\mathbf{s}^Y\}$, $\mathbf{q}^Y := \mathcal{I}\{\mathbf{s}^Y\}$, $\mathbf{p}^\Delta := \mathcal{R}\{\mathbf{s}^\Delta\}$, $\mathbf{q}^\Delta := \mathcal{I}\{\mathbf{s}^\Delta\}$ collecting the active and reactive power injections. The different matrices presented in (6.27) (see Bernstein et al. [2018] for detailed derivations), where we define $(\hat{\mathbf{v}}, \hat{\mathbf{s}}^Y, \hat{\mathbf{s}}^\Delta)$ as a given solution of the fixed-point equation (6.25), can be written as:

$$\begin{aligned} M^Y &:= \left(Y_{LL}^{-1} \operatorname{diag}(\hat{\mathbf{v}}^*)^{-1}, -\mathrm{j} Y_{LL}^{-1} \operatorname{diag}(\hat{\mathbf{v}}^*)^{-1}\right), \\ M^\Delta &:= \left(Y_{LL}^{-1} B^\top \operatorname{diag}(B\hat{\mathbf{v}}^*)^{-1}, -\mathrm{j} Y_{LL}^{-1} B^\top \operatorname{diag}(B\hat{\mathbf{v}}^*)^{-1}\right), \\ K^Y &:= |\operatorname{diag}(\mathbf{w})| \mathcal{R}\{\operatorname{diag}(\mathbf{w})^{-1} M^Y\}, \mathbf{b} := |\mathbf{w}|, \\ K^\Delta &:= |\operatorname{diag}(\mathbf{w})| \mathcal{R}\{\operatorname{diag}(\mathbf{w})^{-1} M^\Delta\}, \\ G^Y &:= \operatorname{diag}(\mathbf{v}_0) Y_{0L}^* (M^Y)^*, G^\Delta := \operatorname{diag}(\mathbf{v}_0) Y_{0L}^* (M^\Delta)^*, \\ \mathbf{c} &:= \operatorname{diag}(\mathbf{v}_0) \left(Y_{00}^* \mathbf{v}_0^* + Y_{0L}^* \mathbf{w}^*\right). \end{aligned} \tag{6.28}$$

In the following, we consider constant matrices obtained from $(\hat{\mathbf{v}}, \hat{\mathbf{s}}^Y, \hat{\mathbf{s}}^\Delta) = (\mathbf{w}, \mathbf{0}, \mathbf{0})$, that is a solution of (6.22). However, one can improve the quality of the linear approximation by constructing the matrices based on the current operating conditions $(\hat{\mathbf{v}}, \hat{\mathbf{s}}^Y, \hat{\mathbf{s}}^\Delta)$, which requires measuring the voltages and power injections at every node in real-time.

First, let us define the vector $\mathbf{u} = ((\mathbf{x}_\mathrm{c}^Y)^\top, (\mathbf{x}_\mathrm{c}^\Delta)^\top) \in \mathbb{R}^U$, where $\mathbf{x}_\mathrm{c}^Y, \mathbf{x}_\mathrm{c}^\Delta$ contain the power injections of the DERs. The number U depends on the number of DERs, and their connection type (1-phase or 3-phase connection). For the sake of clarity, let us consider that the voltage at the substation $\mathbf{v}_0$ cannot be controlled and is held constant to 1 pu. Furthermore, we consider that, for each controllable source, the feasible set describing the hardware limits is defined as $\mathcal{S} := \mathcal{S}^Y \cup \mathcal{S}^\Delta$, with

$$\begin{aligned} \mathcal{S}^Y &:= \{0 \leq \mathbf{p}_{j,\phi}^Y \leq \mathbf{p}_{j,\phi,\max}^Y, (\mathbf{p}_{j,\phi}^Y)^2 + (\mathbf{q}_{j,\phi}^Y)^2 \leq (\mathbf{s}_{j,\phi,\mathrm{nom}}^Y)^2, |\mathbf{q}_{j,\phi}^Y| \leq 0.44 \mathbf{s}_{j,\phi,\mathrm{nom}}^Y\}_{j \in \mathcal{G}^Y, \phi \in \{a,b,c\}}, \\ \mathcal{S}^\Delta &:= \{0 \leq \mathbf{p}_{j,\phi}^\Delta \leq \mathbf{p}_{j,\phi,\max}^\Delta, (\mathbf{p}_{j,\phi}^\Delta)^2 + (\mathbf{q}_{j,\phi}^\Delta)^2 \leq (\mathbf{s}_{j,\phi,\mathrm{nom}}^\Delta)^2, |\mathbf{q}_{j,\phi}^\Delta| \leq 0.44 \mathbf{s}_{j,\phi,\mathrm{nom}}^\Delta\}_{j \in \mathcal{G}^\Delta, \phi \in \{ab,bc,ca\}}, \end{aligned} \tag{6.29}$$

where $\mathcal{G}^Y$,$\mathcal{G}^\Delta$ are the set of nodes to which wye-connected, delta-connected DERs are connected, respectively. The feasible set $\mathcal{S}$ is such that each phase is constrained independently. Finally, let us denote the vector-valued function $\ell(\mathbf{u})$ such that we can write $\mathcal{S} := \{\mathbf{u} \in \mathbb{R}^U \mid \ell(\mathbf{u}) \leq 0\}$ for simplicity. Using appropriate measurements, one can construct an optimization-based feedback controller that naturally tracks the time-varying

grid conditions. Let us define $\tilde{\boldsymbol{\nu}}$ the vector collecting the voltage measurements at each node, and $\tilde{\mathbf{s}}$ the vector collecting the three-phase apparent power at the substation, one can write our feedback-based safe gradient flow as:

$$\begin{aligned} F_\beta(\mathbf{u}, \tilde{\boldsymbol{\nu}}, \tilde{\mathbf{s}}) := \arg \min_{\theta \in \mathbb{R}^U} \quad & \frac{1}{2} \left\| \theta + \nabla f(\mathbf{u}) \right\|_2^2 \\ \text{s.t.} \quad & \beta \left(\underline{V} - \tilde{\boldsymbol{\nu}} \right) \leq K_\text{c}^\top \theta \leq -\beta \left(\tilde{\boldsymbol{\nu}} - \bar{V} \right) \\ & \beta \left(E - \tilde{\mathbf{s}} + S_\text{set} \right) \leq G_\text{c}^\top \theta \leq -\beta \left(\tilde{\mathbf{s}} - S_\text{set} - E \right) \\ & \nabla \ell(\mathbf{u})^\top \theta \leq -\beta \ell(\mathbf{u}). \end{aligned} \tag{6.30}$$

We implement the following controller:

$$\mathbf{u}(t+1) = \mathbf{u}(t) + \Delta t \eta F_\beta(\mathbf{u}(t), \tilde{\boldsymbol{\nu}}(t), \tilde{\mathbf{s}}(t)), \tag{6.31}$$

which is the forward Euler discretization of the feedback controller $\dot{\mathbf{u}} = \eta F_\beta(\mathbf{u}, \tilde{\boldsymbol{\nu}}, \tilde{\mathbf{s}})$, with η as controller gain.

6.3.2 *Experimental results*

6.3.2.1 *Simulation setup*

We consider the IEEE37-node feeder shown in Figure 6.8a with a 4.8 kV operating voltage.

We modified the original benchmark, which contained only delta-connected loads, to incorporate delta and wye-connected DERs. We did not implement DERs' dynamics as they are considered much faster than the controller dynamics [Eggli et al., 2020]. The power setpoints are instantaneously implemented by the DERs. We only consider PV plants as DERs, with the hardware limits defined by the set $\mathcal{S}$ and $\mathbf{p}_\text{max}$ representing the available power derived from the solar irradiance. We also define the following cost function:

$$\sum_{j \in \mathcal{G}^Y} \sum_{\phi \in \{a,b,c\}} c_p (\mathbf{p}^Y_{j,\phi} - \mathbf{p}^Y_{j,\phi,\text{max}})^2 + c_q (\mathbf{q}^Y_{j,\phi})^2 + \sum_{j \in \mathcal{G}^\Delta} \sum_{\phi \in \{ab,bc,ca\}} c_p (\mathbf{p}^\Delta_{j,\phi} - \mathbf{p}^\Delta_{j,\phi,\text{max}})^2 + c_q (\mathbf{q}^\Delta_{j,\phi})^2, \tag{6.32}$$

such that the active power curtailment and the usage of reactive power are penalized, with $c_p = 3$ and $c_q = 1$. The load profiles and maximum available power aggregated for each phase with a granularity of 10 seconds are shown in Figure 6.8b. The network is strongly unbalanced.

The results obtained with the feedback-based safe gradient flow (SGF) are compared with the results when we solve the problem (6.26) with the linear model of the 3-phase power flow equations (6.27). The latter corresponds to a linear formulation of the AC-OPF (L-AC-OPF) solved in an open-loop fashion. We consider that the SGF receives new measurements, computes new power setpoints and DERs deploy the new power

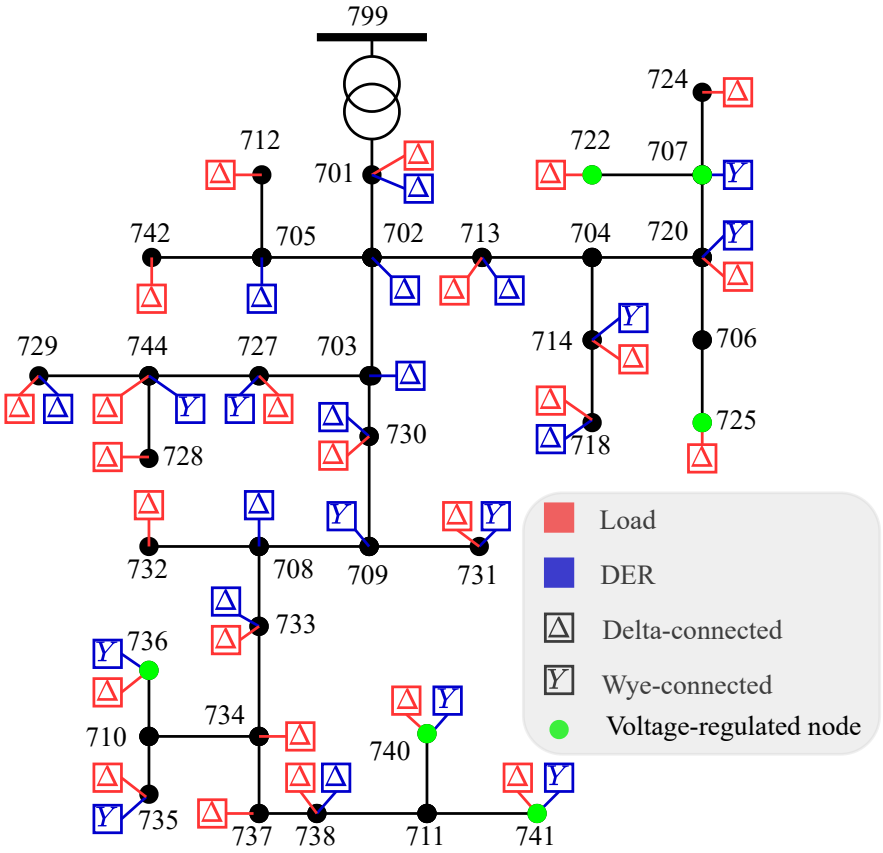

(a) Modified IEEE37-node feeder

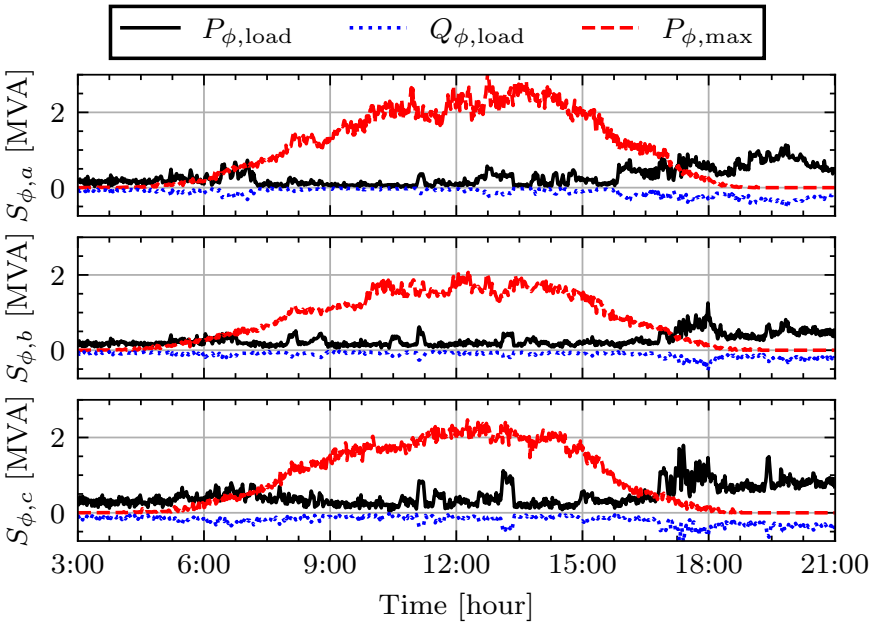

(b) Aggregated load profiles and maximum power available for DERs per phase

Figure 6.8

setpoints every second, while the grid conditions change every 10 seconds. We enforce voltage limits, $\underline{V} = 0.95, \bar{V} = 1.05$, only on a subset of nodes, highlighted in green in Figure 6.8a. These nodes have been selected such that the voltage magnitudes of the other nodes stay within the lower and upper voltage limits. We also enforce power tracking at the substation from hours 9 : 00 to 11 : 00 and from hours 14 : 00 to 15 : 00. Finally, we consider two scenarios, one with accurate estimation of line impedances, and the other with the line impedances underestimated by 20%. It influences the admittance matrix, and therefore the linear model parameters.

6.3.2.2 *Results*

Results with no error in the admittance matrix

In Figure 6.9a, we compare the voltage magnitudes for different phases when the power setpoints are obtained from the L-AC-OPF and SGF algorithms. One can see that the voltage magnitudes of voltage-regulated nodes stay within the limits. However, while the voltage constraints are tight for SGF, the L-AC-OPF yields lower voltage magnitudes. This is due to the linear model, which overestimates the voltage magnitudes for the L-AC-OPF algorithm, while the SGF algorithm uses voltage measurements.

Figure 6.10b shows that both algorithms can track the power setpoints at the substation from hours 9 : 00 to 11 : 00 and from hours 14 : 00 to 15 : 00. However, the error for the L-AC-OPF is larger than the error for the SGF because of the linear model inaccuracy.

We show both algorithms' DERs active power injections in Figure 6.10a. There is more active power curtailment with L-AC-OPF than with SGF because the linear model overestimates the voltage magnitudes, forcing the L-AC-OPF to produce a greater effort. This is also reflected in the value of the cost function as the total cumulative cost over the day is 44.030 for the SGF and 65.201 for L-AC-OPF.

Results with error in the admittance matrix

In Figure 6.9b, we compare the voltage magnitudes for the two algorithms when the linear model is constructed based on underestimated line impedances. The voltages stay within the limit for the SGF, while the L-AC-OPF induces voltage magnitudes excursions outside the admissible values. This shows that feedback-based algorithms are more robust to modeling uncertainties than traditional algorithms solved in an open-loop fashion.

Remark 6.1 (*Discussion on error in the measurements*)**.** *One may say that feedback-based controllers are sensitive to measurement errors, which is true. However, traditional approaches to solving the AC-OPF also require measurements of load consumption, which are also subject to errors. The major difference is that for the proposed SGF algorithm, one can assess the maximum error on voltage measurements, and adapt the voltage thresholds to guarantee safe voltages throughout the network, e. g., if the voltage measurements are perturbed with a maximum error ε, one can tighten the voltage limits such that $[\underline{V}, \bar{V}]$ becomes $[\underline{V} + \varepsilon, \bar{V} - \varepsilon]$. For the L-AC-OPF, the error affects the load consumption, and*

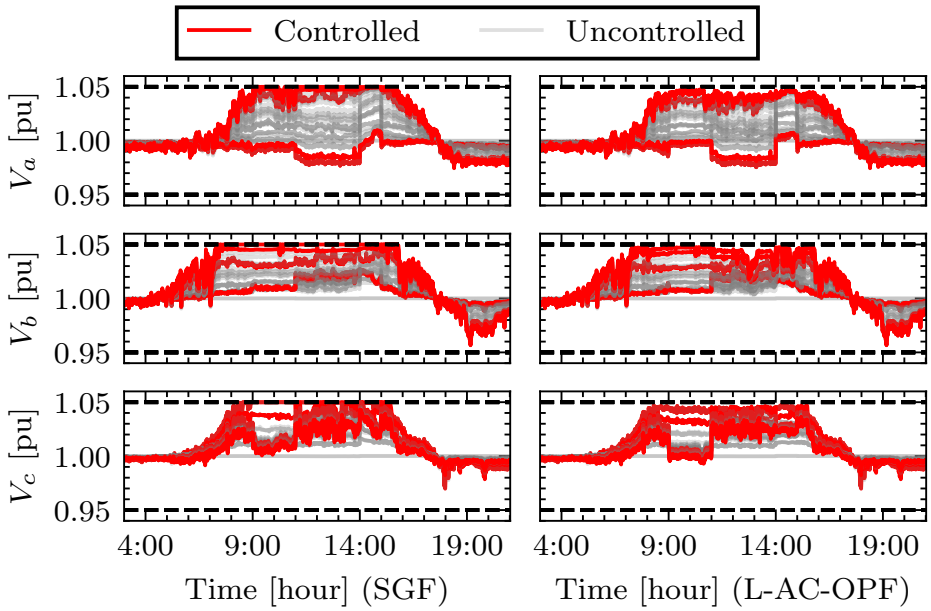

(a)

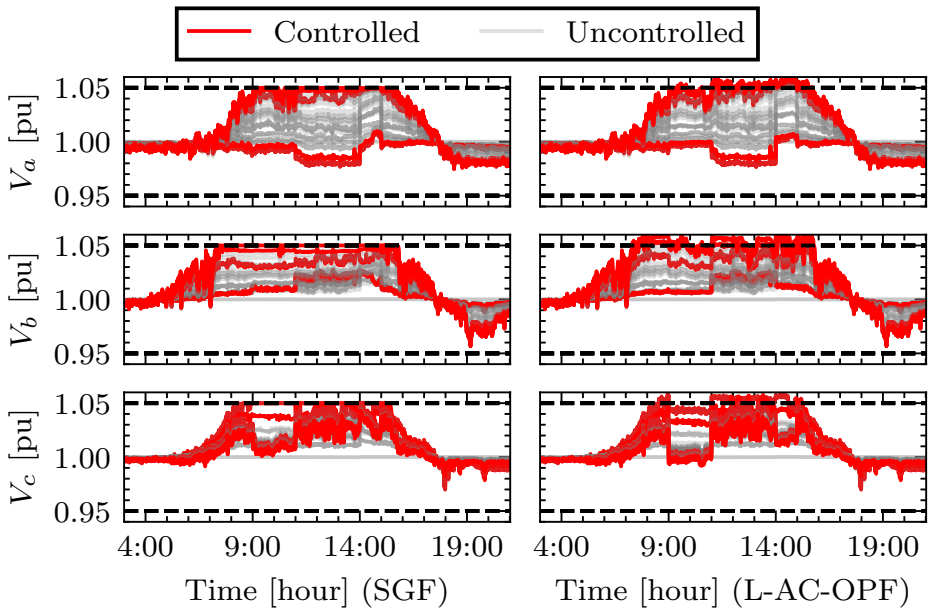

(b)

Figure 6.9: (a) Voltage magnitudes with SGF and L-AC-OPF algorithms. (b) Voltage magnitudes with SGF and L-AC-OPF algorithms with line impedances underestimated by 20%.

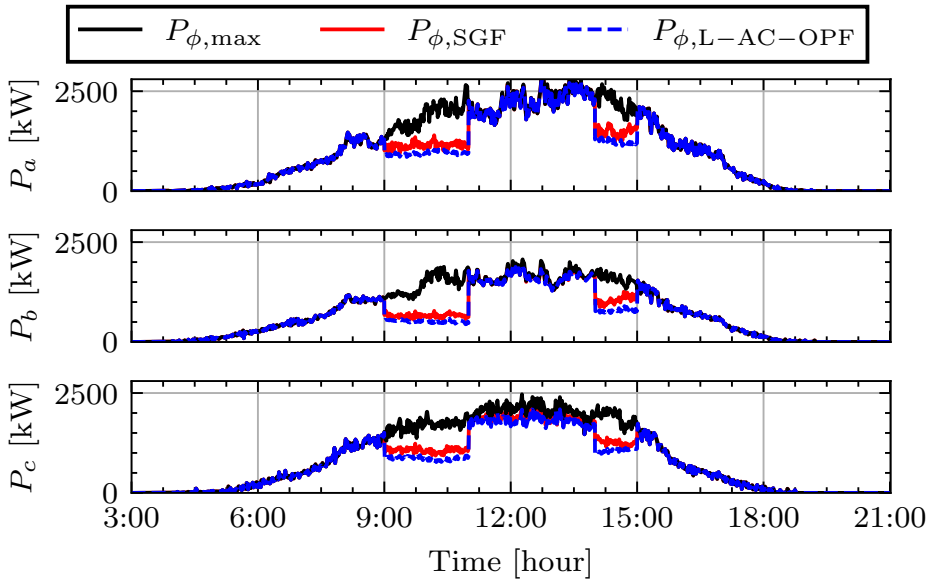

(a)

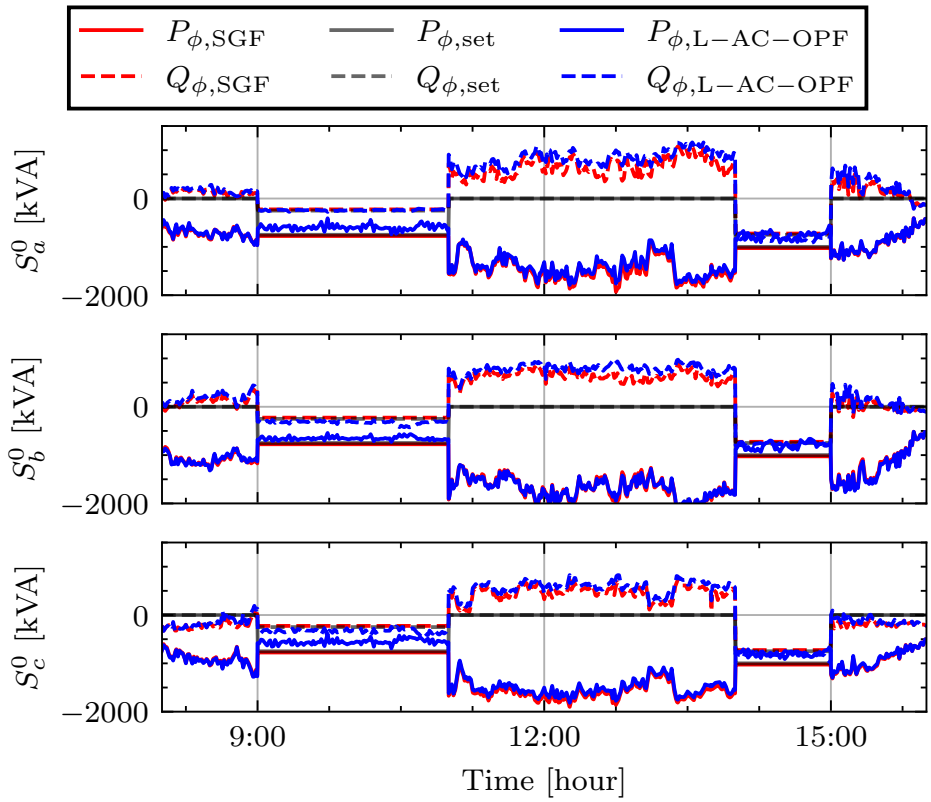

(b)

Figure 6.10: (a) Available active power and DERs active power injections with SGF and L-AC-OPF algorithms. (b) Power tracking at the substation with SGF and L-AC-OPF algorithms.

one needs to propagate this error through the power system model to analyze the effect of those errors on voltages.

6.4 SUMMARY

In this chapter, we have presented a feedback-based safe gradient flow controller to pursue a solution of an AC-OPF problem. The controller is based on the theory of control barrier functions, and it guarantees anytime satisfaction of operational constraints. We have shown that the controller is robust against modelling errors due to the feedback addition. We tested the controller on a single-phase equivalent distribution network, and showed that it leads to no operational constraint violation, while accurately tracking an optimal solution of the AC-OPF problem. The controller has also been tested on the three-phase unbalanced IEEE37-node feeder for the optimal regulation of a virtual power plant, and compared with a linearized version of the AC-OPF. The results show superior performance of the feedback-based safe gradient flow controller compared to the linear AC-OPF, and constraint satisfaction even in the presence of modelling errors due to the feedback addition.

7

DECENTRALIZED CONTROLLER

Outline

In this chapter, we propose a decentralized controller to solve the Problem 1.2 introduced in Section 1.2.2. We consider a two-level control strategy, where the controller gains are determined centrally and then broadcasted to the controllable DERs. The controller gains are computed by solving an optimization problem that contains specifications on the maximum amount of voltage violation that is tolerated. We illustrate the performance of the proposed controller on a single-phase equivalent distribution network and on the unbalanced three-phase IEEE 123-node test feeder. The chapter is organized as follows. In Section 7.1, we review the literature on decentralized controllers for voltage regulation in distribution networks. In Section 7.2, we introduce the proposed incremental Volt/Var controller and illustrate its performance on a single-phase distribution network. In Section 7.3, we present a robust formulation of our decentralized controller. In Section 7.4 we illustrate the performance of the proposed controller on the unbalanced three-phase IEEE 123-node test feeder. Finally, in Section 7.5, we provide a summary.

7.1 LITERATURE REVIEW

In the previous section, we proposed a centralized approach, where a central aggregator determines the DERs' power injections by solving a quadratic programming problem. Usually, the central controller needs a precise knowledge of the network, which may be hard to obtain in practice [Srivastava et al., 2023]. We showed that recent feedback-based methods do not require perfect knowledge of non-controllable power injections, but they rely on a communication infrastructure that is not present in existing distribution networks. In particular, it requires collecting voltage measurements and communicating setpoints in real-time. In this section, we focus on decentralized strategies, which offer simplicity and low implementation cost since they rely only on local measurements in real-time to perform control actions [Zhu and Liu, 2016, Zhou et al., 2021]. The overall idea is illustrated in Figure 7.1, where an offline algorithm computes the gains of the local controllers based on forecasts of load consumption and generation days or hours ahead, and dispatches the computed gains to the DERs. The DERs then implement the controller locally, without the need for real-time communication.

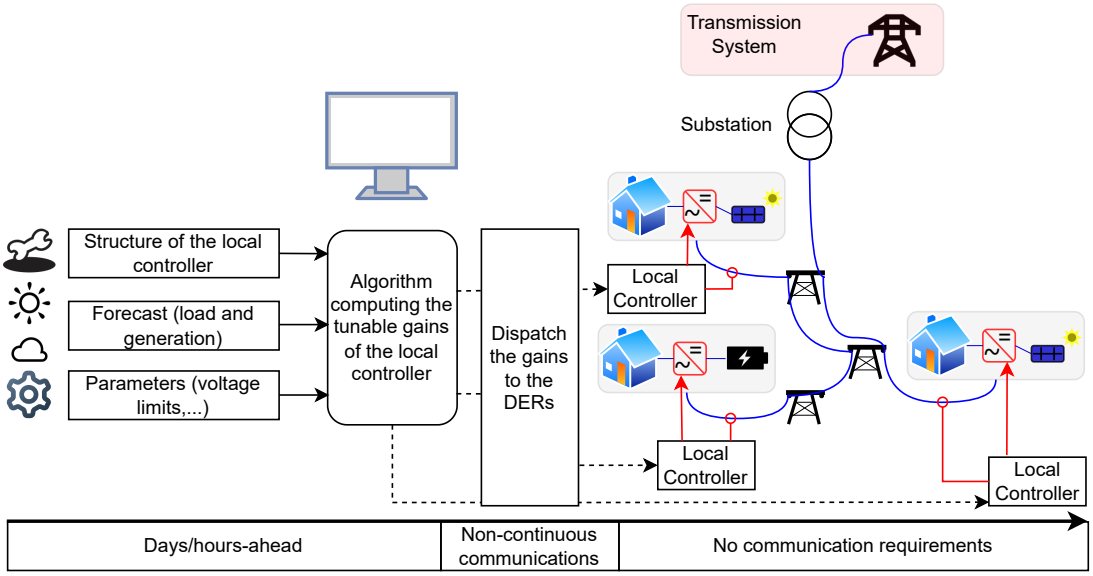

Figure 7.1: Proposed decentralized voltage regulation strategy. The controller gains are computed centrally and then broadcasted to the controllable DERs.

We make a distinction between active and reactive power control. As mentioned in Section 5.2, active power control, such as Volt/Watt strategies [Kashani et al., 2017, Howlader et al., 2020], are well adapted for voltage regulation in distribution networks because of the high R/X ratio. However, they induce higher costs because of the inherent active power curtailment. Therefore, reactive power control is often preferred, even if it is less effective. Notice that Volt/Var control strategies can also induce active power curtailment if reactive power is prioritized over active power.

Volt/Var controllers determine reactive power injections from, e. g., a static function of the local voltage measurements. One example is illustrated in Figure 6.4b, that is based on IEEE standard *IEEE Std 1547-2018*. The slopes of individual Volt/Var curves can be tuned to achieve various objectives by solving appropriate optimization problems [Baker et al., 2018]. A static Volt/Var controller for a DER $g \in \mathcal{G}$ connected to node $n \in \mathcal{N}$ can be written as:

$$q_{g,k+1} = f_g(\tilde{\nu}_{n,k}), \tag{7.1}$$

where f_g is a function of the local voltage magnitude $\tilde{\nu}_{n,k}$ at time index k, and $q_{g,k+1}$ is the reactive power setpoint implemented at the next time step $(k+1)$. However, these static feedback laws can lead to oscillatory behaviors [Jahangiri and Aliprantis, 2013]. Incremental strategies have the following structure:

$$q_{g,k+1} = h_g(\tilde{\nu}_{n,k}, q_{g,k}), \tag{7.2}$$

such that the reactive power at the next time step $(k+1)$ is gradually adjusted based on the previous reactive power setpoint and the voltage magnitude (time index k) [Farivar

et al., 2015]. These are generally favored since they can prevent oscillatory behaviors and offer more flexibility. Notice that in Baker et al. [2018], authors optimize both static Volt/Var and static Volt/Watt curves to minimize voltage deviations, and to ensure a controller stabilizing the system. However, stability constraints for static Volt/Var control are more restrictives than for incremental strategies, and thus, incremental strategies can provide better reactive power compensation Farivar et al. [2015].

Notice that purely local reactive power control strategies can fail at keeping the voltage within prescribed limits even if a solution exists due to improper dispatch of the reactive power available [Bolognani et al., 2019]. On the other hand, local control strategies are perfectly adapted to current distribution network technology since they do not rely on advanced communication infrastructures.

Chance-constrained approaches to design optimal rules for *non*-incremental Volt/Var control are proposed in [Wei et al., 2023, Nazir et al., 2019]. These works consider a separate set of gains for each DER. This may be challenging in practice, as it requires knowledge of each DER location and an advanced offline communication infrastructure to properly dispatch the gains. We also mention some representative works in the context of data-driven methods to learn a Volt/Var controller [Karagiannopoulos et al., 2019]. For learning-based strategies, it is often difficult to analyze the closed-loop stability [Eggli et al., 2020]. Some exceptions are, e. g., [Gupta et al., 2023, 2024]; however, the controllers in these works do not minimize reactive power usage, potentially causing additional losses in the distribution network. In Yuan et al. [2024], closed-loop stability for a general class of Volt/Var controllers is guaranteed but historical data are needed for training the learning-based controllers. The work presented in Cui et al. [2022], investigates the use of reinforcement learning to derive local Volt/Var control policies in distribution networks. Lipschitz constraints are established to guarantee exponentially stabilizing controllers. A cost function combining voltage deviations and control actions was considered. In the context of learning-based Volt/Var, it is difficult to account for network topology changes. Indeed, changes in topology may require collecting new data and re-training learning-based controllers, which is time-consuming. In Serna Torre and Hidalgo-Gonzalez [2022], authors propose a linear Volt/Var controller and a methodology for adapting the controller to varying network topologies. However, this requires solving multiple instances of the optimal power flow problem.

7.1.1 *Incremental Volt/Var control*

Leveraging the inverters' capabilities, we propose a two-level Volt/Var control strategy, driven by the following practical and architectural considerations:
(a) Piecewise linear droop Volt/Var rules, as suggested by the IEEE standard *IEEE Std 1547-2018*, offer fast response to deviations of local voltage magnitude [Zhu and Liu, 2016, Zhou et al., 2021].

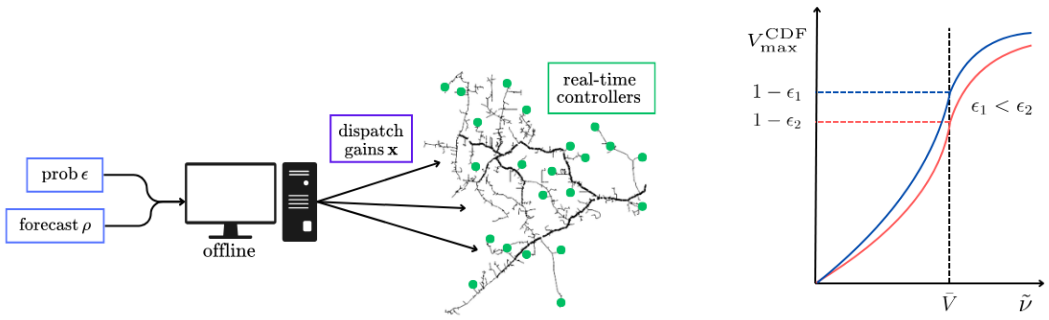

(a) (b)

Figure 7.2: (a) Proposed voltage regulation strategy. Based on the forecast $\boldsymbol{\rho}$ and the probability ϵ to violate voltage limits, the controller gains $\mathbf{x}$ are computed centrally and then broadcasted to the controllable DERs. (b) Illustrative explanation of the impact of the parameter ϵ on the total amount of voltage violations. A smaller ϵ results in a more constrained optimization problem and therefore in fewer voltage violations.

(b) Local incremental Volt/Var methods offer advantages over the piecewise linear droop Volt/Var rule in terms of utilization of reactive power resources and avoidance of possible oscillations [Jahangiri and Aliprantis, 2013, Farivar et al., 2015].
(c) Local Volt/Var methods often do not guarantee voltage regulation; communication and coordination are typically required [Bolognani et al., 2019].

The proposed method enjoys the advantages of the local incremental controllers (acting at a fast time scale locally), with regulation performance ensured by designing the control parameters via an optimization-based task (solved occasionally at the higher level). In particular, the optimization-based task allows us to specify the maximum amount of voltage violation that is tolerated. The only communication needed is between a central aggregator where the controller parameters are computed and the inverters, which receive the updated controller parameters from the aggregator. In particular, we do not require *real-time* communication as the controller parameters are obtained using forecasts for which uncertainties are taken into account in the optimization-based task. In Figure 7.1, the structure of the local controllers is given by (7.2), and the controller parameters are determined by solving an optimization problem at the central aggregator. In terms of parameters, we also consider a prescribed probability for voltage violations.

The proposed approach is illustrated in Figure 7.2. This approach can be viewed as a two-level control where: *(i)* the coefficients and gains of the local controllers are computed centrally and then broadcasted to the local controllers (the coefficients and gains are updated at a slow time scale, for example at hourly intervals); and *(ii)* the DERs implement the controllers, with the received coefficients and gains, for real-time voltage regulation. In real-time, the control is fully decentralized, in the sense that the controller is implemented locally at each DER without DER-to-DER communications.

7.1.2 *Contributions*

The proposed decentralized controller has the following contributions:
(*c1*) A chance-constrained optimization problem is formulated to ensure that voltage violations cannot occur more often than according to a given probability.
(*c2*) A single set of gains suitable for all DERs is determined, thus simplifying the optimization problem to be solved at the upper level and keeping the communication infrastructure requirements low. Furthermore, *fairness* in sharing control efforts is implicitly embedded by having the same gains for all DERs.
(*c3*) With respect to a standard Volt/Var controller, this approach aims to minimize the generator's reactive power injections. The controller gains are determined in advance based on forecast data for power generation and loads. To account for a variety of possible distributions of the forecasting errors, a conservative approximation of the chance constraints is derived [Nemirovski and Shapiro, 2007].
(*c4*) Compared to data-driven methods that require historical data to train the local controllers, our local controllers have a generic structure that can accommodate any topology of distribution network. Therefore, not only can this approach easily handle planned topology changes but, even in case of unplanned changes, it is still reliable since network conditions are taken into account as feedback.
(*c5*) This approach uses an algorithm based on Successive Convex Approximation (SCA) methods proposed in Scutari et al. [2014] to derive a convex, and therefore tractable formulation of our chance-constrained problem.

7.2 PROPOSED INCREMENTAL VOLT/VAR CONTROLLER

Ideally, one wants to minimize the total reactive power usage while maintaining voltages inside a given feasible set. In the following, we consider the problem of providing reactive power compensation to regulate voltage magnitudes in a distribution network. We consider a single-phase distribution network to streamline the notation. The extension to a three-phase unbalanced distribution network, and the stability analysis of the proposed controller is illustrated later on. We re-write as follows our OPF problem defined in (5.3) as an optimal reactive power flow problem, i. e., only the reactive powers of the controllable generators can be controlled:

$$\begin{aligned} \min_{\mathbf{q}\in\mathbb{R}^G} \quad & C_v(\boldsymbol{\nu}) + C_p(\mathbf{q}) \\ \text{s.t.} \quad & \underline{V} \le \nu_i \le \bar{V} \quad \forall i \in \mathcal{M} \\ & \nu_i = H_i(\mathbf{q}; \mathbf{p}_{\text{av}}, \mathbf{p}_l, \mathbf{q}_l) \quad \forall i \in \mathcal{M} \\ & q_i \in \mathcal{Q}_i \quad \forall i \in \mathcal{G} \end{aligned} \tag{7.3}$$

where $\mathcal{Q} := \mathcal{Q}_1 \times \mathcal{Q}_2 \times ... \times \mathcal{Q}_G$ is the set of feasible values for the reactive powers of the generators, $\mathbf{p}_{\text{av}} \in \mathbb{R}^G$ collects the non-controllable active power of the generator

and $\mathbf{q} \in \mathbb{R}^G$ collects the controllable reactive power injection of the generators. As previously discussed, collecting data, solving the non-linear and non-convex problem (7.3) and broadcasting the setpoints to the inverters every second is challenging. In this chapter, we aim to solve the following problem.

Problem 7.1. *Design feedback controllers to approximate the solution of an optimal reactive power flow problem (7.3) with limited computational resources and in a decentralized fashion, i. e., each controller uses only local voltage measurements to compute its reactive power output and the operation does not necessitate continuous communications with neighbors or a centralized entity.* □

To outline the proposed framework, we consider the case where there is one DER per node in the network and the map H does not change over time. Recall that H represents the practical solution of the power flow equations. Additionally, we make the following assumption.

Assumption 7.1 (*Feasibility*)**.** *For any $\mathbf{q} \in \mathcal{Q}$, there exists a solution such that $\underline{V} \leq H(\mathbf{q}; \mathbf{p}_{\text{av}}, \mathbf{p}_l, \mathbf{q}_l) \leq \bar{V}$.* □

This assumption ensures that there is enough reactive power reserve to regulate the voltages. We will review this assumption and our setup choices later, and discuss how they could be relaxed.

We identify three different time scales for our proposed method to perform voltage regulation in distribution networks. In order from the shortest to the longest, they correspond to the time scales that characterize the following events: *(i)* controller law updates, *(ii)* forecast updates and *(iii)* controller gains updates.

7.2.1 *Controller design*

To begin with, we consider only the shortest time scale, which is related to the controller law updates. Let us discretize the temporal domain as $t = k\tau$, where $k \in \mathbb{N}_+$ and $\tau \in \mathbb{R}_{>0}$ is a given time interval, small enough to resolve variations in the time-dependent disturbances, i. e., less than a second. We consider the following feedback controller:

$$\mathbf{q}_{k+1} = \mathbf{q}_k + \eta(\mathbf{1} - \hat{\boldsymbol{\nu}}_k) - (1 - \eta)\alpha\mathbf{q}_k, \tag{7.4}$$

where $\alpha \in \mathbb{R}_{\geq 0}$, $\eta \in [0, 1]$, and $\hat{\boldsymbol{\nu}}_k = \hat{H}(\mathbf{q}_k; \mathbf{z}_k) = X\mathbf{q}_k + \boldsymbol{\rho}_k$ with $\mathbf{z} := (\mathbf{p}_{\text{av}}, \mathbf{p}_l, \mathbf{q}_l)$ that represents the uncontrollable power injections, and $X \in \mathbb{R}^{N \times N}$ is a linear approximation of the power flow equations. Finally, $\boldsymbol{\rho}_k = H(\mathbf{0}, \mathbf{z}_k)$ denotes the voltage profile obtained by setting the controllable reactive powers to 0. The linearized power flow equations can be derived from the bus injection model [Dall'Anese and Simonetto, 2016], see equation (6.12), or from the branch flow model [Li et al., 2014]. In the following, we consider the linearized power flow equations based on the branch flow model [Baran and Wu,

1989], since it guarantees X being positive definite [Farivar et al., 2013]. This approximation has been used in [Li et al., 2014, Eggli et al., 2020], and its quality has been discussed in [Farivar et al., 2013]. Notice that $\boldsymbol{\rho}_k = H(\mathbf{0}, \mathbf{z}_k)$ is derived from the true power flow equations, i. e., by solving (5.2) using a fixed-point method. Substituting this approximation in (7.4), the controller can be written as:

$$\mathbf{q}_{k+1} = A(\eta, \alpha)\mathbf{q}_k + B(\eta, \boldsymbol{\rho}_k), \tag{7.5}$$

where $A(\eta, \alpha) := (1 - (1 - \eta)\alpha)\mathbb{I} - \eta X$ and $B(\eta, \boldsymbol{\rho}_k) := \eta(\mathbf{1} - \boldsymbol{\rho}_k)$.

Existence and uniqueness of the equilibrium: Denoting $\boldsymbol{\rho} = \boldsymbol{\rho}_k$ for a given k, the equilibrium for (7.5) is defined as:

$$\begin{aligned} \mathbf{q}^* &= [\eta X + (1 - \eta)\alpha\mathbb{I}]^{-1}\, \eta(\mathbf{1} - \boldsymbol{\rho}) \\ \hat{\boldsymbol{\nu}}^* &= X\,[\eta X + (1 - \eta)\alpha\mathbb{I}]^{-1}\, \eta(\mathbf{1} - \boldsymbol{\rho}) + \boldsymbol{\rho}. \end{aligned} \tag{7.6}$$

Since X is positive definite and $\alpha \in \mathbb{R}_{\geq 0}$, $\eta \in [0, 1]$, the matrix $\eta X + (1 - \eta)\alpha\mathbb{I}$ in (7.6) is always invertible and the equilibrium is unique. One can check that for $\eta = 0$ and $\alpha > 0$, $\mathbf{q}^* = \mathbf{0}$ and $\hat{\boldsymbol{\nu}}^* = \boldsymbol{\rho}$, while for $\eta > 0$ and $\alpha = 0$ or $\eta = 1$, $\mathbf{q}^* = X^{-1}(\mathbf{1} - \boldsymbol{\rho})$ and $\hat{\boldsymbol{\nu}}^* = \mathbf{1}$.

Increasing the gain α decreases the use of reactive power, while increasing the gain η steers the voltage magnitudes to the nominal voltage profile.

Stability analysis: The controller (7.5) is asymptotically stable if and only if $\rho(A(\eta, \alpha)) < 1$, where $\rho(\cdot)$ denotes the spectral radius. This condition is verified if:

$$\mathbf{0} < (1 - \eta)\alpha\mathbf{1} + \eta\boldsymbol{\lambda}_X < 2\mathbf{1}, \tag{7.7}$$

where $\boldsymbol{\lambda}_X \in \mathbb{R}^N$ is the vector containing the eigenvalues of the matrix X. Moreover the matrix X is positive definite by construction, and since η, α satisfy $\alpha \in \mathbb{R}_{\geq 0}$, $\eta \in [0, 1]$, we always have $(1 - \eta)\alpha\mathbf{1} + \eta\boldsymbol{\lambda}_X \geq \mathbf{0}$. The equality holds only if $\eta = \alpha = 0$, which guarantees a stable controller since $\mathbf{q}_{k+1} = \mathbf{q}_k$.

7.2.2 *Controller gains design*

The performance of the controller (7.5) depends on the choice of η and α. In the following, we introduce an optimization-based method to design the gains.

Given a matrix X, a time-varying vector $\boldsymbol{\rho}_k = H(\mathbf{0}, \mathbf{z}_k)$, and the feasible set $\mathcal{Q}$, we formulate the following problem at time $k\tau$:

$$\min_{\alpha \in \mathbb{R}_{\geq 0}, \eta \in [0,1]} \quad \|\mathbf{q}_k(\alpha, \eta)\|^2 \tag{7.8a}$$

$$\text{s.t.} \quad \mathbf{q}_k(\alpha, \eta) \in \mathcal{Q} \tag{7.8b}$$

$$\underline{V} \leq X\mathbf{q}_k(\alpha, \eta) + \boldsymbol{\rho}_k \leq \bar{V} \tag{7.8c}$$

$$(1 - \eta)\alpha\mathbf{1} + \eta\boldsymbol{\lambda}_X < 2\mathbf{1} \tag{7.8d}$$

where $\mathbf{q}_k(\alpha,\eta) = [\eta X + (1-\eta)\alpha\mathbb{I}]^{-1}\eta(\mathbf{1}-\boldsymbol{\rho}_k)$ is a non-linear function of η and α. For a given time $k\tau$, the goal is to minimize the reactive power usage $\|\mathbf{q}_k(\alpha,\eta)\|^2$, while satisfying operational constraints, by appropriately selecting the gains η and α.

Remark 7.2 (*Convergence to equilibrium*)**.** *We make a slight abuse of notation as the function $\mathbf{q}_k(\alpha,\eta)$ represents the equilibrium of the controller (7.4) for given gains and voltages $\boldsymbol{\rho}_k$. We assume that the time constant τ is sufficiently small to cope with the dynamics of the distribution networks. Therefore, the controller reaches its equilibrium before $\boldsymbol{\rho}$ changes. In practice, $\boldsymbol{\rho}$ changes continuously, so the controller always pursues a new equilibrium. However, it is reasonable to assume that, given a sufficiently small τ, the controller is always close to its equilibrium.* □

An alternative formulation of problem (7.8) can be derived using an appropriate change of variable. This facilitates the application of the successive convex approximation strategy presented next. Therefore, we introduce the optimization variable $\mathbf{x} = [\frac{\alpha}{\eta}, -\alpha]^\top \in \mathbb{R}_{\geq 0}\times\mathbb{R}_{\leq 0}$, rewrite $\mathbf{q}_k(\mathbf{x}) = \left[X + \mathbf{1}^\top\mathbf{x}\mathbb{I}\right]^{-1}(\mathbf{1}-\boldsymbol{\rho}_k)$, specify $\mathcal{Q}$ in terms of box constraints, and reformulate the problem (7.8) as

$$\begin{aligned} \min_{\mathbf{x}} \quad & h_0^k(\mathbf{x}) \\ \text{s.t.} \quad & h_i^k(\mathbf{x}) \leq 0 \quad \forall i \in \{1,...,8\} \end{aligned} \tag{7.9}$$

where

$$\begin{aligned} & h_0^k(\mathbf{x}) = \|\mathbf{q}_k(\mathbf{x})\|^2, \quad h_1^k(\mathbf{x}) = \mathbf{q}_k(\mathbf{x}) - \mathbf{q}_{\max},\ h_2^k(\mathbf{x}) = -\mathbf{q}_k(\mathbf{x}) + \mathbf{q}_{\min}, \\ & h_3^k(\mathbf{x}) = X\mathbf{q}_k(\mathbf{x}) + \boldsymbol{\rho}_k - \bar{V},\ h_4^k(\mathbf{x}) = -X\mathbf{q}_k(\mathbf{x}) - \boldsymbol{\rho}_k + \underline{V}, \\ & h_5(\mathbf{x}) = \left(\mathbf{1}^\top\mathbf{x} - 2\right)\mathbf{1} + \boldsymbol{\lambda}_X,\ h_6(\mathbf{x}) = -\mathbf{1}^\top\mathbf{x}, \quad h_7(\mathbf{x}) = -x_1, \quad h_8(\mathbf{x}) = x_2, \end{aligned} \tag{7.10}$$

with x_1, x_2 scalar components of $\mathbf{x}$ and $\mathbf{1} = [1,1]^\top \in \mathbb{R}^2$. The objective function h_0 is a scalar function, as well as h_6, h_7 and h_8. All other constraint functions h_i with $i \in \{1,...,5\}$ are vector-valued. Another advantage of performing the change of variables is that function $h_5(\mathbf{x})$ gives a tighter bound on (7.8d) with respect to the old formulation, with the equality reached for $\eta = 1$. The controller gains derived from (7.9) ensure asymptotic stability of the controller defined in (7.4) as long as $\eta < 1$. The conditions $\eta < 1$ is always verified as $\eta = 1$ implies $\hat{\boldsymbol{\nu}}^* = \mathbf{1}$ which leads to a suboptimal solution (unless $\underline{V} = \bar{V} = \mathbf{1}$).

The problem (7.9) can be solved in real-time, using directly voltage measurements $\boldsymbol{\rho}_k$, or non-controllable power measurements $\mathbf{z}_k$ and then recovering $\boldsymbol{\rho}_k = H(0,\mathbf{z}_k)$ at time $k\tau$. For each time $k\tau$, new controller gains η,α can be computed and broadcasted to controllable DERs. However, collecting measurements at every nodes, solving (7.9) and then dispatching the controller gains to the controllable DERs in *real-time* is unfeasible because of the communication burden and the computational time required to solve the problem. One could envision solving (7.9) for every time $k\tau$ using forecasts of $\boldsymbol{\rho}_k$. However,

it is not realistic to have such frequent forecast updates, since τ should be sufficiently small to cope with the distribution network dynamics. Furthermore, $\boldsymbol{\rho}_k$ is affected by large uncertainties as it inherits them from $\mathbf{z}_k$ through $\boldsymbol{\rho}_k = H(\mathbf{0}, \mathbf{z}_k)$. Moreover, we would like to find optimal controller gains η and α over a longer time period, to avoid broadcasting new values at every time $k\tau$, or to avoid storing a large number of gains in each controller. In the following, we introduce a chance-constrained formulation which takes into account uncertainties in the forecast $\mathbf{z}_k$, and consider a multi-period optimization problem to update the controller gains occasionally.

Remark 7.3 (*Choice of the coefficients*)**.** *In principle, we could use a grid search approach for η and α in order to find the optimal pair of values that satisfies the constraints and minimize the cost. However, we choose to take an optimization-based approach since it is not straightforward how to select the granularity to perform the screening over the values of α and η. Moreover, while η is in the closed interval $[0, 1]$, the only requirement on the coefficient α is to be non-negative. Therefore, one key question pertains to how to select an interval $[0, \bar{\alpha}]$ for α when building a grid for $[0, 1] \times [0, \bar{\alpha}]$. Setting $\bar{\alpha}$ requires an apriori knowledge of the locations of the minima of the function to be minimized, which we assume is not available.* □

7.2.3 *Multi-period chance-constrained formulation*

Given that our forecast $\boldsymbol{\rho}_k = H(\mathbf{0}, \mathbf{z}_k)$ is subject to uncertainty in the vector $\mathbf{z}_k$, we implement probabilistic constraints in our optimization problem in order to enforce voltage regulation with prescribed probability. The available DERs' powers at time $k\tau$ are modelled by $\mathbf{p}_{\mathrm{av},k} = \bar{\mathbf{p}}_{\mathrm{av},k} + \boldsymbol{\delta}_{\mathrm{av},k}$, while the active and reactive load consumptions are expressed as $\mathbf{p}_{l,k} = \bar{\mathbf{p}}_{l,k} + \boldsymbol{\delta}_{\mathrm{pl},k}$ and $\mathbf{q}_{l,k} = \bar{\mathbf{q}}_{l,k} + \boldsymbol{\delta}_{\mathrm{ql},k}$, respectively. Writing $\boldsymbol{\delta}_k := (\boldsymbol{\delta}_{\mathrm{av},k}, \boldsymbol{\delta}_{\mathrm{pl},k}, \boldsymbol{\delta}_{\mathrm{ql},k})$, and $\bar{\mathbf{z}}_k := (\bar{\mathbf{p}}_{\mathrm{av},k}, \bar{\mathbf{p}}_{l,k}, \bar{\mathbf{q}}_{l,k})$, we have $\boldsymbol{\rho}_k = H(\mathbf{0}, \bar{\mathbf{z}}_k + \boldsymbol{\delta}_k)$ where $\boldsymbol{\delta}_k$ follows a given distribution function.

It is reasonable to assume that a new forecast for $\boldsymbol{\rho}_k$ will be available after a certain time interval $\Delta\tau$ with $\Delta \in \mathbb{N}_+$ (for example, Δ could be such that $\Delta\tau = 15$ minutes). In practice, this means that within a time window of duration $\Delta\tau$, $\boldsymbol{\rho}_k$ will be the same, regardless of the value of the index k. Therefore, we will drop the index k in the following, and consider $\boldsymbol{\rho}^m$ instead to underline that the forecast $\boldsymbol{\rho}^m$ will be updated at each time $t = m\Delta\tau$ with $m \in \mathbb{N}_+$. This introduces a longer time scale, whose magnitude is related to how often forecast updates occur.

Ultimately, our goal is to determine controller gains to be deployed over an even longer time interval $T\tau$ where $T = b\Delta$ with $b \in \mathbb{N}_+$, e. g., b is such that $T\tau = 1$ hour. Figure 7.3 provides a visual representation of the relationship between the three different time scales relevant to this problem.

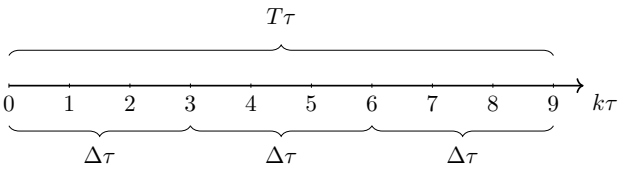

Figure 7.3: Comparison between different time scales of the problem, assuming $\tau = 1s$.

We consider an extension of (7.9) as a chance-constrained multi-period optimization problem:

$$\begin{aligned} \min_{\mathbf{x}} \quad & \sum_{m=1}^{b} \mathbb{E}\{h_0(\mathbf{x}; \boldsymbol{\rho}^m)\} \\ \text{s.t.} \quad & \Pr\{h_{i,n}(\mathbf{x}; \boldsymbol{\rho}^m) \leq 0\} \geq 1 - \epsilon_i \quad \forall i \in \{1,2,3,4\}, n \in \mathcal{N},\ m \in \{1,..,b\} \\ & h_i(\mathbf{x}) \leq 0 \quad \forall i \in \{5,6,7,8\} \end{aligned} \tag{7.11}$$

where we sum over b intervals of magnitude Δ, corresponding in total to a period of time $T\tau$. Notice that for $b = 1$, we recover a single-interval formulation. $\Pr\{A\}$ denotes probability of an event A to happen, meaning that in problem (7.11) the constraints $h_i(\mathbf{x}; \boldsymbol{\rho}^m) \leq 0$ for $i = 1,2,3,4$ are satisfied with a probability $1 - \epsilon_i$, where $\epsilon_i \in (0,1)$. Solving problem (7.11) for the optimization variable $\mathbf{x}$, we can retrieve the values of the gains α and η to be deployed during a time interval of length $T\tau$. When following this approach we lose optimality in exchange for convenience: problem (7.11) can be solved using a coarser forecast and controller gains are designed to cover wider time windows, which is a great advantage from a practical point of view. Finally, notice that the objective function $h_0(\mathbf{x}; \boldsymbol{\rho}^m)$ also depends on $\boldsymbol{\rho}^m$, thus we minimize its expected value.

We seek a tractable approximation for the chance constraints in (7.11) since we do not know the probability distribution function of $\boldsymbol{\delta}_k$, neither the map H. The chance constraints to be approximated are of the form $\Pr\{h(\mathbf{x}; \boldsymbol{\rho}) \leq 0\} \geq 1 - \epsilon$, where the function $h(\mathbf{x}, \boldsymbol{\rho})$ depends on the optimization variable $\mathbf{x}$ and the random vector $\boldsymbol{\rho}$. Consider a so-called generating function $\psi : \mathbb{R} \to \mathbb{R}$ nonnegative, nondecreasing, and convex that satisfies the conditions $\psi(x) > \psi(0)\, \forall x > 0$ and $\psi(0) = 1$. Given a positive scalar $z > 0$, we have that the following bound holds for all $z > 0$ and $\mathbf{x}$ [Nemirovski and Shapiro, 2007]:

$$\Pr\{h(\mathbf{x}; \boldsymbol{\rho}) > 0\} \leq \mathbb{E}_{\boldsymbol{\rho}}\{\psi(z^{-1} h(\mathbf{x}, \boldsymbol{\rho}))\}. \tag{7.12}$$

As a consequence, the inequality

$$\inf_{z>0} \{z \mathbb{E}_{\boldsymbol{\rho}}\{\psi(z^{-1} h(\mathbf{x}, \boldsymbol{\rho}))\} - z\epsilon\} \leq 0 \tag{7.13}$$

is a conservative approximation of the foremention chance constraint $\Pr\{h(\mathbf{x};\boldsymbol{\rho}) \leq 0\} \geq 1-\epsilon$. Finally, we choose the generating function as $\psi(x) = [1+x]_+$, where $[x]_+ := \max\{x, 0\}$, and rewrite the approximate constraint (7.13) as:

$$\inf_{z\in\mathbb{R}} \{\mathbb{E}_{\boldsymbol{\rho}}\{[h(\mathbf{x},\boldsymbol{\rho}) + z]_+\} - z\epsilon\} \leq 0, \tag{7.14}$$

where replacing $\inf_{z>0}$ with $\inf_{z\in\mathbb{R}}$ does not affect the final expression.

Each probabilistic constraint in (7.11) will be replaced by the approximation (7.14):

$$\mathbb{E}_{\boldsymbol{\rho}^m}\{[h_{i,n}(\mathbf{x};\boldsymbol{\rho}^m) + u^m_{i,n}]_+\} - u^m_{i,n}\epsilon \leq 0, \tag{7.15}$$

where $u^m_{i,n}$ are real and positive auxiliary optimization variables. Moreover, since the max operator $[.]_+$ is not differentiable, we replace it with a smooth approximation and define:

$$g_{i,n}(\mathbf{x}, u_{i,n}; \boldsymbol{\rho}^m) = \frac{1}{2}\left(h_{i,n}(\mathbf{x}) + u_{i,n} + \sqrt{\xi^2 + (h_{i,n}(\mathbf{x}) + u_{i,n})^2}\right) - u_{i,n}\epsilon \quad \forall i \in \{1,..,4\}, n \in \mathcal{N}, m \in \{1,..,b\} \tag{7.16}$$

with ξ small and non-zero. Differentiability of the functions g_i will be required later where we will convexify problem (7.17) introduced below. The expected values in (7.15) can be estimated empirically via sample averaging for a sufficiently large number of samples N_s, leading to a new formulation of the optimization problem:

$$\min_{\mathbf{x}, u^m_{i,n}} \quad \sum_{m=1}^{b} \frac{1}{N_s}\sum_{s=1}^{N_s} h_0(\mathbf{x};\boldsymbol{\rho}^m[s]) \tag{7.17a}$$

$$\text{s.t.} \quad \frac{1}{N_s}\sum_{s=1}^{N_s} g_{i,n}(\mathbf{x}, u^m_{i,n}; \boldsymbol{\rho}^m[s]) \leq 0 \quad \forall i \in \{1,..,4\}, n \in \mathcal{N},\ m \in \{1,..,b\} \tag{7.17b}$$

$$h_i(\mathbf{x}) \leq 0 \quad \forall i \in \{5,..,8\} \tag{7.17c}$$

where we will draw N_s samples $\boldsymbol{\rho}^m[s]_{s=1}^{N_s}$ of the random vector $\boldsymbol{\rho}^m$. Problem (7.17) constitutes a conservative approximation of the initial chance constrained problem (7.11), meaning that an optimal solution to (7.17) is a feasible suboptimal solution to (7.11).

Remark 7.4 (*Conservative approximation*)**.** *Our constraints have been rewritten in a form that is in line with the concept of conditional value at risk (CVaR). A slightly different approach would have been to reformulate the chance-constrained problem* (7.17) *into a convex approximation without demanding it to be conservative, as in e. g., Wei et al. [2023]. Recall that for a random variable x, we have that*

$$\mathbb{E}[\mathbf{1}_{[0,+\infty]}(x)] = \Pr\{x \geq 0\}, \tag{7.18}$$

where $\mathbf{1}_A$ *denotes the indicator function of a set* A*, i. e.,* $\mathbf{1}_A(x) = 1$ *if* $x \in A$ *and* $\mathbf{1}_A(x) = 0$ *otherwise. In order to construct a conservative approximation we introduce the auxiliary variable* $z > 0$ *and the generating function* $\psi(x)$ *for which we can derive the following upper bound:*

$$\mathbb{E}[\psi(zx)] \geq \mathbb{E}[\mathbf{1}_{[0,+\infty]}(zx)] = \Pr\{x \geq 0\}, \tag{7.19}$$

which is the same as (7.12) *when changing* z *to* z^{-1}*.* □

At first one might try to solve problem (7.17) with any software package for nonlinear optimization. However, it is not straightforward to implement the inverse matrix contained in $\mathbf{q}(\mathbf{x})$ in a computationally efficient way. Therefore, we seek a different strategy that may be computationally more affordable. In particular, we will leverage the algorithm proposed in Scutari et al. [2014] which follows the ideas of Successive Convex Approximation (SCA) methods. More specifically, the method solves a sequence of strongly convex inner approximation of an initial non-convex problem. In particular, each intermediate problem is strongly convex and can be written as:

$$\begin{aligned} \min_{\mathbf{x}, u_{i,n}^m} \quad & \sum_{m=1}^{b} \frac{1}{N_s} \sum_{s=1}^{N_s} \tilde{h}_0(\mathbf{x}; \boldsymbol{\rho}^m[s], \mathbf{x}_p) \\ \text{s.t.} \quad & \frac{1}{N_s} \sum_{s=1}^{N_s} \tilde{g}_{i,n}(\mathbf{x}, u_{i,n}^m; \boldsymbol{\rho}^m[s], \mathbf{x}_p) \leq 0 \quad \forall i \in \{1,..,4\}, n \in \mathcal{N},\ m \in \{1,..,b\} \\ & h_i(\mathbf{x}) \leq 0 \quad \forall i \in \{5,..,8\} \end{aligned} \tag{7.20}$$

where $\tilde{g}_{i,n}(\mathbf{x}, u_{i,n}^m; \boldsymbol{\rho}^m[s], \mathbf{x}_p)$ approximates $g_{i,n}(\mathbf{x}, u_{i,n}^m; \boldsymbol{\rho}^m[s])$ around $\mathbf{x} = \mathbf{x}_p$. For given samples $\boldsymbol{\rho}^m[s]$, the problem (7.20) is solved for successive values of $\mathbf{x}_p$ until convergence. The surrogate functions in (7.20) are defined as:

$$\tilde{h}_0(\mathbf{x}; \boldsymbol{\rho}^m[s], \mathbf{x}_p) = \|\mathbf{q}(\mathbf{x}_p) + (\mathbf{x} - \mathbf{x}_p)^\top \nabla \mathbf{q}(\mathbf{x}_p)\|^2 + \frac{d}{2}\|\mathbf{x} - \mathbf{x}_p\|^2 \tag{7.21}$$

and

$$\begin{aligned} &\tilde{g}_{i,n}(\mathbf{x}, u_{i,n}^m; \boldsymbol{\rho}^m[s], \mathbf{x}_p) = \\ &\frac{1}{2}\left(\tilde{h}_{i,n}(\mathbf{x}) + u_{i,n}^m + \sqrt{\xi^2 + (\tilde{h}_{i,n}(\mathbf{x}) + u_{i,n}^m)^2}\right) - u_{i,n}^m \epsilon \quad \forall i \in \{1,..,4\}, n \in \mathcal{N}, m \in \{1,..,b\} \end{aligned} \tag{7.22}$$

with

$$\begin{aligned} \tilde{h}_{i,n}(\mathbf{x}; \boldsymbol{\rho}^m[s], \mathbf{x}_p) =& h_{i,n}(\mathbf{x}_p) + (\mathbf{x} - \mathbf{x}_p)^\top \nabla h_{i,n}(\mathbf{x}_p) + (\mathbf{x} - \mathbf{x}_p)^\top M_{i,n}(\mathbf{x} - \mathbf{x}_p) \\ & \forall i \in \{1,..,4\}, n \in \mathcal{N}, m \in \{1,..,b\} \end{aligned} \tag{7.23}$$

where $M_{i,n} \in \mathbb{R}^{2\times 2}$ is derived to ensure that $\tilde{h}_{i,n}(\mathbf{x}; \boldsymbol{\rho}^m[s], \mathbf{x}_p)$ is a global majorizer of $h_{i,n}(\mathbf{x}_p; \boldsymbol{\rho})$ (see Appendix A.2.1). To lighten the notation, we omit the $\boldsymbol{\rho}^m$ dependence on

the right-hand side of equations (7.21–7.23) but recall that $\mathbf{q}(\mathbf{x};\boldsymbol{\rho}) = \left[X + \mathbf{1}^\top \mathbf{x} \mathbb{I}\right]^{-1}(\mathbf{1} - \boldsymbol{\rho})$ with $\boldsymbol{\rho} = H(\mathbf{0}, \mathbf{z})$, and the functions $h_{i,n}(\mathbf{x};\boldsymbol{\rho})$ are defined in equation (7.10). The surrogate functions $\tilde{h}_0$, $\tilde{g}_i$ and $\tilde{h}_i$ defined in equations (7.21–7.23) satisfy the assumptions listed in Scutari et al. [2014], and are therefore suitable for the SCA method.

Next we present our algorithm to solve (7.20). First, let us define the set $\mathcal{K}$ defined by equations (7.17c), i. e., the set defined by the convex constraints of problem (7.17). Let us also define the set $\mathcal{X}$ defined by equations (7.17c) and (7.17b), such that $\mathcal{X} \subset \mathcal{K}$. Then, Algorithm 7.1 is guaranteed to converge towards a stationary solution of problem (7.20) under the assumptions specified in Scutari et al. [2014] and presented in Appendix A.2.2.

Algorithm 7.1: *Optimal Gain Design (OGD) via SCA*

Initialization: $\gamma_p \in (0, 1]$, $\mathbf{x}_0 \in \mathcal{X}$. Set $p = 0$.
[1.] Compute the solution $\mathbf{x}^*(\mathbf{x}_p)$ of (7.20).
[2.] Set $\mathbf{x}_{p+1} = \mathbf{x}_p + \gamma_p(\mathbf{x}^*(\mathbf{x}_p) - \mathbf{x}_p)$
[3.] If $\|\mathbf{x}_{p+1} - \mathbf{x}_p\| < e$ with $e > 0$, then STOP.
[4.] $p \leftarrow p + 1$ and go to step 1.

Remark 7.5 (*Choice of the initial point*)**.** *Notice that the initial point $\mathbf{x}_0$ must belong to the set $\mathcal{X}$. In order to obtain a feasible $\mathbf{x}_0$, we first start with a small η and a large α (0.5 and 3.5, respectively). The equilibrium $\mathbf{q}^*$ for $\mathbf{x} = \mathbf{x}_0$ corresponds to small reactive injections/consumptions such that reactive powers are within the DERs' limits and the stability constraints are met. If the voltage constraints are met, then one can keep $\mathbf{x}_0$ and does not need to go to step 1 of Algorithm 7.1, since it corresponds to a solution with negligible reactive power usage. If the voltage constraints are not met, we slightly increase the value of η and decrease the value of α, then check the voltage constraints again. We repeat these steps until we find a feasible $\mathbf{x}_0$. If we cannot find a feasible $\mathbf{x}_0$, i. e., the set $\mathcal{X}$ is empty, one should modify the prescribed probability ϵ to allow for more voltage violations.* □

7.2.4 *Controller implementation*

We assume that each controller is equipped with sensing capabilities, i. e., it is capable of measuring the voltage magnitudes at the node where it is located. For any given DER $g \in \mathcal{G}$ connected to node $n \in \mathcal{N}$, the following incremental Volt/Var control is implemented:

$$q_{g,k+1} = \mathsf{proj}_{\mathcal{Q}_g}[q_{g,k} + \eta(1 - \tilde{\nu}_{n,k}) - (1 - \eta)\alpha q_{g,k}] \tag{7.24a}$$

$$p_{g,k+1} = \min\left(p_{g,k}, \sqrt{s_g^2 - q_{g,k+1}^2}\right), \tag{7.24b}$$

with s_g the nominal rated size of DER g. Equation (7.24a) represents the reactive power update of DER g connected at node n. The projection operation ensures that $q_{g,k}$ is

always in the feasible set $\mathcal{Q}_g$ of reactive powers for DER g. The approximated voltage $\hat{\nu}_{n,k}$ written in the initial controller formulation (7.4) has been replaced by the voltage measurement $\tilde{\nu}_{n,k}$, which makes this controller fully decentralized (we no longer rely on the matrix X, and the impact of other DERs' reactive power is implicitly taken into account through the network feedback). Equation (7.24b) indicates that we prioritize reactive power over active power. By prioritizing reactive power over active power, we further mitigate overvoltage issues as the active power injection is reduced and reactive compensation is used. However, this induces active power curtailment which is costly. We will investigate this issue in the next section, where we will present our numerical results. The good behavior of the controller with reactive power prioritization is verified throughout simulations.

Note that even if the stability analysis does not consider the projection operation of (7.24), our conclusions in terms of stability are unchanged as long as we consider a single-phase model. Note that the projection map can be decoupled on a per-node basis since $\mathcal{Q} = \mathcal{Q}_1 \times \ldots \times \mathcal{Q}_N$ with $\mathcal{Q}_i$ the set of admissible reactive powers for the ith inverter; thus, computed locally at each inverter. Assuming that we have enough reactive power to regulate voltages, at equilibrium we have that

$$\mathbf{q}^* = \mathsf{proj}_{\mathcal{Q}}[A(\eta,\alpha)\mathbf{q}^* + B(\eta,\rho)] \tag{7.25}$$

where $A(\eta,\alpha)$ and $B(\eta,\rho)$ were defined in (7.5). This means that $\mathbf{q}^*$ is a fixed point of the map $\mathbf{q} \mapsto \mathsf{proj}_{\mathcal{Q}}[A(\eta,\alpha)\mathbf{q}^* + B(\eta,\rho)]$. Then, we have that

$$\begin{aligned} \|\mathbf{q}_{k+1} - \mathbf{q}^*\| &= \|\mathsf{proj}_{\mathcal{Q}}[A\mathbf{q}_k + B] - \mathsf{proj}_{\mathcal{Q}}[A\mathbf{q}^* + B]\| \\ &\leq \|A\mathbf{q}_k + B - A\mathbf{q}^* - B\| \\ &= \|A\mathbf{q}_k - A\mathbf{q}^*\| \\ &\leq \|A\|\|\mathbf{q}_k - \mathbf{q}^*\| \end{aligned} \tag{7.26}$$

where we used the non-expansiveness property of the projection map in the first inequality, along with standard inequalities of the norms. We thus obtain:

$$\|\mathbf{q}_k - \mathbf{q}^*\| \leq \|A(\eta,\alpha)\|^k \|\mathbf{q}_0 - \mathbf{q}^*\|\,. \tag{7.27}$$

Therefore, the controller is stable if the induced ℓ_2 norm of the matrix $A(\eta,\alpha)$ satisfies the condition $\|A(\eta,\alpha)\| < 1$.

We recall that if A is symmetric, then $\|A\| = \sqrt{\lambda_{\max}(A^*A)} = \sqrt{\rho(A)^2} = \rho(A)$. Since X is positive definite and symmetric by construction [Farivar et al., 2013], it follows that $A(\eta,\alpha)$ is symmetric too. Therefore, we can conclude that if $\rho(A(\eta,\alpha)) < 1$, then the projected controller renders the equilibrium $\mathbf{q}^*$ globally asymptotically stable. This condition is verified if (7.7) holds.

Figure 7.4 illustrates the different stages of the framework proposed in this work. We compute the gains η and α for a given time interval $T\tau$ by solving the problem (7.20) until convergence based on forecasts of $\mathbf{z}_k$. The samples $\boldsymbol{\rho}^m[s]$ are generated by solving

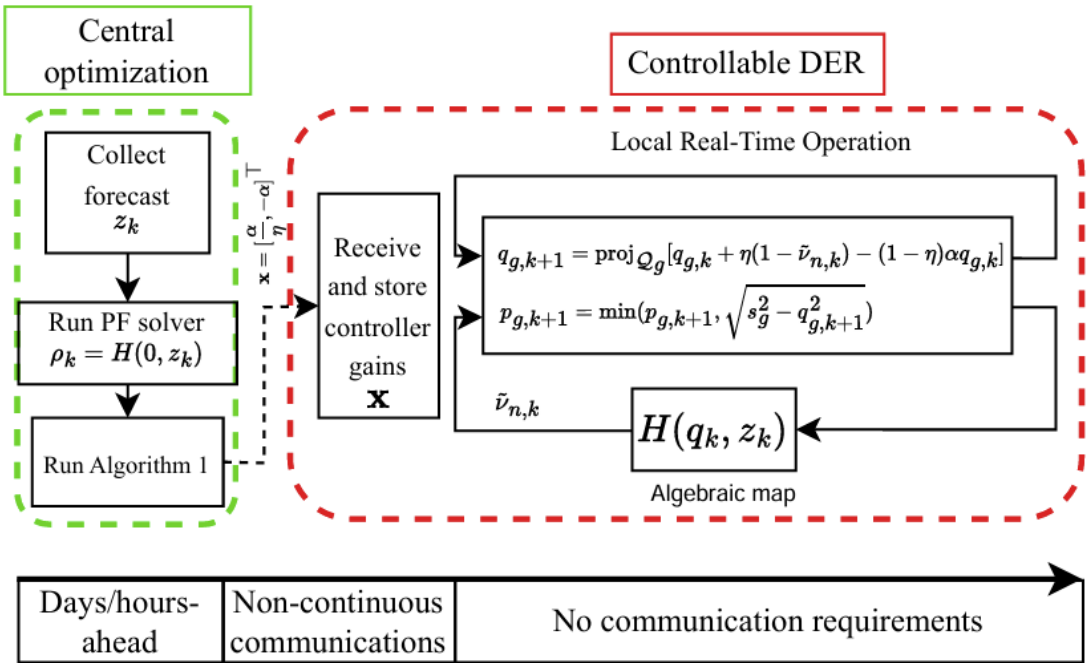

Figure 7.4: Block diagram of the proposed framework.

multiple power flows for different values of $\mathbf{z}_k = \bar{\mathbf{z}}_k + \boldsymbol{\delta}_k$, where $\boldsymbol{\delta}_k$ follows a given probability distribution function. In practice those forecasts can be obtained from typical load and production profiles for different times of the day. The gains can be computed the day before deployment or hours in advance depending on the availability of the forecast and the computational time required to solve (7.20) until convergence. They are then broadcasted to the controllable DERs. Notice that we do not need to differentiate between DERs as the gains are the same for any DER connected to the network.

In the following, we address the previously introduced assumptions. First, our current framework enforces one and only one DER per node. This requirement is rather restrictive, even though it has already been adopted in the literature, e. g., Li et al. [2014]. We can easily relax this assumption by considering only the entries in the matrix X that correspond to the nodes where a controllable DER is located. The drawback is that we can only guarantee voltage satisfaction for a subset $\mathcal{N}_{\text{red}} \subset \mathcal{N}$ of nodes. However, the effect of other controllable devices can be embedded in the map H. For instance, on-load tap changers (OLTC) or switched capacitor banks can drive the forecast voltage profiles $\boldsymbol{\rho} = H(\mathbf{0}, \mathbf{z})$ inside the admissible voltages. Our methodology can be combined with other traditional regulation methods, and an optimal combination of slow acting controllers, such as OLTC, with our fast acting controllers can be envisioned. Furthermore, if multiple DERs are connected to the same node, one can aggregate the DERs and model them as one single device associated with one controller. The reactive power setpoint produced by controller (7.4) is then appropriately dispatched to the different DERs.

Second, in the present setup the network topology does not change with time. However, in our current framework, topological changes that can be forecast (because of maintenance or planned operation) can easily be integrated. Indeed, those changes impact the matrix X. By appropriately choosing the time interval $T\tau$ and recomputing X, one can derive gains that would be well adapted to this new network topology. This assumption is much harder to relax for learning-based methods since it requires building new datasets, and learning new equilibrium functions, which can be time-consuming. When it comes to unplanned changes, e. g., sudden line tripping or unplanned operations, our controllers take into account the network conditions as feedback, and do not worsen the situation. Nevertheless, evaluation of the robustness with respect to unplanned changes remains to be investigated.

Finally, Assumption 7.1 tackles the feasibility issue of the optimal reactive power flow problem. It may happen that, under our controller architecture, there is not enough reactive power reserve to satisfy the voltage constraints. This problem is implicitly addressed through our chance-constrained formulation. Indeed, increasing the value of ϵ enlarges the feasible set. For $\epsilon = 1$, the problem (7.20) is always feasible.

7.2.5 *Experimental results*

7.2.5.1 *Simulation setup*

We consider the low voltage network (0.4 kV) shown in Figure 7.5a. We used a modified network from Sarajlic and Rehtanz [2019], in which photovoltaic power (PV) plants have been placed at each node, with inverter-rated size picked randomly among $\{20, 25, 31\}$ kVA. The DERs dynamics are not implemented, as they are considered to be much faster than the controller dynamics [Eggli et al., 2020]. As such, when the controller update law produces a new reactive power setpoint, it is instantaneously implemented by the controllable DER. In this thesis, we only consider PV plants as DERs, but any type of inverter-interfaced generation for which the reactive power can be controlled could be considered. Figure 7.5b shows the aggregated loads and maximum available active power for PV plants throughout the day. The data is from the Open Power System Data, and have been modified to match the initial loads and PV plants nominal values present in the network. The reactive power demand is set such that the power factor is 0.95 (leading). This represents a typical summer day, with high PV production. We will show that, under these conditions, the electrical distribution network undergoes both overvoltages and undervoltages.

In the following, we assume the controllable DERs to be equipped with an overvoltage protection for PV plants inspired by the CENELEC EN50549-2 standard EN50549-2 [2019] that we already discussed in Section 6.2.4.

In the simulation, the voltage service limits are set to 1.05 and 0.95 p.u., respectively. The load and PV production profiles have a granularity of 1 second, i. e., active/reactive

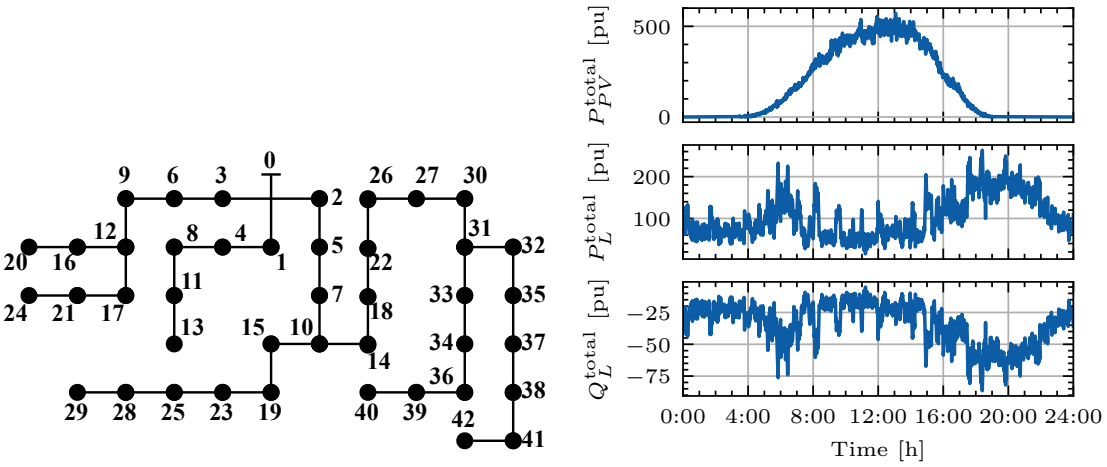

(a) (b)

Figure 7.5: (a) Low-voltage 42-node network. (b) Aggregated non-controllable active power injections, and active/reactive power consumption.

power consumption and maximum available active power for PV plants change every 1 second. The time horizon $T\tau$ is set to 1 hour, and the forecast update $\Delta\tau$ to 30 minutes. The reactive power setpoints update τ is set to 100 ms. We compare our proposed controller, based on Algorithm 7.1 (OGD-CCO), with: (a) a static Volt/Var control (VoltVar); and, (b) no control (ON/OFF).

Static Volt/Var control: It is inspired by the standard *IEEE Std 1547-2018* that is illustrated in Figure 6.4b, with maximum reactive power consumed/absorbed set to 44% of the nominal power of the DER and reached for voltages 1.05/0.95 pu, respectively. The deadband ranges between 0.99 and 1.01 pu. Active power prioritization is implemented. Therefore, the maximum reactive power that can be produced or consumed corresponds to the minimum between 44% of the nominal apparent power s_g and the reactive power reserve of the inverter $\sqrt{s_g^2 - p_g^2}$, with p_g the active power injection of DER g.

No control: Set controller gains $\eta = \alpha = 0$, and reactive powers to 0.

7.2.5.2 *Results*

In Figure 7.6, we illustrate the dynamics of the controllers associated with DER connected to two different nodes and the corresponding voltage magnitudes.

We compare the voltage magnitudes resulting from the deployment of different controllers against the case without controllers and without overvoltage protection. We fixed $T\tau$ to 1 hour, i. e., the controller gains change every hour. It is clear that the VoltVar control overuses reactive power, as there is no need to control the voltages between hours 16:00 – 17:00, or after 22:00. The ON/OFF strategy sees large fluctuations in voltages due to constant connection and disconnection of DERs.

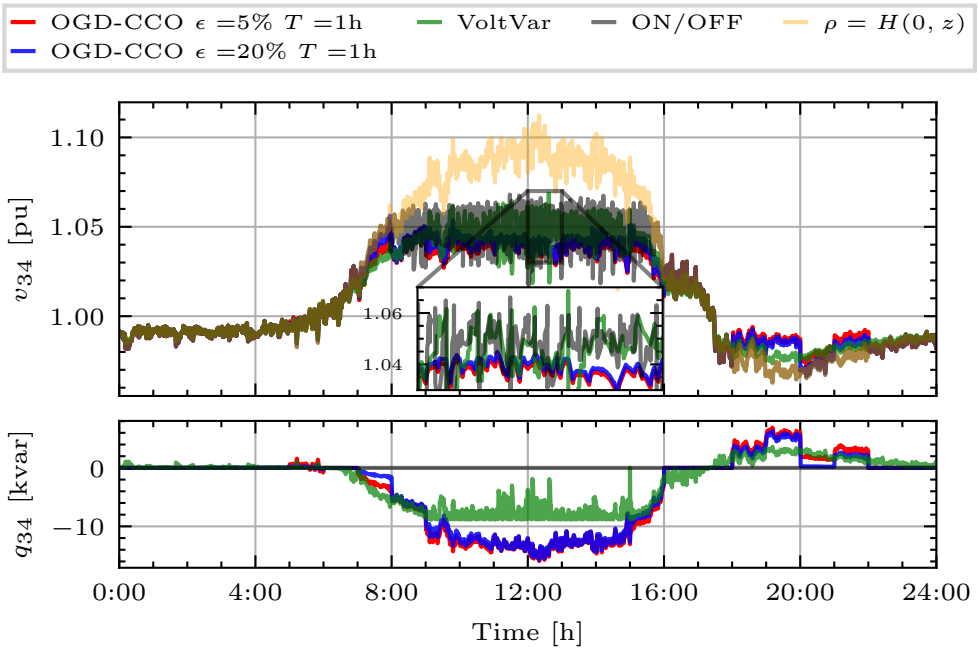

(a)

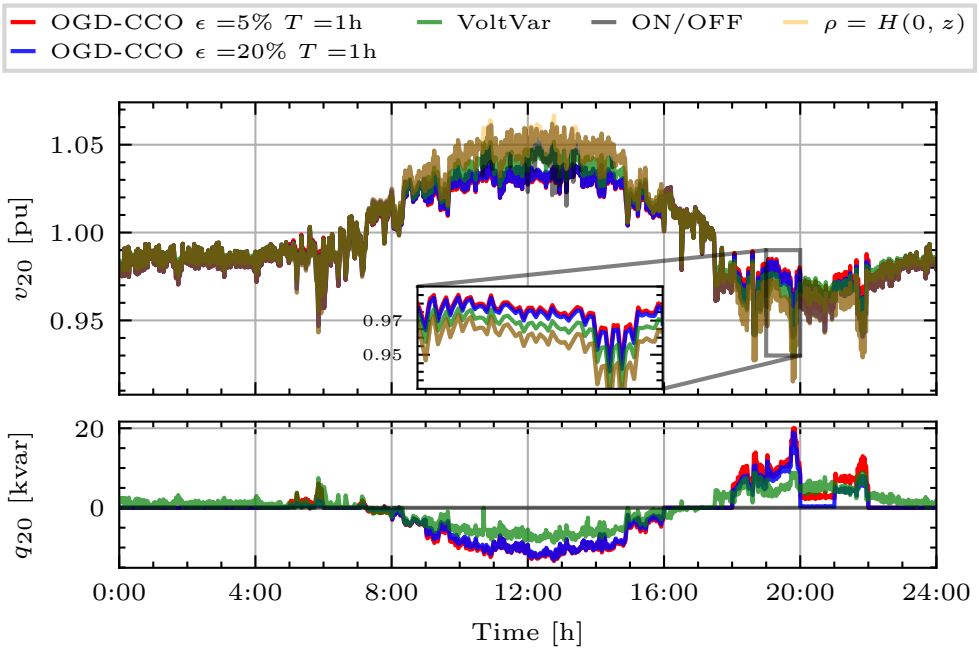

(b)

Figure 7.6: DER reactive power (q) and measurement of voltage magnitudes (v) for two given nodes: (a) node 34 and (b) node 20.

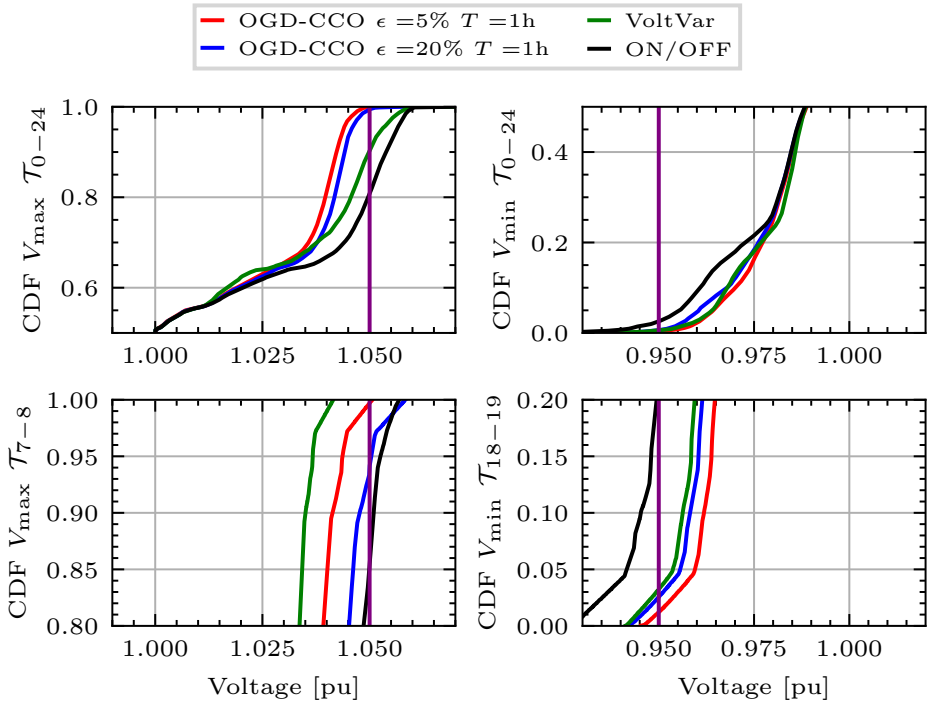

(a)

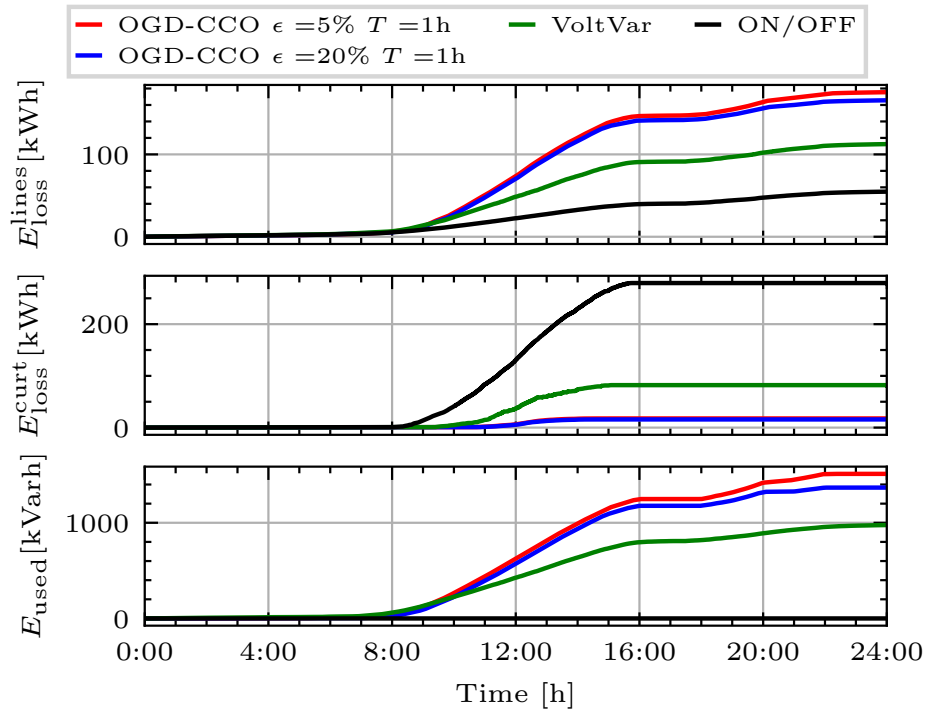

(b)

Figure 7.7: (a) Cumulative distribution function for the vectors $\mathbf{V}_{\max}$, and $\mathbf{V}_{\min}$. (b) Energy lost in the lines and because of curtailment, and reactive energy usage.

The cumulative distribution functions (CDF) for maximum and minimum voltages during the simulation are shown in Figure 7.7a. At each time t between hours h_1 and h_2, we pick the maximum and minimum voltages throughout the network and store them into two distinct vectors. We then plot the cumulative distribution functions of those vectors. We define the vectors $\mathbf{V}_{\max} = \{\max \tilde{\nu}_{i,k}\}_{i\in\mathcal{N},k\in\mathcal{T}}$ and $\mathbf{V}_{\min} = \{\min \tilde{\nu}_{i,k}\}_{i\in\mathcal{N},k\in\mathcal{T}}$, where $\mathcal{T}_{h0-h1}$ is the set of time indices between hour $h0$ and hour $h1$. For $\mathcal{T}_{0-24}$, i. e., for the entire duration of the simulation, our proposed method crosses the 1.05 p.u. line above 95% for the maximum voltage, and lower than 5% for the undervoltage. This means that the voltage constraints are satisfied at least 95% of the time, which is consistent with our choice of $\epsilon = 0.05$ and $\epsilon = 0.2$. We also show the CDF during two other intervals, between hours 7:00 – 8:00 for overvoltages and 18:00 – 19:00 for undervoltages. Notice that a larger ϵ allows for more voltage constraint violations. The VoltVar control sees overvoltages more than 10% of the time while performing similarly to our method for undervoltages. The ON/OFF strategy sees overvoltages more than 20% of the time.

Figure 7.7b displays, from top to bottom, the energy lost in the lines, the energy lost because of active power curtailment, and the cumulative reactive energy usage for the different strategies considered in this work. The line losses are computed based on the line currents squared times the line resistances. Although the usage of reactive power is *practically free*, it induces larger line currents, hence larger power losses. We make a distinction between losses caused by active power curtailment and line losses since the former are covered by the network user while the latter are covered by the system operator. However, the system operator can in turn increase network tariffs to compensate for line losses due to overuse of reactive power compensation.

Our controller applies reactive power prioritization, which naturally induces active power curtailment if the DER injects a large amount of active power into the network. On the other hand, the VoltVar and ON/OFF strategies may experience active power curtailment because of prolonged overvoltage violations. Taking all these competing factor into consideration, the total energy loss is much more important for the ON/OFF strategy, while it is equivalent for our controller and the VoltVar control.

These results emphasize the advantages of having gains that are updated to take into account forecast changes in the network conditions. For instance, based on the forecasts, one can observe in Figure 7.6 that the voltages are close to the nominal voltage early in the morning. When computing the gains for that time period, one obtains gains such that the reactive power compensation is almost deactivated as there are no voltage violations forecasted. On the other hand, the constant gains of static VoltVar curves are set such that reactive power compensation is provided as soon as the voltage magnitudes deviate and leave the controller deadband, leading to an overusage of reactive power. One can also see that the parameter ϵ acts as a lever on the total usage of reactive power. If the reactive power is very expensive, and voltage violations are not extremely important, one could increase the value of ϵ to reduce the total usage of reactive energy.

In Figure 7.8, we show the maximum duration of voltage violations. The vector $\Gamma_{\mathcal{V}}$ is built such that, if an overvoltage or undervoltage occurs in the network at a given time step $k\tau$, we count and add up every voltage violations for the subsequent time steps. When, at a subsequent time step, no voltage violation occurs, the total number of voltage violation is appended to the vector, and the counter is reset to 0. The vector $\Gamma_{\mathcal{V}}$ indicates the duration of voltage violations. This is an important number, since usually electrical devices can cope with short and limited over or under voltages, but may be damaged during prolonged, large excursions from nominal voltages. The parameter ϵ sets the maximum time the voltage can exceed the voltage limits. Figure 7.8 shows that a smaller ϵ leads to shorter voltage violations, while both ON/OFF and VoltVar strategies lead to substantially longer voltage violations.

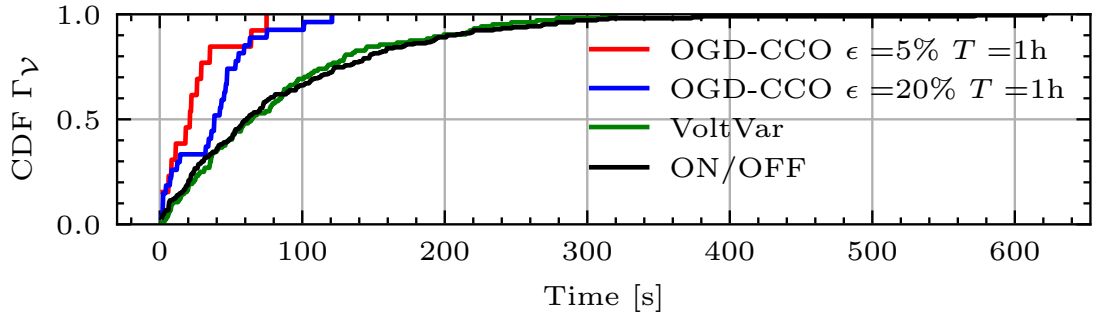

Figure 7.8: Cumulative distribution function for voltage violations.

7.3 A ROBUST FORMULATION

In this section, we consider a robust formulation of our chance-constrained optimization problem. The overall idea is to consider the worst-case scenario such that, for given controller gains, the voltage and reactive power constraints are always satisfied for any $\boldsymbol{\rho}_k$ with $k \in \mathcal{T}_{h1-h2}$. In particular, we consider solving the problem:

$$\max_{\boldsymbol{\rho}_k, k \in \mathcal{T}_{h1-h2}} \left(\min_{\mathbf{q} \in \mathcal{C}(\boldsymbol{\rho}_k)} \|\mathbf{q}\|^2 \right), \tag{7.28}$$

with $\mathcal{C}(\boldsymbol{\rho}_k) := \{\mathbf{q} : \mathbf{q} \in \mathcal{Q}, \underline{V} \leq X\mathbf{q} + \boldsymbol{\rho}_k \leq \bar{V}\}$. Let $\boldsymbol{\rho}^*_{h1-h2}$ denote an optimal solution to (7.28). The proposed heuristic (7.28) gives the $\boldsymbol{\rho}^*_{h1-h2}$ that leads to the largest objective value $\|\mathbf{q}\|^2$. We claim that if $\mathbf{q} \in \mathcal{C}(\boldsymbol{\rho}^*_{h1-h2})$, then $\mathbf{q} \in \mathcal{C}(\boldsymbol{\rho}_k)$ $\forall k \in \mathcal{T}_{h1-h2}$.

The validity of our heuristic (7.28) is illustrated using a simple example. Consider a two-node network; the voltage magnitude of node 1 is set to 1 pu, and node 1 is connected to node 2 through a line of inductance 1 pu. The linearized power flow equation gives $\hat{\nu} = q + \rho$, where the quantities are defined for node 2. We consider three different values of ρ, for different $k \in \{1, 2, 3\}$; $\rho_1 = 1.04, \rho_2 = 1.06, \rho_3 = 0.93$ and infinite

reactive power reserve. Solving the ORPF problem $\min_{q\in\mathcal{C}(\rho_k)} q^2$ for $k \in \{1,2,3\}$, one gets: $q_1 = 0, q_2 = -0.01, q_3 = 0.02$. Following (7.28), we have $\rho^* = \rho_3 = 0.93$. The equilibrium function of our controller is:

$$q^* = \frac{1}{\eta + (1-\eta)\alpha}\eta(1-\rho). \tag{7.29}$$

Replacing ρ by ρ^*, fixing $\eta = 0.8$, and knowing that $q^* = q_3 = 0.02$ minimizes the reactive power usage and satisfies the voltage constraints, we have $\alpha = 10$. The expression (7.29), with the fixed controller gains, becomes $q^* = 0.2857(1-\rho)$. Then, we can plug ρ_2 in (7.29) with the fixed controller gains, and we have $q^* = -0.017$, and $\hat{\nu}^* = 1.043 \leq 1.05$. The voltage constraint is also verified for ρ_1, and shows that the constraint is satisfied for all ρ_k with $k \in \{1,2,3\}$ by picking $\rho^* = \rho_3$ according to (7.28) to design the controller gains.

Now let us consider some reactive power constraints with $q_{\min} = -0.015$ and $q_{\max} = 0.03$. Nothing changes; $\rho^* = \rho_3$ and the equilibrium function for ρ_2 gives $q^* = -0.017$. Notice that $q^* \leq q_{\min}$: the reactive power constraint is not satisfied. However, in the real implementation of our controller, the DER will inject $q = -0.015$, which ensures $\hat{\nu} = 1.045 \leq 1.05$. In the case where $q_{\min} > -0.01$, then the initial ORPF for ρ_2 is not feasible, since $q_2 \leq -0.01$ is required to meet the voltage constraint. We make the following remark about the feasibility of the ORPF problem:

Remark 7.1 (*Feasibility of the robust formulation*)**.** *When solving problem (7.28), one first needs to make sure that the set $\mathcal{C}(\boldsymbol{\rho}_k)$ is not empty for some values of k. In that case, one can either consider (i) a larger set $\mathcal{V} := \{\hat{\nu} : \underline{V} \leq \hat{\nu} \leq \bar{V}\}$, or (ii) pick $\boldsymbol{\rho}^*_{h1-h2}$ following equation (7.28) for all $k \in \{k : k \in \mathcal{T}_{h1-h2}, \mathcal{C}(\boldsymbol{\rho}_k) \neq \emptyset\}$. This guarantees feasibility of the ORPF problem for a given $\boldsymbol{\rho}^*_{h1-h2}$, however, notice that in the case (ii) the worst-case scenario might be excluded and one cannot guarantee that they will be no voltage violations between hours $h1$ and $h2$. Notice that, given our controller architecture, the feasible set of (7.9) may still be empty even after applying (i) or (ii). In such cases, one should pick a different value of $\boldsymbol{\rho}^*_{h1-h2}$ to ensure that the set $\mathcal{X}$, that also considers the constraints related to our controller architecture, is not empty.*

In Figure 7.9a, we show the cumulative distribution functions (CDF) for maximum and minimum voltages for the entire duration of the simulation. Our method slightly exceeds the voltage limits because of some transients, while the VoltVar and the ON/OFF strategies withstand more important voltage violations, though limited by the overvoltage protection.

In Figure 7.9b, we show the total energy lost and the reactive energy usage. VoltVar and our method are equivalent in terms of active power losses, in particular VoltVar suffers from larger curtailment while our method induces larger losses in the lines since it uses more reactive power compensation due to reactive power prioritization. Our method uses more reactive power, but keeps the voltages within fixed limits. If the cost of reactive power usage exceeds the cost of violating voltage constraints, one could either change the voltage limits, or pick a different $\boldsymbol{\rho}^*_{h1-h2}$ to reduce the total reactive energy usage.

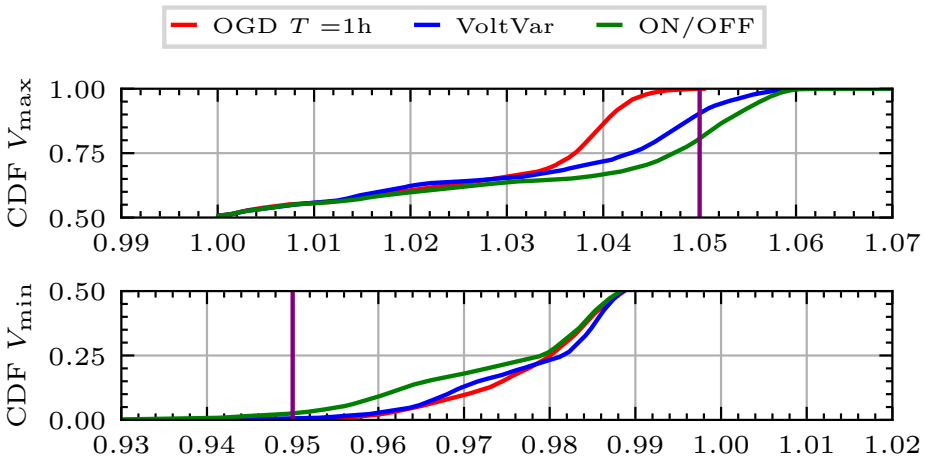

(a)

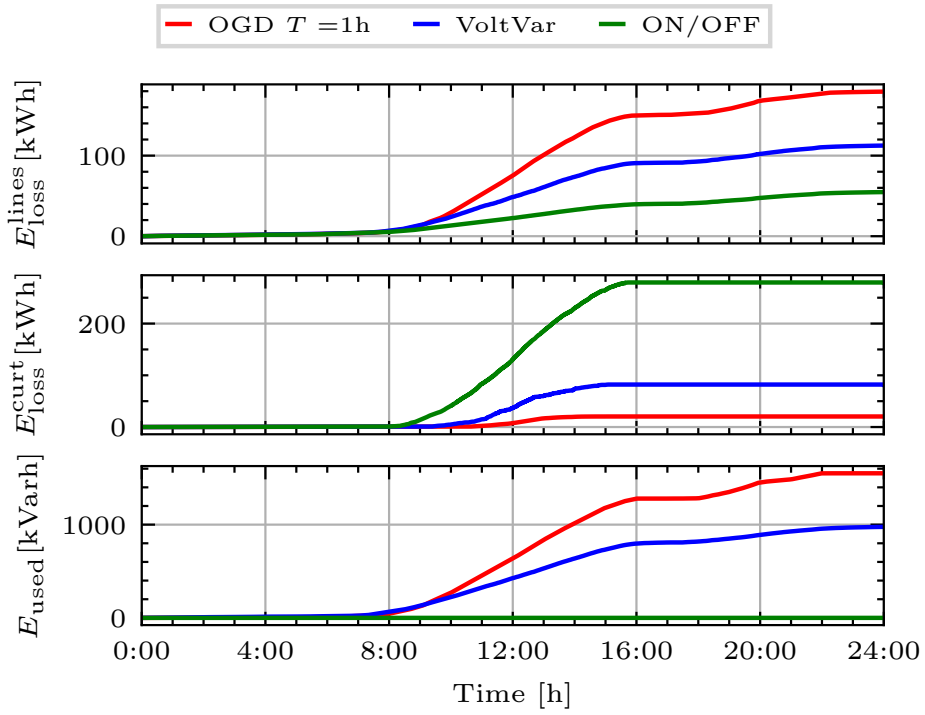

(b)

Figure 7.9: (a) Cumulative distribution function for the vectors $\mathbf{V}_{\max}$, and $\mathbf{V}_{\min}$. (b) Energy lost in the lines and because of curtailment, and reactive energy usage.

7.4 EXTENSION TO A THREE-PHASE UNBALANCED DISTRIBUTION SYSTEM

In this section, we show how our algorithm can be naturally applied to a three-phase unbalanced distribution network and present some simulation results. For this purpose, we consider the IEEE 123-node test system [IEEE, 1992].

First, we characterize the stability of our control algorithm applied to multi-phase distribution networks. We use the approximation proposed in Kekatos et al. [2015], where $\hat{\boldsymbol{\nu}}_k = X\mathbf{q}_k + \boldsymbol{\rho}_k$, with $\hat{\boldsymbol{\nu}}_k := [(\hat{\nu}^{\phi}_{1,k})^2, ..., (\hat{\nu}^{\phi}_{N,k})^2]^\top \in \mathbb{R}^{3N}$, $X \in \mathbb{R}^{3N\times 3N}$, $\mathbf{q}_k := [q^{\phi}_{1,k}, ..., q^{\phi}_{N,k}]^\top \in \mathbb{R}^{3N}$, $\boldsymbol{\rho}_k := [(\rho^{\phi}_{1,k})^2, ..., (\rho^{\phi}_{N,k})^2]^\top \in \mathbb{R}^{3N}$, where we use the superscript ϕ to denote $(\hat{\nu}^{\phi}_{n,k})^2 := [(\hat{\nu}^{a}_{n,k})^2, (\hat{\nu}^{b}_{n,k})^2, (\hat{\nu}^{c}_{n,k})^2]$. We follow the approach of Kekatos et al. [2015] for the derivation of the matrix X, which is based on the branch flow model and the phase impedance matrices for the lines. Notice that, since it is based on the branch flow model, the approximation considers the squared voltage magnitudes; however, this does not affect our method as the linear approximation (and, thus, the matrix X) is used only to design the controller gains and one can simply modify the voltage limits $\bar{V}, \underline{V}$ in our optimization-based approach to consider squared voltages. For this case-study, we assume that DERs are wye-connected, and their reactive powers on each phase can be independently controlled. For the multi-phase case and for a DER $g \in \mathcal{G}$ connected to a node $n \in \mathcal{N}$, the implementation of the controller derived in equations (7.24) becomes:

$$q^{\phi}_{g,k+1} = \mathsf{proj}_{\mathcal{Q}^{\phi}_g}[q^{\phi}_{g,k} + \eta(1 - \tilde{\nu}^{\phi}_{n,k}) - (1-\eta)\alpha q^{\phi}_{g,k}] \tag{7.30a}$$

$$p^{\phi}_{g,k+1} = \min\left(p^{\phi}_{g,k}, \sqrt{(s^{\phi}_g)^2 - (q^{\phi}_{g,k+1})^2}\right), \tag{7.30b}$$

where $\phi \in \{a, b, c\}$, and where reactive power limits $\mathcal{Q}^{\phi}_g$ and rated powers s^{ϕ}_g are defined on a per-phase basis. In particular, we consider that our controllable DERs are balanced, share the same rated power s^{ϕ}_g among each phase and thus have the same reactive power limits $\mathcal{Q}^{\phi}_g$ for each $\phi \in \{a, b, c\}$. Each phase of each DER is regulated independently. Notice that in our simulations, the system is unbalanced because the uncontrollable power injections are not equal among each phase.

The matrix X of our linear approximation of the three-phase IEEE 123-node test system is positive-definite, which ensures the existence and the uniqueness of the equilibrium. However, it is not symmetric, and, thus, the stability analysis of the projected controller performed in Section 7.2.4 no longer holds since $\rho(A(\eta,\alpha)) \leq \|A(\eta,\alpha)\|$. We derive some conditions that highlight the role of X; to this end, consider the following inequality:

$$\begin{aligned}\|A(\eta,\alpha)\| &= \|(1-(1-\eta)\alpha)\mathbb{I} - \eta X\| \\ &\leq \|(1-(1-\eta)\alpha)\mathbb{I}\| + \|\eta X\| \\ &\leq |1-(1-\eta)\alpha| + \eta\|X\|\,.\end{aligned} \tag{7.31}$$

Thus, a sufficient condition for the controller to be stable in the multi-phase setup is:

$$|1-(1-\eta)\alpha| + \eta\|X\| < 1 \tag{7.32}$$

which can be written

$$0 < (1-\eta)\alpha - \eta\|X\| < 2 - 2\eta\|X\|\,. \tag{7.33}$$

It yields to the following two constraints when we divide both sides by η, and introduce the variable $\mathbf{x}$:

$$0 < \mathbf{1}^\top \mathbf{x} - \|X\| \tag{7.34a}$$

$$(\mathbf{1}^\top \mathbf{x} - 2) + \|X\| \leq 0\,. \tag{7.34b}$$

Notice that, as in the single-phase equivalent, we replace $2/\eta$ with 2 such that we obtain a tighter bound on the second constraint as $\eta \in [0, 1]$. Although the stability constraints slightly differ from the one presented for the single-phase equivalent, they remain linear with respect to $\mathbf{x}$.

The results obtained on the IEEE 123-node test system are presented next. The simulation setup is the same as the one presented in 7.2.5. The DERs are PV inverters. At each node, a three-phase wye-connected PV inverter is installed, and its rated size is picked randomly among four different inverter sizes $\{60, 120, 160, 200\}$ kVA. The aggregated non-controllable power injections are shown in Figure 7.10a, where one can observe that the system is unbalanced. The DERs dynamics are not implemented, as they are considered to be much faster than the controller dynamics.

Notice that in this multi-phase setup, the static Volt/Var control is unstable and leads to an oscillatory behavior that can be observed in Figure 7.10b. This unstable behaviour can be mitigated by adjusting the gains of the static Volt/Var control, but this will impact the voltage regulation capabilities. Therefore, we compare our method for two prescribed probabilities ϵ with the no control (ON/OFF) strategy.

The cumulative distribution functions (CDF) for maximum and minimum voltages during the simulation are shown in Fig. 7.11a. For the entire duration of the simulation, our method with both prescribed probabilities ($\epsilon = 5\%$ and $\epsilon = 20\%$) performs better than the no control strategy in terms of voltage regulation. Notice that the percentage of voltage violation is consistent with respect to the prescribed probabilities; the CDFs cross the purple line over 95% and over 90% for probabilities $\epsilon = 5\%$, $\epsilon = 20\%$, respectively.

Figure 7.11b shows the energy usage of the different methods. One can observe that, while our method uses more reactive energy, it leads to less active power curtailment because of limited voltage violations. One can also see that the total energy lost with the ON/OFF strategy (both coming from active power curtailment and lines losses) is more significant than the energy lost with our method. In particular, our method with a prescribed probability of $\epsilon = 5\%$ leads to almost no active power curtailment.

Finally, Figure 7.12 shows the maximum duration of voltage violations. When we tolerate less voltage violations (smaller prescribed probability ϵ), the voltage violations are shorter. Notice that in this metric, we consider that there is a voltage violation at time t if at least one voltage among all the nodal voltages for at least one phase is out

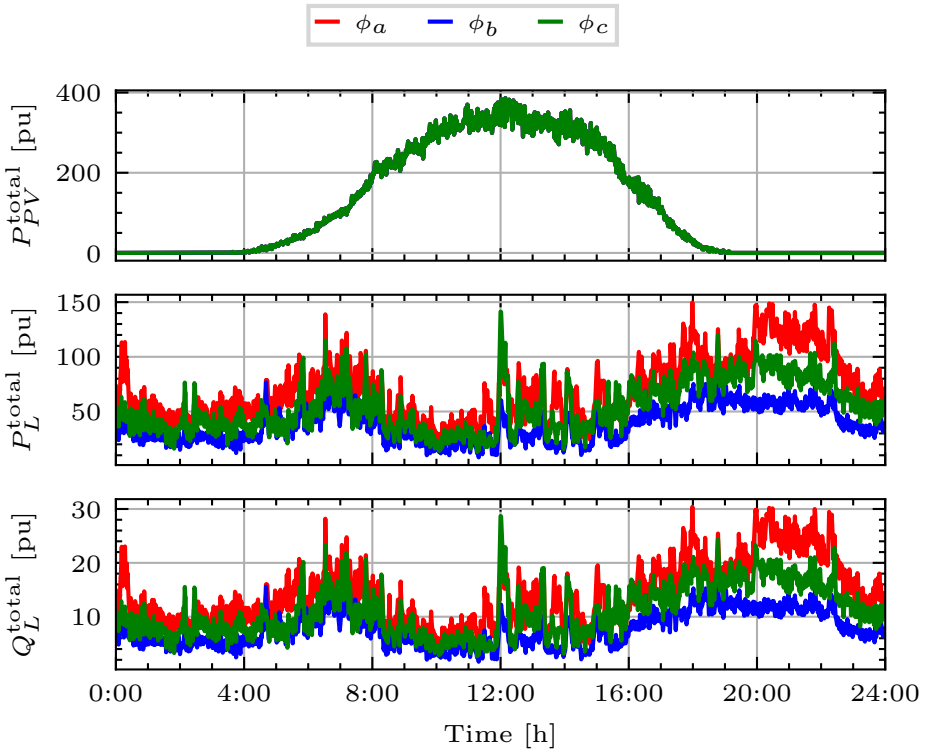

(a)

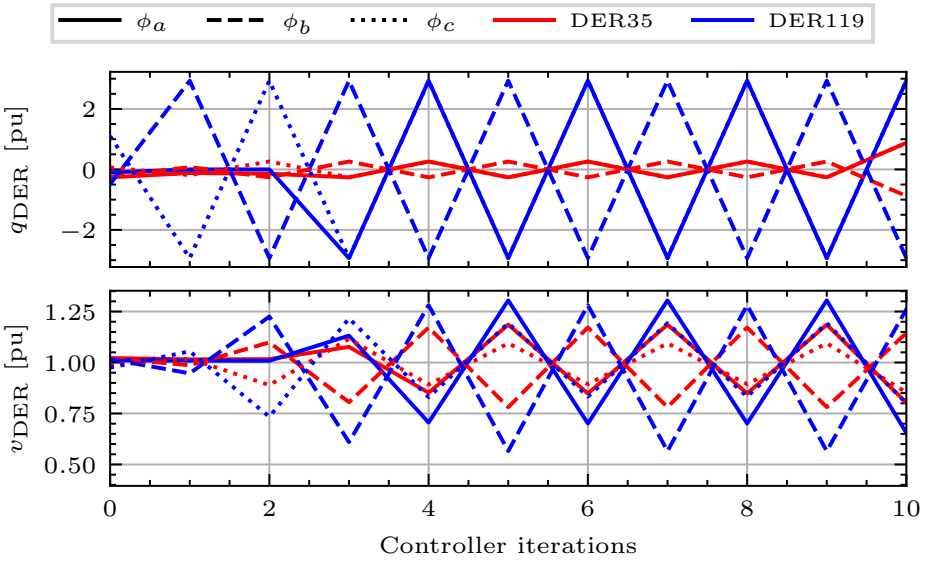

(b)

Figure 7.10: (a) Aggregated non-controllable active power injections, and active/reactive power consumption for the IEEE 123-node test system. (b) Reactive power updates using the static VoltVar for two DERs in the IEEE 123-node test system, where q_{DER} denotes the reactive power of the DER and v_{DER} the voltage magnitude measured at the node where it is connected to.

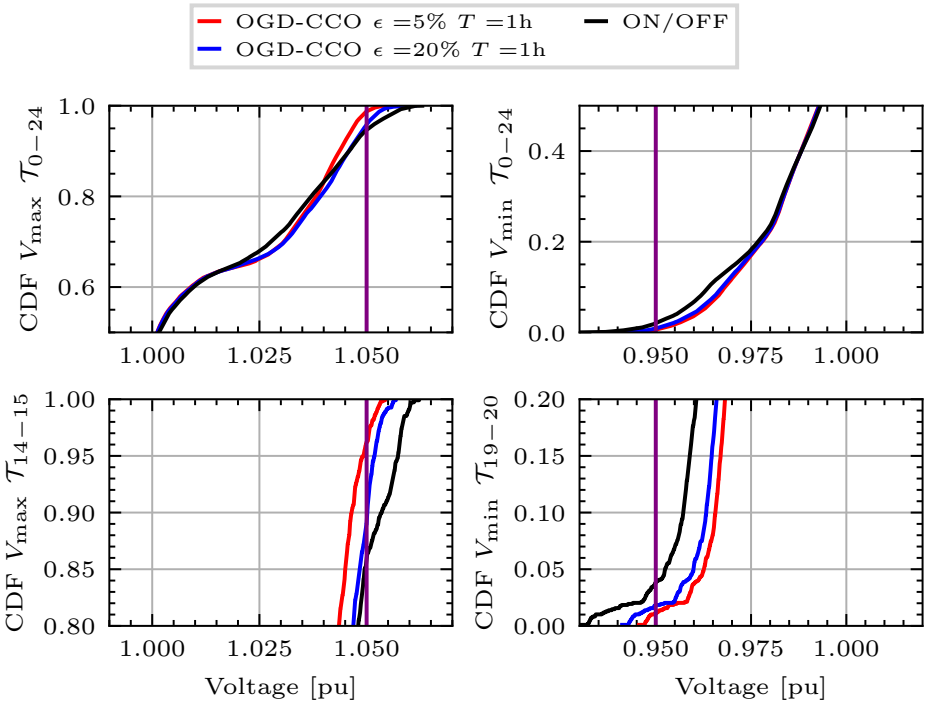

(a)

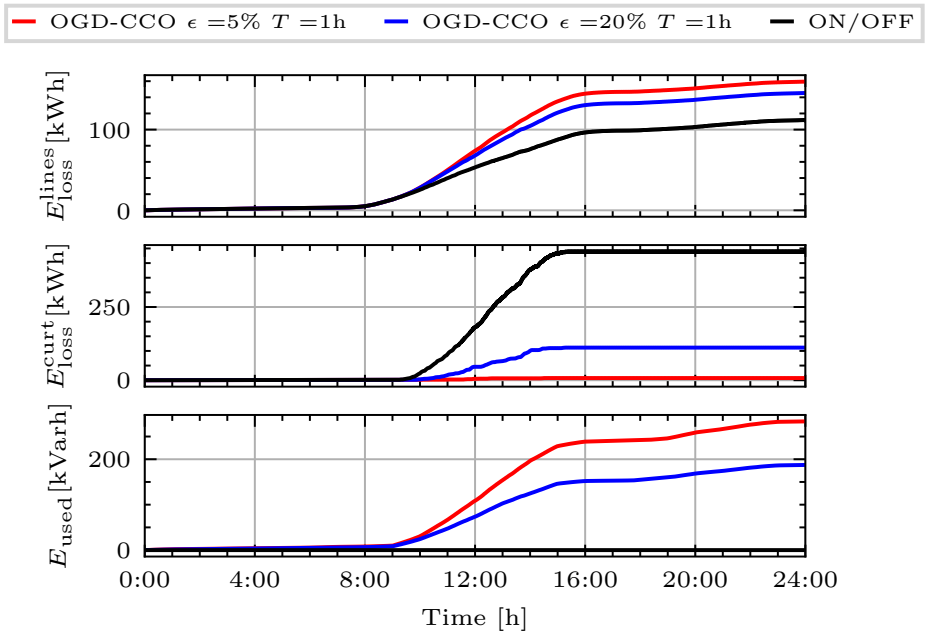

(b)

Figure 7.11: (a) Cumulative distribution function for the vectors $\mathbf{V}_{\max}$ and $\mathbf{V}_{\min}$ for the IEEE 123-node test system. (b) Energy lost in the lines and because of curtailment, and reactive energy usage for the IEEE 123-node test system.

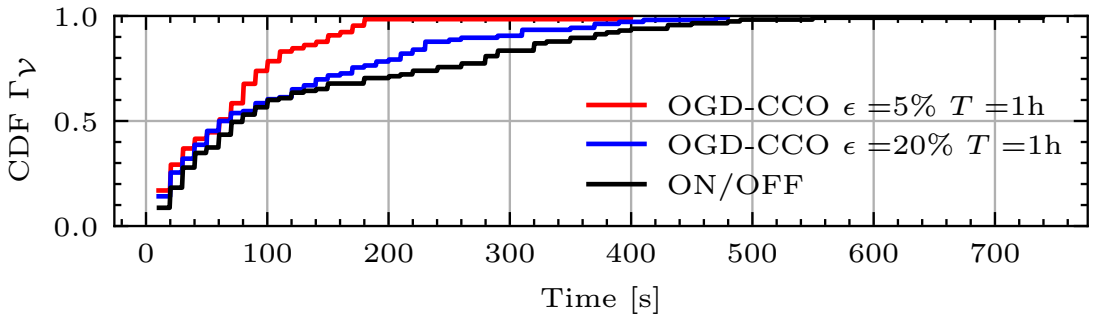

Figure 7.12: Cumulative distribution function for voltage violations for the IEEE 123-node test system.

of the admissible limits. This metric does not indicate the maximum duration of voltage violations for a specific node, but rather provides an overview of the system.

7.5 SUMMARY

In this chapter, we proposed an incremental Volt/Var control strategy for voltage regulation in distribution networks. We showed the stability of our controller and introduce a methodology to compute the gains of our controller based on a multi-period chance-constrained formulation of an optimal reactive power flow problem. Our methodology only needs limited and non-continuous communications; that is, the same controller gains are broadcasted to individual controllers. Our chance-constrained formulation tackles uncertainties in power injections. Moreover, the feasibility issue of local Volt/Var control, i. e., if there is enough reactive power reserve to satisfy the voltage constraints given the architecture of the controller, is implicitly taken into account by allowing the system operator to tolerate a prescribed probability of voltage violations. Our method shows better performance compared to static Volt/Var curves with fixed parameters, and limited and short voltage violations that are consistent with the prescribed probability. We also introduced a robust formulation of our incremental Volt/Var control strategy, based on a simple heuristic that determines the worst-case scenario in terms of voltage regulation.

8

DISTRIBUTED CONTROLLER

Outline

In this chapter, we present a distributed controller for voltage regulation in distribution networks to solve the Problem 1.2 introduced in Section 1.2.2. The AC-OPF problem is decomposed and solved using a consensus-based Alternating Direction Method of Multipliers (ADMM) approach. We leverage the iterative procedure of ADMM to convexify the branch flow model by appropriately estimating the branch currents using consensus variables. We provide experimental results to demonstrate the effectiveness of the proposed approach on a 122-node single-phase distribution network. The chapter is organized as following. In Section 8.1, we review the literature on distributed controllers for voltage regulation in distribution networks. In Section 8.2, we present the proposed consensus-based ADMM approach, and we provide experimental results to demonstrate the effectiveness of the proposed approach. Finally, we summarize the chapter in Section 8.3.

8.1 LITERATURE REVIEW

Distributed control strategies are a trade-off between centralized and decentralized control strategies. They only need reduced communication to take decisions locally, but can reach similar performance as a central controller. This makes them particularly well-suited for the voltage regulation problem in distribution networks. Additionally, they can ensure data privacy and improve robustness against cyber-attacks or communication failure. Compared to a central controller, there is no aggregator in distributed control strategies, so that there is no single-point of failure. In Li et al. [2019] and Bolognani et al. [2014], authors use a dual-ascent method to solve an optimization problem that is decomposed over each electrical node. After updating the Lagrangian multipliers, they are exchanged among neighbors through a communication network. In Zhang et al. [2014], authors also employ a dual-ascent method, but they exchange Lagrangian multipliers to equalize the angle differences across a line from both ends.

In Šulc et al. [2014], authors show that the Alternating Direction Method of Multipliers (ADMM) has superior convergence properties to dual-ascent methods, and consider consensus-based version of ADMM. The convergence properties of distributed algorithms are actually important when it comes to real-time control of distribution network, since long convergence times lead to suboptimal operation of the system. In Xu and

Wu [2020], the problem is split into several zones consisting of several electrical nodes, and a consensus-based ADMM is also implemented. They use a quasi-Newton approach for the dual update to further enhance convergence properties. A convex surrogate of a distributed AC-OPF problem is solved using ADMM in Zhang et al. [2017], although they use a centralizer to compute voltage-related vectors and to broadcast them to the different controllable units.

8.1.1 *Solving an AC-OPF using consensus-based ADMM*

In this thesis, we propose a fully distributed optimization algorithm to perform real-time voltage control of distribution networks. By fully distributed, we mean that each node solves its own subproblem, and only requires communication with neighboring nodes. We do not rely on any type of central coordinator. The proposed distributed control minimizes the communication burden and ensures data privacy; each electrical node is responsible for computing its power setpoints. We leverage the convergence properties of consensus-based ADMM and its iterative procedure to pursue a solution of an AC-OPF problem. ADMM exhibits improved convergence properties compared to dual ascent methods, in particular for problems with ill-conditioned dual functions, as it uses a quadratic regularization term to deal with nonsmooth terms [Zhang et al., 2021].

8.1.2 *Contributions*

The contributions of this work are the following:
(*c1*) No need for a central coordinator. Small optimization problems are solved at each electrical node using local estimations for power and voltage magnitude measurements.
(*c2*) A linear version of the branch flow model is implemented based on estimation of the branch currents. Unlike common linearization methods, the losses are not neglected; they are evaluated for each line and each iteration. This method allows the use of a convex model which does not need the usual loss minimization term for the convex relaxation to be exact, as discussed in Remark 6.2.

8.2 PROPOSED CONSENSUS-BASED ADMM APPROACH

We consider the branch flow model introduced in (6.19) that we recall here:

$$\min_{\mathbf{u}\in\mathbb{R}^{2G}} \quad \sum_{j\in\mathcal{N}} f_j(p_j, q_j) \tag{8.1a}$$

$$\text{s.t.} \quad p_j - p_{l,j} = \sum_{n\in\mathcal{C}_j} P_{jn} - (P_{aj} - r_{aj}\beta_{aj}) \qquad \forall j \in \mathcal{N} \tag{8.1b}$$

$$q_j - q_{l,j} = \sum_{n \in \mathcal{C}_j} Q_{jn} - (Q_{aj} - x_{aj}\beta_{aj}) \qquad \forall j \in \mathcal{N} \tag{8.1c}$$

$$\alpha_j = \alpha_a - 2(r_{aj}P_{aj} + x_{aj}Q_{aj}) + (r_{aj}^2 + x_{aj}^2)\beta_{aj} \qquad \forall j \in \mathcal{N} \tag{8.1d}$$

$$\beta_{aj} = \frac{P_{aj}^2 + Q_{aj}^2}{\alpha_a} \qquad \forall j \in \mathcal{N} \tag{8.1e}$$

$$(p_i, q_i) \in \mathcal{U}_i \qquad \forall i \in \mathcal{G} \tag{8.1f}$$

$$\underline{V}^2 \leq \alpha_j \leq \bar{V}^2 \qquad \forall j \in \mathcal{M} \tag{8.1g}$$

where, compared to the formulation proposed in (6.19), we consider an objective function that can be decomposed node by node. It corresponds to the sum of objective values defined at each node. Furthermore, we applied the following change of variable $\alpha_i = \nu_i^2$ and $\beta_{ij} = I_{ij}^2$. The decision variables p_j, q_j and the objective function are specific to each node, i. e., they depend only on quantities defined at node j. However, there are coupling constraints, i. e., constraints that are coupling quantities that are shared among different nodes. For instance, consider a node a connected to node j through a line of impedance $r_{aj}+\mathrm{j}x_{aj}$, one can write $\nu_a e^{\mathrm{j}\delta_a} - \nu_j e^{\mathrm{j}\delta_j} = (r_{aj}+\mathrm{j}x_{aj})I_{aj}e^{\mathrm{j}\phi_{aj}}$, that is Ohm's law in phasor form. Voltage magnitudes at nodes a and j are linked via the current through the line connecting a to j, and its impedance. Therefore, one cannot directly decompose the optimal power flow problem because of the power flow constraints. In this work, we employ the consensus-based ADMM [Boyd et al., 2011] to distribute the problem because of its enhanced convergence properties compared to other distributed methods.

We consider the following conventions. The network is radial, it is represented using a directed graph rooted at the substation node that is node 0. Each of the other nodes ($j \neq 0$) has a unique ancestor a and any number of children that belongs to the set $\mathcal{C}_j$. A positive power flows from the ancestor to the children and all branch powers are considered on the side of the ancestor node (see Figure 8.1 for the conventions used).

In the consensus-based ADMM, coupled variables are turned into local copies, and an additional consensus constraint imposes the equality of local copies to a shared consensus variable. The consensus constraint is then dualized. The consensus variables are computed as the mean of the local copies. As a result, a communication network matching the electrical network must be created to share corresponding local variables between neighboring nodes.

The ADMM iterative procedure is implemented as follows:
Step 1: Solve the subproblem at each node j,
Step 2: Exchange local copies with the neighbors of j,
Step 3: Update the consensus variables.
Step 4: Update scaled dual variables corresponding to the consensus variables using dual ascent.

These four steps are repeated until convergence of primal and dual variables.

8.2.1 *Iterative procedure*

Step 1: The subproblem solved at each node j is:

$$\min_{p_j,q_j} \quad f_j(p_j,q_j)+n_j(\boldsymbol{\varepsilon}^j)+m_j(\alpha_j^j,\alpha_a^j) \tag{8.2a}$$

$$\text{s.t} \quad p_j - p_{l,j} = \sum_{n\in\mathcal{C}_j} P_{jn}^j - \left(P_{aj}^j - r_{aj}\beta_{aj}^j\right), \tag{8.2b}$$

$$q_j - q_{l,j} = \sum_{n\in\mathcal{C}_j} Q_{jn}^j - \left(Q_{aj}^j - x_{aj}\beta_{aj}^j\right), \tag{8.2c}$$

$$\alpha_j^j = \alpha_a^j - 2\left(r_{aj}P_{aj}^j + x_{aj}Q_{aj}^j\right) + \left(r_{aj}^2 + x_{aj}^2\right)\beta_{aj}^j, \tag{8.2d}$$

$$p_j, q_j \in \mathcal{U}_j, \tag{8.2e}$$

$$\underline{V}^2 \leq \alpha_j^j \leq \bar{V}, \tag{8.2f}$$

where $\boldsymbol{\varepsilon}^j$ is a vector containing the coupling variables related to node j, i. e., $\alpha_j^j, \alpha_a^j, P_{aj}^j, Q_{aj}^j$ and $\{P_{jn}^j, Q_{jn}^j\}_{n\in\mathcal{C}_j}$. Notice that our algorithm requires an estimate of the network branch impedances $(r_{aj}+\mathrm{j}x_{aj})$.

The penalty term n_j comes from the augmented Lagrangian in its scaled form [Boyd et al., 2011]:

$$\begin{aligned} n_j(\boldsymbol{\varepsilon}^j) = \frac{\rho}{2}(&\|P_{aj}^j - \bar{P}_{aj}^j + \gamma_{aj}^j\|_2^2 + \|Q_{aj}^j - \bar{Q}_{aj}^j + \delta_{aj}^j\|_2^2 \\ &+ \|\alpha_a^j - \bar{\alpha}_a^j + \lambda_a^j\|_2^2 + \|\alpha_j^j - \bar{\alpha}_j^j + \lambda_j^j\|_2^2 \\ &+ \sum_{n\in\mathcal{C}_j}(\|P_{jn}^j - \bar{P}_{jn}^j + \gamma_{jn}^j\|_2^2 + \|Q_{jn}^j - \bar{Q}_{jn}^j + \delta_{jn}^j\|_2^2)), \end{aligned} \tag{8.3}$$

with the penalty parameter or update step ρ, initialized at 1 and updated using a heuristic described in Boyd et al. [2011], $\gamma_{aj}^j, \gamma_{jn}^j, \lambda_j^j, \lambda_a^j, \delta_{aj}^j, \delta_{jn}^j$ are dual variables associated with consensus constraints, and quantities defined with $\bar{(\cdot)}$ represent consensus variables. We explained in *Step 3* how those quantities are computed. Notice that the constraint (8.1e) does not appear in the local subproblems, although the branch currents β_{ij} appear in the other constraints. This constraint renders the problem non-convex, and in this thesis, we leverage the iterative procedure of the ADMM to consider branch currents as parameters that are updated at each iteration of the procedure using:

$$\beta_{aj}^j = \frac{(\bar{P}_{aj}^j)^2 + (\bar{Q}_{aj}^j)^2}{\bar{\alpha}_a^j} \tag{8.4}$$

The last term m_j is a second penalty term for voltage deviation compared to the measured value:

$$m_j(\alpha_j^j,\alpha_a^j) = c_v((\alpha_j^j - \tilde{\nu}_j^2)^2 + (\alpha_a^j - \tilde{\nu}_a^2)^2). \tag{8.5}$$

This aims to keep the local copies of the squared voltage magnitude variables close to the measured values. In distribution network, the substation node sets the reference voltage for the system, and the voltage values at other nodes are derived from this reference and the power flow in the lines. The outer nodes thus rely on information from ancestors to determine their own voltage in the ADMM algorithm. Due to the distributed and iterative nature of ADMM, this information takes some time to propagate through the network, resulting in underestimation of voltage values and lasting overvoltages. This is actually one of the major drawback of distributed control strategies, as they take some time to converge to the optimal solution. Adding this term with a weight factor $c_v > c_q$ speeds up the convergence to solutions that satisfy Kirchhoff's laws. This term ensures faster voltage regulation while optimal operation is still reached when the algorithm has converged.

Remark 8.1 (*Penalty term*)**.** *Notice that, if one considers a perfect voltage model, and no measurement errors, the penalty term defined in* (8.5) *becomes zero when the ADMM procedure has converged toward a solution of problem* (8.1)*. However, in practice, there exist some modelling uncertainties and measurements are noisy such that the penalty term is never equal to zero.*

With respect to (8.1), a superscript j represents a local copy of a variable considered at node j and a is associated to the ancestor of node j, i. e., α_a^j denotes the squared voltage magnitude of the ancestor node a of node j seen from node j, while α_j^j denotes the squared voltage magnitude of node j seen from node j.

Step 2: The communication graph described in Figure 8.1 shows the variables to be exchanged after each node has solved its subproblem.

Step 3: The consensus variables are updated by computing the average value of all the local copies:

$$\bar{\alpha}_j^j = \frac{\alpha_j^j + \sum_{n\in\mathcal{C}_j} \alpha_j^n}{(|\mathcal{C}_j|+1)}, \tag{8.6a}$$

$$\bar{P}_{aj}^j = \frac{(P_{aj}^j + P_{aj}^a)}{2}, \tag{8.6b}$$

$$\bar{Q}_{aj}^j = \frac{(Q_{aj}^j + Q_{aj}^a)}{2}, \tag{8.6c}$$

$$\bar{P}_{jn}^j = \frac{(P_{jn}^j + P_{jn}^n)}{2}, \ \forall\, n \in \mathcal{C}_j \tag{8.6d}$$

$$\bar{Q}_{jn}^j = \frac{(Q_{jn}^j + Q_{jn}^n)}{2}, \ \forall\, n \in \mathcal{C}_j. \tag{8.6e}$$

We only use communication with adjacent buses in the algorithm. In order to update $\bar{\alpha}_a^j$, information from the children nodes $n \in \mathcal{C}_a$ of the ancestor a is needed, since all the children nodes have a local copy of the ancestor voltage. This consensus variable is thus

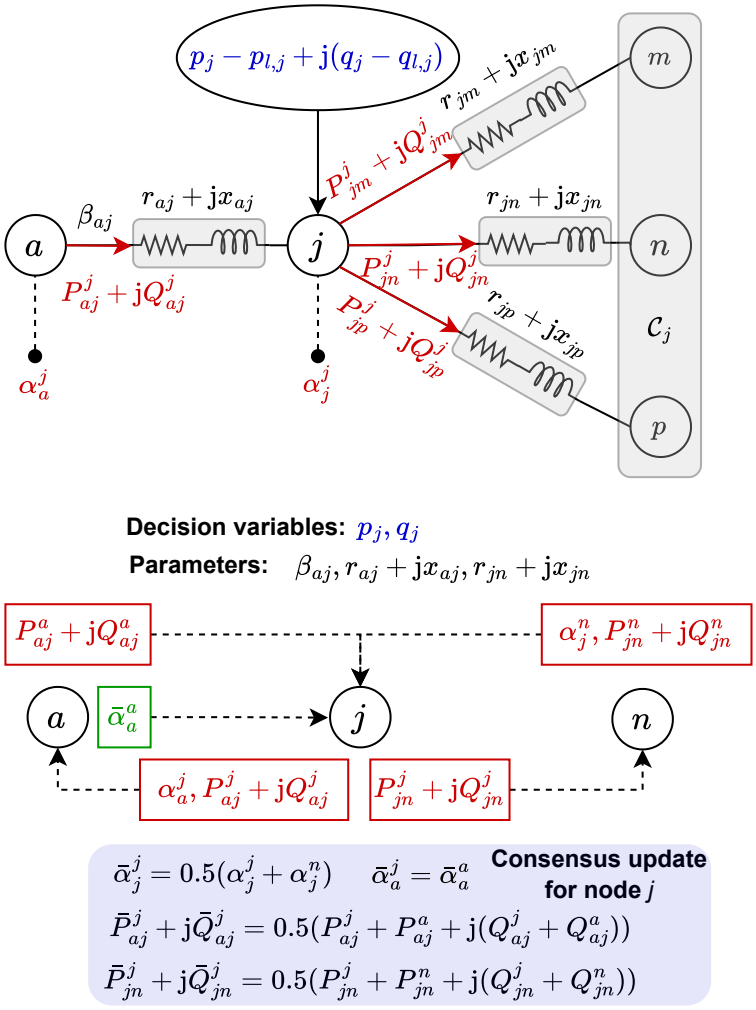

Figure 8.1: Communication graph for node j.

only updated in node a with data from all its children, then transmitted to the children node, including node j.

Step 4: The scaled dual variables are updated with a gradient ascend method:

$$\lambda_j^j = \lambda^j + \alpha_j^j - \bar{\alpha}_j^j, \tag{8.7a}$$
$$\lambda_a^j = \lambda_a^j + \alpha_a^j - \bar{\alpha}_a^j, \tag{8.7b}$$
$$\gamma_{jn}^j = \gamma_{jn}^j + P_{jn}^j - \bar{P}_{jn}^j, \ \forall n \in \mathcal{C}_j \tag{8.7c}$$
$$\gamma_a^j = \gamma_a^j + P_a^j - \bar{P}_a^j, \tag{8.7d}$$
$$\delta_{jn}^j = \delta_{jn}^j + Q_{jn}^j - \bar{Q}_{jn}^j, \ \forall n \in \mathcal{C}_j \tag{8.7e}$$
$$\delta_a^j = \delta_a^j + Q_a^j - \bar{Q}_a^j. \tag{8.7f}$$

8.2.2 *Experimental results*

8.2.2.1 *Simulation setup*

We use a Dickert benchmark LV network as described in Dickert et al. [2013], which is available in Pandapower [Thurner et al., 2018]. The parameters for the Dickert network are *long* range feeders, *multiple customers*, *cables* as line type, and the case type is *average* with a total of 122 nodes. We keep the same initial electrical loads, and add PV systems. We distribute 109 PV systems randomly in the network, corresponding to a penetration rate of 90%. The rated size of the inverters is selected among three different sizes $\{8, 9, 10\}$ kVA. Time-domain values for load consumption and PV production with a minute resolution come from Open Power System Data. We derived 40 load profiles and 40 PV production profiles collected over several days to simulate active and reactive load consumption patterns and PV system orientations. The data are linearly interpolated to create profiles with second resolution, and are shown in Figure 8.3a.

The simulations are run for one day, from sunrise to sunset. Considering the very low computation time and the direct communication between nodes, the frequency of the ADMM algorithm is estimated to be 10 Hz. Every 0.1 second, the inverters receive new setpoints. We consider that the inverters directly implement the power setpoint received. Then, we measure voltage magnitudes measurements and feed them back in equation (8.2). Considering the one-second resolution for PV and load data, ADMM has 10 iterations to approach convergence before the state of the system is modified. Each second, after system modification, the algorithm benefits from previous operating points as a warm start. Operating points stay similar and dual variables for the problem are already close to convergence. Perfect communication and synchronicity between neighboring inverters is considered for these simulations.

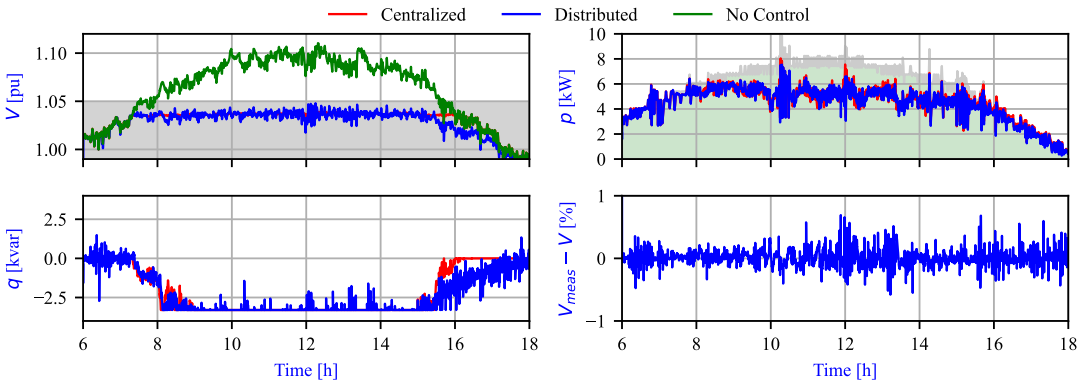

Figure 8.2: Results for one specific bus equipped with a PV inverter. V denotes the local copies of the voltage magnitude for one specific node, while V_{meas} is the actual voltage magnitude that has been measured. q and p denote the reactive power and active power injected by the DER, respectively.

8.2.2.2 *Results*

Figure 8.2 compares the performance of the centralized model and the distributed model. The voltage magnitude at one problematic node is shown in the top-left figure. We compare three different simulations. The first two use centralized and distributed models to compute power setpoints. In the third one, no control action is taken (reactive power set to zero and no active power curtailment). The voltage level in the latter case exceeds the 1.05 pu threshold, whereas it does not in the other two cases. Even if the local voltage measurements are not outside voltage limits, the distributed algorithm curtails the active power to avoid overvoltages in other nodes. It can achieve the same results as a centralized model without needing a coordinator with complete observability of the system state. However, the magnitude of the voltage in our model may differ from the network's actual voltage (resulting from the solution of a power flow using the power setpoints computed with the distributed algorithm), as explained before.

The bottom right plot displays the differences between the actual voltage and the voltage perceived by the distributed agents. Finally, we compare the computed power setpoints for the centralized and distributed algorithms. It is noticeable that the distributed model accurately follows the optimal power setpoints computed with the centralized model.

In Figure 8.4, we compare the energy curtailed (integral of the total active power curtailed over a specified period) for three control algorithms, the centralized version of equation (8.1), the distributed approach and the CENELEC EN50549-2 standard [EN50549-2, 2019] already discussed previously, that corresponds here to a *decentralized* control strategy.

The control algorithms are compared in terms of overvoltages in Figure 8.3b (except the centralized method since it avoids overvoltage). As can be seen, compared to the scenario

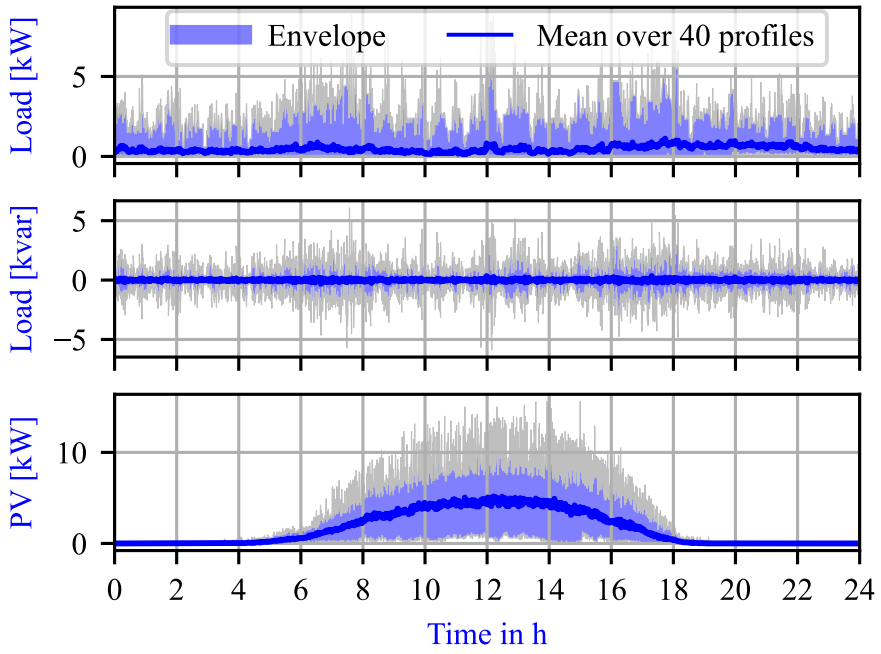

(a)

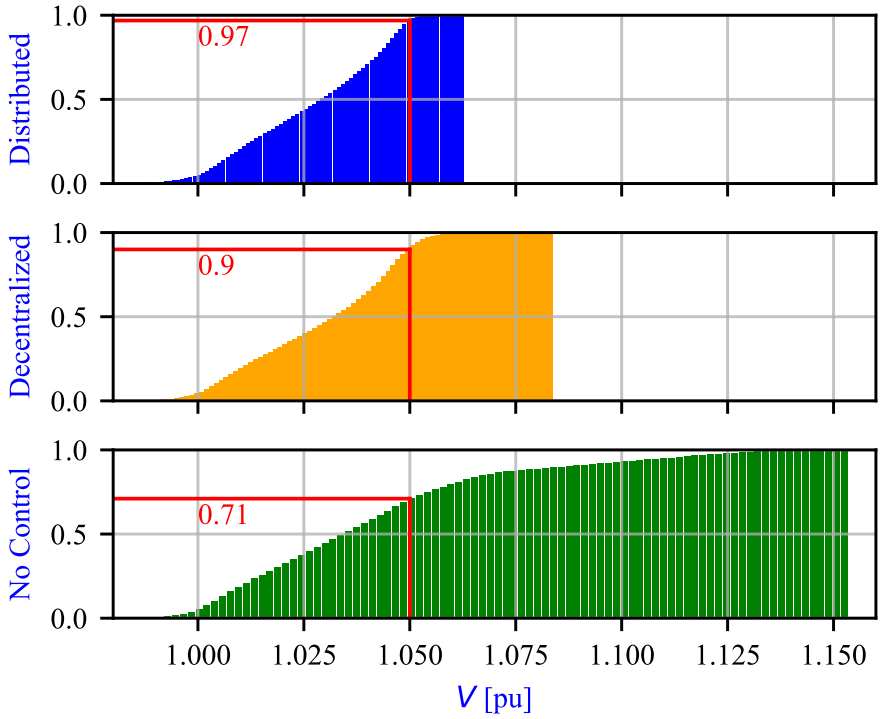

(b)

Figure 8.3: (a) PV production and load profiles for one day with second resolution. (b) Cumulative distribution functions of voltages for all nodes in three simulations, where V denote the voltage magnitude measured throughout the network.

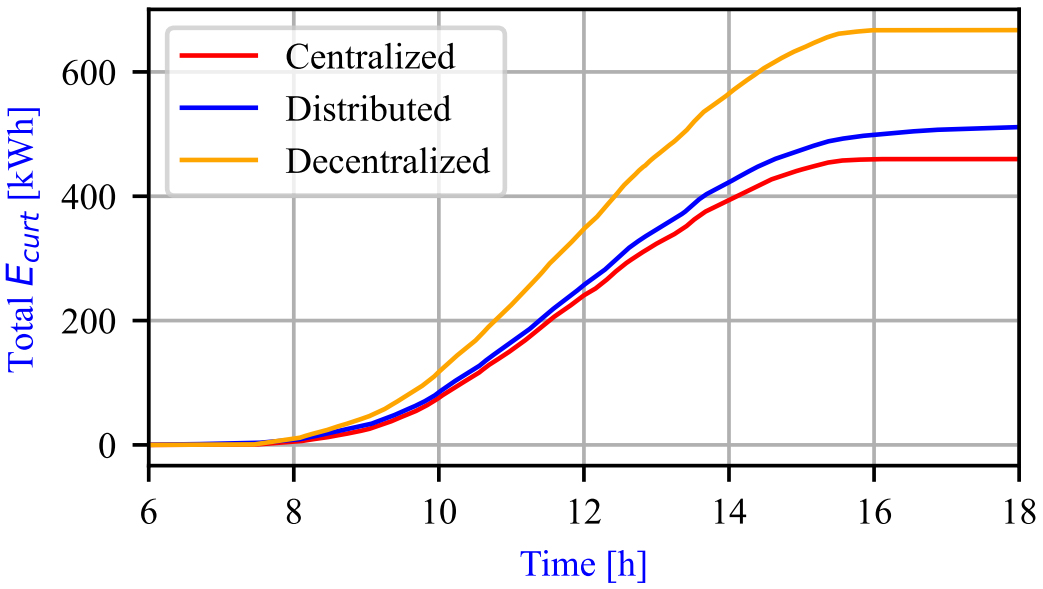

Figure 8.4: Energy curtailed for the three control algorithms.

with no control, the distributed algorithm limits the number of voltage violations and the maximum overvoltage.

Table 8.1 shows the comparative results for the four simulations. The centralized optimizer shows the ideal results, with minimal energy curtailment and no voltage violations. The results for the proposed distributed method are relatively close to ideal, with greatly reduced communication needs. The decentralized controller show relatively good voltage regulation, at the expense of very large power curtailment.

Table 8.1: Results for the full simulations.

	Control algorithm			
	No Ctrl	***Dec. Ctrl***(CENELEC standard)	***ADMM***	***Cent. Op.***
Energy produced	5009kWh	4342kWh	4498kWh	4549kWh
Energy curtailed	0 kWh	697 kWh	511 kWh	460 kWh
Energy lost	212 kWh	123 kWh	186 kWh	191 kWh
Production peak	697 kW	579 kW	591 kW	601 kW
Consumption	679 kWh			
Reactive control	0 kvarh	0 kvarh	1129 kvarh	1031 kvarh
Max. voltage	1.15 pu	1.08 pu	1.06 pu	1.05 pu
% of overvoltages	29	10	3	0

8.3 SUMMARY

In this chapter, we solved an AC-OPF problem using a consensus-based ADMM, that only requires neighbor-to-neighbor communication. We solve one subproblem per electrical node, and each node communicates with its neighboring nodes. The proposed method can reach similar results as an optimal centralized controller. We used a branch flow model to model the power flow equations. We obtain a convex formulation for the branch flow model, by appropriately estimating the branch currents, using the iterative procedure of ADMM. The global optimum can be reached without minimizing the network losses in the model objective thanks to the iterative evaluation of the branch currents. We showed numerical results on a 122-node single-phase distribution networks, and performance comparable to a centralized controller, with less communication requirements.

9

CONCLUSION AND PERSPECTIVES

9.1 CONCLUSION

In this part, we proposed three different control algorithms to perform voltage regulation in distribution networks.

Centralized algorithms require a complex communication infrastructure that is not always available in distribution networks. They often require a detailed model of the network, and full information about the system's state. However, recent works in online feedback-based optimization reduce the requirements in terms of modelling and observability of the system. These algorithms work in interaction with the grid; the feedback controller converges toward an equilibrium that is a solution of the optimization problem. There are two main advantages of real-time closed-loop implementation of optimization algorithms; *(i)* they naturally track time-varying conditions since they manifest themselves in the feedback received by the controller, *(ii)* they do not require detailed model of the system. We mention the requirements in terms of system's observability. While solving the non-convex AC-OPF requires collecting load measurements at every node, our feedback-based method only requires voltage measurements at nodes where we want to perform voltage regulation. In particular, one can create some clusters of nodes where voltage regulation is required, and only collect voltage measurements at the cluster's leader. This would greatly reduce the requirements in terms of communication infrastructure. Compared to other feedback-based method, we proposed an algorithm that leverages control barrier functions. Hence, we can guarantee that the voltage remains at anytime within the admissible limits. The proposed method relies on a quadratic programming problem that can be solved in real-time. We showed that our feedback-based safe gradient flow exhibits similar performance compared to solving the non-convex AC-OPF problem, even though our safe gradient flow is based on a linear approximation of the power flow equations. This is because the voltage model is replaced by voltage measurements in feedback-based methods, which make them robust against modelling uncertainties. However, we note that, even though communication requirements are reduced, the method still requires communication between some nodes and a central aggregator, which may not be available in all distribution networks.

We proposed a decentralized control algorithm that does not require communication for real-time operation. The gains of the local controller are computed days/hours ahead by a central aggregator with an algorithm based on a chance-constrained formulation of the optimal reactive power flow (ORPF) problem. The gains are then dispatched days/hours ahead, and in real-time, there is no communication. It is well-known that, even though

a solution of the ORPF problem exists, a decentralized controller may not be able to find it. That is because decentralized controllers only have access to local information, and do not have full system's observability. Hence, they cannot be compared with centralized controller in terms of performance, since there exist solutions they cannot reach. In the proposed approach, we leverage a chance-constrained formulation of the ORPF problem to *(i)* account for uncertainties in load consumptions and renewable energy productions, and *(ii)* to allow the system operator to tolerate a prescribed probability of voltage violations. We showed that our method can achieve better performance compared to static Volt/Var curves with fixed parameters, and limited and short voltage violations that are consistent with the prescribed probability. Although in real-time, the proposed method does not require any communication with a central aggregator, it still requires occasional communication to obtain gains for the incremental Volt/Var controller. Notice that the communication requirements are kept as low as possible because the same gains are broadcasted to all the nodes. We also introduced a robust formulation of our incremental Volt/Var control strategy, based on a simple heuristic that determines the worst-case scenario in terms of voltage regulation. While decentralized controllers can be implemented in current distribution networks, they may not be able to reach the global optimum, and lead to over-usage of some resources.

We proposed a distributed controller based on ADMM that can achieve similar results as a centralized controller. This controller only requires communication between neighboring nodes, and does not require a central aggregator. That corresponds to a trade-off between a centralized controller and a decentralized controller. Additionally, they can ensure data privacy and improve robustness against cyber-attacks or communication failure, since there is no single-point of failure, while reaching the same global optimum as a centralized controller. We considered a consensus-based ADMM approach to decompose and solve an AC-OPF problem formulated with the branch flow model as they present improved convergence properties compared to primal-dual methods for instance. We showed that the distributed algorithm can reach similar results as the centralized algorithm, with greatly reduced communication needs. We also leveraged the iterative procedure of the ADMM to estimate branch currents to allow us to use a convex version of the AC-OPF problem. Distributed methods present many advantages, however, they tend to be difficult to implement in practice. For instance, in our approach, we considered synchronicity for the communication between neighboring nodes, which may not be possible in practice. Furthermore, we did not derive any guarantee in terms of stability of our distributed controllers.

9.2 PERSPECTIVES

In the following, we discuss some perspectives for each of the proposed control algorithms.

Centralized controller: There are two main drawbacks for our approach; *(i)* it requires a central aggregator, and *(ii)* one needs to rely on an optimization solver to obtain the

output of the map $F_\beta(\mathbf{u}, \tilde{\mathbf{v}})$. One could envision decomposing the problem of solving the map $F_\beta(\mathbf{u}, \tilde{\mathbf{v}})$, and obtain a distributed controller instead. For instance, authors in [Mestres et al., 2024] propose a distributed controller for safe navigation of multi-agent systems, that is based on a projected saddle-point dynamics. This method could be adapted to solve the map $F_\beta(\mathbf{u}, \tilde{\mathbf{v}})$ for the voltage regulation problem in a distributed manner. Instead of relying on an optimization solver, one could imagine learning the map $F_\beta(\mathbf{u}, \tilde{\mathbf{v}})$ using machine learning techniques. Interesting works on neural networks could be used to solve the QP problem 100 times faster than existing solvers [Amos and Kolter, 2017]. However, the question remains on how to ensure that the neural network will provide the same guarantees as the optimization solver.

Decentralized controller: The main drawback of our decentralized controller is that it does not use optimally the resources of the different assets. One could envision using machine learning techniques such as in Yuan et al. [2024] to learn the optimal gains of the incremental Volt/Var controller, or reinforcement learning such as in Cui et al. [2022] to learn optimal policies for each asset. However, it is not clear what one should do if the network topology changes, and how to combine those machine learning methods with other traditional regulation methods such as OLTCs. In particular, we believe that our decentralized controller is fairly flexible, and can easily be combined with traditional regulation methods through our voltage forecasts $\rho_k = H(\mathbf{0}, \mathbf{z}_k)$, since the map H can incorporate the impact of any regulation method. Nevertheless, decentralized control algorithms cannot compete with centralized controller in terms of performance, since they do not have full observability of the system. Therefore, they should be combined with slower controllers that could track at a slower time-scale a solution that minimizes the usage of resources.

Distributed controller: The main drawbacks of our distributed controller are the requirements in terms of synchronicity in the communication, the lack of stability guarantees, and the number of iterations required to converge toward a solution of the optimization problem. Notice that we did not perform extensive studies about the stability guarantees, although consensus-based ADMM has been proved to converge toward the optimum of a convex optimization problem under relatively mild assumptions Boyd et al. [2011]. To improve convergence rate of consensus-based ADMM, one can consider time-varying penalty parameters ρ such as in Zeng et al. [2022]. Also, notice that techniques to ensure convergence of ADMM with asynchronous communications has also been discussed [Rikos et al., 2023].

Part III

GENERAL CONCLUSION

10 GENERAL CONCLUSION

This thesis is divided into two parts: in the first part, we develop new power converter models suitable for system-level analysis, while the second part focuses on the development of new control strategies for active distribution networks. In this chapter, we discuss the main contributions of this thesis and why the development of power converter models is essential when designing control strategies for active distribution networks.

In Part I, Chapter 2 is dedicated to the introduction of different modelling techniques for power converters. In particular, we introduced switched models, averaged models, and small-signal models. Switched models are non-linear and time-varying systems, every conduction configuration of the power converter is represented by a linear or a non-linear system. On the other hand, averaged models are time-invariant systems, derived by averaging inputs, states and outputs over the switching period of the power converter. Finally, small-signal models are obtained by linearizing the averaged model around a given operating point. Although linear small-signal models can be used to design power converters' local controllers, they are not appropriate for system-level studies. We showed that, modelling the closed-loop system, i. e., the power converter and its controller, with a linear model does not yield good performance, particularly if the dynamics of the closed-loop system depend on the operating point.

In Chapter 3 we introduced a methodology to derive large-signal black-box models of power converters in order to find a solution to the Problem 1.1. First, we aim at deriving models that can capture the dynamics of the system around different operating points. Our multimodel approach combines different linear submodels responses using a neural network-based weighting function. The different linear models are identified from measurements collected on the converter. The neural network is then trained using data collected during normal operation of the power converter. We focused on developing models that can be easily obtained running simple experiments on the power converter and do not require specific equipment. These are measurement-based models such that the models *(i) do not require a-priori knowledge about their internal structure*. The model can be further improved using a *partitioning procedure* where the trained neural network is analyzed. To minimize the complexity of the model, linear submodels that do not bring any improvement to the global model response are removed, and the algorithm suggests where to add new linear submodels. Our multimodel approach is therefore *(ii) computationally lightweight* compared to detailed models, and it can be used to simulate large systems for *(iii) system-level studies*. We illustrate the approach on different power

converters, and also in the context of small systems, where our model is used to simulate the dynamics of a system composed of different assets.

In Part II, Chapter 5 is dedicated to the introduction of the voltage regulation problem in distribution networks. We showed that the massive integration of renewable energy resources can lead to voltage issues in distribution networks, and that traditional regulation techniques may fail at solving those issues. We introduced the voltage regulation problem as an optimization problem, and then proposed different control techniques to solve the Problem 1.2. In particular, we propose three different control strategies that *(i) track the solution of an AC optimal power flow problem to regulate the voltages in the network by steering the setpoints of the distributed energy resources* and *(ii) that are appropriate for real-time operation.* Each control strategy has their own requirements in terms of communication and knowledge about the system, but *(iii) they do not require extensive monitoring of the distribution network.*

In Chapter 6, we proposed a centralized online optimization method that drives the distributed energy resources power setpoints to a solution of the AC optimal power flow problem. The controller ensures anytime satisfaction of voltage constraints when no model and measurement errors are present. Our controller is centralized, it requires collecting measurements throughout the network and communicating power setpoints to the different DERs. However, compared to traditional techniques for solving the AC-OPF that require collecting load consumption at every nodes, our controller collects voltage measurements only at nodes where one wants to regulate the voltages, which significantly reduces the communication burden. Our controller is very flexible, as one can easily take into account other operational constraints besides the voltage limits. For instance, we developed a controller to regulate a virtual power plant based on the same approach.

In Chapter 7, we proposed decentralized controllers, where only local measurements are required to compute the DER setpoint. Notice that we focused on Volt/Var control, such that the optimization problem introduced in Chapter 5 is slightly modified to only consider reactive power as controllable variable. We propose an incremental Volt/Var strategy, where the gains are obtained by solving an optimization problem. The optimization problem is solved centrally, but the method does not require continuous communication. To take into account uncertainty in load and generation and to keep communication minimal, the optimization problem is formulated as a multi-period chance-constrained optimization problem. The controllers for each DER regulate the voltages at their node such that the voltage constraints are satisfied with a prescribed probability. Compared to the centralized method, the decentralized method does not require continuous communication, and is suitable with current distribution network technology. However, the controllers cannot ensure anytime satisfaction of the voltage constraints, since decentralized methods may not be able to converge toward a solution of the optimization problem

(even if such solution exists) since it only relies on local information [Bolognani et al., 2019].

Finally, in Chapter 8, we proposed a distributed controller, where the AC optimal power flow problem is decomposed and solved node by node, with only local communication between neighboring nodes. We used the Alternating Direction Method of Multipliers (ADMM) to solve the optimization problem. The iterative method allows us to approximate the branch currents, and therefore solve a convex optimization problem at each node. This method does not require a communication infrastructure as complex as for the centralized controller, and does not present a *single-point of failure*. Notice that if the centralized controller is attacked, and no longer works, one cannot regulate the voltages throughout the network. Decentralized and distributed methods do not present a central aggregator, and therefore are more robust against attacks. However, our distributed controller requires synchronous communication, and the convergence time might be long.

We have presented three different control strategies for the voltage regulation in active distribution networks. Each control strategy has its own requirements in terms of communication, computational resources, and knowledge about the system. It is clear that advanced system monitoring, and development of communication infrastructure in active distribution networks can maximize our usage of renewable energy resources, and activate some flexibilities to slowly move toward zero-carbon emission targets. However, as of today, current distribution networks technology does not meet those requirements, and intermediate solutions such as the decentralized controller we proposed can be a first step in the right direction. Also, the system's scale may prohibit the usage of a centralized controller, and safety concerns such as the presence of a *single-point of failure*, may prevent centralized controllers to be deployed in practice. That is where we believe distributed controllers can be interesting, thanks to the limited communication requirements, and the problem decomposition which reduces the computational burden.

In the following, we discuss an important assumption that we made throughout this manuscript. When we design the system-level controllers in Part II, we assume that DERs' dynamics are much faster than the controller dynamics, such that the power setpoints sent by the system-level controller are instantaneously implemented. This assumption is discussed in Eggli et al. [2020], where authors mention the timescale separation of the power system phenomena and of the different control loops. This is a reasonable assumption for physical system with fast-decaying dynamics. However, for other systems, one must enforce that the controller is sufficiently slower than the plant dynamics to ensure the stability of the closed-loop system. Actually, it has been shown that if there is no timescale separation, it can lead to an unstable closed-loop system [Hauswirth et al., 2020]. However, as mentioned in Bianchi and Dörfler [2024], in some cases, it would be desirable to run the controller at the same timescale as the plant dynamics to improve the transient behavior. Actually, we mentioned in this manuscript that traditional offline

algorithms are not appropriate for controlling active distribution networks, since the computation time might be too long compared to the variability of the load and renewable energy production, and it can thus lead to suboptimal solutions. On the other hand, if we have to run our online optimization algorithms slower to guarantee the stability of the system, we also might end up with suboptimal solutions. Authors in Bianchi and Dörfler [2024] show that under some assumptions, online optimization algorithms can be run at the same timescale as the plant dynamics, and still guarantee the stability of the closed-loop system. However, that raises some questions. When one considers more complex systems with different assets and different dynamics, can we always theoretically guarantee the stability of the closed-loop system? Can we always verify the assumptions that are required to ensure the stability of the closed-loop system? In practice, active distribution networks contain many different assets, provided by different manufacturers, and with dynamics that are not always well-known. We believe that theoretical guarantees are important, but one should always run some simulations to guarantee that the system behaves as expected. Therefore, we believe that the development of new models for power converters is essential when designing control strategies for active distribution networks. We need models that are computationally lightweight, in order to simulate large test systems. Those models should be valid around different operating points, as the system is expected to operate in different conditions. Furthermore, interpretability is also a key aspect, as one needs to understand how the system behaves and how the control strategies might render the closed-loop system unstable. That is a crucial aspect for the integration of new control strategies in active distribution networks, that would allow for a greater integration of renewable energy resources, and distributed energy resources in general, in order to meet our carbon emission targets.

Part IV

APPENDIX

APPENDIX

A.1 FEEDBACK-BASED SAFE GRADIENT FLOW

A.1.1 *Stability analysis and constraint satisfaction guarantees*

In our technical analysis, we make use of the following assumptions. The assumptions are stated for given values of the non-controllable powers $\mathbf{p}_l, \mathbf{q}_l$.

Assumption A.1 (*Jacobian errors*)**.** $\exists\ E_h < +\infty, E_J < +\infty$ *such that* $\|\hat{H}(\mathbf{u}; \mathbf{p}_l, \mathbf{q}_l) - H(\mathbf{u}; \mathbf{p}_l, \mathbf{q}_l)\| \leq E_h$ *and* $\|J_{\hat{H}}(\mathbf{u}) - J_H(\mathbf{u})\| \leq E_J$ *for any* $\mathbf{u} \in \mathcal{B}(\mathbf{u}^*, r_1)$. □

Assumption A.2 (*Measurement errors*)**.** $\exists\ E_M < +\infty$ *such that* $\|\tilde{\boldsymbol{\nu}} - \boldsymbol{\nu}\| \leq E_M$. □

Assumptions A.1-A.2 are motivated by the following observations: (i) the linear map error $\|\hat{H}(\mathbf{u}; \mathbf{p}_l, \mathbf{q}_l) - H(\mathbf{u}; \mathbf{p}_l, \mathbf{q}_l)\|$ is bounded and small in a neighborhood of the optimizer (as confirmed in Figure 6.5f in our numerical results, and by the analytical findings in [Bolognani and Zampieri, 2015, Dhople et al., 2015]), and (ii) in realistic monitoring and SCADA systems, the measurement of the voltage magnitudes are affected by a small (or even negligible) error.

In our analysis, we view (6.16) as a perturbed version of the initial formulation of the safe gradient flow ($F_\beta(\mathbf{u}, H(\mathbf{u}; \mathbf{p}_l, \mathbf{q}_l))$). To begin with, we have the following result.

Lemma A.3 (*KKT and equilibrium*)**.** *Consider the problem* (6.1) *satisfying Assumptions 5.1-6.1. There exists* $\boldsymbol{\mu}^*$ *such that* $(\mathbf{u}^*, \boldsymbol{\mu}^*)$ *is a KKT point for* (6.1) *if and only if* $\mathbf{u}^*$ *is an equilibrium of* $\dot{\mathbf{u}} = \eta F_\beta(\mathbf{u}, H(\mathbf{u}; \mathbf{p}_l, \mathbf{q}_l))$. □

Before analyzing the stability of the proposed feedback-based SGF, we provide some notation and intermediate results that will be used in the proof of our main result.

Let $\Omega := J_{\hat{H}}(\mathbf{u}) - J_H(\mathbf{u})$ and denote by ω_i the i-th row of Ω. Moreover, let $\mathbf{e} := \tilde{\boldsymbol{\nu}} - \boldsymbol{\nu}$ denote the measurement errors. Then, define $\bar{F}_\beta(\mathbf{u}, \Omega, \mathbf{e})$ as

$$
\begin{aligned}
&\bar{F}_\beta(\mathbf{u}, \Omega, \mathbf{e}) \\
&:= \arg\min_{\boldsymbol{\theta}} \|\boldsymbol{\theta} + \nabla C_p(\mathbf{u}) + (J_H(\mathbf{u}) + \Omega)^\top \nabla C_v(\boldsymbol{\nu} + \mathbf{e})\|^2 \\
&\quad \text{s.t.} -(\nabla H_i(\mathbf{u}) + \omega_i)^\top \boldsymbol{\theta} \leq -\beta\,(\underline{V} - \nu_i - e_i) \quad \forall i \in \mathcal{M} \\
&\qquad (\nabla H_i(\mathbf{u}) + \omega_i)^\top \boldsymbol{\theta} \leq -\beta\,(\nu_i + e_i - \bar{V}) \quad \forall i \in \mathcal{M} \\
&\qquad J_{\ell_i}(\mathbf{u})^\top \theta \leq -\beta \ell_i(p_i, q_i) \qquad\qquad \forall i \in \mathcal{G}
\end{aligned}
$$

where $\boldsymbol{\nu} = H(\mathbf{u}; \mathbf{p}_l, \mathbf{q}_l)$. Note that $F_\beta(\mathbf{u}, H(\mathbf{u}; \mathbf{p}_l, \mathbf{q}_l)) = \bar{F}_\beta(\mathbf{u}, \mathbb{0}, \mathbb{0})$ and $\hat{F}_\beta(\mathbf{u}, \tilde{\boldsymbol{\nu}}) = \bar{F}_\beta(\mathbf{u}, J_{\hat{H}}(\mathbf{u}) - J_H(\mathbf{u}), \tilde{\boldsymbol{\nu}} - \boldsymbol{\nu})$. Let $\mathcal{E}_J := \{\Omega : \|\Omega\| \leq E_J\}$ and $\mathcal{E}_M := \{\mathbf{e} : \|\mathbf{e}\| \leq E_M\}$ for brevity. We make the following assumption on $\bar{F}_\beta$.

Assumption A.4 (*Regularity*)**.** *For any $\mathbf{u} \in \mathcal{B}(\mathbf{u}^*, r_1)$, and any Ω and $\mathbf{e}$ satisfying Assumptions A.1-A.2, the problem (6.16b) is feasible, and satisfies the Mangasarian-Fromovitz Constraint Qualification and the constant-rank condition Liu [1995].* □

Since the constraints in the problem defining $\bar{F}_\beta(\mathbf{u}, \Omega, \mathbf{e})$ (and, hence, our safe gradient flow (6.16)) are based on techniques from CBFs [Ames et al., 2019, Allibhoy and Cortés, 2024], Assumption A.4 guarantees that there always exists a direction for the setpoints to satisfy the constraints of the OPF. Moreover, this assumption allows us to derive the following result.

Lemma A.5 (*Lipschitz continuity*)**.** *Let Assumption A.4 hold, and assume that $\mathbf{u} \mapsto C_p(\mathbf{u})$, $\boldsymbol{\nu} \mapsto C_v(\boldsymbol{\nu})$ are twice continuously differentiable over $\mathcal{B}(\mathbf{u}^*, r_1)$ and $\mathcal{V} := \{\boldsymbol{\nu} \in \mathbb{R}^M : \underline{V} \leq \nu_i + e_i \leq \bar{V}, \forall i \in \mathcal{M}, \boldsymbol{\nu} = H(\mathbf{u}; \mathbf{p}_l, \mathbf{q}_l), \|\mathbf{e}\| \leq E_M, \mathbf{u} \in \mathcal{B}(\mathbf{u}^*, r_1)\}$, respectively. Then:*
(i) For any $\Omega \in \mathcal{E}_J$ and $\mathbf{e} \in \mathcal{E}_M$, $\mathbf{u} \mapsto \bar{F}_\beta(\mathbf{u}, \Omega, \mathbf{e})$ is locally Lipschitz at $\mathbf{u}$, $\mathbf{u} \in \mathcal{B}(\mathbf{u}^*, r_1)$.
(ii) For any $\mathbf{u} \in \mathcal{B}(\mathbf{u}^*, r_1)$ and $\Omega \in \mathcal{E}_J$, $\mathbf{e} \mapsto \bar{F}_\beta(\mathbf{u}, \Omega, \mathbf{e})$ is Lipschitz with constant $\ell_{F_v} \geq 0$ over $\mathcal{E}_M$.
(iii) For any $\mathbf{u} \in \mathcal{B}(\mathbf{u}^*, r_1)$ and $\mathbf{e} \in \mathcal{E}_M$, $\Omega \mapsto \bar{F}_\beta(\mathbf{u}, \boldsymbol{\nu}, \Omega, \mathbf{e})$ is Lipschitz with constant $\ell_{F_J} \geq 0$ over $\mathcal{E}_J$. □

Lemma A.5 follows from [Liu, 1995, Theorem 3.6], and by the compactness of the sets $\mathcal{E}_M$ and $\mathcal{E}_J$. This result ensures existence and uniqueness of solutions for the proposed feedback-based safe gradient flow [Khalil, 2002, Ch. 3].

Our main stability result critically relies on these results. Before stating it, we introduce some useful quantities that play a role in the main result; in particular, they are related to local properties of $F_\beta(\mathbf{u}, H(\mathbf{u}; \mathbf{p}_l, \mathbf{q}_l))$. Recall that $\mathbf{u}^*$ is the local optimizer of (6.1). We define $\boldsymbol{\nu}^* := H(\mathbf{u}^*; \mathbf{p}_l, \mathbf{q}_l)$, $E := \frac{\partial F_\beta(\mathbf{u}, H(\mathbf{u}; \mathbf{p}_l, \mathbf{q}_l))}{\partial \mathbf{u}} \big|_{\mathbf{u}=\mathbf{u}^*}$, $e_1 := -\lambda_{\max}(E)$, and $e_2 := -\lambda_{\min}(E)$.

Then, we can write the dynamics as $F_\beta(\mathbf{u}, H(\mathbf{u}; \mathbf{p}_l, \mathbf{q}_l)) = E(\mathbf{u} - \mathbf{u}^*) + \hat{g}(\mathbf{u})$, where $\hat{g}(u)$ satisfies $\|\hat{g}(\mathbf{u})\| \leq L\|\mathbf{u} - \mathbf{u}^*\|^2$, $\forall \mathbf{u} \in \mathcal{B}(\mathbf{u}^*, r_2)$, for some $L > 0$ and $r_2 > 0$ (see Khalil [2002]). Define $r := \min\{r_1, r_2\}$ and

$$s_{\min} := \begin{cases} 0, & \text{if } r \geq \frac{e_1}{L}, \\ 1 - \frac{rL}{e_1}, & \text{if } r < \frac{e_1}{L}. \end{cases}$$

Since $\mathcal{U}$ is compact, $J_H(\mathbf{u})$ is Lipschitz on $\mathcal{U}$ with constant ℓ_H.

We are now ready to state the main stability result for (6.16).

Theorem A.6 (*Practical local exponential stability*)**.** *Consider the OPF problem* (6.1) *satisfying Assumptions 5.1-6.1, a linear map* $\hat{H}$ *satisfying Assumption A.1, measurements* $\tilde{\boldsymbol{\nu}}$ *satisfying Assumption A.2, and the controller* (6.16) *satisfying Assumption A.4. Let* $\mathbf{u}(t)$*,* $t \geq t_0$*, be the unique trajectory of* (6.16)*. Assume that the set* $\mathcal{S} := \left\{ s : s_{\min} < s \leq 1,\ e_1^{-3} e_2 L(\ell_{F_J} E_J + \ell_{F_v} E_M) < s - s^2 \right\}$ *is not empty. Then, for any* $s \in \mathcal{S}$*, it holds that*

$$\|\mathbf{u}(t)-\mathbf{u}^*\| \leq \sqrt{\frac{e_2}{e_1}} e^{-e_1 \eta s (t-t_0)} \|\mathbf{u}(t_0)-\mathbf{u}^*\| \qquad + \frac{e_2(\ell_{F_J} E_J + \ell_{F_v} E_M)}{s e_1^2} \left(1 - e^{-e_1 \eta s (t-t_0)}\right), \tag{A.1}$$

for any initial condition $\mathbf{u}(t_0)$ *such that* $\|\mathbf{u}(t_0) - \mathbf{u}^*\| \leq \sqrt{\frac{e_1}{e_2}} \frac{e_1}{L}(1-s)$. △

Proof. First, we express our controller as:

$$\begin{aligned}
\dot{\mathbf{u}} &= \eta \hat{F}_\beta(\mathbf{u}, \tilde{\boldsymbol{\nu}}) \\
&= \eta \bar{F}_\beta(\mathbf{u}, \mathbb{0}, \mathbb{0}) \\
&\quad + \eta[\bar{F}_\beta(\mathbf{u}, J_{\hat{H}}(\mathbf{u}) - J_H(\mathbf{u}), \tilde{\boldsymbol{\nu}} - \boldsymbol{\nu}) - \bar{F}_\beta(\mathbf{u}, \mathbb{0}, \tilde{\boldsymbol{\nu}} - \boldsymbol{\nu})] \\
&\quad + \eta[\bar{F}_\beta(\mathbf{u}, \mathbb{0}, \tilde{\boldsymbol{\nu}} - \boldsymbol{\nu}) - \bar{F}_\beta(\mathbf{u}, \mathbb{0}, \mathbb{0})]
\end{aligned}$$

where we added and subtracted $\bar{F}_\beta(\mathbf{u}, \mathbb{0}, \mathbb{0})$ and $\bar{F}_\beta(\mathbf{u}, \mathbb{0}, \tilde{\boldsymbol{\nu}} - \boldsymbol{\nu})$, and we re-organized the terms. The feedback-based SGF can then be understood as a perturbation of the nominal gradient flow $\bar{F}_\beta(\mathbf{u}, \mathbb{0}, \mathbb{0})$.

By [Allibhoy and Cortés, 2024, Lemma 5.11 and Theorem 5.6(iii)], $\bar{F}_\beta(\mathbf{u}, \mathbb{0}, \mathbb{0})$ is differentiable at $\mathbf{u}^*$ and its Jacobian $E = \frac{\partial \bar{F}_\beta(\mathbf{u}, \mathbb{0}, \mathbb{0})}{\partial \mathbf{u}} \big|_{\mathbf{u}=\mathbf{u}^*}$ is negative definite. Recall that $e_1 = -\lambda_{\max}(E)$ and $e_2 = -\lambda_{\min}(E)$. Let $P := \int_0^\infty (\exp(E\zeta)^\top \exp(E\zeta) d\zeta$, and then by [Khalil, 2002, Theorem 4.12], it holds that $PE + E^\top P = -\mathbf{I}_n$, and $\frac{1}{2e_2}\|u - u^*\|_2^2 \leq (u-u^*)^\top P (u-u^*) \leq \frac{1}{2e_1}\|u-u^*\|_2^2$. Let $V_1(\mathbf{u}) := (\mathbf{u}-\mathbf{u}^*)^\top P (\mathbf{u}-\mathbf{u}^*)$; then we bound $2(\mathbf{u}-\mathbf{u}^*)^\top P \bar{F}_\beta(\mathbf{u}, \mathbb{0}, \mathbb{0})$ and then leverage this bound to estimate $\dot{V}_1$:

$$\begin{aligned}
&2(\mathbf{u}-\mathbf{u}^*)^\top P \bar{F}_\beta(\mathbf{u}, \mathbb{0}, \mathbb{0}) \\
&\quad = (\mathbf{u}-\mathbf{u}^*)^\top \left(PE + E^\top P\right)(\mathbf{u}-\mathbf{u}^*) \\
&\qquad + 2(\mathbf{u}-\mathbf{u}^*)^\top P \hat{g}(\mathbf{u}) \\
&\quad \leq -\|\mathbf{u}-\mathbf{u}^*\|^2 + \frac{1}{e_1}\|\mathbf{u}-\mathbf{u}^*\| L \|\mathbf{u}-\mathbf{u}^*\|^2 \\
&\quad \leq \left(-1 + \frac{L}{e_1}\|\mathbf{u}-\mathbf{u}^*\|_2\right)\|\mathbf{u}-\mathbf{u}^*\|_2^2 \leq -s\|\mathbf{u}-\mathbf{u}^*\|^2
\end{aligned}$$

where the last inequality holds if $\|\mathbf{u}-\mathbf{u}^*\| \leq \frac{e_1}{L}(1-s)$, for any $s \in (s_{\min}, 1]$. Then,

$$\dot{V}_1 = 2(\mathbf{u}-\mathbf{u}^*)^\top P \dot{u}$$

$$
\begin{aligned}
&= 2\eta(\mathbf{u}-\mathbf{u}^*)^\top P\bar{F}_\beta(\mathbf{u},\mathbb{0},\mathbb{0}))\\
&+ 2\eta(\mathbf{u}-\mathbf{u}^*)^\top P[\bar{F}_\beta(\mathbf{u},J_{\hat{H}}-J_H,\tilde{\boldsymbol{\nu}}-\boldsymbol{\nu})-\bar{F}_\beta(\mathbf{u},\mathbb{0},\tilde{\boldsymbol{\nu}}-\boldsymbol{\nu})]\\
&+ 2\eta(\mathbf{u}-\mathbf{u}^*)^\top P[\bar{F}_\beta(\mathbf{u},\mathbb{0},\tilde{\boldsymbol{\nu}}-\boldsymbol{\nu})-\bar{F}_\beta(\mathbf{u},\mathbb{0},\mathbb{0})]\\
&\leq -\eta s\|\mathbf{u}-\mathbf{u}^*\|^2 + 2\eta\ell_{F_J}\|\mathbf{u}-\mathbf{u}^*\|\|P\|\|J_H-J_{\hat{H}}\|\\
&+ 2\eta\ell_{F_v}\|\mathbf{u}-\mathbf{u}^*\|\|P\|\|\tilde{\boldsymbol{\nu}}-\boldsymbol{\nu}\|\\
&\leq -\eta s\|\mathbf{u}-\mathbf{u}^*\|^2 + \eta\frac{\ell_{F_J}E_J+\ell_{F_v}E_M}{e_1}\|\mathbf{u}-\mathbf{u}^*\|\\
&\leq -2e_1\eta s V_1 + \eta\sqrt{2e_2}\frac{\ell_{F_J}E_J+\ell_{F_v}E_M}{e_1}\sqrt{V_1}.
\end{aligned}
$$

Define $V_2(\mathbf{u}) := \sqrt{V_1(\mathbf{u})}$. Then,

$$
\begin{aligned}
\dot{V}_2 = \frac{\dot{V}_1}{2\sqrt{V_1}} \leq& \frac{-2e_1\eta s V_1 + \eta\sqrt{2e_2}\frac{\ell_{F_J}E_J+\ell_{F_v}E_M}{e_1}\sqrt{V_1}}{2\sqrt{V_1}}\\
=& -e_1\eta s V_2 + \eta\sqrt{2e_2}\frac{\ell_{F_J}E_J+\ell_{F_v}E_M}{2e_1}
\end{aligned}
$$

In addition, we note that that for any $a \geq 0,\ b > 0$, $y(t) = y(t_0)\exp(-b(t-t_0)) + \frac{a}{b}(1-\exp -b(t-t_0))$ is the solution of $\dot{y} = -by + a, y(t_0) = y(t_0)$. Hence by the Comparison Lemma [Khalil, 2002, Lemma 3.4], it follows that

$$
\begin{aligned}
V_2(t) \leq& V_2(t_0)e^{-e_1\eta s(t-t_0)}\\
&+ \frac{\sqrt{2e_2}(\ell_{F_J}E_J+\ell_{F_v}E_M)}{2se_1^2}\left(1-e^{-e_1\eta s(t-t_0)}\right).
\end{aligned}
$$

Thus, one has that

$$
\begin{aligned}
\|\mathbf{u}(t)-\mathbf{u}^*\| \leq& \sqrt{2e_2}V_2(t)\\
\leq& \sqrt{2e_2}V_2(t_0)e^{-e_1\eta s(t-t_0)}\\
&+ \frac{2e_2(\ell_{F_J}E_J+\ell_{F_v}E_M)}{2se_1^2}\left(1-e^{-e_1\eta s(t-t_0)}\right)\\
\leq& \sqrt{\frac{1}{2e_1}}\sqrt{2e_2}e^{-e_1\eta s(t-t_0)}\|\mathbf{u}(t_0)-\mathbf{u}^*\|\\
&+ \frac{e_2(\ell_{F_J}E_J+\ell_{F_v}E_M)}{se_1^2}\left(1-e^{-e_1\eta s(t-t_0)}\right)\\
=& \sqrt{\frac{e_2}{e_1}}e^{-e_1\eta s(t-t_0)}\|\mathbf{u}(t_0)-\mathbf{u}^*\|\\
&+ \frac{e_2(\ell_{F_J}E_J+\ell_{F_v}E_M)}{se_1^2}\left(1-e^{-e_1\eta s(t-t_0)}\right).
\end{aligned}
$$

which proves the result. The limits for $t \to +\infty$ can be computed straightforwardly. □

The assumption that $\mathcal{S}$ is not empty is necessary to guarantee that the trajectory of $\mathbf{u}(t)$ never exits the region of attraction of the optimizer $\mathbf{u}^*$. We can notice that the first term on the right-hand-side of (A.1) decays over time; the second term models the effect of the measurement errors and of the errors in the computation of the Jacobian. In particular, we can notice that, as $t \to +\infty$, the right-hand side of (A.1) becomes

$$\lim_{t\to+\infty} \|\mathbf{u}(t) - \mathbf{u}^*\| \leq s^{-1} e_1^{-2} e_2 (\ell_{F_J} E_J + \ell_{F_v} E_M). \tag{A.2}$$

The asymptotic error can be reduced by increasing the accuracy in the measurement of the voltages (i.e., reducing E_M), or allocating more computational power to compute the Jacobian of the power flow equations (i.e., reducing E_J). The following result characterizes the feasibility of the solution $u(t)$.

Lemma A.7 (*Practical forward invariance*)**.** *Let the conditions in Theorem A.6 be satisfied, and let* $\mathbf{u}(t)$*,* $t \geq t_0$*, be the unique trajectory of* (6.16)*, and* $\boldsymbol{\nu}(t)$ *be the corresponding voltage magnitudes. Define the set*

$$\mathcal{F}_e := \{\mathbf{u} : \mathbf{u} \in \mathcal{U}, \underline{V}_e \leq H_i(\mathbf{u}; \mathbf{p}_l, \mathbf{q}_l) \leq \bar{V}_e, \forall i \in \mathcal{M}\} \tag{A.3}$$

with $\underline{V}_e := \underline{V} - E_M - 2E_{\hat{H}}$*,* $\bar{V}_e := \bar{V} + E_M + 2E_{\hat{H}}$*, and* $E_{\hat{H}} := \max_{\mathbf{u}\in\mathcal{U}} \|\hat{H}(\mathbf{u}; \mathbf{p}_l, \mathbf{q}_l) - H(\mathbf{u}; \mathbf{p}_l, \mathbf{q}_l)\|$*. Then, the feedback-based SGF* (6.16) *renders a set* $\mathcal{F}_s$*, with* $\mathcal{F} \subseteq \mathcal{F}_s \subseteq \mathcal{F}_e$*, forward invariant.* □

Proof. The proof leverages Nagumo's Theorem Nagumo [1942]. For the feedback-based SGF $\hat{F}_\beta(\mathbf{u}, \boldsymbol{\nu})$ in (6.16), it holds that $-\nabla \hat{H}_i(\mathbf{u})^\top \hat{F}_\beta \leq -\beta\,(\underline{V} - \tilde{\nu}_i)$. Recall that $\tilde{\nu}_i = H(\mathbf{u}; \mathbf{p}_l, \mathbf{q}_l) + e_i$, for $i \in \mathcal{M}$. It follows that

$$\begin{aligned}
&- \nabla \hat{H}_i(\mathbf{u})^\top \hat{F}_\beta \leq -\beta\,(\underline{V} - H(\mathbf{u}; \mathbf{p}_l, \mathbf{q}_l) - e_i) \\
&= -\beta(\underline{V} - \hat{H}(\mathbf{u}; \mathbf{p}_l, \mathbf{q}_l) - e_i + (H(\mathbf{u}; \mathbf{p}_l, \mathbf{q}_l) - \hat{H}(\mathbf{u}; \mathbf{p}_l, \mathbf{q}_l))) \\
&\leq -\beta((\underline{V} - E_M - E_{\hat{H}}) - \hat{H}(\mathbf{u}; \mathbf{p}_l, \mathbf{q}_l))
\end{aligned}$$

where $E_{\hat{H}} := \max_{\mathbf{u}\in\mathcal{U}} \|H(\mathbf{u}; \mathbf{p}_l, \mathbf{q}_l) - \hat{H}(\mathbf{u}; \mathbf{p}_l, \mathbf{q}_l)\|$. Similarly, it also holds that $\nabla \hat{H}_i(\mathbf{u})^\top \hat{F}_\beta \leq -\beta(\hat{H}(\mathbf{u}; \mathbf{p}_l, \mathbf{q}_l) - (\bar{V} + E_M + E_{\hat{H}}))$. Thus, the set

$$\begin{aligned}
\mathcal{F}_s := \{&\mathbf{u} : \underline{V} - E_M - E_{\hat{H}} \leq \hat{H}_i(\mathbf{u}; \mathbf{p}_l, \mathbf{q}_l) \leq \bar{V} + E_M + E_{\hat{H}}, \\
&\forall i \in \mathcal{M}, \mathbf{u} \in \mathcal{U}\}
\end{aligned}$$

is forward invariant under (6.16). Note that $\mathcal{F}_s$ is a subset of $\mathcal{F}_e$, and this concludes the proof. □

Lemma A.7 establishes forward invariance of a set $\mathcal{F}_s$, which is a subset of $\mathcal{F}_e$ and an inflation of $\mathcal{F}$ (more details about $\mathcal{F}_s$ are provided in the proof); clearly, $\mathcal{F}_e$ tends to the set $\mathcal{F}$ with the decreasing of the error in the computation of the Jacobian and the measurement errors, which implies that $\mathcal{F}_s$ tends to $\mathcal{F}$ too. If these errors are small, the voltage violation is practically negligible.

In the case of no errors in the measurements and in the computation of the Jacobian, we have the following results.

Corollary A.8 (*Error-free implementation*)**.** *Let all the conditions in Theorem A.6 be satisfied, and assume that there are no measurement errors, i.e., $E_M = 0$, and no errors in the Jacobian, i.e., $E_J = 0$ and. Let $\mathbf{u}(t)$, $t \geq t_0$, be the unique trajectory of (7.4). Then it holds that*

$$\|\mathbf{u}(t) - \mathbf{u}^*\| \leq \sqrt{\frac{e_2}{e_1}}\|\mathbf{u}(t_0) - \mathbf{u}^*\|e^{-e_1\eta s(t-t_0)}$$

and $\lim_{t\to+\infty} \|\mathbf{u}(t) - \mathbf{u}^*\| = 0$. △

Lemma A.9 (*Forward invariance in error-free implementation*)**.** *Let the conditions in Theorem A.6 be satisfied, and assume that there are no measurement errors (i.e., $E_M = 0$). Let $\mathbf{u}(t)$, $t \geq t_0$, be the unique trajectory of (7.4), and $\boldsymbol{\nu}(t)$ be the corresponding trajectory of the voltages. Then, (7.4) renders the set $\mathcal{F}$ forward-invariant. In particular: (i) if $\nu_i(t_0) \in [\underline{V}, \bar{V}]$, then $\nu_i(t) \in [\underline{V}, \bar{V}]$ for all $t \geq t_0$; (ii) if $\nu_i(t_0) \notin [\underline{V}, \bar{V}]$, then there exists $t' \geq t_0$ such that $\nu_i(t) \in [\underline{V}, \bar{V}]$ for all $t \geq t'$.* □

Corollary A.8 quantifies the error in the convergence to $\mathbf{u}^*$, and certify local exponential stability properties for the proposed method. Lemma A.9 establishes that, for the case with no measurement errors and with the exact computation of the Jacobian matrix, the proposed method ensures that voltages are satisfied anytime.

A.2 INCREMENTAL VOLT/VAR CONTROL

A.2.1 *Derivations of M*

In this section, we derive the matrices $M_{i,n}$ appearing in (7.23) to ensure that $\tilde{h}_{i,n}(\mathbf{x}; \boldsymbol{\rho}^m[s], \mathbf{x}_p)$ is a global majorizer of $h_{i,n}(\mathbf{x}_p; \boldsymbol{\rho})$. First, let us build the Jacobian matrices $\nabla h_i(\mathbf{x})$ for $i = 1, 2, 3, 4$ from the Jacobian matrix $\nabla \mathbf{q}(\mathbf{x})$. Notice that the partial derivatives of the vector $\mathbf{q}(\mathbf{x})$ with respect to the first and second component of the vector $\mathbf{x}$ are identical:

$$\frac{\partial \mathbf{q}(\mathbf{x})}{\partial x_1} = \frac{\partial \mathbf{q}(\mathbf{x})}{\partial x_2} = P \operatorname{diag}(\gamma(\mathbf{x}))P^{-1}(\mathbf{1} - \boldsymbol{\rho}) \tag{A.4}$$

where $\gamma(\mathbf{x}) = [-\frac{1}{(\mathbf{1}^\top \mathbf{x} + \lambda_{X,1})^2}, ..., -\frac{1}{(\mathbf{1}^\top \mathbf{x} + \lambda_{X,N})^2}]^\top$. Since X is positive definite, and $\mathbf{1}^\top \mathbf{x} \geq 0$ by constraint, the vector $\gamma(\mathbf{x})$ has bounded elements.

We can now construct $\nabla \mathbf{q}(\mathbf{x}) = \left[\frac{\partial \mathbf{q}(\mathbf{x})}{\partial x_1}, \frac{\partial \mathbf{q}(\mathbf{x})}{\partial x_2}\right]^\top \in \mathbb{R}^{2\times N}$ as

$$\nabla \mathbf{q}(\mathbf{x}) = [P \operatorname{diag}(\gamma(\mathbf{x}))P^{-1}(\mathbf{1} - \boldsymbol{\rho}), P \operatorname{diag}(\gamma(\mathbf{x}))P^{-1}(\mathbf{1} - \boldsymbol{\rho})]^\top. \tag{A.5}$$

Recalling the definitions (7.10) of the vector-valued functions h_i, we can write:

$$\begin{aligned} &\nabla h_1(\mathbf{x}) = \nabla \mathbf{q}(\mathbf{x}), \quad \nabla h_2(\mathbf{x}) = -\nabla \mathbf{q}(\mathbf{x}) \\ &\nabla h_3(\mathbf{x}) = X\nabla \mathbf{q}(\mathbf{x}), \quad \nabla h_4(\mathbf{x}) = -X\nabla \mathbf{q}(\mathbf{x}) \end{aligned} \tag{A.6}$$

In order to determine $M_{i,n}$ such that $M_{i,n} - \nabla^2 h_{i,n}(\mathbf{x}) \succeq 0$, we first derive the Hessian matrix of $h_{i,n}(\mathbf{x})$:

$$\nabla^2 h_{i,n}(\mathbf{x}) = c_{i,n}(\mathbf{x}) \begin{pmatrix} 1 & 1 \\ 1 & 1 \end{pmatrix} \tag{A.7}$$

where $c_{i,n}(\mathbf{x}) \in \mathbb{R}$. We define $c_i(\mathbf{x}) = [c_{i,1}(\mathbf{x}), ..., c_{i,N}(\mathbf{x})]^\top$ and from eqs (A.5) and (A.6) it is easy to retrieve:

$$\begin{aligned} &c_1(\mathbf{x}) = P \operatorname{diag}(d_\gamma(\mathbf{x})) P^{-1}(\mathbf{1} - \boldsymbol{\rho}), \quad c_2(\mathbf{x}) = -c_1(\mathbf{x}) \\ &c_3(\mathbf{x}) = X c_1(\mathbf{x}), \quad c_4(\mathbf{x}) = -X c_1(\mathbf{x}) \end{aligned} \tag{A.8}$$

where $d_\gamma(\mathbf{x}) = [\frac{2}{(\mathbf{1}^\top \mathbf{x} + \lambda_{X,1})^3}, ..., \frac{2}{(\mathbf{1}^\top \mathbf{x} + \lambda_{X,N})^3}]^\top$. Given that the quantity $\mathbf{1}^\top \mathbf{x}$ is always positive, setting $\mathbf{1}^\top \mathbf{x} = 0$ in $d_\gamma(\mathbf{x})$ gives us an upper bound on the value of $\nabla^2 h_{i,n}(\mathbf{x})$. Therefore, we write $\bar{c}_i = c_i(\mathbf{x})|_{\mathbf{1}^\top \mathbf{x} = 0}$ for $i = 1, 2, 3, 4$ and find:

$$M_{i,n} = 2 \begin{pmatrix} \max(0, \bar{c}_{i,n}) & 0 \\ 0 & \max(0, \bar{c}_{i,n}) \end{pmatrix} \quad \forall n \in \mathcal{N} \tag{A.9}$$

such that $\tilde{h}_{i,n}(\mathbf{x}; \mathbf{x}_p)$ is a global majorizer of $h_{i,n}(\mathbf{x})$ $\forall \mathbf{x} \in \mathbb{R}^2$.

A.2.2 *Convergence guarantees for Algorithm 7.1*

In this section, we show that the assumptions considered in Scutari et al. [2014] for the SCA method to converge are applicable to our problem (7.17). To this end, define $\mathcal{W} \in \mathbb{R}^N$ such that $\boldsymbol{\rho} \in \mathcal{W}$.

We start by observing the following properties and facts related to problem (7.17).

[A1] The set $\mathcal{K}$ is closed and convex. The set $\mathcal{K}$ is constructed with linear constraints.

[A2] The functions $\mathbf{x} \mapsto h_0(\mathbf{x}, \boldsymbol{\rho})$ and $\mathbf{x} \mapsto g_{i,n}(\mathbf{x}, u_{i,n}; \boldsymbol{\rho})$ are continuously differentiable on $\mathcal{K}$, for any $\boldsymbol{\rho} \in \mathcal{W}$. This follows from the differentiability of $\mathbf{q}(\mathbf{x}; \boldsymbol{\rho})$; since X is positive definite by construction, and $\mathbf{1}^\top \mathbf{x} \geq 0$ by constraint, it follows that $\nabla \mathbf{q}(\mathbf{x})$ always exists and is bounded.

[A3] The gradient $\nabla_{\mathbf{x}} h_0(\mathbf{x}; \boldsymbol{\rho})$ is Lipschitz continuous on $\mathcal{K}$ with constant $L_{\nabla h_0}$, uniformly in $\boldsymbol{\rho}$. This follows from the fact that $\nabla^2 \mathbf{q}(\mathbf{x})$ is bounded on $\mathcal{K}$.

[A4] For some $\mathbf{x}_0 \in \mathcal{X}$, $\{\mathbf{x} \in \mathcal{X} : h_0(\mathbf{x}; \boldsymbol{\rho}) \leq h_0(\mathbf{x}_0; \boldsymbol{\rho})\}$ is compact, for any given $\boldsymbol{\rho} \in \mathcal{W}$.

Next, we note that the surrogate function $\tilde{h}_0 : \mathcal{K} \times \mathcal{W} \times \mathcal{X} \to \mathbb{R}$ is continuously differentiable with respect to $\mathbf{x}$ and satisfies the following conditions.

[A5] The map $\mathbf{x} \mapsto \tilde{h}_0(\mathbf{x}; \boldsymbol{\rho}, \mathbf{x}_p)$ is strongly convex on $\mathcal{K}$ with constant $c \geq d > 0$, for any given $\mathbf{x}_p \in \mathcal{X}$ and $\boldsymbol{\rho} \in \mathcal{W}$.

[A6] We have that $\nabla \tilde{h}_0(\mathbf{x}_p; \boldsymbol{\rho}, \mathbf{x}_p) = \nabla h_0(\mathbf{x}_p; \boldsymbol{\rho})$ for any given $\mathbf{x}_p \in \mathcal{X}$ and $\boldsymbol{\rho} \in \mathcal{W}$. to see this, define $f(\cdot) = \|\cdot\|^2$ so and express $h_0(\mathbf{x}) = f(\mathbf{q}(\mathbf{x}))$ and $\tilde{h}_0(\mathbf{x}; \mathbf{x}_p) = f(\mathbf{q}(\mathbf{x}_p) + (\mathbf{x} - \mathbf{x}_p)^\top \nabla \mathbf{q}(\mathbf{x}_p)) + \frac{d}{2}\|\mathbf{x} - \mathbf{x}_p\|^2$. We can write $\nabla h_0(\mathbf{x}) = \nabla \mathbf{q}(\mathbf{x}) \nabla f(\mathbf{q}(\mathbf{x}))$, and $\nabla \tilde{h}_0(\mathbf{x}; \mathbf{x}_p) =$

$\nabla \mathbf{q}(\mathbf{x}) \nabla f(\mathbf{q}(\mathbf{x}) + (\mathbf{x} - \mathbf{x}_p)^\top \nabla \mathbf{q}(\mathbf{x})) + d(\mathbf{x} - \mathbf{x}_p)$. It is clear that at $\mathbf{x} = \mathbf{x}_p$ we have $\nabla \tilde{h}_0(\mathbf{x}_p; \mathbf{x}_p) = \nabla h_0(\mathbf{x}_p)$.

[A7] The map $(\mathbf{x}, \mathbf{x}_p) \mapsto \nabla \tilde{h}_0(\mathbf{x}; \boldsymbol{\rho}, \mathbf{x}_p)$ is continuous on $\mathcal{K} \times \mathcal{X}$ for any given $\boldsymbol{\rho} \in \mathcal{W}$.

Finally, the surrogate constraint functions $\tilde{g}_{i,n} : \mathcal{K} \times \mathbb{R}_{\geq 0} \times \mathcal{W} \times \mathcal{X} \to \mathbb{R}$ $\forall i \in \{1, 2, 3, 4\}, n \in \mathcal{N}$ satisfy the following.

[A8] The map $(\mathbf{x}, u_{i,n}) \mapsto \tilde{g}_{i,n}(\mathbf{x}, u_{i,n}; \boldsymbol{\rho}, \mathbf{x}_p)$ is convex on $\mathcal{K} \times \mathbb{R}_{\geq 0}$ for any given $\boldsymbol{\rho} \in \mathcal{W}$ and $\mathbf{x}_p \in \mathcal{X}$. to see this, note that the composite function $\tilde{g}_{i,n} = f(\tilde{h}_{i,n} + u_{i,n}) - u_{i,n}\epsilon$ is given by the outer function $f(y) = \frac{1}{2}\left(y + \sqrt{\xi^2 + (y)^2}\right)$ which is strictly increasing and convex and by the inner function $\tilde{h}_{i,n} + u_{i,n}$ which is convex by construction; it then follows that $\tilde{g}_{i,n}$ is also convex.

[A9] $\tilde{g}_{i,n}(\mathbf{x}_p, u_{i,n}; \boldsymbol{\rho}, \mathbf{x}_p) = g_{i,n}(\mathbf{x}_p, u_{i,n}; \boldsymbol{\rho})$ for any given $\mathbf{x}_p \in \mathcal{X}$, $u_{i,n} \in \mathbb{R}_{\geq 0}$ and $\boldsymbol{\rho} \in \mathcal{W}$.

[A10] $g_{i,n}(\mathbf{x}, u_{i,n}; \boldsymbol{\rho}) \leq \tilde{g}_{i,n}(\mathbf{x}, u_{i,n}; \boldsymbol{\rho}, \mathbf{x}_p)$ for all $\mathbf{x} \in \mathcal{K}$, $u_{i,n} \in \mathbb{R}_{\geq 0}$ and for any given $\mathbf{x}_p \in \mathcal{X}$, $\boldsymbol{\rho} \in \mathcal{W}$.

[A11] The map $(\mathbf{x}, u_{i,n}, \mathbf{x}_p) \mapsto \tilde{g}_{i,n}(\mathbf{x}, u_{i,n}; \boldsymbol{\rho}, \mathbf{x}_p)$ is continuous on $\mathcal{K} \times \mathbb{R}_{\geq 0} \times \mathcal{X}$ for any given $\boldsymbol{\rho} \in \mathcal{W}$.

[A12] $\nabla \tilde{g}_{i,n}(\mathbf{x}_p, u^m_{i,n,p}; \boldsymbol{\rho}, \mathbf{x}_p) = \nabla g_{i,n}(\mathbf{x}_p, u^m_{i,n,p}; \boldsymbol{\rho})$ for all $\mathbf{x}_p \in \mathcal{X}$, $u^m_{i,n,p} \in \mathbb{R}_{\geq 0}$ and for any given $\mathbf{x}_p \in \mathcal{X}$, $\boldsymbol{\rho} \in \mathcal{W}$. To see this, using the chain rule we obtain

$$\begin{aligned} \frac{\partial g_{i,n}(\mathbf{x}, u)}{\partial \mathbf{x}} &= \frac{1}{2}\left(1 + \frac{h_{i,n}(\mathbf{x}) + u}{\sqrt{\xi^2 + (h_{i,n}(\mathbf{x}) + u)^2}}\right) \frac{\partial h_{i,n}}{\partial \mathbf{x}}, \\ \frac{\partial g_{i,n}(\mathbf{x}, u)}{\partial u} &= \frac{1}{2}\left(1 + \frac{h_{i,n}(\mathbf{x}) + u}{\sqrt{\xi^2 + (h_{i,n}(\mathbf{x}) + u)^2}}\right) - \epsilon. \end{aligned} \tag{A.10}$$

The claim is verified since $\frac{\partial \tilde{h}_{i,n}}{\partial \mathbf{x}}(\mathbf{x}_p; \boldsymbol{\rho}, \mathbf{x}_p) = \frac{\partial h_{i,n}}{\partial \mathbf{x}}(\mathbf{x}_p; \boldsymbol{\rho})$ and $\tilde{h}_{i,n}(\mathbf{x}_p; \boldsymbol{\rho}, \mathbf{x}_p) = h_{i,n}(\mathbf{x}_p; \boldsymbol{\rho})$ for all $\mathbf{x}_p \in \mathcal{X}$ and any given $\boldsymbol{\rho} \in \mathcal{W}$.

[A13] The map $(\mathbf{x}, u_{i,n}, \mathbf{x}_p) \mapsto \nabla \tilde{g}_{i,n}(\mathbf{x}, u_{i,n}; \boldsymbol{\rho}, \mathbf{x}_p)$ is continuous on $\mathcal{K} \times \mathbb{R}_{\geq 0} \times \mathcal{X}$ for any given $\boldsymbol{\rho} \in \mathcal{W}$.

Given the above properties [A1]–[A13], the following holds when using Algorithm 7.1 to solve (7.17).

Proposition A.1. *Consider the problem (7.17), and use Algorithm 7.1 with a step-size γ_p. Assume that one of the following two conditions is satisfied:*

- $0 < \inf_p \gamma_p \leq \sup_p \gamma_p \leq \gamma^{\max} \leq 1$ *and* $2c \geq \gamma^{\max} L_{\nabla h_0}$,
- $\mathcal{X}$ *is compact,* $\mathbf{x}^*(\mathbf{x}_p) \in \mathcal{X}$ *is regular for every* $\mathbf{x}_p \in \mathcal{X}$ *and* $\gamma^p \in (0, 1]$, $\gamma_p \to 0$, $\sum_p \gamma_p = +\infty$.

Then, every regular limit point of $\{\mathbf{x}_p\}$ is a stationary solution of (7.17). Furthermore, none of such points is a local maximum of $h_0(\mathbf{x})$. □

The result of Proposition A.1 follows from [Scutari et al., 2014, Theorem 1]. It asserts that the Algorithm 7.1 converges to a stationary solution of (7.17), and this solution is guaranteed not to be a local maximum.

B

REFERENCES

Adeniran, A. A. and El Ferik, S. (2016). Modeling and identification of nonlinear systems: A review of the multimodel approach-part 1. *IEEE Transactions on Systems, Man, and Cybernetics: Systems*, 47(7):1149–1159.

Al-Greer, M., Armstrong, M., Ahmeid, M., and Giaouris, D. (2018). Advances on system identification techniques for DC-DC switch mode power converter applications. *IEEE Transactions on Power Electronics*, 34(7):6973–6990.

Alam, M. J. E., Muttaqi, K. M., and Sutanto, D. (2014). A multi-mode control strategy for var support by solar PV inverters in distribution networks. *IEEE transactions on power systems*, 30(3):1316–1326.

Alam, M. S., Al-Ismail, F. S., Salem, A., and Abido, M. A. (2020). High-level penetration of renewable energy sources into grid utility: Challenges and solutions. *IEEE access*, 8:190277–190299.

Allibhoy, A. and Cortés, J. (2024). Control barrier function-based design of gradient flows for constrained nonlinear programming. *IEEE Transactions on Automatic Control*, 69(6).

Alonge, F., D'Ippolito, F., Raimondi, F. M., and Tumminaro, S. (2007). Nonlinear modeling of DC/DC converters using the hammerstein's approach. *IEEE Transactions on Power Electronics*, 22(4):1210–1221.

Ames, A. D., Coogan, S., Egerstedt, M., Notomista, G., Sreenath, K., and Tabuada, P. (2019). Control barrier functions: Theory and applications. In *European control conference*, pages 3420–3431.

Amos, B. and Kolter, J. Z. (2017). Optnet: Differentiable optimization as a layer in neural networks. In *International conference on machine learning*, pages 136–145. PMLR.

Angioni, A., Schlösser, T., Ponci, F., and Monti, A. (2015). Impact of pseudo-measurements from new power profiles on state estimation in low-voltage grids. *IEEE Transactions on Instrumentation and Measurement*, 65(1):70–77.

Antoniadou-Plytaria, K. E., Kouveliotis-Lysikatos, I. N., Georgilakis, P. S., and Hatziargyriou, N. D. (2017). Distributed and decentralized voltage control of smart distribution networks: Models, methods, and future research. *IEEE Transactions on Smart Grid*, 8(6):2999–3008.

Arnedo, L., Boroyevich, D., Burgos, R., and Wang, F. (2008). Polytopic black-box modeling of DC-DC converters. In *2008 IEEE Power Electronics Specialists Conference*, pages 1015–1021. IEEE.

Bacha, S., Munteanu, I., Bratcu, A. I., et al. (2014). Power electronic converters modeling and control. *Advanced textbooks in control and signal processing*, 454:454.

Baker, K. (2020). Emulating AC OPF solvers for obtaining sub-second feasible, near-optimal solutions. *arXiv preprint arXiv:2012.10031*.

Baker, K., Bernstein, A., Dall'Anese, E., and Zhao, C. (2018). Network-cognizant voltage droop control for distribution grids. *IEEE Transactions on Power Systems*, 33(2):2098–2108.

Baran, M. and Wu, F. (1989). Optimal capacitor placement on radial distribution systems. *IEEE Transactions on Power Delivery*, 4(1):725–734.

Bernstein, A. and Dall'Anese, E. (2019). Real-time feedback-based optimization of distribution grids: A unified approach. *IEEE Transactions on Control of Network Systems*, 6(3):1197–1209.

Bernstein, A., Wang, C., Dall'Anese, E., Le Boudec, J.-Y., and Zhao, C. (2018). Load flow in multiphase distribution networks: Existence, uniqueness, non-singularity and linear models. *IEEE Transactions on Power Systems*, 33(6):5832–5843.

Bianchi, M. and Dörfler, F. (2024). A stability condition for online feedback optimization without timescale separation. *arXiv preprint arXiv:2412.10964*.

Bolognani, S., Carli, R., Cavraro, G., and Zampieri, S. (2014). Distributed reactive power feedback control for voltage regulation and loss minimization. *IEEE Transactions on Automatic Control*, 60(4):966–981.

Bolognani, S., Carli, R., Cavraro, G., and Zampieri, S. (2019). On the need for communication for voltage regulation of power distribution grids. *IEEE Transactions on Control of Network Systems*, 6(3):1111–1123.

Bolognani, S. and Dörfler, F. (2015). Fast power system analysis via implicit linearization of the power flow manifold. In *2015 53rd Annual Allerton Conference on Communication, Control, and Computing (Allerton)*, pages 402–409. IEEE.

Bolognani, S. and Zampieri, S. (2015). On the existence and linear approximation of the power flow solution in power distribution networks. *IEEE Transactions on Power Systems*, 31(1):163–172.

Boyd, S., Parikh, N., Chu, E., Peleato, B., Eckstein, J., et al. (2011). Distributed optimization and statistical learning via the alternating direction method of multipliers. *Foundations and Trends® in Machine learning*, 3(1):1–122.

Capitanescu, F. (2016). Critical review of recent advances and further developments needed in AC optimal power flow. *Electric Power Systems Research*, 136:57–68.

Chai, E., Celanovic, I., and Poon, J. (2013). Validation of frequency-and time-domain fidelity of an ultra-low latency hardware-in-the-loop (HIL) emulator. In *2013 IEEE 14th Workshop on Control and Modeling for Power Electronics (COMPEL)*, pages 1–5. IEEE.

Chen, Y., Bernstein, A., Devraj, A., and Meyn, S. (2020). Model-free primal-dual methods for network optimization with application to real-time optimal power flow. In *American Control Conference*, pages 3140–3147.

Cheng, G., Lin, Y., Abur, A., Gómez-Expósito, A., and Wu, W. (2023). A survey of power system state estimation using multiple data sources: PMUs, SCADA, AMI, and beyond. *IEEE Transactions on Smart Grid*, 15(1):1129–1151.

Colot, A., Bastin, B., Ewbank, B., Frebel, F., Bidaine, B., and Cornélusse, B. (2023a). Hybrid power solution modelling based on artificial intelligence. *IET Conference Proceedings*, 2023:3114–3119.

Colot, A., Chen, Y., Cornélusse, B., Cortés, J., and Dall'Anese, E. (2025a). Optimal power flow pursuit via feedback-based safe gradient flow. *IEEE Transactions on Control Systems Technology*, 33(2):658–670.

Colot, A., Cornélusse, B., Cortés, J., and Dall'Anese, E. (2024a). Feedback-based safe gradient flow for optimal regulation of virtual power plants. In *IET Conference Proceedings CP904*, volume 2024, pages 1–6. IET.

Colot, A., Ewbank, B., Glavic, M., and Cornélusse, B. (2023b). A C-HIL based data-driven DC-DC power electronics converter model for system-level studies. In *2023 IEEE PES Innovative Smart Grid Technologies Europe (ISGT EUROPE)*, pages 1–5.

Colot, A., Giannitrapani, A., Paoletti, S., and Cornélusse, B. (2023c). Enhanced neural network-based polytopic model for large-signal black-box modeling of power electronic converters. In *2023 IEEE Belgrade PowerTech*, pages 01–06.

Colot, A., Paoletti, S., Giannitrapani, A., Glavic, M., and Cornélusse, B. (2025b). Interpretable large-signal black-box models of power electronic converters: a multimodel approach. *Submitted to IEEE Transactions on Power Delivery*.

Colot, A., Perotti, E., Glavic, M., and Dall'Anese, E. (2024b). Incremental Volt/Var control for distribution networks via chance-constrained optimization. *Accepted for publication in IEEE Transactions on Power Systems*.

Colot, A., Perotti, E., Glavic, M., and Dall'Anese, E. (2024c). A robust incremental Volt/VAR control for distribution networks. In *2024 IEEE PES Innovative Smart Grid Technologies Europe (ISGT EUROPE)*, pages 1–5. IEEE.

Colot, A., Shenoy, V., Cavraro, G., Dall'Anese, E., and Poveda, J. I. (2024d). On the stability of power transmission systems under persistent inverter attacks: A bi-linear matrix approach. *IEEE Control Systems Letters*, 8:1853–1858.

Colot, A., Stegen, T., and Cornélusse, B. (2023d). Fully distributed real-time voltage control in active distribution networks with large penetration of solar inverters. In *2023 IEEE Belgrade PowerTech*, pages 01–06.

Cui, W., Li, J., and Zhang, B. (2022). Decentralized safe reinforcement learning for inverter-based voltage control. *Electric Power Systems Research*, 211:108609.

Cvetkovic, I., Jaksic, M., Boroyevich, D., Mattavelli, P., Lee, F. C., Shen, Z., Ahmed, S., and Dong, D. (2011). Un-terminated, low-frequency terminal-behavioral dq model of three-phase converters. In *2011 IEEE Energy Conversion Congress and Exposition*, pages 791–798. IEEE.

D'Adamo, C., Jupe, S., and Abbey, C. (2009). Global survey on planning and operation of active distribution networks-update of CIGRE C6.11 working group activities. In *CIRED 2009-20th international conference and exhibition on electricity distribution-Part 1*, pages 1–4. IET.

Dall'Anese, E., Guggilam, S. S., Simonetto, A., Chen, Y. C., and Dhople, S. V. (2017). Optimal regulation of virtual power plants. *IEEE Transactions on Power Systems*, 33(2):1868–1881.

Dall'Anese, E. and Simonetto, A. (2016). Optimal power flow pursuit. *IEEE Transactions on Smart Grid*, 9(2):942–952.

Dhople, S. V., Guggilam, S. S., and Chen, Y. C. (2015). Linear approximations to AC power flow in rectangular coordinates. In *2015 53rd Annual Allerton Conference on Communication, Control, and Computing (Allerton)*, pages 211–217.

Dickert, J., Domagk, M., and Schegner, P. (2013). Benchmark low voltage distribution networks based on cluster analysis of actual grid properties. In *2013 IEEE Grenoble Powertech Conference*, pages 1–6. IEEE.

Eggli, A., Karagiannopoulos, S., Bolognani, S., and Hug, G. (2020). Stability analysis and design of local control schemes in active distribution grids. *IEEE Transactions on Power Systems*, 36(3):1900–1909.

EN50549-2, C. (2019). Requirements for generating plants to be connected in parallel with distribution networks - Part 2: connection to a MV distribution network - generating plants up to and including type B. *CENELEC*, pages 1–84.

Farivar, M., Chen, L., and Low, S. (2013). Equilibrium and dynamics of local voltage control in distribution systems. In *52nd IEEE Conference on Decision and Control*, pages 4329–4334.

Farivar, M., Zho, X., and Chen, L. (2015). Local voltage control in distribution systems: An incremental control algorithm. In *2015 IEEE International Conference on Smart Grid Communications (SmartGridComm)*, pages 732–737.

Fiacco, A. V. (1976). Sensitivity analysis for nonlinear programming using penalty methods. *Mathematical programming*, 10(1):287–311.

Francés, A., Asensi, R., García, O., Prieto, R., and Uceda, J. (2016a). A black-box modeling approach for DC nanogrids. In *2016 IEEE Applied Power Electronics Conference and Exposition (APEC)*, pages 1624–1631. IEEE.

Francés, A., Asensi, R., García, O., Prieto, R., and Uceda, J. (2016b). The performance of polytopic models in smart DC microgrids. In *2016 IEEE Energy Conversion Congress and Exposition (ECCE)*, pages 1–8. IEEE.

Frances, A., Asensi, R., Garcia, O., Prieto, R., and Uceda, J. (2017). Modeling electronic power converters in smart DC microgrids-An overview. *IEEE Transactions on Smart Grid*, 9(6):6274–6287.

Frances, A., Asensi, R., and Uceda, J. (2019). Blackbox polytopic model with dynamic weighting functions for DC-DC converters. *IEEE Access*, 7:160263–160273.

Gan, L. and Low, S. H. (2016). An online gradient algorithm for optimal power flow on radial networks. *IEEE Journal on Selected Areas in Communications*, 34(3):625–638.

Gupta, R. K. and Molzahn, D. K. (2024). Analysis of fairness-promoting optimization schemes of photovoltaic curtailments for voltage regulation in power distribution networks.

Gupta, S., Kekatos, V., and Chatzivasileiadis, S. (2024). Optimal design of Volt/VAR control rules of inverters using deep learning. *arXiv:2211.09557*.

Gupta, S., Mehrizi-Sani, A., Chatzivasileiadis, S., and Kekatos, V. (2023). Deep learning for scalable optimal design of incremental Volt/VAR control rules. *IEEE Control Systems Letters*, 7:1957–1962.

Hauswirth, A., Bolognani, S., Hug, G., and Dörfler, F. (2016). Projected gradient descent on riemannian manifolds with applications to online power system optimization. In *54th Annual Allerton Conference on Communication, Control, and Computing*, pages 225–232.

Hauswirth, A., Bolognani, S., Hug, G., and Dörfler, F. (2018). Generic existence of unique lagrange multipliers in AC optimal power flow. *IEEE Control Systems Letters*, 2(4):791–796.

Hauswirth, A., Bolognani, S., Hug, G., and Dörfler, F. (2020). Timescale separation in autonomous optimization. *IEEE Transactions on Automatic Control*, 66(2):611–624.

Hidalgo, R., Abbey, C., and Joós, G. (2010). A review of active distribution networks enabling technologies. In *IEEE PES General Meeting*, pages 1–9. IEEE.

Howlader, A. M., Sadoyama, S., Roose, L. R., and Chen, Y. (2020). Active power control to mitigate voltage and frequency deviations for the smart grid using smart pv inverters. *Applied Energy*, 258:114000.

Hussain, A., Garg, M. M., Korukonda, M. P., Hasan, S., and Behera, L. (2018). A parameter estimation based MPPT method for a PV system using Lyapunov control scheme. *IEEE Transactions on Sustainable Energy*, 10(4):2123–2132.

IEEE (1992). IEEE PES test feeders.

Jahangiri, P. and Aliprantis, D. C. (2013). Distributed Volt/VAr control by PV inverters. *IEEE Transactions on Power Systems*, 28(3):3429–3439.

Karagiannopoulos, S., Aristidou, P., and Hug, G. (2019). Data-driven local control design for active distribution grids using off-line optimal power flow and machine learning techniques. *IEEE Transactions on Smart Grid*, 10(6):6461–6471.

Kashani, M. G., Mobarrez, M., and Bhattacharya, S. (2017). Smart inverter volt-watt control design in high PV penetrated distribution systems. In *2017 IEEE Energy Conversion Congress and Exposition (ECCE)*, pages 4447–4452.

Kekatos, V., Zhang, L., Giannakis, G. B., and Baldick, R. (2015). Voltage regulation algorithms for multiphase power distribution grids. *IEEE Transactions on Power Systems*, 31(5):3913–3923.

Kersting, W. H. (2007). *Distribution System Modeling and Analysis*. 2nd ed., Boca Raton, FL: CRC Press.

Khalil, H. K. (2002). Nonlinear systems. *Patience Hall*.

Konstantopoulos, G. C. and Alexandridis, A. T. (2015). Enhanced control design of simple DC-DC boost converter-driven DC motors: Analysis and implementation. *Electric Power Components and Systems*, 43(17):1946–1957.

Kroposki, B., Bernstein, A., King, J., Vaidhynathan, D., Zhou, X., Chang, C.-Y., and Dall'Anese, E. (2020). Autonomous energy grids: Controlling the future grid with large amounts of distributed energy resources. *IEEE Power and Energy Magazine*, 18(6):37–46.

Kundur, P. (1994). *Power System Stability and Control*. McGraw-Hill.

Li, J., Xu, Z., Zhao, J., and Zhang, C. (2019). Distributed online voltage control in active distribution networks considering PV curtailment. *IEEE Transactions on Industrial Informatics*, 15(10):5519–5530.

Li, N., Qu, G., and Dahleh, M. (2014). Real-time decentralized voltage control in distribution networks. In *2014 52nd Annual Allerton Conference on Communication, Control, and Computing (Allerton)*, pages 582–588.

Liu, J. (1995). Sensitivity analysis in nonlinear programs and variational inequalities via continuous selections. *SIAM Journal on Control and Optimization*, 33(4):1040–1060.

Liu, Y., Xi, Z., Liang, Z., Song, W., Bhattacharya, S., Huang, A., Langston, J., Steurer, M., Litzenberger, W., Anderson, L., et al. (2009). Controller hardware-in-the-loop validation for a 10 MVA ETO-based STATCOM for wind farm application. In *2009 IEEE Energy Conversion Congress and Exposition*, pages 1398–1403. IEEE.

McDonald, J. (2013). Solar power impacts power electronics in the smart grid. *Power Electronics*.

Mestres, P., Nieto-Granda, C., and Cortés, J. (2024). Distributed safe navigation of multi-agent systems using control barrier function-based controllers. *IEEE Robotics and Automation Letters*.

Molzahn, D. K., Dörfler, F., Sandberg, H., Low, S. H., Chakrabarti, S., Baldick, R., and Lavaei, J. (2017). A survey of distributed optimization and control algorithms for electric power systems. *IEEE Transactions on Smart Grid*, 8(6):2941–2962.

Morstyn, T., Hredzak, B., and Agelidis, V. G. (2018). Control strategies for microgrids with distributed energy storage systems: An overview. *IEEE Transactions on Smart Grid*, 9(4):3652–3666.

Muscas, C., Pau, M., Pegoraro, P. A., and Sulis, S. (2014). Effects of measurements and pseudomeasurements correlation in distribution system state estimation. *IEEE Transactions on Instrumentation and Measurement*, 63(12):2813–2823.

Nagumo, M. (1942). Über die lage der integralkurven gewöhnlicher differentialgleichungen. *Proceedings of the Physico-Mathematical Society of Japan. 3rd Series*, 24:551–559.

Nazir, F. U., Pal, B. C., and Jabr, R. A. (2019). A two-stage chance constrained Volt/Var control scheme for active distribution networks with nodal power uncertainties. *IEEE Transactions on Power Systems*, 34(1):314–325.

Nelles, O. (1997). Orthonormal basis functions for nonlinear system identification with local linear model trees (LOLIMOT). *IFAC Proceedings Volumes*, 30(11):639–644.

Nellikkath, R. and Chatzivasileiadis, S. (2022). Physics-informed neural networks for AC optimal power flow. *Electric Power Systems Research*, 212:108412.

Nemirovski, A. and Shapiro, A. (2007). Convex approximations of chance constrained programs. *SIAM Journal on Optimization*, 17(4):969–996.

Olives-Camps, J. C., del Nozal, Á. R., Mauricio, J. M., and Maza-Ortega, J. M. (2022). A model-less control algorithm of DC microgrids based on feedback optimization. *International Journal of Electrical Power & Energy Systems*, 141:108087.

Ortmann, L., Hauswirth, A., Caduff, I., Dörfler, F., and Bolognani, S. (2020). Experimental validation of feedback optimization in power distribution grids. *Electric Power Systems Research*, 189:106782.

Pavella, M., Ernst, D., and Ruiz-Vega, D. (2000). *Transient stability of power systems: A unified approach to assessment and control*. Kluwer Academic Publishers.

Raz, T. (2024). ML interpretability: Simple isn't easy. *Studies in History and Philosophy of Science*, 103:159–167.

Rezaee, M., Moghadam, M. S., and Ranjbar, S. (2020). Online estimation of power system separation as controlled islanding scheme in the presence of inter-area oscillations. *Sustainable Energy, Grids and Networks*, 21:100306.

Rikos, A. I., Jiang, W., Charalambous, T., and Johansson, K. H. (2023). Asynchronous distributed optimization via ADMM with efficient communication. In *2023 62nd IEEE Conference on Decision and Control (CDC)*, pages 7002–7008. IEEE.

Rojas-Dueñas, G., Riba, J.-R., Kahalerras, K., Moreno-Eguilaz, M., Kadechkar, A., and Gomez-Pau, A. (2020). Black-box modelling of a DC-DC buck converter based on a recurrent neural network. In *2020 IEEE International Conference on Industrial Technology (ICIT)*, pages 456–461. IEEE.

Rojas-Dueñas, G., Riba, J.-R., and Moreno-Eguilaz, M. (2021). Black-box modeling of dc–dc converters based on wavelet convolutional neural networks. *IEEE Transactions on Instrumentation and Measurement*, 70:1–9.

Sadeghzadeh, A. and Garoche, P.-L. (2023). Autoencoder neural networks for LPV embedding of nonlinear systems. *IFAC-PapersOnLine*, 56(2):9062–9067.

Sahoo, S., Wang, H., and Blaabjerg, F. (2021). On the explainability of black box data-driven controllers for power electronic converters. In *2021 IEEE Energy Conversion Congress and Exposition (ECCE)*, pages 1366–1372. IEEE.

Sarajlic, D. and Rehtanz, C. (2019). Low voltage benchmark distribution network models based on publicly available data. In *IEEE PES Innovative Smart Grid Technologies Europe*.

Schoukens, J. and Ljung, L. (2019). Nonlinear system identification: A user-oriented road map. *IEEE Control Systems Magazine*, 39(6):28–99.

Scutari, G., Facchinei, F., Lampariello, L., and Song, P. (2014). Parallel and distributed methods for nonconvex optimization. In *2014 IEEE International Conference on Acoustics, Speech and Signal Processing (ICASSP)*, pages 840–844.

Serna Torre, P. and Hidalgo-Gonzalez, P. (2022). Decentralized optimal power flow for time-varying network topologies using machine learning. *Electric Power Systems Research*, 212:108575.

Srivastava, P., Haider, R., Nair, V. J., Venkataramanan, V., Annaswamy, A. M., and Srivastava, A. K. (2023). Voltage regulation in distribution grids: A survey. *Annual Reviews in Control*, 55:165–181.

Stanojev, O., Guo, Y., Aristidou, P., and Hug, G. (2022). Multiple ancillary services provision by distributed energy resources in active distribution networks. *arXiv preprint arXiv:2202.09403*.

Šulc, P., Backhaus, S., and Chertkov, M. (2014). Optimal distributed control of reactive power via the alternating direction method of multipliers. *IEEE Transactions on Energy Conversion*, 29(4):968–977.

Sun, Y., Chen, X., Yang, S., Rusli, Tseng, K. J., and Amaratunga, G. (2017). Micro PMU based monitoring system for active distribution networks. In *2017 IEEE 12th International Conference on Power Electronics and Drive Systems (PEDS)*, pages 518–522.

Takagi, T. and Sugeno, M. (1985). Fuzzy identification of systems and its applications to modeling and control. *IEEE transactions on systems, man, and cybernetics*, (1):116–132.

Tang, Y., Dvijotham, K., and Low, S. (2017). Real-time optimal power flow. *IEEE Transactions on Smart Grid*, 8(6):2963–2973.

Tarrasó, A., Lai, N. B., and Rodriguez, P. (2021). Resynchronization strategy for a 200 KVA grid-forming power converter. In *2021 IEEE Energy Conversion Congress and Exposition (ECCE)*, pages 1000–1005. IEEE.

Taylor, J. A., Dhople, S. V., and Callaway, D. S. (2016). Power systems without fuel. *Renewable and Sustainable Energy Reviews*, 57:1322–1336.

Thurner, L., Scheidler, A., Schäfer, F., Menke, J.-H., Dollichon, J., Meier, F., Meinecke, S., and Braun, M. (2018). pandapower–an open-source python tool for convenient modeling, analysis, and optimization of electric power systems. *IEEE Transactions on Power Systems*, 33(6):6510–6521.

Tremblay, O. and Dessaint, L.-A. (2009). Experimental validation of a battery dynamic model for ev applications. *World Electric Vehicle Journal*, 3(2):289–298.

Valdivia, V., Barrado, A., Lazaro, A., Sanz, M., del Moral, D. L., and Raga, C. (2013). Black-box behavioral modeling and identification of DC-DC converters with input current control for fuel cell power conditioning. *IEEE Transactions on Industrial Electronics*, 61(4):1891–1903.

Van Overschee, P. and De Moor, B. (2012). *Subspace identification for linear systems: Theory-Implementation-Applications*. Springer Science & Business Media.

Walling, R., Saint, R., Dugan, R. C., Burke, J., and Kojovic, L. A. (2008). Summary of distributed resources impact on power delivery systems. *IEEE Transactions on power delivery*, 23(3):1636–1644.

Wang, C., Bernstein, A., Le Boudec, J.-Y., and Paolone, M. (2017). Existence and uniqueness of load-flow solutions in three-phase distribution networks. *IEEE Transactions on Power Systems*, 32(4):3319–3320.

Wei, J., Gupta, S., Aliprantis, D. C., and Kekatos, V. (2023). A chance-constrained optimal design of Volt/VAR control rules for distributed energy resources. In *2023 North American Power Symposium (NAPS)*, pages 1–6.

Xu, T. and Wu, W. (2020). Accelerated ADMM-based fully distributed inverter-based Volt/Var control strategy for active distribution networks. *IEEE Transactions on Industrial Informatics*, 16(12):7532–7543.

Yuan, Z., Cavraro, G., Singh, M. K., and Cortés, J. (2024). Learning provably stable local Volt/Var controllers for efficient network operation. *IEEE Transactions on Power Systems*, 39(1):2066–2079.

Zeng, S., Kody, A., Kim, Y., Kim, K., and Molzahn, D. K. (2022). A reinforcement learning approach to parameter selection for distributed optimal power flow. *Electric Power Systems Research*, 212:108546.

Zhang, B., Lam, A. Y., Domínguez-García, A. D., and Tse, D. (2014). An optimal and distributed method for voltage regulation in power distribution systems. *IEEE Transactions on Power Systems*, 30(4):1714–1726.

Zhang, Y., Dall'Anese, E., and Hong, M. (2021). Online proximal-admm for time-varying constrained convex optimization. *IEEE Transactions on Signal and Information Processing over Networks*, 7:144–155.

Zhang, Y., Hong, M., Dall'Anese, E., Dhople, S. V., and Xu, Z. (2017). Distributed controllers seeking AC optimal power flow solutions using ADMM. *IEEE Transactions on Smart Grid*, 9(5):4525–4537.

Zhou, X., Farivar, M., Liu, Z., Chen, L., and Low, S. H. (2021). Reverse and forward engineering of local voltage control in distribution networks. *IEEE Transactions on Automatic Control*, 66(3):1116–1128.

Zhu, H. and Liu, H. J. (2016). Fast local voltage control under limited reactive power: Optimality and stability analysis. *IEEE Transactions on Power Systems*, 31(5):3794–3803.

Zhu, Y. and Xu, Z. (2008). A method of LPV model identification for control. *IFAC Proceedings Volumes*, 41(2):5018–5023.